

Mucosal landscape of the gut:
Development and application of 3D imaging
tools for interrogation of host-microbe
mucosal interface in mice and humans

Thesis by
Roberta Poceviciute

In Partial Fulfillment of the Requirements for
the degree of
Doctor of Philosophy

The logo for the California Institute of Technology (Caltech), featuring the word "Caltech" in a bold, orange, sans-serif font.

CALIFORNIA INSTITUTE OF TECHNOLOGY
Pasadena, California

2020
Defended July 16, 2020

© 2020

Roberta Poceviute
ORCID: 0000-0002-6649-2170

ACKNOWLEDGEMENTS

When I defended my thesis at 12 pm local (Los Angeles) time, at home in Lithuania, some 6,000 miles and 10 time zones away, it was 10 pm. The journey to and through Caltech has been more complicated than just hopping on a plane – many milestones had to be accomplished and opportunities sequestered. In retrospect, although in part I can attribute the successes to my inherent talents and character traits and hard work, I am largely in debt to life's generous circumstances and the environment that both supported and challenged me.

I have been lucky to have a colorful childhood and grow up surrounded by a loving and devoted family. My mother has always given the bigger, better piece to others, and to me in particular. She is a nurse, and as a child I would eagerly join her on her overnight shifts at the children's hospital, which seemed a lot more fun than playing at home by myself. I would play a double game of being both a patient and a nurse. I would pick out a free bed in one of the rooms with the kids of my age, make friends and, of course, enjoy the best part of being sick – the treats brought by their parents. When it was time for the nurses to distribute the medications, I would sneak into the rooms and watch how they dispensed the medications for each patient. I would join my mother as she visited each child, and I would be responsible for handing the tiny cups with colorful tablets to them. My dad was more of a trouble maker; he owned a motorcycle and would take me on open-air rides, memories that I remember only vaguely, but with a thrill. My grandparents and extended family were also a big part of my childhood. My grandmother has been an incredibly active woman, with enough energy to both work as an accountant and manage the family's big farm in her spare time. She has been devoted to our extended family and the local community, attending all the birthday parties and weddings, and lending a helping hand to people in need. A passionate traveler with trips all the way to India and Cuba, my grandmother was tasked to take me to the sea every summer to help my lungs recover from chronic bronchitis. We would never rely on a normal mode of transportation like a bus or a car. No, my grandma and I would hop on her company's truck on its long four-hour trip to the port. My grandfather was less active, and he loved baking pancakes whenever I visited. With excitement, he would bring the first still-hot pancake and throw it into my bed as an alarm clock. Keen on cars, speed, and trouble, my three uncles were a great source of excitement and adventure to me. I remember with nostalgia the hot summer days when we would drive to one of the lakes in the area, with the breeze coming in through the open windows and loud summer tunes blasting through the speakers. Nowadays, I see my family only rarely, but my childhood memories fill me with warmth and keep me feeling close during the years between my visits. And my family remains my most passionate cheer leaders, supporting me through the ups and downs despite the many miles that separate us.

Besides being obligated to help my grandparents on the farm, I grew up with few restrictions. I could spend time with friends past midnight on the weekends; in the summertime I was free to choose my hobbies, and I was not constrained to any career path. Although my grades were good, I too watched the clock anxiously until it clicked the time-to-go-home o'clock. Then, with relief, I would swap my backpack with books for my second backpack with art supplies and head to the local Alytus art school where I could finally lose track of time. The

art school was different than the regular school: the teachers were present in the classroom only sporadically, they did not command us to be quiet, and, as I later learned, they regarded clean easels and clean walls as a sign of suppressed creativity and freedom. Art teachers left an indelible impression on me. Vidas Janušonis, a pensive drawing teacher, would make his rounds through the classroom, stopping by each student to examine our progress in ominous silence. Then, with much deliberation, he would address the flaws with a calm, deep voice; what struck me was his focus on our drawings rather than general textbook teachings. Redas Diržys, the principal of the art school, was an altogether different animal to me. He taught the theory of modern art, depicting the inexplicable life and work of the modernists with humor and fresh criticism and shattering our preconceived notions of beauty and importance; in retrospect, the latter was perhaps the sole purpose of the class. Every time I went home during my undergraduate and graduate studies, I paid a visit to the art school to receive a booster against stagnation in my thinking.

To add thrill to school routine, I developed an obsession for science competitions. In the ninth grade, I qualified for the national chemistry competition, which I took very seriously, and studied any textbook and solved any problem that I could find. The national competition was intimidating at first, with students from big cities and sophisticated backgrounds talking loudly and with confidence. The last night was most petrifying: the solutions were posted on the walls, and we could study them until we were called in for a brief opportunity to look at our graded exams and appeal the score in person. Agitation was in the air as the students discussed their mistakes and schemed plans to gain more points. Barely noticed, I stood to the side and listened to their conversation, relieved and excited that my score was nearly perfect and I had nothing to appeal. The next day, to the surprise of my teachers and family, I picked up my first place diploma, which was like a master key that opened so many doors. I was immediately invited to participate in the chemistry boot camps at Vilnius University, where I studied alongside the upperclassmen who were preparing for international competitions. The boot camps were led and organized by Professor Rimantas Raudonis, whose patience and clarity of thought was fundamental to many young chemists, including me. Many other professors and university students were involved as well, including his wife, Jolanta Raudonienė, who was in charge of most laboratory sessions. Although she welcomed us with a big smile and laughter, she was a tough mentor who never let us get away with clumsiness or laziness, and I can attribute many of my good laboratory practices to her. The days were long, starting at 9 am and ending as late as 9 pm, composed of lectures, problem solving, and experiments. As a result of this well-organized training and our friendly competitiveness, we all progressed rapidly. Looking back, I view my gold medal at the International Chemistry Olympiad as a predictable consequence rather than the product of chance or talent alone. This accomplishment and all the training that led to it had undeniably opened the door to MIT for me.

In addition, I was invited to participate in a few-weeks-long National Student Academy sessions for recognized students during the summer and winter break, which I remember as the time of shared curiosity, openness, and friendship. Here we would spend part of the day focusing on one of our chosen subjects ranging from math to music, and part of the day learning about culture, socioeconomics, and politics, with ample time to socialize and enjoy

the seaside where the sessions took place. Jolanta Donskienė, one of the organizers, was instrumental to the success of these sessions owing to her undeniable (but warm and caring) authority, which instilled a sense of responsibility in us and permitted the good time to continue with minimal restrictions. The participation of her husband, Leonidas Donskis, was also essential to the nourishing atmosphere; a professor of philosophy and politics, a talk show host, a representative to European Parliament, a writer, and an art connoisseur, he had much to share with us. However, I best remember him for his passionate impromptu guitar concerts and the soulful atmosphere that they created with every note so deep that it felt infinite. Many other prominent figures of Lithuanian life also stopped by the sessions, including but not limited to the prime minister, the CEO of the major bank, and Mirga Gražinytė-Tyla, now a renowned classical music conductor with concerts even at LA's Walt Disney Concert Hall (I tried to never miss her concerts during my time at Caltech). Twice at these sessions I was honored to receive the Maestro Mstislav Rostropovich stipend, a much appreciated gift that allowed me to pay for a laptop, foreign university-level chemistry textbooks, as well as applications to US universities. I still cannot fully grasp the impact that these sessions had on me, especially the less tangible aspects, such as a well-rounded education, diverse network, and lasting friendships.

It was also at one of these sessions that I learned of Kaunas Technology University High School and their mission to provide the highest quality education to high school students from around the country. Professor Bronislavas Burgis had a vision to have the high school right across the street from Kaunas Technology University with professors teaching some of the classes and students from around the country living for free in university dormitories. Although I missed the entrance exams by a year, Professor Burgis welcomed me with great enthusiasm and generous accommodations. Recognizing that the students may underestimate their potential because they grow up in a small country, Burgis showed great confidence that we were among the top students in the world and was committed to helping us realize our goals. Burgis was also a bold and eccentric character, and his unconventional thoughts and ideas were of great amusement to me and perhaps were instrumental to founding this unconventional school. At Kaunas Technology University High School, I met chemistry teacher Birutė Maciulevičienė, who quickly recognized that regular chemistry classes were too easy for me and that I was better off mentoring junior chemistry enthusiasts towards chemistry competitions. Opportunity to teach was not only a great way to solidify my knowledge, but also to familiarize myself with teaching early on. However, I was perhaps most grateful for her unconditional support, which was much needed to persevere among the mounting pressures and expectations.

After I learned that I was accepted to MIT, I was tormented by feelings of excitement and terror until I arrived to the MIT campus. I applied to MIT because it ranked among the top schools in the world, however, I did not bother asking what that meant in practice until I was accepted (perhaps for the better because I may not have applied if I questioned it any earlier). I packed my suitcases very carefully, including what I thought was essential to my survival at MIT: the most powerful laptop that my mom and I could find in our town, all of the chemistry books that I had accumulated, a pillow, and a blanket. Upon the start of the freshman year, I quickly realized that I had a leg up in chemistry; therefore, in fear of an easy

ride if I majored in chemistry, I decided to major in chemical and biological engineering instead. While at MIT, I explored various career paths, including by undertaking an internship in a large biotech company, another internship in a small startup, and working in an academic research lab. Without a doubt, the latter was the most fulfilling to me, which ultimately determined my decision to pursue a PhD. To a large degree, I attribute my positive experience to my mentor Armon Sharei, a graduate student in chemical engineering co-advised by Klaus Jensen and Bob Langer. A risk taker, a scientist with great foresight and insight, and an exceptionally talented mentor, Armon created a nourishing environment for me and other fellow undergraduates to grow as young scientists and discover a passion for research. His success as a mentor was due in part to his moderation in mentorship, with enough space for us to experience and exercise independence. For instance, although Armon had always been a few steps ahead of me, he was courteous and let me arrive at the conclusions myself, and was not irritated when I made a mistake. Armon also added a sense of pride and thrill to my experience, for example, by entrusting me to use the core facility that undergraduate students were prohibited from, a secret that the facility manager never noticed. Finally, working with Armon was utterly fun both inside and outside the laboratory, with unrestrained laughter, group lunches, and birthday celebrations into the night (which generally resumed the next day with all of us now wearing lab coats). The memory of this fulfilling and exhilarating experience not only influenced my decision to pursue a PhD, but also guided me through research and mentorship opportunities that I had at Caltech.

My decision to come to Caltech was influenced by my encounter with Professor Rustem Ismagilov, who later became my graduate research advisor, during a graduate school visit. Back then, when I was contemplating on potential future directions, I was most captivated by the research into the brain. However, Rustem brought up an even more intriguing concept to me: the gut-brain axis. Never having heard of it before, I returned to MIT perplexed by the mysterious connection. This newly discovered fascination later served as a much needed fuel to power me through the long years of graduate school, even though my thesis ultimately only focused on the gut because it alone was an inexhaustible source of unanswered research questions. Rustem's dedication to building human and material capital alike made my graduate research possible. Furthermore, because Rustem involved the entire group in grant writing, equipment purchasing, hiring, and managing collaborations, I had an opportunity to experience first-hand the hard and strategic work that goes into securing resources and gathering a diverse group of scientists and engineers to tackle multidisciplinary research questions. My multifaceted graduate school experience, together with Rustem's insightful advice and the space that I was given to reflect on those challenges, largely contributed to my growth as an independent scientist. Finally, although I already liked and was trained to work fast, Rustem further challenged my productivity by being an epitome of efficiency, with prompt email responses and frequent one-on-one meetings despite being in charge of a large and diverse group. In fact, if there was ever a competition for the most responsive advisor, I predict that Rustem would certainly be in the race for the first place.

My resourceful and utterly entertaining thesis committee – Sarkis Mazmanian, Jared Leadbetter, and John Brady – were a much appreciated source of new ideas and alternative approaches to doing science. I first encountered Jared in a microbial-metabolism course,

where I, relying on his guidance, was thrilled to isolate environmental microbes capable of utilizing melatonin, a hormone produced in the brain to modulate sleep cycle, as a sole source of carbon and nitrogen. Jared agreed to be part of my thesis committee, and we continued to *talk microbes* throughout my PhD. I remember our conversations being particularly fun, taking unexpected turns and reaching unexplored depths because, as I quickly learned, Jared was an exceptionally curious, knowledgeable, and talkative character. In fact, our conversations were so much fun that they always ran overtime into our other commitments. Sarkis, a strikingly different character, was a source of succinct and grounding advice, some of which I remember word by word and ponder to this day. Although his schedule was packed, he always found time for me, and I honored every opportunity I had (including his lectures on mucosal immunology) to learn from this leading expert of host-microbe interactions in the gut. John Brady taught the graduate course in transport, which was by far the toughest subject I had encountered at Caltech. However, due to his mischievous, challenge-seeking, and boredom-evading demeanor, John managed to turn this challenging class into a uniquely fun experience, so fun that I approached 20-h-long homework assignments and overwhelming exams with a smile. From John I learned how to have fun while solving challenging problems, and how to utilize chemical engineering principles to approach multidisciplinary problems. Trying to predict the course of my committee meetings was pointless: something unexpected was bound to happen whenever these different personalities with expertise in diverse fields gathered together in a single room.

Perhaps, as Rustem had intended, leveraging our group's diverse expertise was cornerstone to my graduate work. I collaborated most closely with Octavio Mondragón-Palomino, a postdoctoral scholar who joined the group to pursue 3D imaging of mouse intestinal mucosa. When I was looking for a new project in my third year of graduate school, Rustem suggested that I collaborate with Octavio, who had recently joined the group. Rustem's foresight led to a fruitful learning and collaborative experience that eventually led to a fulfilling independent project for me. At the beginning, Octavio served as my mentor, collaborator, and companion whose patience and perseverance enabled progress through the toughest stages of the project, and up to this day Octavio remains a good friend and ally. I was also fortunate to be coached by and work with Said Bogatyrev, a senior member of the group, who generously shared his inexhaustible knowledge of the literature and his careful evaluation of various techniques, especially those pertaining to animal experiments. Even more impressively, Said was generous with his time, helping me hands-on at various stages of my project to both get the projects started and close them up. Finally, Said's investigation into the role of fecal re-ingestion in shaping the small-intestine microbiota has helped me to re-evaluate my own findings. In collaboration with Said, Jacob Barlow, a junior graduate student in the group, provided robust, easy-to-follow, and ready-to-use protocols for absolute quantification of bacteria, which saved me a lot of time and accelerated my progress. Furthermore, Jacob's curiosity of the many projects in the group and his insightful questions and comments during the group meetings helped me refine the framing of my projects. I was also honored to receive help from Anna Romano, an impressively careful and detail-oriented research scientist, on optimization, validation, and measurement of host gene expression, and later profiling of gut microbiota composition.

Mentoring the two cheerful and talented undergraduate students, Hazel Dilmore and Heli Takko, was one of the most fulfilling experiences of my graduate school. Even before they joined the group, I enjoyed planning their research projects, taking into consideration their time constraints, prior experiences, and future interests; after they joined, I had even more fun guiding them through their projects and, to the best of my ability, creating a positive experience for them. Heli contributed to the *in vitro* optimization of hybridization chain reaction (HCR) tagging of bacteria and image analysis based on machine learning (in fact, our collaborator in Finland, Antti Lignell, suggested that Heli should come for a summer and transfer their expertise in machine learning to us), whereas Hazel was responsible for the profiling of gut microbiota composition as well as optimization, validation, and measurement of secreted inflammatory markers in the intestinal contents. They both progressed rapidly and made tangible contributions to my projects. However, I was perhaps most appreciative of their company and cheerfulness, which I heavily relied on as an antidote to the pressures of leading research projects.

Although I did not work as closely with other members of the group, I can attest that everyone made crucial contributions to my work regardless of the scope. In fact, I had a lot of fun matching a problem to the right expertise in the group – normally, chatting with the right person quickly provided a solution to a problem. Over time, I gathered that chemistry and chemical engineering related issues could be addressed by simply announcing them to Erik Jue, Justin Rolando, Dmitriy Zhukov, and later also Si Hyung Jin (who all sat in the same aisle of the office, which we referred to as the *corner*). For instance, I am indebted to Erik for suggesting how to prevent air bubble formation during imaging, a seemingly simple but in practice very frustrating problem. Erik also pointed me and Octavio to a stock of plastic in the lab that he rescued from disposal, and this plastic turned out to be a perfect solid support to our hydrogel-tissue hybrids. Justin was a go-to person whenever surfactants were involved, let it be synthesis of specialty surfactants for microfluidic devices, selection of optimal surfactants for the wash of hydrogel-tissue hybrids, or measurement of bile acids in intestinal contents. Justin, with contributions from rotation student James Park, was also instrumental to deciphering reaction mechanisms and understanding at a molecular level the macroscopic characteristics of hydrogel-tissue hybrids. Finally, I could rely on Dmitriy and Si Hyung whenever I needed help with microfluidic devices and silanization. Joanne Lau, together with Said Bogatyrev, invested a lot of time and effort in maintaining anaerobic chambers and assisting with the anaerobic culture of bacteria; furthermore, because Joanne was my closest office neighbor, she was the first person I turned to when I needed to talk through my experimental design or results. Our lab's dedicated bio- and chemical-safety coordinators, Mary Arrastia, Emily Savela, Jenia Khorosheva, Justin Rolando, and Matt Cooper, as well as Caltech's Lauriane Quenee and Nathan Siladke, worked hard to ensure our safety and mitigate the effect of our experiments on the environment. In addition to the current and most recent group members, long-gone former group members – Songzi Kou, Liang Ma and Mikhail Karymov – were also an important part of my journey by mentoring me through my initial projects in microfluidics and teaching me the fundamentals in microscopy.

Some group members enriched my understanding of microbe-microbe and host-microbe interactions not through direct collaborations, but through sharing their findings and providing feedback to my work. Tahmineh Khazaei, for instance, used computational and *in vitro* tools to study metabolic coupling between *Klebsiella pneumonia* and *Bacteroides thetaiotaomicron*, close relatives of bacterial isolates used in my project; in so doing, she further motivated my work and provided additional hypotheses to explain my observations. Sujit Datta, Asher Preska Steinberg, and Michael Porter studied the physical mechanisms of mucus compression and bacterial aggregation, and learning about their work deepened my appreciation of the complexity of host-microbe and microbe-microbe interactions in the gut and the various factors that govern them. Due to their inexhaustible knowledge of physiology and medicine, our two MD-PhD students, Eric Liaw and Alex Winnett, also provided valuable feedback and context for my work. Even after I collected and analyzed the data, a lot of work remained to be done to communicate findings to a broader audience. Keen on framing, Rustem was instrumental at this stage. Tasha Shelby, our lab manager and scientific editor, also made major contributions by carefully reading and editing my drafts to ensure that our writing accurately captured the intended message and conveyed it effectively to a broad audience. Furthermore, Tasha contributed beyond her role as an editor, spotting logical errors and suggesting additional points worthy of discussion. Similarly, Rustem, Tasha, and the rest of the group were instrumental to polishing my oral presentations and my thesis defense in particular. I was humbled to receive a lot of carefully thought-through feedback that guided the final version of my talk.

In addition to our group and my thesis committee, other members of the Caltech community as well as outside collaborators shaped and contributed to my work. HCR experts – Harry Choi, Maayan Schwarzkopf, Grace Shin, and Antti Lignell – provided help at various stages of the projects. Early on, Octavio and I received advice from Harry Choi and Antti Lignell on the implementation of HCR v2.0 for visualization of bacteria in hydrogel-tissue hybrids of mouse intestine. Throughout the years, Grace Shin worked around the clock to synthesize custom HCR reagents and, towards the end, encouraged me to consider the superior HCR v3.0 technology. At the end, amidst the chaos of the pandemic, Maayan Schwarzkopf found time to design HCR v3.0 probes and assisted me in the selection of the degenerate universal HCR v3.0 probes. Throughout the years, the biological imaging facility at Caltech led by Andres Collazo and assisted by Giada Spigolon, Blaise Ndjamen, and Steven Wilbert provided training and technical assistance with confocal fluorescence microscopy; moreover, they enthusiastically engaged in lengthy discussions on the technical challenges of complex imaging experiments and the best strategies to work around the limitations of physics. A lot of responsibility was taken off of our shoulders by the reliable and attentive animal care staff, who cared for our experimental animals on our behalf. Additionally, OLAR personnel and the veterinarian technicians were a great resource when planning complicated animal experiments and performing delicate procedures. Outside collaborators at Cedars-Sinai Medical Center – Suzanne Devkota, Mark Pimentel, and their group members – expanded our understanding of host-microbe interactions beyond animal models and enabled the translation of our developed tools to clinical studies. For instance, Rustem and Mark Pimentel have been leading a translational collaboration between Cedars-Sinai Medical Center and Caltech; the opportunity to hear Pimentel’s latest findings and

feedback on our development of quantitative tools helped me recognize the potential of our 3D imaging technology in clinical research. Finally, Suzanne Devkota generously shared resected human gut samples from IBD surgeries, which is helping us translate our 3D imaging tools to human gastrointestinal tissues. I first learned about Suzanne's ongoing research at her organized Keystone Symposia and, immediately after hearing her talk, recognized an opportunity for a collaboration. I was later pleasantly surprised that Suzanne not only responded to my email the same day, but also facilitated the paperwork such that I could pick up the first human gut sample within two weeks of contacting her. Perhaps this is a perfect example of a fruitful conference: stimulating in the moment and enabling new science even after it ends.

Countless other people and resources at Caltech made my journey smoother. Being an international student, I heavily relied on International Student Programs, Laura Flower Kim and Daniel Yoder in particular who enthusiastically welcomed me to Caltech and assisted with immigration paperwork throughout the years. Registrar's and graduate student offices as well as chemical engineering option representative, Konstantinos Giapis, kept me on track towards fulfilling PhD requirements, and numerous administrators – Sohee Lee, Allison Kinard, Kathy Bubash, Martha Hepworth, and Katie Fisher – helped with scheduling, kept me on track regarding various obligations, and relieved me of administrative tasks. In particular, I am grateful to Sohee Lee who took an extra step to help organize our group's celebrations, even bringing party balloons in her small car to cheer me up after my thesis defense, as well as Martha Hepworth who would notify me of packages and was particularly excited for me whenever I received a package from home.

Graduate school would have been less fun and less endurable without the cheerful and supportive friends I found at Caltech. My lab mate Tahmineh Khazaei was one of the most precious immaterial gifts that I received at Caltech, whose support and encouragement carried me through the toughest challenges and whose sense of humor made me laugh on the most somber days. Despite our distinct cultural backgrounds, Tami would understand me before I even had a chance to explain myself fully, and in retrospect I see how rare and precious such mutual understanding is. Said Bogatyrev was also not only a great colleague but also a committed friend who cared for me throughout the years and at the finish line, even bringing me food when I was too focused on my thesis to think about eating. Both Tami and Said continued to support me through the challenging times of the pandemic, ready to talk on the phone whenever I needed support. Justin Rolando, a well-rounded character with interests in music, travel, sports and even flying, was behind many indelible adventures that I had in graduate school, like attending classical music concerts at Walt Disney Concert Hall and flying over LA in a small four-person plane. Although I may have spent less time with Erik Jue outside the lab, time and time again I learned that Erik was a reliable friend ready to listen and give his best advice. Due to their friendly and easy-going demeanor, both Dmitriy Zhukov and Asher Preska Steinberg were like a source of tranquility to me, and talking to them always lightened up my day. Finally, Tasha Shelby again exceeded the expectations as a lab manager, caring for my wellbeing inside and outside the lab and making time to listen and offer help and advice. In addition to my colleagues, my roommates – Kelly Mauser, Paul Magyar, Sean Symon, Melissa Buttner, and Jingxin Liang – were my other

support system who welcomed me every night with empathy and shared their own experiences in other disciplines, expanding my appreciation for Caltech's diverse scientific community. Caltech art house and tango club provided not only a break from science and an opportunity to exercise the other side of my brain but also friendship and a sense of community both inside and outside Caltech. Jim Barry in particular was like my other mentor at Caltech whose enthusiasm for my artistic ideas as well as advice on their implementation helped me materialize a number of surrealistic paintings (Fig. A1), whereas Anastasia Chmeritskaya and Mark Van Vlack were an inexhaustible source of support, wisdom and new perspective to my every day challenges.

Although I pursued a PhD far away from home and family, I had many opportunities to enjoy the sisterhood and brotherhood of the Lithuanian community at Caltech and California in general. To my pleasant surprise, I was not the only Lithuanian at Caltech and, soon after arriving to Caltech, I met Jonas and Vilia Zmuidzinas, who cared for me throughout my graduate studies. They welcomed me to their Thanksgiving and traditional Lithuanian Christmas Eve dinners, which I remember for the exceptionally delicious dishes, hospitable company, and inexhaustible conversations. At these dinners, I had an opportunity to meet their family, including Jonas's stepmother and Vilia's mother who left Lithuania during WWII and were like the most precious history books to me. Lithuanian Consulate General in LA and Lithuanian communities in both LA and SF organized many events, facilitating connections and friendships among Lithuanians of different backgrounds. At these events, I met Vaida Kidykaitė, Julius Narkus and Tautvydas Kymantas, with whom we shared many adventures and celebrations and learned about each other's different career paths. Rūta Meilutytė, Margiris Meilutis, and Mindaugas Meilutis, the three siblings, brought a particularly authentic piece of home to LA. Based in Lithuania and having lived in LA for a year, they caught me up on life and culture in Lithuania and were great companions in exploring California, with adventures into the different parts of LA, roads trips to the other-worldly desserts, delicious meals, and soulful conversations. Finally, I did not lack visitors from Lithuania, with Vladas Oleinikovas being the most frequent one. Perhaps due to our similar paths, Vladas remained one of my best friends and most passionate advocates, and perhaps due to his active extraverted personality, Vladas not only revived old memories but also brought new adventures every time he visited.



Figure A1. Roberta Poceviute. *Brainwashed*, 2018. Acrylic on canvas, 24 x 36 inches. Although I cannot claim with certainty, *Brainwashed* was perhaps inspired by the concept of the gut-brain axis that I learned about at Caltech. To me, the creative process is ill-defined and poorly controlled; although I recognize commonly encountered objects and concepts in my paintings, I do not combine them deliberately, but rather wait until a composition worthy of realization appears in my imagination. The generous resources at Caltech Art House and Jim Barry's insightful advice have made the realization of *Brainwashed* and other paintings possible.

ABSTRACT

Mammalian gastrointestinal tract is inhabited by trillions of microbes that, in number, amount to the total number of cells in the human body. These microbes, collectively known as microbiota, are found on the skin and in body cavities, and come in close contact with the host on mucosal surfaces. Here, pivotal host-microbe interactions likely take place because close proximity to the host enhances the uptake of microbial metabolites by the host and enables direct contact. To aid the investigation of these interactions, we developed an imaging technology that preserves fragile mucosal structure, enables to explore large areas of mucosal surface, and image the structurally and biochemically complex host-microbe interface in 3D in a mouse. However, 3D imaging presents challenges, such as slow transport of large molecular weight reagents and low signal/background ratio at depth, and these challenges are further exacerbated in particularly thick samples, such as small intestinal samples with long finger-like villus protrusions and thick human gut samples. Therefore, we further advanced our technology to improve sensitivity and specificity at depth, and we have taken steps to translate our technology to precious resected human gut samples from inflammatory bowel disease patients. Finally, we applied these tools to interrogate *Enterobacteriaceae* – *Bacteroidaceae* interactions in the small intestine of a mouse weakened by malnutrition. Using complementary tools, we have first determined that *Bacteroidaceae* required malnutrition to increase in number in the jejunum digesta, whereas *Enterobacteriaceae* required both malnutrition and *Bacteroidaceae*. With imaging, we visualized that in malnourished controls, bacteria were effectively cleared after digesta passage, whereas in malnourished mice co-gavaged with *Enterobacteriaceae* and *Bacteroidaceae* bacteria were retained, suggestive of bacterial adherence to and colonization of mucosa. Finally, we detected a rare event of abundant bacterial colonization of small intestinal mucosa and captured in 3D.

PUBLISHED CONTENT AND CONTRIBUTIONS

Octavio Mondragón-Palomino, Roberta Pocevičiute, Antti Lignell, Jessica Griffiths, Long Cai, and Rustem F. Ismagilov. “3D imaging for the quantitative discovery of spatial patterns in the microbiota of the intestinal mucosa.” 2020. In revision.

R.P.: Major contributor to the development of the sample preparation method. Developed the assay for the optimization of lysozyme treatment. Collected all data of lysozyme treatment optimization. Collected samples for sequencing with OMP. Analyzed all data of lysozyme treatment optimization experiments in coordination with OMP. Contributed to the analysis of data from *in vitro* hybridization assays in shallow gels. Created Fig. 2c and Supplementary Figs. S1-S2. Supplied plots for Supplementary Fig. S4, and color intensity plot for final version of Fig. 5b. Wrote methods and results/discussion of lysozyme treatment optimization.

TABLE OF CONTENTS

Acknowledgements.....	iv
Abstract.....	xv
Published Content and Contributions.....	xvi
Table of Contents.....	xvii
List of Figures and Tables.....	xviii
Nomenclature.....	xxi
Chapter 1: Thesis Introduction and Summary	1
References.....	9
Chapter 2: Abstract and Significance.....	11
Introduction.....	12
Results.....	14
Discussion.....	29
Methods	32
References.....	35
Supplementary Information	38
Chapter 3: Introduction.....	61
Results.....	65
Discussion.....	82
Methods	85
References.....	96
Supplementary Information	99
Chapter 4: Introduction.....	103
Results.....	106
Discussion.....	140
Methods	143
References.....	154
Supplementary Information	157

LIST OF FIGURES AND TABLES

<i>Number</i>	<i>Page</i>
1. Figure A1. Roberta Pocevičute. <i>Brainwashed</i> , 2018. Acrylic on canvas, 24 x 36 inches.....	xii
2. Figure 1. Sample preparation and imaging for 3D mapping of the mucosal microbiota's spatial structure.....	15
3. Figure 2. Sensitivity and specificity of fluorescence imaging of bacteria embedded in acrylamide gels using dual embedding.....	18
4. Figure 3. Spatial structure of the host-microbiota interface.....	20
5. Figure 4. Multiscale imaging shows that the cecal mucosa is colonized in patches.....	22
6. Figure 5. Multiplexed staining of the native mucosal microbiota is specific and comprehensive.....	24
7. Figure 6. Statistical analysis of the composition of single-crypt communities reveals spatial and demographic patterns.....	26
8. Figure 7. Quantification of the spatial organization of bacterial colonies inside crypts.....	28
9. Figure S1. Lysozyme treatment optimization using <i>Bacteroides fragilis</i> as a model Gram-negative bacterium.....	49
10. Figure S2. Empirical cumulative distributions functions (ECDF) of HCR staining of <i>Bacteroides fragilis</i> over entire image stacks.....	50
11. Figure S3. Experimental workflow to obtain the formamide hybridization curves of HCR probes with taxon-specific detection sequences.....	51
12. Figure S4. Formamide bar plots for the hybridization of taxon-specific HCR probes to their ideal targets.....	52
13. Figure S5. Large-scale imaging of the proximal colon and the distal ileum.....	53

14. Figure S6. Scatter plots of the abundances (voxel counts) for pairs of bacterial taxa inside crypts, and the value of Spearman's correlation.....	54
15. Figure S7. T-distributed stochastic neighbor embedding method (tSNE) for crypt classes identified by a hierarchical clustering analysis.....	54
16. Table S1. Detection sequences in HCR probes and their ideal bacterial targets.....	56
17. Table S2. HCR initiator sequences and the corresponding fluorescent hairpins used in this study.....	57
18. Figure 3.1. A protective surface hydrogel retains loosely adherent bacteria and mucus in a mouse proximal colon.....	66
19. Figure 3.2. Schematic of a general two-step hydrogel embedding protocol for prompt hydrogel fortification of the fragile mucosa and the subsequent hydrogel embedding of the underlying tissue with surface and tissue hydrogel formulations.....	69
20. Figure 3.3. Optimization of hydrogel chemistry improves antibody penetration into a hydrogel.....	70
21. Figure 3.4. Adoption of HCR v3.0 mitigates false positive signal amplification at depth <i>in vitro</i>	74
22. Figure 3.5. Design of the universal degenerate split HCR v3.0 probe set.....	76
23. Figure 3.6. Comparison of the degenerate universal HCR v3.0 probe set and EUB338 HCR v2.0 probe in a mouse proximal colon.....	79
24. Figure 3.7. Multi-modal staining of mouse small intestinal tissue.....	80
25. Figure 3.8. 3D imaging of resected human gut from one IBD patient using optimized hydrogel chemistry.....	82
26. Table 3.1. Surface-gel and tissue-gel monomer mix chemistries.....	87
27. Figure 3.S1. Hydrogel-tissue hybrid wash with a formaldehyde scavenger improves antibody staining.....	100
28. Figure 3.S2. Protective surface gel can act as a reagent sink.....	101

29. Table 3.S1. HCR v2.0 and HCR v3.0 probe sequences.....	102
30. Figure 4.1. Experiments aiming to reproduce the published EE mouse model.....	108
31. Figure 4.2. Relative abundance of major bacterial taxa in jejunum digesta and feces assessed by 16S rRNA gene amplicon sequencing.....	111
32. Figure 4.3. Absolute quantification of gavaged and selected resident bacteria in jejunum digesta and feces across six mouse groups as assessed by 16S rRNA gene amplicon sequencing.....	114
33. Figure 4.4. Pilot experiment showing empty jejunum segments of malnourished mice without fasting.....	120
34. Figure 4.5. Image analysis of bacterial aggregates shown in Fig. 4.4B.....	123
35. Figure 4.6. Inspection of large opaque surface aggregates detected in fasted mice by eye and their imaging by microscopy.....	127
36. Figure 4.7. Image analysis of CLARITY-processed tissues displayed in Fig.4.6 and Fig.4.S7 with two mice per group and one tissue per mouse.....	129
37. Figure 4.8. Imaging of mucosal bacteria detected in MAL+EC&BAC day 28 mouse.....	131
38. Figure 4.9. Imaging of mucus and mucosal bacteria detected in MAL+EC&BAC day 28 mouse.....	134
39. Figure 4.10. Visualization of host components in large surface aggregates detected in MAL+EC&BAC day 31 mouse.....	137
40. Figure 4.11. Cross-sectional view of large surface aggregates detected in MAL+EC&BAC day 31 mouse.....	139
41. Figure 4.S1. Absolute quantification of 16S rRNA gene copies of three key families that are solely represented by a single genus.....	158
42. Figure 4.S2. Absolute quantification of 16S rRNA gene copies of <i>Bacteroides</i> and <i>Parabacteroides</i> genera in jejunum digesta and feces.....	160

43. Figure 4.S3. Absolute quantification of <i>Enterobacteriaceae</i> in mouse GIT by different methods and across experiments as well as mice.....	162
44. Figure 4.S4. Absolute quantification of 16S rRNA gene copy abundance of the resident bacterial orders in jejunum digesta and feces across six mouse groups.....	164
45. Figure 4.S5. HCR v3.0 probes designed using full 16S rRNA sequences of the gavaged bacterial isolates.....	166
46. Figure 4.S6. Photos of empty jejunum segments after clearing.....	167
47. Figure 4.S7. Low magnification tile scans and example CLARITY images of tissues shown in Fig.3.S6.....	168

NOMENCLATURE

Microbiota. Microbes that associate multicellular organisms.

Host. Multicellular organisms that hosts microbiota.

Mucosa. Epithelial surface exposed to the environment, including the microbiota.

Mucus. Host-secreted biological hydrogel that maintains homeostasis on the mucosa.

Small intestine. Part of the gastrointestinal tract responsible for food digestion and nutrient absorption and characterized by low microbial loads.

Large intestine. Part of the gastrointestinal tract responsible for waste processing and characterized by high microbial loads.

Villus. Finger-like protrusions of small intestinal epithelium into the lumen that increase the absorptive area.

Intervillus space. Mucosal space in between villus protrusions.

Crypt. Indentation of intestinal epithelial surface found in both small and large intestines.

SIBO. Small intestinal bacterial overgrowth characterized by either quantitative (increase in total bacterial load) or qualitative (for example, presence of colonic anaerobes) changes to small intestinal microbiota.

IBD. Inflammatory bowel disease characterized by severe inflammation of the mucosa.

CLARITY. 3D imaging method that stabilizes tissue proteins, DNA and RNA, but removes light-scattering lipids for improved imaging depth.

Chapter 1

INTRODUCTION AND SUMMARY

In this thesis, I describe two advances: first, the development of a novel 3D imaging technology for studies of host-microbe interactions in the mucosa of the mammalian gut, and second, the application of this technology in an animal model to investigate the association of *Enterobacteriaceae* and *Bacteroidaceae* in the small intestine and the role of this association in the context of malnutrition and environmental enteropathy (EE).

Imaging is a key technique in understanding host-microbe and microbe-microbe interactions on the mucosal surfaces of the intestine. Other commonly used methods like sequencing normally require sample homogenization and, as a result, report average levels of target analyte, e.g. bacterial load or host marker expression, across space. This averaging may be suitable in the study of luminal and fecal microbiota because microbiota in these locations have been shown to be well-mixed^{1,2}; however, averaging is not appropriate in the study of mucosal microbiota because the mucosal landscape of the host is complex, and villi, crypts, and epithelial folds prevent thorough mixing. Such spatial heterogeneity in the composition of mucosal microbiota, as well as the proximity of microbes to the host, can result in great spatial variability in host-microbe interactions in the mucosa. Therefore, the study of mucosal microbiota requires imaging modalities that can map exact microbial locations with respect to each other as well as with respect to host cells and secretions, e.g., mucus. Additionally, host-microbe and microbe-microbe interactions are three-dimensional (3D), so the optimal imaging modality should enable visualization of 3D spatial structure across large areas of tissue to fully capture and quantify the spatial heterogeneity of this region.

In Chapter 2 of this thesis, I describe the development of an imaging technology capable of visualizing the spatial structure of the host-microbe interface on mucosal surfaces. The gold standard of imaging has been imaging thin sections of tissue; however, thin sections cannot convey the 3D spatial structure unless a laborious 3D reconstruction from many separate

sections is performed. Recently, advances have been made to image microbial communities in 3D. For example, imaging dimensionality of sections was increased by increasing section thickness and stabilizing luminal contents and mucus with a hydrophilic resin; however, the thicker sections were still only 12.5 μm thick and captured only limited area of the mucosal surface³. The breakthrough in 3D imaging has taken place in the field of neuroscience where the original CLARITY method was developed⁴⁻⁷. CLARITY relies on the idea that tissue lipids are largely responsible for light scattering and shallow imaging depth, however, they can be removed with a strong surfactant while nucleic acid and protein staining targets can be stabilized in their native location by a hydrogel. CLARITY methodology has already been adopted in the field of microbiology and microbiota. For example, in combination with sensitive detection of bacteria by hybridization chain reaction (HCR v2.0^{8,9}), CLARITY was used to visualize bacteria in the sputum of cystic fibrosis patients and their association with secreted mucus and free host cells¹⁰. However, host epithelium was not captured by this method. CLARITY has also been used to preserve and clear an intact mouse gut^{11,12}; however, bacteria were not visualized by these methods. Considering the advantages and limitations of these existing methods, in Chapter 2 of this thesis we describe the development of a novel acrylamide hydrogel-based imaging technology that retains bacteria and mucus on the mucosal surfaces, is compatible with lipid clearing for 3D imaging, and allows for sensitive visualization of bacteria with respect to each other, host epithelial surface, and mucus secretions by staining bacteria using HCR v2.0. The resulting hydrogel-tissue hybrids allow to explore large areas of mucosal surfaces and image target events at higher magnification in 3D.

In Chapter 3 of this thesis, I address the technical challenges of applying our 3D imaging technology to particularly thick samples (100 - 500 μm). Specifically, although acrylamide hydrogel was necessary to retain loosely adherent bacteria and mucus and to stabilize the underlying tissue during clearing (Fig.3.1), it also slowed reagent transport during staining and washing. As a result, during reagent incubation, the ratio of reaction rate to diffusion rate, or Damköhler number, was high leading to reagent accumulation at the surface and weak staining deep in the hydrogel-tissue hybrid^{13,14}. Furthermore, in the case of reagents

with high molecular weight, e.g. antibodies, our original hydrogel chemistry was essentially impermeable (Fig.3.3, A-B). Similarly, during reagent wash, reagents deep in the hydrogel-tissue hybrids were not effectively removed. In the case of HCR tagging of bacteria, poor removal of HCR v2.0 probes resulted in amplified background (Fig.3.6, A, D, and J) and amplified false-positive signal (Fig.3.5, A-B). To address these issues, we further developed the hydrogel chemistry such that it still retains loosely adherent bacteria mucus, but makes the gel more permeable to antibodies (Fig.3.3). Furthermore, to mitigate amplified non-target signal of HCR, we translated the new version of HCR probes (HCR v3.0¹⁵) for more specific bacterial detection at greater depths into the mucosa (Figs.3.6-7). These new technological developments enabled us to better characterize host cells with antibody staining and improved the specificity of bacterial detection.

Finally, in Chapter 4 of this thesis, I leverage the advanced clearing and imaging tools developed in Chapters 2-3 to elucidate the dynamics of the association between *Enterobacteriaceae* and *Bacteroidaiceae*, an association that occurs in several disease states. Members of the *Enterobacteriaceae* family can cause severe, drug-resistant urinary tract, lung, and blood infections¹⁶, and they are also thought to drive dysbiosis in the gut^{17,18}. Curiously, *Enterobacteriaceae* co-occur with *Bacteroidaceae* in several clinical contexts of the gastrointestinal tract (GIT), such as colon cancer¹⁹ inflammatory bowel disease (IBD)²⁰, and small intestinal bacterial overgrowth (SIBO)¹⁸. The association of these taxa in the small intestine (SI) is particularly intriguing because the higher oxygen levels in the SI than in the colon²¹ should suppress the growth of strictly anaerobic *Bacteroidaceae*. However, metabolic modeling and *in vitro* bioreactor experiments in our lab have recently shown that oxygen consumption by the facultative anaerobes in the *Enterobacteriaceae* family permits the growth of strict anaerobes in the *Bacteroidaceae* family whereas degradation of complex carbohydrates by *Bacteroidaceae* supports *Enterobacteriaceae* growth²². Understanding the impact of such synergistic SI communities on the host is relevant because compared with the colon, the SI has a 15x larger surface area²³, and the SI is not protected by a firm continuous mucus layer^{24,25}, suggesting that the host-microbe relationships in the SI may be more intimate than in the colon. In health, mucosal immunity, digestive secretions, and intestinal

motility²⁶⁻²⁸ protect the host from bacterial colonization of SI mucosa. Therefore, even if it occurs, bacterial colonization of SI mucosa is likely rare, transient, and elusive to our observation. Nonetheless, we hypothesized that in dysbiosis, the likelihood of bacterial colonization of SI mucosa would increase such that now it can be captured.

As a clinically relevant application of this 3D imaging technology, I chose to study the association of these two taxa using a mouse model of environmental enteropathy (EE) that was established by co-gavaging malnourished mice with both *Escherichia coli* (*E. coli*) and *Bacteroides/Parabacteroides* spp.²⁹. EE is a chronic inflammatory subclinical condition of the SI primarily impacting millions of children in the developing world and thought to arise from frequent oral re-ingestion of food and water contaminated with fecal matter³⁰. We hypothesized that in a host weakened by malnutrition and challenged with the synergistic *Enterobacteriaceae–Bacteroidaceae* pair, the likelihood of bacterial colonization of SI mucosa would increase, and that our tools developed in Chapters 2 and 3 would enable us to capture them 3D.

Thus, we applied the technology developed in Chapters 2 and 3 to the EE mouse model to answer a series of questions about *Enterobacteriaceae* and *Bacteroidaceae* association in the SI. First, we asked whether *E. coli* colonizes the SI and what factors are required for its colonization. In this analysis, we used bacterial quantification tools developed in our laboratory that enable absolute quantification of individual bacterial taxa³¹. We found that a malnourishing low-fat and low-protein diet (MAL) was required for *Bacteroides/Parabacteroides* spp. (BAC) to colonize the mouse SI and to reach $\sim 10^6$ 16S rRNA gene copies per gram of digesta, whereas co-gavage with *E. coli* (EC) was not required (Fig.4.3, C-D). In contrast, both the MAL diet and co-gavage with *Bacteroides/Parabacteroides* spp. were required for *E. coli* to colonize the SI at 10^6 - 10^7 16S rRNA gene copies per gram of digesta abundance (Fig.4.3B). The co-gavage was also required for *E. coli* to expand in other locations in the gastrointestinal tract (GIT) (Fig.4.3B). In contrast, neither the MAL diet nor the co-gavage with *E. coli* were required for *Bacteroides/Parabacteroides* spp. to expand to the colon and reach the loads of the resident

B. theta (Fig.4.3, C-E). Therefore, my hypothesis was supported: *E. coli* colonized the SI, but required host weakening by malnutrition and the presence of *Bacteroides/Parabacteroides* spp.

Second, I asked whether the gavaged bacteria remained in the SI or were cleared with the passage of digesta. In our experience, in healthy mice of the same age, bacteria are cleared and few bacteria remain in the SI. Our imaging technology enabled us to scan large areas of the mucosal surface to identify these rare events of bacteria remaining in the SI. To ensure that segments empty of digesta could be identified in the mid-SI, we always fasted animals for 1 hour prior to euthanasia. We detected large opaque aggregates visible to the naked eye that were indicative of bacteria in three of four mice in the MAL+EC&BAC treatment, in one of the four mice in the MAL+BAC treatment, but in none of the mice in MAL+EC or MAL+PBS treatments (Fig.4.6A and Fig.S6). Cleared hydrogel-tissue hybrids were then stained with DAPI to visualize epithelium and with HCR v3.0 probes for total bacteria, *Bacteroides/Parabacteroides* spp. and *E. coli*. Tile-scanning at low magnification for epithelium and total bacteria detected that bacteria were densely packed in these large surface aggregates with the rest of the tissue appearing sterile and resembling the tissue samples where large surface aggregates were not detected (Fig.4.6A and Fig.4.S7). Closer examination of the large aggregates at higher magnification with taxon-specific probes detected an abundance of *Bacteroides/Parabacteroides* spp. in one MAL+BAC and one MAL+EC&BAC mouse (Fig.4.6B). Image segmentation and quantification of bacterial volume identified that *Bacteroides/Parabacteroides* spp. made up >10% of total bacteria (Fig.4.7, A-B), while 16S rRNA gene copy analysis detected *Bacteroides/Parabacteroides* spp. at only $\sim 10^6$ 16S rRNA gene copies per gram of digesta equivalent to on the order of 0.1% of total 16S rRNA load (Fig.4.3, A, C, and D). Although probe cross-reactivity may partially explain the differences, our results did not exclude the possibility that *Bacteroides/Parabacteroides* spp. were present in empty SI and even fractionally enriched compared to the digesta. In contrast, *E. coli* were less prevalent in the bacterial aggregates and amounted to on the order of 0.1% of total bacteria (Fig.4.7C), which was consistent with *E. coli* load in the digesta measured at $\sim 10^6$ - 10^7 16S rRNA gene copies per gram of digesta

and equivalent to 0.1-1% of total bacteria (Fig.4.3 A-B). Furthermore, consistent with 16S rRNA gene copy quantification (Chapter 4, Fig.3B), *E. coli* could not be detected on the mucosa of any of the MAL+EC mice (Chapter 4, Fig.7C). One MAL+EC&BAC mouse had a different composition of large surface aggregates in its SI, with a lower abundance of total bacteria and depletion of *E. coli* and *Bacteroides/Parabacteroides* spp. However, free mammalian nuclei were abundant, and high abundance of free nuclei could also be detected in one MAL+EC mouse (Figs.4.6B-4.7D). Overall, our data showed that malnutrition and co-gavage with *E. coli* and *Bacteroides/Parabacteroides* spp. increase bacterial retention in the SI after a 1 h fast. Additionally, our findings suggested that *E. coli* and *Bacteroides/Parabacteroides* spp. were among the remaining bacteria and that *Bacteroides/Parabacteroides* spp. were fractionally enriched, suggestive of their colonization of empty SI segments.

Third, I reasoned that the observed increased bacterial retention in the MAL+EC&BAC group correlated with the increased likelihood of bacterial colonization of the SI mucosa, and that now the hypothesized colonization can be captured. Furthermore, acknowledging that large surface aggregates may represent aggregation of gavaged bacteria in the lumen (and thus our detection of the gavaged bacteria may represent host response to bacterial retention in the SI), we reasoned that bacterial presence in the mucosa could be direct evidence that bacteria colonized the SI. To sensitively and specifically visualize bacteria deep in the mucosa, the adoption of HCR v3.0 probes to stain bacteria described in Chapter 3 was key because the previously used HCR v2.0 probes were prone to giving amplified background and false positive signal at these depths (Figs.3.4-5). Imaging of small bacterial aggregates detected in one MAL+EC&BAC mouse revealed that these bacteria penetrated deep in between and around the villi (Fig.4.8). Like large surface aggregates, *Bacteroides/Parabacteroides* spp. were abundant (on the order of 10% of total bacteria by volume; Fig.4.8F). Again, *E. coli* were sparse, but could be detected to associate with *Bacteroides/Parabacteroides* spp. (Fig.4.8F). The spatial structure we observed visually was consistent with the 16S rRNA gene copy analysis, which demonstrated that *Bacteroides/Parabacteroides* spp. did not require gavage with *E. coli* to colonize the SI of

malnourished mice, but facilitated *E. coli*'s colonization (Fig.4.3, B-D). We hypothesized that the ability of *Bacteroides* spp. to adhere to³² and forage on³³ mucus may mediate their ability to colonize SI mucosa. Indeed, wheat germ agglutinin (WGA) staining for N-acetylglucosamine (which is abundant in mucus^{25,34}) and HCR staining for bacteria showed that bacteria were co-localized with N-acetylglucosamine (Fig.4.9). These results provide evidence that *Bacteroides/Parabacteroides* spp. can colonize the intervillus space of malnourished mice.

Finally, reasoning that the observed large surface aggregate represented host response to bacterial expansion in SI digesta and colonization of SI mucosa, I interrogated the structure of the observed large surface aggregates for host components. Previously, it was reported that co-gavage was required to induce EE features in malnourished mice, including additional weight loss or reduced weight gain with respect to malnutrition alone, villus blunting, and increased intestinal inflammation and permeability²⁹. Our lab (and others) have not been able to reproduce the EE model, including the reported weight changes. We have observed only a slight trend towards higher transcription of TNF- α and IL-6 genes in response to bacterial gavages in the ileum (Fig.4.1 D-E). Considering that severe tissue inflammation was not induced, we reasoned that our detected large surface bacterial aggregates effectively maintained homeostasis and that these events warrant more attention. Curiously, in one mouse in MAL+EC&BAC treatment, abundant free mammalian nuclei surrounded bacteria, suggesting that either host cells played a role in aggregation or that they were also subject to aggregation. To determine whether the free mammalian nuclei we observed were damaged epithelial cells or infiltrating immune cells, we leveraged the technological developments described in Chapter 3, specifically the improvements in hydrogel permeability that permitted antibody entry into the hydrogel-tissue hybrid (Fig.3.3). Antibody staining for EpCAM, epithelial cell marker, IgA, secretory antibodies, and Ly6G, neutrophil marker, concluded that epithelial cells dominated these aggregates (Fig.4.10). Furthermore, the aggregates appeared structured with mucus and bacteria partitioning to the center and epithelial cells – to the outer shell. The observed events raised a hypothesis that

the observed epithelial damage may not only be the consequence of host response to bacterial colonization, but also a mechanism to clear bacteria from the mucosa.

In summary, this thesis describes a novel 3D imaging technology and its usefulness in studying microbial communities in the GIT at multiple scales and in 3D with simultaneous visualization of bacteria, host tissue, cells, and secretions. As a proof of concept, I demonstrate the application of this technology to one specific, clinically relevant association between two microbial families, *Enterobacteriaceae* and *Bacteroidaceae*, known to associate with each other in several human disease states. Application of our 3D imaging technology, corroborated by absolute quantification of 16S rRNA gene copy analysis, showed that the strictly anaerobic *Bacteroides/Parabacteroides* spp. more effectively expanded in the SI of malnourished compared with well-nourished mice, suggesting that malnourished children may also be prone to SI colonization by these strictly anaerobic colonic species. While *Bacteroides/Parabacteroides* spp. did not require *E. coli* co-gavage to expand in the SI, *E. coli* required *Bacteroides/Parabacteroides* spp. expand in the SI. Furthermore, we concluded that MAL+EC&BAC treatment not only led to the expansion of the gavaged bacteria in the digesta, but also increased bacterial retention after digesta passage. We reasoned that this increased bacterial retention correlated with the rare event of mucosal colonization. Indeed, in one MAL+EC&BAC mouse, we detected abundant bacteria in the intervillus space and captured this bacterial colonization in 3D for the first time. Our data concluded that gavaged bacterial isolates (or at least their higher order taxonomic groups) were present in the detected mucosal bacterial community and that *Bacteroides/Parabacteroides* spp. may have been fractionally enriched, possibly by adhering to and foraging on mucus. Although, fractionally, *E. coli* were not enriched in the empty segments or the mucosa compared with the digesta, their retention in the SI was significant because it may allow *E. coli* to seed at a higher density upon arrival of the next meal. Our findings are complementary to previously published work on this EE mouse model. Previously, it was shown that induction of EE phenotype in malnourished mice required co-gavage with both *Bacteroides/Parabacteroides* spp. and *E. coli*; additionally, our data demonstrates that expansion of *E. coli* in the SI of malnourished mice only occurs after

gavage with only *Bacteroides/Parabacteroides* spp. Thus, our findings suggest that expansion of *E. coli* in the SI weakened by malnutrition and enabled by *Bacteroides/Parabacteroides* spp. can lead to EE. Similarly, in humans, colonization of the SI by *Bacteroides/Parabacteroides* spp. may act as a carrier of other disease-promoting species.

References

1. Cremer, J. *et al.* Effect of flow and peristaltic mixing on bacterial growth in a gut-like channel. *Proc. Natl. Acad. Sci. U. S. A.* **113**, 11414–11419 (2016).
2. Welch, J. L. M., Hasegawa, Y., McNulty, N. P., Gordon, J. I. & Borisy, G. G. Spatial organization of a model 15-member human gut microbiota established in gnotobiotic mice. *Proc. Natl. Acad. Sci. U. S. A.* **114**, E9105–E9114 (2017).
3. Hasegawa, Y., Welch, J. L., Rossetti, B. J. & Borisy, G. G. Preservation of three-dimensional spatial structure in the gut microbiome. *PLoS One* **12**, 1–16 (2017).
4. Richardson, D. S. & Lichtman, J. W. Clarifying Tissue Clearing. *Cell* **162**, 246–257 (2015).
5. Tainaka, K., Kuno, A., Kubota, S. I., Murakami, T. & Ueda, H. R. Chemical Principles in Tissue Clearing and Staining Protocols for Whole-Body Cell Profiling. *Annual Review of Cell and Developmental Biology* **32**, (2016).
6. Gradinaru, V., Treweek, J., Overton, K. & Deisseroth, K. Hydrogel-tissue chemistry : Principles and applications. *Annu. Rev. Biophys.* **47**, 355–76 (2018).
7. Chung, K. *et al.* Structural and molecular interrogation of intact biological systems. *Nature* **497**, 332–7 (2013).
8. Choi, H. M. T. *et al.* Programmable in situ amplification for multiplexed imaging of mRNA expression. *Nat. Biotechnol.* **28**, 1208–1212 (2010).
9. Shah, S. *et al.* Single-molecule RNA detection at depth by hybridization chain reaction and tissue hydrogel embedding and clearing. *Development* **143**, 2862–2867 (2016).
10. DePas, W. H. *et al.* Exposing the three-dimensional biogeography and metabolic states of pathogens in cystic fibrosis sputum via hydrogel embedding, clearing, and rRNA labeling. *MBio* **7**, 1–11 (2016).
11. Neckel, P. H., Mattheus, U., Hirt, B., Just, L. & Mack, A. F. Large-scale tissue clearing (PACT): Technical evaluation and new perspectives in immunofluorescence, histology, and ultrastructure. *Sci. Rep.* **6**, 1–13 (2016).
12. Yang, B. *et al.* Single-cell phenotyping within transparent intact tissue through whole-body clearing. *Cell* **158**, 945–958 (2014).
13. Murray, E. *et al.* Simple, scalable proteomic imaging for high-dimensional profiling of intact systems. *Cell* **163**, 1500–1514 (2015).
14. Kim, S.-Y. *et al.* Stochastic electrotransport selectively enhances the transport of highly electromobile molecules. *Proc. Natl. Acad. Sci.* **112**, E6274–E6283 (2015).
15. Choi, H. M. T. *et al.* Third-generation in situ hybridization chain reaction: Multiplexed, quantitative, sensitive, versatile, robust. *Dev.* **145**, 1–10 (2018).
16. Sheu, C. C., Chang, Y. T., Lin, S. Y., Chen, Y. H. & Hsueh, P. R. Infections caused by carbapenem-resistant Enterobacteriaceae: An update on therapeutic options. *Front. Microbiol.* **10**, (2019).
17. Mukhopadhyay, I., Hansen, R., El-Omar, E. M. & Hold, G. L. IBD-what role do Proteobacteria play? *Nat. Rev. Gastroenterol. Hepatol.* **9**, 219–230 (2012).
18. Bouhnik, Y., Sophie, A. A. & Flourié, B. Bacterial populations contaminating the upper gut in patients with small intestinal bacterial overgrowth syndrome. *Am. J. Gastroenterol.* **94**, 1327–1331 (1999).
19. Dejea, C. M. *et al.* Patients with familial adenomatous polyposis harbor colonic biofilms containing tumorigenic bacteria. *Science.* **359**, 592–597 (2018).
20. Vich Vila, A. *et al.* Gut microbiota composition and functional changes in inflammatory bowel disease and irritable bowel syndrome. *Sci. Transl. Med.* **10**, eaap8914 (2018).

21. He, G. *et al.* Noninvasive measurement of anatomic structure and intraluminal oxygenation in the gastrointestinal tract of living mice with spatial and spectral EPR imaging. *Proc. Natl. Acad. Sci. U. S. A.* **96**, 4586–4591 (1999).
22. Khazaei, T. *et al.* Metabolic bi-stability and hysteresis in a model microbiome community. *Sci. Adv.* 1–20 (2020).
23. Helander, H. F. & Fändriks, L. Surface area of the digestive tract - revisited. *Scand. J. Gastroenterol.* **49**, 681–689 (2014).
24. Atuma, C., Strugala, V., Allen, A. & Holm, L. The adherent gastrointestinal mucus gel layer: Thickness and physical state in vivo. *Am. J. Physiol. Liver Physiol.* **280**, G922–G929 (2001).
25. Johansson, M. E. V., Holmén Larsson, J. M. & Hansson, G. C. The two mucus layers of colon are organized by the MUC2 mucin, whereas the outer layer is a legislator of host-microbial interactions. *Proc. Natl. Acad. Sci. U. S. A.* **108**, 4659–4665 (2011).
26. Bevins, C. L. & Salzman, N. H. Paneth cells, antimicrobial peptides and maintenance of intestinal homeostasis. *Nat. Rev. Microbiol.* **9**, 356–368 (2011).
27. Peterson, D. A., McNulty, N. P., Guruge, J. L. & Gordon, J. I. IgA response to symbiotic bacteria as a mediator of gut homeostasis. *Cell Host Microbe* **2**, 328–339 (2007).
28. Bohm, M., Siwec, R. M. & Wo, J. M. Diagnosis and management of small intestinal bacterial overgrowth. *Nutr. Clin. Pract.* **28**, 289–99 (2013).
29. Brown, E. M. *et al.* Diet and specific microbial exposure trigger features of environmental enteropathy in a novel murine model. *Nat. Commun.* **6**, 7806 (2015).
30. Humphrey, J. H. Child undernutrition, tropical enteropathy, toilets, and handwashing. *Lancet* **374**, 1032–1035 (2009).
31. Barlow, J. T., Bogatyrev, S. R. & Ismagilov, R. F. A quantitative sequencing framework for absolute abundance measurements of mucosal and lumenal microbial communities. *Nat. Commun.* **11**, (2020).
32. Huang, J. Y., Lee, S. M. & Mazmanian, S. K. The human commensal *Bacteroides fragilis* binds intestinal mucin Mucus. *Anaerobe* **17**, 137–141 (2011).
33. Bjursell, M. K., Martens, E. C. & Gordon, J. I. Functional genomic and metabolic studies of the adaptations of a prominent adult human gut symbiont, *Bacteroides thetaiotaomicron*, to the suckling period. *J. Biol. Chem.* **281**, 36269–36279 (2006).
34. Holmén Larsson, J. M., Thomsson, K. A., Rodríguez-Piñeiro, A. M., Karlsson, H. & Hansson, G. C. Studies of mucus in mouse stomach, small intestine, and colon. III. Gastrointestinal Muc5ac and Muc2 mucin O-glycan patterns reveal a regiospecific distribution. *Am. J. Physiol. Gastrointest. Liver Physiol.* **305**, G357–63 (2013).

3D IMAGING FOR THE QUANTITATIVE DISCOVERY OF SPATIAL PATTERNS IN THE MICROBIOTA OF THE INTESTINAL MUCOSA

Abstract

Understanding the synergy between the spatial structure of microbial communities in the gut and the interactions between their components requires the quantification of microbes' spatial order in their native setting, and therefore the ability to acquire entire microbial aggregates and host tissues. We developed a systematic procedure to quantify the 3D spatial structure of the native mucosal microbiota in any part of the intestines with high spatial and taxonomic resolution. We imaged five dominant bacterial taxa in the mucosa of the cecum. Analysis of the spatial distribution of bacteria in the mucosa at different scales revealed strong pairwise correlations between taxa as well as between specific taxa and the ensemble of bacteria or the host. These patterns were consistent with a model in which a strain of *Bacteroidetes* S24-7 may lead the colonization of crypts, along with *Firmicutes* taxa with varied degrees of interdependence. In the context of intestinal diseases where the microbiota may play a causal role, the methodology presented here may be used to identify microbes or interactions that may contribute to the diseased state.

Significance Statement

Many human diseases are causally linked to the gut microbiota, yet the field still lacks mechanistic understanding of the underlying complex interactions because existing tools cannot provide access to microbial communities and their intact native context simultaneously. In this work, we provide a new approach to tissue preservation and clearing that enables visualization, in 3D and at scales ranging from cm to μm , of the complete geography of the host-microbiota interface. We combine this new tool with sequencing and multiplexed labelling of the microbiota to provide the field with a platform on which to discover patterns in the spatial distribution of microbes. This approach will enable

researchers to formulate and test hypotheses about host-microbe and microbe-microbe interactions.

Introduction

The composition of resident microbial communities is driven by nutrient availability¹⁻³, the physical environment^{4,5}, host-microbiota interactions^{6,7}, and interactions within the microbiota^{8,9}. The sum of all these forces may shape the spatial arrangement of intestinal microbes and, in turn, the spatial structure of the microbiota could influence how host-microbe and microbe-microbe interactions occur¹⁰. The synergy between the micro-geography of intestinal bacterial consortia and the interactions of microbes with their environment or other microbes has been studied *in vitro* using synthetic communities and computational simulations¹¹⁻¹⁵. In the context of the gastrointestinal system, studying the connection between the native spatial structure of the microbiota and its function naturally calls for three-dimensional (3D) imaging strategies that enable the simultaneous visualization of bacterial communities and host structures at multiple scales^{16,17}. However, existing 3D imaging approaches remain hindered by the opacity and impermeability of intestinal tissues and their contents. Methods have been developed to obtain cross-sectional slices from paraffin or plastic embedded intestinal tissues^{18,19}. Thin sections eliminate the optical and diffusion barriers that thick tissues present to imaging and molecular staining, but fragment host tissues and microbial assemblies. The advent of tissue-clearing technologies has enabled the imaging of cellular structures in thick tissues like the brain^{20,21}. However, the full potential of tissue-clearing techniques has yet to be realized to quantify the composition and organization of the host-microbiota interface with spatial resolution.

Sequencing of bacterial 16S rRNA genes has been effective at surveying the composition of the bacterial microbiota in different compartments along and across the gastrointestinal tract (GIT). Indeed, sequencing has revealed that the mucosal microbiota is distinct and spatially heterogeneous, and bioinformatics tools have enabled the inference of bacterial networks of interaction²²⁻³². However, sequencing alone cannot be used to reconstruct the spatial order of bacteria and the host with high spatial resolution. Therefore, microscopic imaging of thin

sections of intestinal tissue is the *de facto* approach to study the fine spatial structure of the microbiota and the host^{2,18,19,33}. Thin-section imaging (TSI) is ordinarily coupled with fluorescence *in situ* hybridization (FISH), immunohistochemistry, and other labeling methods that link the molecular identity of bacteria and host elements to their location. For example, TSI has been used to study the spontaneous segregation of *Escherichia coli* and mucolytic bacteria in the colonic mucus layer³⁴, by measuring the distance of different bacterial taxa from the epithelial surface¹⁹, such as during inflammation³⁵. In notable recent examples of the quantitative application of TSI, semi-automated computational image analysis was used to measure the thickness of the colonic mucus layer and the proximity of bacteria to the host as a function of diet¹⁸, and multiplexed FISH was used to investigate the microscopic spatial structure of a 15-member microbiota in the distal colon¹⁹.

Although TSI is valuable to investigate the biogeography of the intestines and the microbiota, it is unable to completely capture the spatial structure of bacterial communities in the gut. The first limitation of TSI is that it sets two-dimensional bounds on the spatial exploration of a heterogeneous, 3D system. TSI sections are typically 5–10 μm thick, whereas topographic epithelial features and mucosal microbial communities can be 1–4 orders of magnitude larger. Mucosal biofilms can be hundreds of microns long³⁶, and bacterial colonies in the colonic crypts have a heterogeneous taxonomic composition with a 3D spatial structure that cannot be charted unless the entire crypt (diameter 50 μm) is imaged^{29,37}.

Quantitative descriptions of the 3D spatial structure of native bacterial biofilms with taxonomic resolution are challenging to develop because of the natural opacity of the intestinal tissue and contents, and the complex composition of the microbiota, in which potentially hundreds of bacterial species coexist. Moreover, a quantitative description of a diverse and spatially heterogeneous system requires abundant data that can only be obtained through unrestricted optical access to samples. Tissue-clearing techniques have been developed for some tissues and organs (including brain, heart, kidney, lung, stomach, and sputum)^{21,38–41}. However, the naïve application of tissue-clearing techniques will not prevent, and may cause in some cases, the loss of mucus and bacterial communities.

Here, we developed an advanced tissue-clearing technique that preserved the spatial structure of the mucosal microbiota and its host context. We combined this method with sequencing of 16S rRNA genes, amplified *in situ* labeling of rRNA, spectral imaging, and statistical analyses. This method is capable of revealing patterns in the composition of the microbiota with taxonomic and spatial resolution. As a demonstration, we use this methodology to reveal strong patterns in the spatial structure of the mucosal microbiota of the cecum at multiple scales, and which are consistent with potential interactions within microbial communities in crypts and with the host.

Results

Sample preparation, staining, and imaging

To achieve unrestricted optical access to the mucosa, we developed a tissue-clarification method that exposes the intestinal mucosa in a fully laid out display (Fig. 1). Mounting tissue samples flat enabled us to image any point of the mucosa using a standard confocal microscope, and clearing the tissue increased the depth of imaging with refractive-index-matching long-working-distance objectives (Supplementary Materials and Methods). However, achieving optical transparency of exposed intestinal tissues posed multiple experimental challenges. Clearing techniques that do not create a hydrogel matrix do not protect and preserve the delicate materials (mucus, biofilms) on the mucosa³⁸, and CLARITY and PACT techniques involve multiple mechanically stressful sample-preparation steps to transform the cellular matrix of tissue into an acrylamide gel^{20,21,39}. Moreover, application of CLARITY or PACT to whole-mount tissues would irreversibly deform them and destroy the patterns of bacterial colonization on the mucosa.

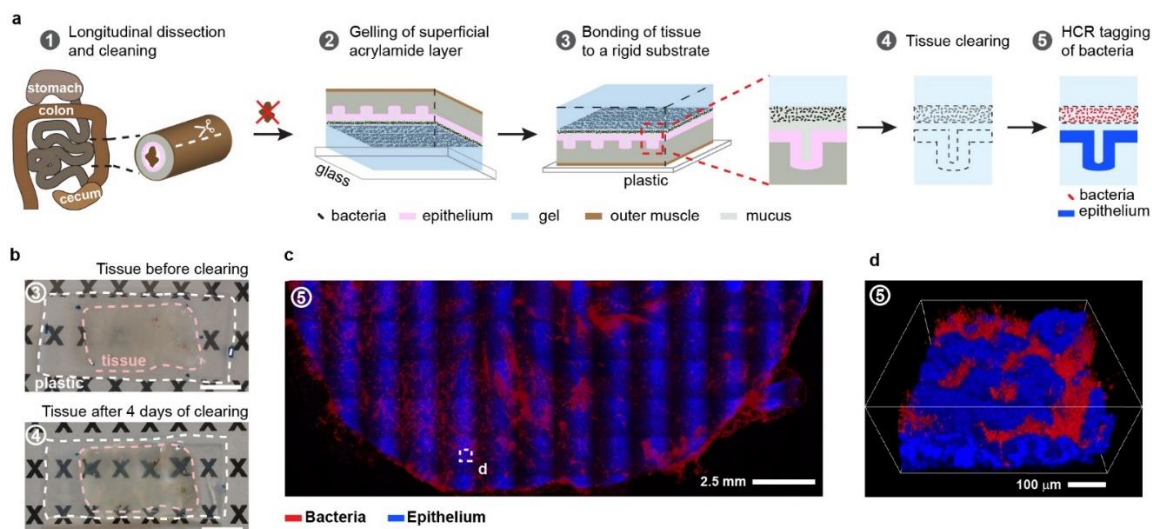


Figure 1. Sample preparation and imaging for 3D mapping of the mucosal microbiota's spatial structure. (a) The workflow of the method has five key steps in which a section of intestinal tissue is prepared for whole-mount confocal imaging of the mucosal microbiota. (b) A sample of preserved murine cecal tissue before and after 4 d of lipid removal. The dimensions and shape of the sample are not visibly altered by clearing. Scale bar: 1 cm. (c) Tiled image of a typical intestinal tissue sample after the method. The image of the cecum was obtained by stitching multiple fields of view acquired at 5X magnification. Bacteria were stained by hybridization chain reaction (HCR) with a eubacterial detection probe, and host nuclei were stained with DAPI. (d) 3D rendering of the confocal imaging of the area enclosed in the dashed white square in (c) shows clearly the location of bacteria with respect to each other and the host.

To maintain the spatial integrity of bacteria and mucus during whole-mount sample preparation, we developed a method that addresses separately the preservation of the materials on the tissue surface from the preservation of the rest of the sample, and that minimizes the duration of steps that can dislodge mucus and biofilms. The overall workflow of our method (Fig. 1a), which we developed in a murine model, was as follows: after careful dissection and removal of intestinal contents, tissues were fixed in paraformaldehyde for 1 h to prevent biochemical decay. Next, we created a capillary layer of acrylamide mix between the exposed mucosa and the glass bottom of a shallow chamber. Upon heating, the acrylamide mix polymerized into a gel layer with a thickness on the order of 100 μm . Once the mucosal surface of the sample was protected, the remainder of the tissue was embedded and gelled. Finally, the uncovered surface of the sample (the muscle side) was glued to a rigid, flat, plastic substrate to keep the sample flat (Fig. 1b). In this configuration, samples could be passively cleared, stained, and imaged without damaging the mucosal surface. A detailed description of the workflow is available in Materials and Methods.

To locate bacteria *in situ*, we fluorescently labelled bacterial 16S rRNA transcripts through hybridization chain reaction (HCR^{42,43}) (Materials and Methods). Standard FISH probes are labelled with up to two fluorophores, which produce a fluorescent emission that is sufficiently intense to image bacteria on thin sections. However, bacteria in the mammalian gut can be found in thick biofilms, epithelial crypts, or across the epithelial barrier, all of which obscure visibility. Therefore, we used HCR for labelling because it increases the intensity of fluorescence by at least one order of magnitude compared to FISH probes⁴².

The method presented here enables the mapping of bacteria on the mucosa at multiple length scales. To reveal patterns of colonization over spatial scales on the order of centimeters, tissue samples were imaged in a laser-scanning confocal microscope at low magnification (5X), and the images were tiled (Fig. 1c). To image the detailed spatial structure of bacterial biofilms with micrometer resolution (Fig. 1d and Supplementary Video 1), we mounted samples in a refractive-index-matching solution ($n = 1.46$) and used a 20X CLARITY objective with a collar for the compensation of spherical aberrations (Materials and Methods).

Sensitivity and specificity of bacterial staining

Sensitive and specific identification of mucosal bacteria through fluorescence imaging was accomplished by optimizing HCR tagging and controlling for off-target effects (Materials and Methods, Supplementary Materials and Methods, and Figs. S1-S4 and S8). Fluorescent tagging through HCR was achieved by making the bacterial cell wall permeable to DNA probes and HCR hairpins. However, the acrylamide gel sheet that we created to protect the mucosal surface of samples formed a barrier for the diffusion of lysozyme (Fig. 2a) that digests the bacterial peptidoglycan. Poor permeabilization of bacteria limits the sensitivity of imaging to the most superficial bacteria and impedes the detection of bacteria deep in the tissue samples. To determine the correct concentration of lysozyme for optimal permeabilization of the cell wall, we created acrylamide gel slabs and embedded them with Gram-positive (*Clostridium scindens*) and Gram-negative (*Bacteroides fragilis*) bacteria. The purpose of these gels was to mimic the geometry and composition of the acrylamide

layer on tissue samples. The gel slabs were obtained by using the same procedure as in the preservation and clearing of tissues, had similar dimensions to tissue samples, and were exposed to lysozyme on one side only (Supplementary Materials and Methods and Figs. S1-S2). The duration of the treatment with lysozyme was kept constant at 6 h, and we varied the concentration of lysozyme in the range 1–5 mg/mL to determine the optimal concentration for bacterial permeabilization. Bacteria were tagged with an HCR probe that included a eubacterial detection sequence (eub338), and we imaged from the surface of the gels to a depth of 600 μm (Fig. 2b). We measured the intensity of HCR tagging of bacteria, which were identified with the blue-fluorescent DNA intercalated dye DAPI (4',6-diamidino-2-phenylindole). The sensitivity of our method was defined as the proportion of bacteria down to 600 μm with a fluorescent signal-to-background ratio ≥ 20 (Fig. 2c). At a lysozyme concentration of 5 mg/mL, sensitivity was 94% and it dropped to $\sim 50\%$ for 1 mg/mL.

Nonspecific detection and amplification are potential sources of background signal in HCR. Control experiments showed that in the absence of a target (GF + eub338) or a detecting probe (SPF + non338), there was no amplification, whereas when both the target and the probe were present (SPF + eub338), there was amplification (Fig. 2d) (Supplementary Materials and Methods). Plotting the intensity values showed that in situ HCR tagging of bacteria produced a signal that is 8.5-9 times as strong as the background in 90% of bacteria (Fig. 2e).

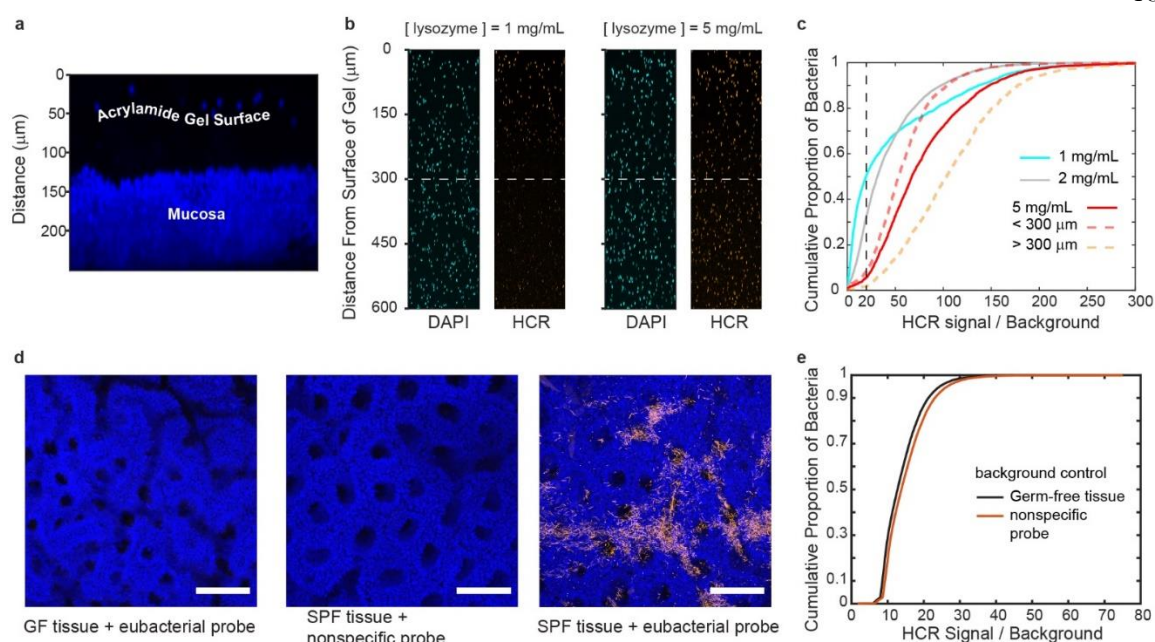


Figure 2. Sensitivity and specificity of fluorescence imaging of bacteria embedded in acrylamide gels using dual embedding. (a) Maximum intensity projection of a digital cross-section (152 μm) of intestinal tissue. The thickness of the protective acrylamide gel layer is revealed by blue-fluorescent beads on its surface. The layer of gel is a diffusive barrier for lysozyme during HCR staining of bacteria. (b) Maximum intensity projections of digital cross-sections (50 μm) of gel slabs seeded with bacteria. The effect of lysozyme concentration on the sensitivity of HCR staining is illustrated. At a suboptimal concentration of lysozyme (1 mg/mL), only bacteria near the surface of the gel can be detected, whereas a concentration of lysozyme of 5 mg/mL enables the detection of bacteria throughout the gel. (c) Experimental cumulative distributions of HCR staining of bacteria embedded in gel slabs that were treated with different lysozyme concentrations. At a lysozyme concentration of 5 mg/mL, approximately 94% of bacteria within 600 μm of the surface have a signal-to-background ratio ≥ 20 (vertical dashed line). (d) Maximal intensity projections of representative luminal views of proximal colon tissue used to test the specificity of HCR staining of bacteria *in situ*. (left) HCR with a eubacterial detection sequence (eub338) in germ-free (GF) tissue, (center) HCR with a nonspecific control probe (non338) on tissue with a microbiota (specific-pathogen-free, SPF), and (right) HCR with a eubacterial detection sequence (eub338) on tissue with a microbiota. Scale bars: 100 μm . (e) Experimental cumulative distribution of the background-to-noise ratio from controls for *in situ* HCR staining of bacteria in panel (d). Three fields ($n=3$) of view from each sample in panel (d) were acquired. The average intensity of the background was calculated from the controls with no target and a nonspecific probe. Bacteria were segmented with an intensity filter to obtain their average HCR fluorescence.

General 3D spatial organization of bacteria in the ileum, cecum, and proximal colon

To evaluate our 3D imaging methods, we imaged bacteria, mucus, and the host epithelium in disparate sections of the GIT with different biological functions, mucosal topographies, and amounts of mucosal materials^{44,45}.

Proximal colon

At low magnification (5X), we observed the crests and valleys of the epithelial folds and that most of the mucosa was covered by food particles and mucus (Supplementary Fig. S5a). At higher magnification (20X), our method enabled the exploration of the 3D organization of the host-microbiota interface in the proximal colon (Fig. 3a). 3D imaging can be analyzed through digital cross-sections with arbitrary orientation and thickness. Examining digital cross-sections, we found that bacteria were mixed with mucus threads and granules in a layer that had an average thickness of 125 μm (Fig. 3b and Supplementary Video 2). We also found that bacteria were separated from the epithelium by a single layer of mucus with an average thickness of 22 μm . 3D imaging provides the ability to examine tissues in their totality through computational 3D rendering. Thus, we were able to scan the tissue and find rare but conspicuous locations where bacteria had penetrated the mucus layer or crossed it and reached a crypt and the sub-epithelial space (Fig. 3c-d).

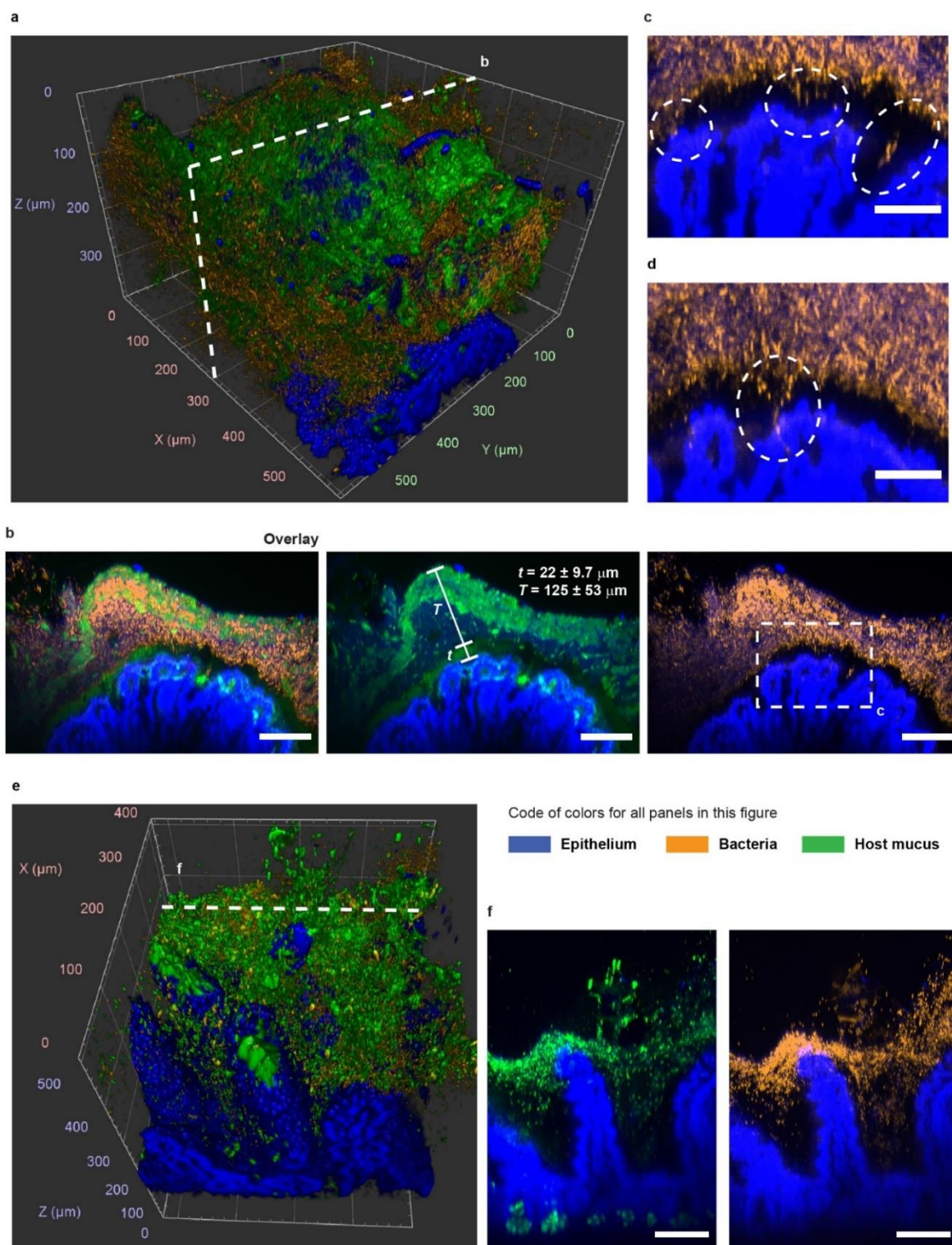


Figure 3. Spatial structure of the host-microbiota interface. (a) 3D rendering of confocal imaging (20X) of the crest of a fold in the proximal colon. The epithelium (blue) is covered by a mix of mucus (green) and bacteria (orange). (b) Maximum intensity projection of the digital cross-section (7 μm) depicted in panel (a). Mucus and bacteria are organized in well-defined layers. Two layers of mucus separate most of bacteria from the mucosa

and from the luminal contents (removed from this area of the sample). The thin layer of mucus that separates the epithelium from the majority of the microbiota in the lumen can be crossed by bacteria in healthy tissue. Scale bars: 100 μm . (c) Zoom-in view from panel (b). Examples of bacteria inside and across the thin mucus layer that lines the epithelium. The mucus layer was not shown here to facilitate the visualization of bacteria. Scale bars: 100 μm . (d) Maximum intensity projection of a digital cross-section (7 μm) from the same sample as in panel (a). Inside the oval is another example of bacteria crossing the thin mucus layer and the epithelium. (e) 3D rendering of confocal imaging (20X) of villi of the small intestine covered with mucus and bacteria. (f) Maximum intensity projections of the digital cross-section (16 μm) depicted in panel (e). Bacteria accumulate on mucus around the top of villi.

Ileum

At low magnification (5X), imaging revealed that bacteria were not uniformly distributed throughout the villi, and were mostly found as part of large agglomerations of food particles and mucus that adhere to the epithelium, as well as bacteria-mucus aggregates around villi (Supplementary Fig. S5b). At higher magnification (20X), 3D imaging showed that bacteria were contained by the mucus to a layer near the top of the villi (Fig. 3e-3f).

Cecum

The epithelial layer of the murine cecum is organized as a regular array of recessed mucus-secreting glands known as crypts⁴⁶. At low magnification (5X), imaging showed that bacteria in the cecal mucosa formed colonies that were associated with one or multiple crypts (Fig. 4a). However, the colonization of crypts was not homogeneous across the tissue. Colonized crypts were spatially clustered and surrounded by crypts with few or no bacteria. In contrast, mucus was somewhat evenly distributed across crypts. 3D imaging at higher magnification (20X) confirmed that not all crypts were occupied by bacterial colonies, but that all crypts secreted mucus (Fig. 4b).

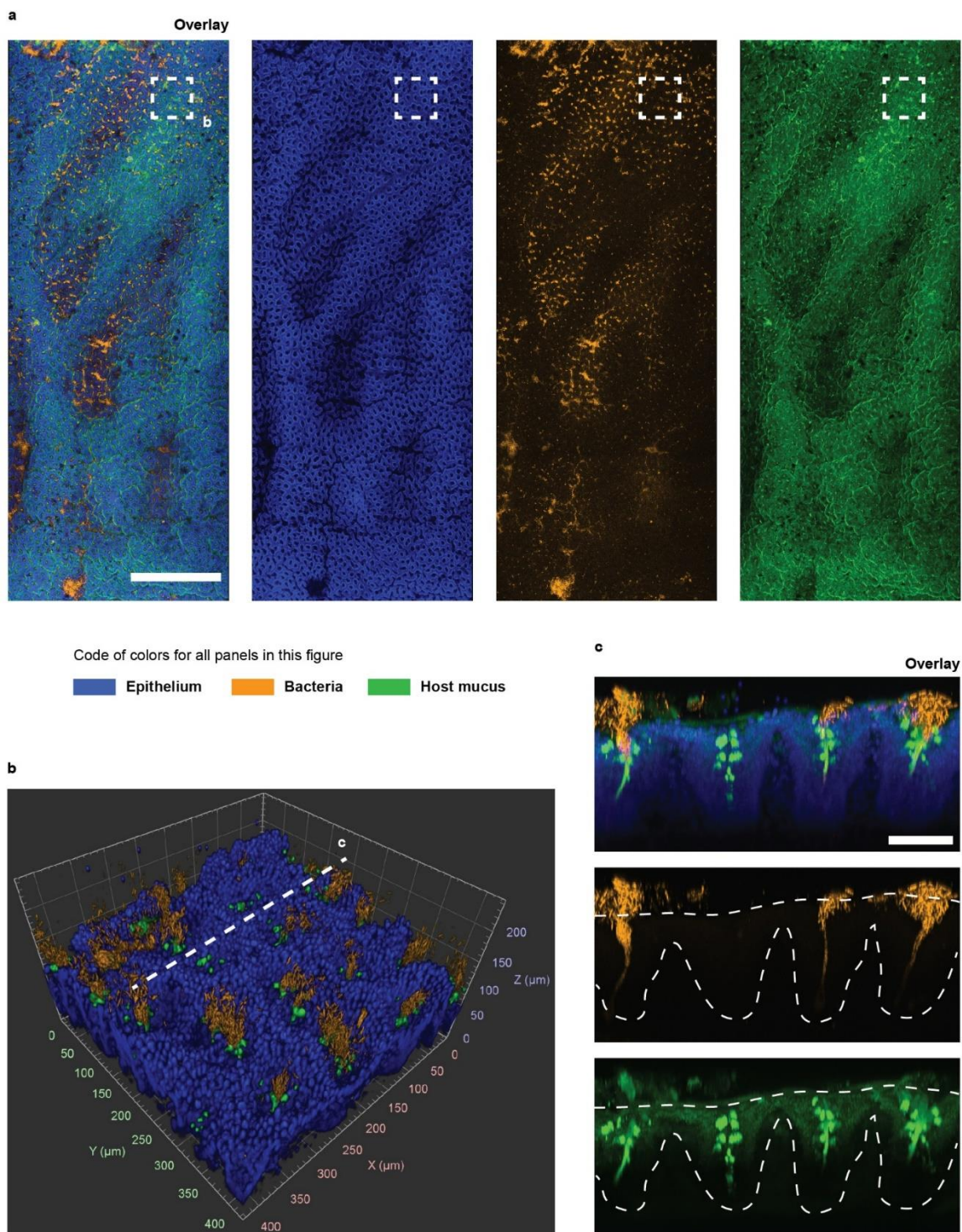


Figure 4. Multiscale imaging shows that the cecal mucosa is colonized in patches. (a) Tiled image of luminal imaging of a tissue sample from the cecum. The image was obtained by stitching multiple fields of view acquired at 5X magnification. Bacteria were stained by HCR with a eubacterial detection probe, the DNA of host cells was stained with DAPI, and the host mucus was stained with WGA lectin. The epithelium of the cecum was lined with crypts, some of which were isolated and some of which were connected to other crypts by crevices. The colonization of the mucosal crypts was discontinuous. Clusters of colonized crypts were

separated by areas with fewer bacteria. The spatial distribution of mucus was more uniform. Scale bar: 1 mm. **(b)** 3D rendering of confocal imaging (20X) of the cecal mucosa enclosed in the square area in panel (a). **(c)** Maximum intensity projection of the digital cross-section (70 μm) is indicated by a dashed line in (b). Bacteria that colonize the cecum occupy the crypts and the mucus these glands secrete. All crypts produce mucus, but not all crypts are colonized by bacteria. Scale bar: 75 μm .

Quantification of the composition and spatial structure of the microbiota of crypts

As shown in our 3D imaging of the mucosa (Figs. 3–4), bacteria occupied spatial niches with different geometries along the GIT. In the proximal colon, bacteria accumulated in a layer that ran parallel to the epithelium, whereas in the cecum, bacteria were split into colonies that were associated with crypts. The microbiota of the cecal mucosa and of intestinal crypts is diverse (refs). However, the spatial structure of these communities remains unexplored.

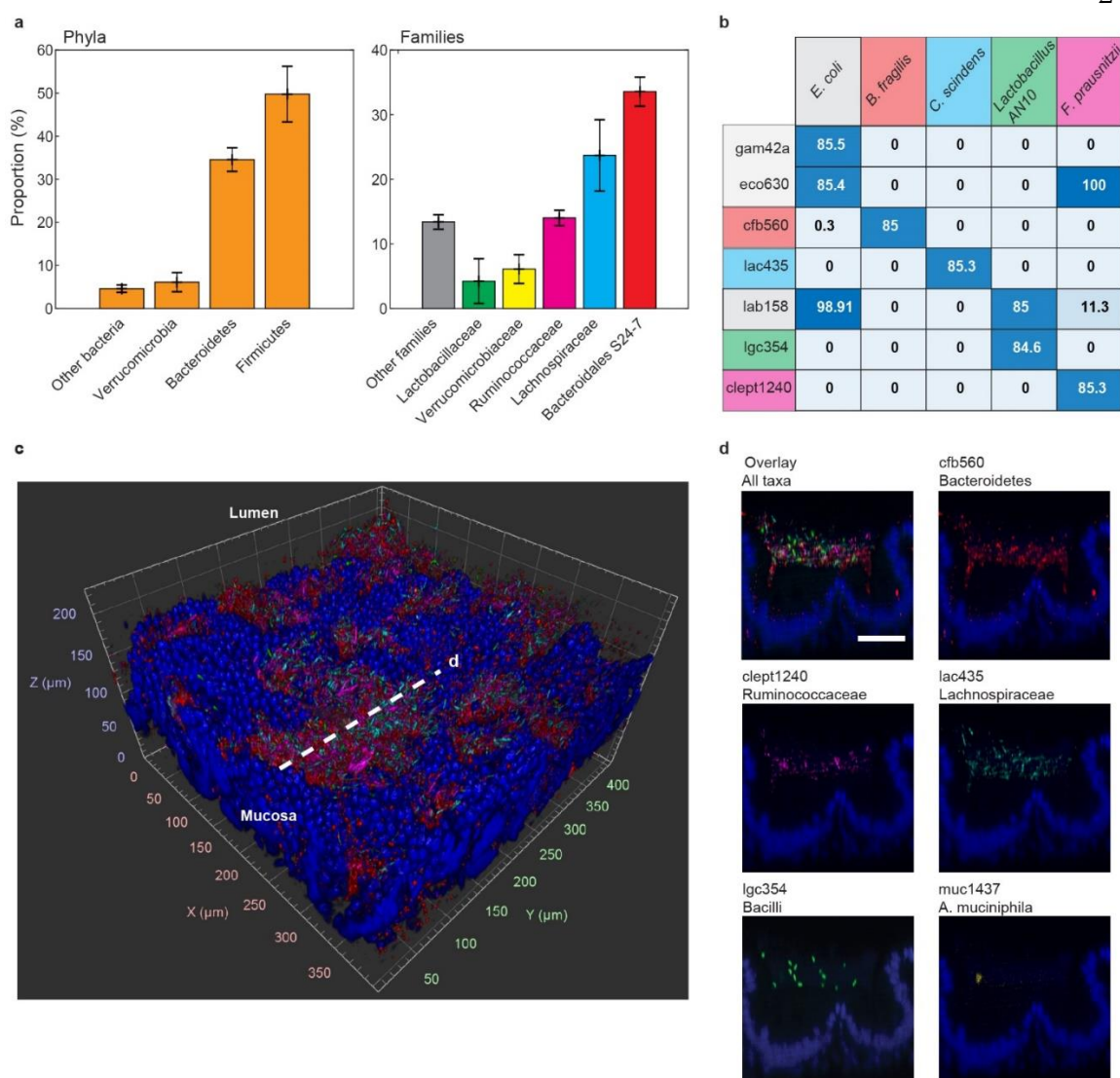


Figure 5. Multiplexed staining of the native mucosal microbiota is specific and comprehensive. (a) Taxonomic composition of the bacterial microbiota of the cecum according to the sequencing of 16S rRNA genes. In both plots, each bar represents the mean proportion of a taxonomic group. Murine cecal mucosa for total DNA extraction was harvested from four mice (n=4). Error bars represent the standard deviation. (b) A matrix of bacterial taxa and detection sequences where each matrix element gives the percentage of bacterial cells experimentally tagged by HCR with each detection sequence. Ideally, a probe only hybridizes bacteria with perfectly homologous rRNA transcripts. Perfectly matching probe–taxon pairs (PMPs) are color coded, for example lac435–*C. scindens*. We set a minimal detection threshold of 85% for PMPs. At this threshold, off-target HCR tagging is maximally reduced and detection sensitivity is maximized. (c) 3D rendering of cecal mucosa imaged at 20X magnification. Bacterial 16S rRNA on the sample was stained with multiple HCR probes with detection sequences cfb560, lac435, lgc350, clept1240, and muc1437. (d) Maximum intensity projection of the digital cross-section (5 μ m) that is depicted in (c) with a dashed orange line. Multiplexed staining with the probes tested in (b) reveals the location of five taxonomic groups in a densely populated dual crypt. Scale bar: 50 μ m.

To explore the spatial order in the microbiota of cecal crypts, we extended our imaging method to enable multiplexed imaging of bacterial targets. First, to identify the taxa we should target for imaging, we sequenced the 16S rRNA gene of the microbiota of the cecum (Fig. 5a), and searched the literature for FISH probes that could specifically detect bacteria belonging to the five taxonomic groups that comprised ~76% of the sequenced reads: *Bacteroidetes*, *Lactobacillaeae*, *Ruminococaceae*, *Lachnospiraceae*, and *Verrucomicrobiaceae* (Fig. 5a).

We tested *in vitro* the sensitivity and specificity of the selected detection sequences in HCR (see Materials and Methods, Supplementary Methods, and Figs. S3-S4). With each probe, except muc1437 for *Akkermansia muciniphila*, we performed HCR on four species of bacteria that were representative of the target taxonomic groups. We used an additional probe for *E. coli* because it was not found in the sequencing of the cecal mucosa and thus served as a further control for the specificity of our probes (Supplementary Table S1). Finally, HCR probes for multiplex *in situ* imaging were designed by pairing a unique HCR hairpin pair to each detection sequence that detected at least 85% of its ideal target bacterium while being insensitive to the rest of the bacterial targets, with the exception of the detection sequence cfb560 that cross-reacts with 0.3% of *E. coli* targets (Fig. 5b). The promiscuous lab158 probe was rejected in favor of the orthogonal lgc354 suite.

Because we had observed that cecal crypts are colonized in patches (Fig. 4a), we performed multiplexed HCR on several cecum samples and imaged the most abundant target taxon (*Bacteroidetes*) at low resolution (5X) (not shown) to locate patches. Within one patch of crypts, we obtained spectral imaging at higher magnification (20X), which was processed computationally to remove the fluorescent spectral overlap (Supplementary Materials and Methods). 3D spectral imaging with linear deconvolution of the cecal mucosa clearly showed multispecies colonization (Fig. 5c and Supplementary Video 3), and distinguished the location of different taxa in dense cryptal colonies (Fig. 5d). We analyzed the taxonomic composition of a subset of 59 abundantly colonized crypts using a commercial 3D image analysis software (Materials and Methods, Supplementary Video 4). We measured the

abundance (number of voxels) and the position of the target taxa inside crypts. Accordingly, the crypt microbiota was 65% *Bacteroidetes*, 18% *Lachnospiraceae*, 13% *Ruminococcaceae*, and 3% *Bacilli*, with an insignificant proportion of *Akkermansia*.

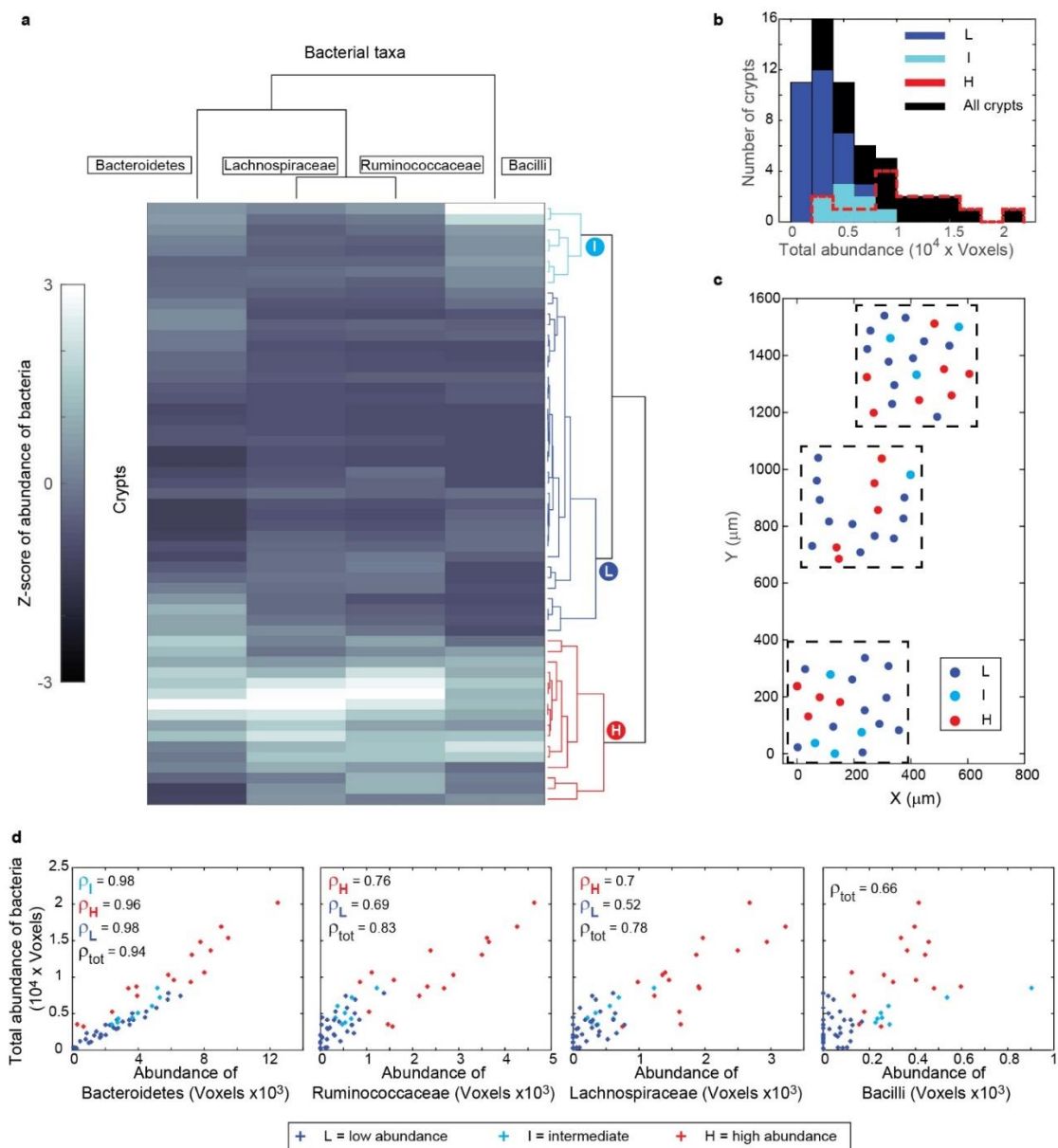


Figure 6. Statistical analysis of the composition of single-crypt communities reveals spatial and demographic patterns. (a) Color density map and dendrograms obtained from the hierarchical clustering analysis (HCA) of bacterial abundance in crypts colonized by four bacterial groups. Based on the abundance of four taxa, three states of the crypt bacterial community (**L**, **I**, **H**) are identified by the hierarchical clustering. In average, the total abundance of bacteria in **H** crypts was the highest, in **I** crypts was intermediate, and in **L** crypts was the lowest. Across all the states, the abundance of *Lachnospiraceae* and *Ruminococcaceae* tracked each

other closely across the entire set of crypts. **(b)** Distribution of the total abundance of bacteria per crypt for the ensemble of crypts (black) and for the three states of crypts: **L** (blue), **I** (cyan), and **H** (red). **(c)** Preservation of the intestinal tissue in whole-mount enabled the mapping of crypt states to the mucosal coordinates to observe their spatial relationships. The three fields of view have crypts in each state, and each state seemed to form sets of contiguous crypts of different sizes. **(d)** Scatterplots of the total abundance of bacteria per crypt as a function of the abundance of each taxon and reported for each state. The statistically significant correlations (significance level 0.05) are reported for all crypts (ρ_{tot}) and for each crypt state (ρ_L, ρ_I, ρ_H).

To search for patterns in the distribution of bacteria across crypts, we performed a hierarchical clustering analysis (HCA) of the abundance of bacteria with single-crypt resolution (Materials and Methods). The number of voxels of each channel was z-scored to give a normalized abundance of bacteria based on their spatial fluorescent signal. The result of the clustering is represented as a color density map, which shows the abundance of each taxonomic group (columns) across the ensemble of crypts (rows) (Fig. 6a). Columns and rows are arranged by similarity, which is represented by tree-like hierarchies for bacterial taxa and crypts.

In the vertical axis, the HCA identified three states of the crypt microbiota (Fig. 6a), which were further confirmed by a t-Distributed Stochastic Neighbor Embedding clustering algorithm to form distinct groups (Supplementary Fig. S7). The three states correspond approximately to (H) crypts that are populated above the average for each taxon, (L) below the average for each taxon, and (I) at an intermediate total amount (I). The average total abundance of bacteria within each state is $\sim (H, I, L) = (10000, 5000, 3000)$ Voxels (Fig. 6b). To examine the distribution of these states in the patch of crypts (Fig. 6c), we mapped their location to the mucosa, finding that crypts in each state seemed to form spatially distinct sets (chains or clusters) in the imaged region.

In the horizontal axis (taxa), the dendrogram showed that the abundance of *Lachnospiraceae* and *Ruminococcaceae* in single crypts were the most similar. This close association was supported by a statistically significant Spearman's correlation of 0.95 (Supplementary Fig. S6). The other pairwise correlations among taxa were positive, but not as strong. Next, to evaluate the strength of the association of each taxon to single-crypt communities, we plotted the total abundance of bacteria in each crypt as a function of the abundance of each taxon

(Fig. 6d) and calculated the corresponding Spearman's correlation. We found that the abundance of each taxon is positively correlated with the total abundance of bacteria per crypt. However, these correlations did not hold for all crypt states and all taxa. For example, the abundance of *Bacteroidetes* is correlated to the total bacteria in each crypt overall and for each state, but for Bacilli the correlation across the set of crypts is not reflected in significant correlations for each state (Supplementary Information).

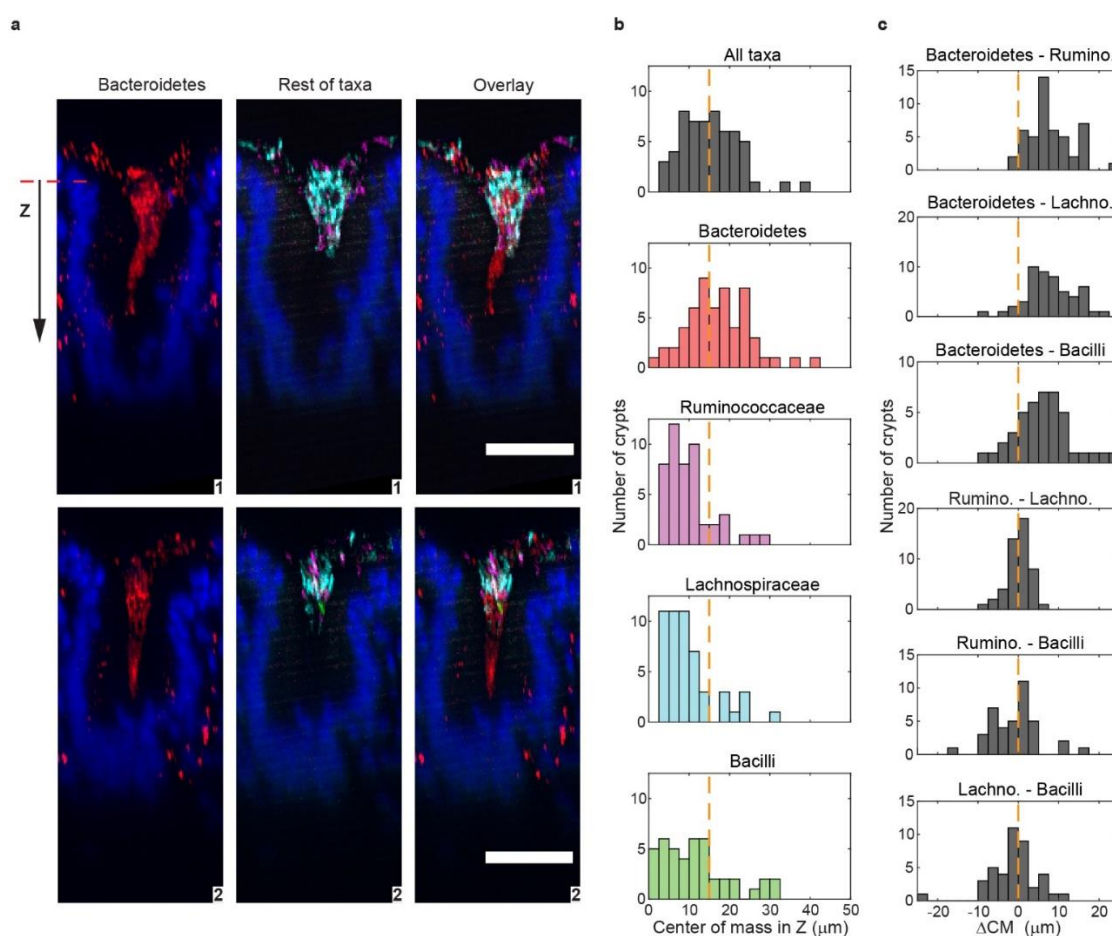


Figure 7. Quantification of the spatial organization of bacterial colonies inside crypts. (a) Maximal intensity projections of the digital cross-sections (10 μm) of two representative cecal crypts. Four taxa were imaged: Bacteroidetes (red), and three taxa in the Firmicutes phylum: Ruminococcaceae (magenta), Lachnospiraceae (cyan), and Bacilli (green). Nuclei of the epithelial layer of the crypt are colored in blue. Bacteroidetes spanned the length of each colony, whereas Firmicutes remained near the luminal end of crypts that was used as the spatial reference in our analysis. The red fluorescent signal outside the crypts was considered an artifact of staining and was not included in the analysis. (b) Distributions of the center of mass of taxa over the ensemble of crypts. Because each taxon was not found in every crypt, the number of crypts in each distribution was different ($n = 57$ (all taxa), 57, 48, 51, 43). Most Firmicutes were found between the median

center of mass and the luminal end of the crypt, whereas Bacteroidetes dominated the space between the median and the bottom of crypts.

We also investigated whether the position of bacteria along the axis of crypts (perpendicular to the plane of the mucosa) displayed order. We measured the vertical component of the center of mass of each taxon inside each crypt, taking the luminal end of cavities as spatial reference (Fig. 7a). We found that bacteria were distributed around a median depth of $z_0 = 15 \mu\text{m}$ (Fig. 7b). However, each taxon was unevenly distributed around z_0 . As shown qualitatively in the digital cross-sections of two crypts (Fig. 7a), *Lachnospiraceae*, *Ruminococcaceae*, and *Lactobacilli* are physically segregated from *Bacteroidetes*. *Firmicutes* are clustered above z_0 in most of crypts (84%, 83% and 74%), whereas *Bacteroidetes* are found below z_0 in 58% of crypts (Fig. 7b). We further quantified the physical segregation of taxa inside crypts through the pairwise distance between the center of mass of taxa ΔCM (Fig. 7c). We calculated ΔCM in each crypt for the six possible pairs of bacterial groups and plotted the resulting distribution over the ensemble of crypts. We found that the mean distance $\overline{\Delta CM}$ between Lachnospiraceae and Ruminococcaceae, and between these two groups and Bacilli was close to zero and smaller than the mean distance between Bacteroidetes and the rest of the bacterial taxa. Moreover, the values of ΔCM are narrowly distributed around the mean ($\sigma = 3 \mu\text{m}$), whereas the standard deviation for the other distributions is larger ($5.4 \mu\text{m} \leq \sigma \leq 7.4 \mu\text{m}$).

Discussion

This study presents a new approach to investigate the biogeography of the intestinal microbiota *in situ*. By systematically reconciling 3D imaging and tissue clearing with multiplexed staining of bacterial rRNA, we enabled the quantification of the composition of the mucosal microbiota with taxonomic and high spatial resolution. The large size of samples in whole-mount display enabled mapping of bacterial biofilms and aggregates over the scale of centimeters to microns. This is an important capability because the physical and biological interactions that shape the spatial structure of microbial communities take place over a wide range of spatial scales^{47–49}. We used these novel capabilities to find patterns in the spatial

distribution of bacteria at multiple scales as well as strong statistical correlations between the abundance of the members of these communities.

3D imaging on the scale of tissue samples (1 cm) showed that a great proportion of murine cecal crypts are colonized by bacteria²⁹, and enabled the discovery that this colonization is organized in millimeter-long patches. Large-scale imaging also showed that bacteria colonize the surface of the ileal mucosa at high density within specific areas where microbes attach to mucus or to food particles that adhere to the tissue. Unlike the ileum and the cecum, a large portion of the proximal colon was uniformly covered by layers of mucus and bacteria that are analogous to the dual mucus layer observed in the distal colon³³. The ability of our method to image diverse materials on the surface of the intestinal tissue and to confirm previous observations about the general organization of the microbiota showed that it is effective at preserving the mucosa.

Multiplexed 3D imaging of bacteria at the scale of a single patch of crypts (1 mm) revealed the spatial distribution of four dominant taxonomic groups. We found that bacteria populated mucosal crypts in a way that enabled the classification of these colonies into three different states by the total abundance of bacteria: high (H), intermediate (I), and low (L). Positive pairwise correlations in the abundance of taxa per crypt supported the observation that they form a community within individual crypts (Fig. 6a and Supplementary Fig. S6). However, these correlations were of different strengths. The abundance of *Lachnospiraceae* and *Ruminococcaceae* were highly correlated ($\rho = 0.94$) across crypts in the patch, whereas the correlation of Bacilli's abundance to the abundance of *Bacteroidetes* was half as strong ($\rho = 0.5$). This is in agreement with the hypothesis that relations between the members of the community are of different intensities. In line with this hypothesis, the strength of correlations between the abundance of each taxon and the total abundance of bacteria per crypt indicated that *Bacteroidetes* ($\rho_{\text{tot}} = 0.94$) had a stronger relation to the ensemble of bacteria in each crypt than the other three taxa ($\rho_{\text{tot}} = 0.83, 0.78, \text{ and } 0.66$). Moreover, the strong correlation of *Bacteroidetes* to the total abundance of bacteria was maintained within

each crypt state (L, I, H), whereas for Bacilli, correlations within each state were not significant.

Within single crypts (100 μm), the statistics of the distribution of bacteria showed that *Lachnospiraceae* and *Ruminococcaceae* strongly colocalized near the luminal end of crypts, and that Bacilli accumulated in the same area, but were distributed in a wider range around *Lachnospiraceae* and *Ruminococcaceae*. Additionally, *Bacteroidetes* overlapped with all taxa, but were the only group capable of deeply colonizing crypts.

The evidence provided by the sequencing of bacterial 16S rRNA genes and the statistical patterns in the spatial abundance of bacteria across multiple scales suggests a model for the colonization of crypts in the healthy mammalian cecum. In this model, *Bacteroidetes* S24-7 would drive the colonization of crypts, as supported by its ability to penetrate crypts (Fig. 7) and its strong correlation to crypt communities (Fig. 6d). Families *Ruminococcaceae* and *Lachnospiraceae* might depend on each other to colonize crypts according to their highly correlated abundance and position inside crypts (Fig. 6a and 7). In turn, the strong correlations between these abundant *Firmicutes* families and *Bacteroidetes* S24-7 (Supplementary Fig. S6), or the ensemble of bacteria (Fig. 6d), support the hypothesis of interactions with the other members of crypt colonies. Finally, the correlation in the abundance and location of Lactobacilli with *Lachnospiraceae* and *Ruminococcaceae* (Supplementary Figure S6, Fig. 7b-c) might indicate its dependence on the more abundant *Firmicutes* or a shared niche, and would be in line with Lactobacilli's weak correlation to the ensemble of crypt bacteria (Fig. 6d). The proposed model would be supported by the genetic capacity of *Bacteroidetes* S24-7 to thrive on plant and host glycans, and to mount immune evasion strategies and tolerance to oxidative stress, enabling its survival in the closest neighborhood to the host⁵⁰.

A key component of the method presented here is the combination of sequencing of 16S rRNA genes and technologies to multiplex *in situ* hybridization. Spectral imaging with linear deconvolution was instrumental to disentangle the fluorescent emission from each taxon. Like in 2D imaging of the microbiota^{19,51}, we anticipate that spectral imaging will be an

essential element in improved 3D methods. Sensitive and specific multiplexed labeling of diverse and dense bacterial colonies was possible by combining off-the-shelf detection probes against 16S rRNA and orthogonal signal amplification methods (HCR). Hundreds of *in situ* hybridization probes are available^{52,53} and can be tested against the continuously improved rRNA databases^{54,55}. However, the continued expansion of the multiplexing capacity of HCR, or of any other *in situ* hybridization scheme that is compatible with 3D imaging, will be crucial to link the 3D spatial structure of bacterial consortia to the potential interactions between single species or strains in native communities.

By virtue of its ability to find patterns in the spatial distribution of the mucosal microbiota at multiple scales, we expect that the method presented here will be of general applicability to generating testable hypotheses on the interactions within the microbiota and of the microbiota with its environment, including the host. Our method may be a valuable tool in the context of intestinal diseases in which the microbiota has a causative role, because it may help pinpoint key microbes or interactions that are important for the stability of pathogenic communities⁵⁶, such as in colorectal cancer where the synergistic pathogenicity of bacteria is not understood yet⁵⁷.

Materials and methods

Sources and strains of laboratory mice

Intestinal tissue for sequencing and imaging was obtained from adult male SPF C57BL/6J mice (The Jackson Laboratory, Sacramento, CA, USA). In the rearing facility at Caltech, SPF mice were housed four to a cage and given sterile food and water *ad libitum*. SPF mice were sourced from the same room at the provider's facility to minimize the environmental sources of variability in the microbiota of mice. GF tissue for imaging was obtained from a male mouse from a colony of gnotobiotic mice with B6 background maintained at Caltech.

Tissue preservation and clearing for imaging

Tissue samples for imaging of the mucosal microbiota were prepared as detailed in the Supplementary Materials and Methods. Briefly, all samples went through the following treatments sequentially. (A) C57BL/6J mice of 20–21 weeks of age were euthanized through

a transcordial perfusion of cold saline that cleared their vasculature of blood. (B) Tissues were cut open longitudinally and the bulk contents were cleared with sterile tweezers and the gentle application of sterile PBS. (C) The clean tissues in whole-mount were fixed in 4% PFA for ~ 1 h. (D) In an anaerobic chamber, tissues were floated for 15 min on a pool of monomer mix so that the muscle side was facing up, while components of the mix could penetrate the bacterial biofilms and other contents on the tissues. The monomer mix was removed using a pipette and the sample was incubated at 37 °C in an anaerobic chamber for 3 h to form the acrylamide gel layer at the glass-tissue interface. (E) The muscle side of tissue samples was embedded in an acrylamide matrix without bisacrylamide. This step is necessary to turn the tissue matrix into a hydrogel. Embedding lasted 3 h, after which the excess acrylamide mix was removed and the tissue was polymerized for 3 h at 37 °C. (F) Tissue samples were removed from the glass slides with a sterile razor-blade and glued onto a piece of semi-rigid plastic. (G) After samples were turned into a hydrogel and before they were passively cleared, we permeabilized bacteria according to the parameters prescribed by the optimization of lysozyme treatment (Supplementary Materials and Methods). (H) Permeabilized samples were enclosed in tissue cassettes and cleared for 4 d in 8% w/v sodium dodecyl sulfate (SDS) in PBS, pH = 8.3 at 37 °C. SDS was vigorously stirred. SDS was removed by washing in stirred 1X PBS for 2 d at 25 °C.

HCR staining of bacterial 16S rRNA

We designed HCR probes (Supplementary Tables S1-S2) and used them to image the location of total bacteria and specific taxa on intestinal tissue. The specific reagents and treatments used for HCR staining are described in detail in the Supplementary Materials and Methods.

Imaging of tissues

a. Microscopy

In situ imaging of the mucosal microbiota was carried out with an upright Zeiss LSM 880 laser-scanning confocal microscope capable of spectral acquisition and of housing a

CLARITY optimized long-working-distance objective. The objectives and lasers used for the acquisition at different scales are specified in the Supplementary Information.

b. Mounting medium

For imaging with a 5X objective, samples were mounted either in 1X PBS or in a refractive-index-matching solution (RIMS) and protected with a coverslip to prevent evaporation. For imaging with the refractive-index matched 20X objective, samples were always mounted in RIMS. Samples were saturated in RIMS for at least 10h with gentle shaking before imaging. We added a layer of immersion oil on top of the pool of RIMS to prevent water evaporation and maintain a constant refractive index during experiments (16916-04, Electron Microscopy Sciences, Hatfield, PA, USA). RIMS was prepared following an available protocol³⁹. We substituted Histodenz by Iohexol (CAS 66108-95-0, Janestic Co., Ltd, China). We consistently obtained a solution with refractive index $n \sim 1.46$ according to measurements with a digital refractometer (#13950000, AR2000, Reichert Analytical Instruments, NY, USA).

Image processing and analysis

a. Computational image processing.

Image stacks of mucosal bacteria obtained by *in situ* confocal imaging were visualized and processed in commercial software (Vision4D 3.0, Arivis AG, Germany). A detailed account of computational image processing is provided in the Supplementary Materials and Methods.

b. Statistical analysis of bacterial abundance and spatial distribution

The abundance of bacteria in each crypt was determined as the voxel count of probes targeting each taxon and the abundance of each taxon across crypts was normalized by z-scoring the voxel count for each channel. Z-scoring allowed the counts between channels to be more representative for the actual bacterial abundances. Individual crypts were treated as a volumetric unit hosting the bacteria, and HCA was performed to study the relationship (co-existence) of the species where both the crypts and bacterial taxa were clustered based on their cosine-similarities. The three most prominent branches of the clustered groups were

chosen for further analysis and mapped back into the spatial context showing the distributions of these crypt classes in the intestines. T-distributed stochastic neighbor embedding method (t-SNE) was further used for dimension-reduction to show the relationship between the branches and the cosine pairwise distance metrics. Computations were performed with a Hewlett-Packard Z840 Workstation with dual Intel Xeon E5-2630 v4 CPUs and 128GB of RAM on Microsoft Windows 10 Enterprise operating system. MATLAB v. R2017b was used for the data analyses. In MATLAB, the *P*-values for Spearman's correlation for small sample sizes are calculated using permutation distributions.

Author contributions

Conceptualization, O.M.P. and R.F.I.; Investigation, O.M.P, R.P., A.L., J.G., and R.F.I.; Resources, A.L., L.C., and R.F.I.; Writing, O.M.P, R.P., A.L., J.G., and R.F.I.; Funding Acquisition, O.M.P, A.L., L.C., and R.F.I. A detailed list of contributions by non-corresponding authors is included at the end of the Supplemental Information.

Acknowledgments

This work was funded in part by a Burroughs Wellcome Fund Career Award at the Scientific Interface (#1016969, to O.M.P.), a Biology & Biological Engineering divisional fellowship (to O.M.P.), a seeding grant from Caltech's Center for Environmental Microbial Interactions (CEMI), Army Research Office (ARO) Multidisciplinary University Research Initiative (MURI) contract #W911NF-17-1-0402, and an Innovator Award from the Kenneth Rainin Foundation (Grant 2018-1207). We acknowledge technical advice from Nick Flytzanis, Ben Deverman, Ken Chan, and Said Bogatyrev. We thank Andres Collazo and the Beckman Imaging Facility for help with imaging, and we thank Natasha Shelby for contributions to writing and editing this manuscript.

References

1. Koropatkin, N. M., Cameron, E. a. & Martens, E. C. How glycan metabolism shapes the human gut microbiota. *Nat. Rev. Microbiol.* **10**, 323–335 (2012).
2. Lee, S. M. *et al.* Bacterial colonization factors control specificity and stability of the gut microbiota. *Nature* **501**, 426–429 (2013).
3. Sonnenburg, J. L. Glycan foraging in vivo by an intestine-adapted bacterial symbiont. *Science.* **307**, 1955–1959 (2005).
4. Swidsinski, A. *et al.* Viscosity gradient within the mucus layer determines the mucosal barrier function and the spatial organization of the intestinal microbiota. *Inflamm. Bowel Dis.* **13**, 963–970 (2007).
5. Albenberg, L. *et al.* Correlation between intraluminal oxygen gradient and radial partitioning of intestinal microbiota. *Gastroenterology* **147**, 1055-1063.e8 (2014).
6. Round, J. L. *et al.* The Toll-Like receptor 2 pathway establishes colonization by a commensal of the human microbiota. *Science.* **332**, 974–977 (2011).
7. Donaldson, G. P. *et al.* Gut microbiota utilize immunoglobulin A for mucosal colonization. *Science.* **360**, 795–800 (2018).
8. Lustrì, B. C., Sperandio, V. & Moreira, C. G. Bacterial chat: Intestinal metabolites and signals in host-

- microbiota-pathogen interactions. *Infect. Immun.* **85**, 1–14 (2017).
9. Fischbach, M. A. & Sonnenburg, J. L. Eating for two: How metabolism establishes interspecies interactions in the gut. *Cell Host Microbe* **10**, 336–347 (2011).
 10. Nadell, C. D., Drescher, K. & Foster, K. R. Spatial structure, cooperation and competition in biofilms. *Nat. Rev. Microbiol.* **14**, 589–600 (2016).
 11. McLoughlin, K., Schluter, J., Rakoff-Nahoum, S., Smith, A. L. & Foster, K. R. Host selection of microbiota via differential adhesion. *Cell Host Microbe* **19**, 550–559 (2016).
 12. Ozgen, V. C., Kong, W., Blanchard, A. E., Liu, F. & Lu, T. Spatial interference scale as a determinant of microbial range expansion. *Sci. Adv.* **4**, 1–10 (2018).
 13. Tecon, R. & Or, D. Cooperation in carbon source degradation shapes spatial self-organization of microbial consortia on hydrated surfaces. *Sci. Rep.* **7**, 1–11 (2017).
 14. Estrela, S. & Brown, S. P. Metabolic and demographic feedbacks shape the emergent spatial structure and function of microbial communities. *PLoS Comput. Biol.* **9**, (2013).
 15. Momeni, B., Brileya, K. A., Fields, M. W. & Shou, W. Strong inter-population cooperation leads to partner intermixing in microbial communities. *Elife* **2013**, 1–23 (2013).
 16. Biteen, J. S. *et al.* Tools for the microbiome: Nano and beyond. *ACS Nano* **10**, 6–37 (2016).
 17. Tropini, C., Earle, K. A., Huang, K. C. & Sonnenburg, J. L. The gut microbiome: Connecting spatial organization to function. *Cell Host and Microbe* (2017). doi:10.1016/j.chom.2017.03.010
 18. Earle, K. A. *et al.* Quantitative imaging of gut microbiota spatial organization. *Cell Host Microbe* **18**, 478–488 (2015).
 19. Mark Welch, J. L., Hasegawa, Y., McNulty, N. P., Gordon, J. I. & Borisy, G. G. Spatial organization of a model 15-member human gut microbiota established in gnotobiotic mice. *Proc. Natl. Acad. Sci.* **114**, E9105–E9114 (2017).
 20. Chung, K. *et al.* Structural and molecular interrogation of intact biological systems. *Nature* **497**, 332–337 (2013).
 21. Yang, B. *et al.* Single-cell phenotyping within transparent intact tissue through whole-body clearing. *Cell* **158**, 945–958 (2014).
 22. Turnbaugh, P. J. *et al.* The effect of diet on the human gut microbiome: A metagenomic analysis in humanized gnotobiotic mice. *Sci. Transl. Med.* **1**, 6ra14–6ra14 (2009).
 23. Wang, M., Ahrné, S., Jeppsson, B. & Molin, G. Comparison of bacterial diversity along the human intestinal tract by direct cloning and sequencing of 16S rRNA genes. *FEMS Microbiol. Ecol.* **54**, 219–231 (2005).
 24. Zhang, Z. *et al.* Spatial heterogeneity and co-occurrence patterns of human mucosal-associated intestinal microbiota. *ISME J.* **8**, 881–893 (2014).
 25. Li, H. *et al.* The outer mucus layer hosts a distinct intestinal microbial niche. *Nat. Commun.* **6**, 8292 (2015).
 26. Yasuda, K. *et al.* Biogeography of the intestinal mucosal and luminal microbiome in the rhesus macaque. *Cell Host Microbe* **17**, 385–391 (2015).
 27. Paul B. Eckburg *et al.* Diversity of the human intestinal microbial flora. *Science.* **308**, 1635–1638 (2005).
 28. Elizabeth K. Costello, Christian L. Lauber, Micah Hamady, N. F. & Jeffrey I. Gordon, R. K. Bacterial community variation in human body habitats across space and time. *Science.* **326**, 1694–1697 (2009).
 29. Pédrón, T. *et al.* A crypt-specific core microbiota resides in the mouse colon. *MBio* **3**, 1–7 (2012).
 30. Richard, M. L. *et al.* Mucosa-associated microbiota dysbiosis in colitis associated cancer. *Gut Microbes* **9**, 131–142 (2018).
 31. Nava, G. M., Friedrichsen, H. J. & Stappenbeck, T. S. Spatial organization of intestinal microbiota in the mouse ascending colon. *ISME J.* **5**, 627–638 (2011).
 32. Faust, K. & Raes, J. Microbial interactions: From networks to models. *Nat. Rev. Microbiol.* **10**, 538–550 (2012).
 33. Licht, T. R. *et al.* Role of lipopolysaccharide in colonization of the mouse intestine by *Salmonella typhimurium* studied by in situ hybridization. *Infect. Immun.* **64**, 3811–3817 (1996).
 34. Huang, J. Y., Lee, S. M. & Mazmanian, S. K. The human commensal *Bacteroides fragilis* binds intestinal mucin. *Anaerobe* **17**, 137–141 (2011).
 35. Johansson, M. E. V *et al.* Bacteria penetrate the normally impenetrable inner colon mucus layer in both

- murine colitis models and patients with ulcerative colitis. *Gut* **63**, 281–291 (2014).
36. Swidsinski, A., Weber, J., Loening-baucke, V., Hale, L. P. & Lochs, H. Spatial organization and composition of the mucosal flora in patients with inflammatory bowel disease. *J. Clin. Microbiol.* **43**, 3380–3389 (2005).
 37. Johansson, M. E. V. *et al.* The inner of the two Muc2 mucin-dependent mucus layers in colon is devoid of bacteria. *Proc. Natl. Acad. Sci.* **105**, 15064–15069 (2008).
 38. Ariel, P. A beginner's guide to tissue clearing. *Int. J. Biochem. Cell Biol.* **84**, 35–39 (2017).
 39. Treweek, J. B. *et al.* Whole-body tissue stabilization and selective extractions via tissue-hydrogel hybrids for high-resolution intact circuit mapping and phenotyping. *Nat. Protoc.* **10**, 1860–1896 (2015).
 40. DePas, W. H. *et al.* Exposing the three-dimensional biogeography and metabolic states of pathogens in cystic Fibrosis sputum via hydrogel embedding, clearing, and rRNA labeling. *MBio* **7**, e00796-16 (2016).
 41. Fung, C. *et al.* High-resolution mapping reveals that microniches in the gastric glands control *Helicobacter pylori* colonization of the stomach. *PLOS Biol.* **17**, e3000231 (2019).
 42. Choi, H. M. T., Beck, V. A. & Pierce, N. A. Next-generation in situ hybridization chain reaction: Higher gain, lower cost, greater durability. *ACS Nano* **8**, 4284–4294 (2014).
 43. Fraser, S. E. *et al.* Programmable in situ amplification for multiplexed imaging of mRNA expression. *Nat. Biotechnol.* **28**, 1208–1212 (2010).
 44. Nguyen, T. L. A., Vieira-Silva, S., Liston, A. & Raes, J. How informative is the mouse for human gut microbiota research? *Dis. Model. Mech.* **8**, 1–16 (2015).
 45. Bowcutt, R. *et al.* Heterogeneity across the murine small and large intestine. *World J. Gastroenterol.* **20**, 15216–15232 (2014).
 46. Snipes, R. L. Anatomy of the cecum of the laboratory mouse and rat. *Anat. Embryol. (Berl.)* **162**, 455–474 (1981).
 47. Ramette, A. & Tiedje, J. M. Multiscale responses of microbial life to spatial distance and environmental heterogeneity in a patchy ecosystem. *Proc. Natl. Acad. Sci.* **104**, 2761–2766 (2007).
 48. Kolenbrander, P. E., Palmer, R. J., Periasamy, S. & Jakubovics, N. S. Oral multispecies biofilm development and the key role of cell-cell distance. *Nat. Rev. Microbiol.* **8**, 471–480 (2010).
 49. Cordero, O. X. & Datta, M. S. Microbial interactions and community assembly at microscales. *Curr. Opin. Microbiol.* **31**, 227–234 (2016).
 50. Ormerod, K. L. *et al.* Genomic characterization of the uncultured Bacteroidales family S24-7 inhabiting the guts of homeothermic animals. *Microbiome* **4**, 36 (2016).
 51. Mark Welch, J. L., Rossetti, B. J., Rieken, C. W., Dewhirst, F. E. & Borisy, G. G. Biogeography of a human oral microbiome at the micron scale. *Proc. Natl. Acad. Sci.* **113**, E791–E800 (2016).
 52. Greuter, D., Loy, A., Horn, M. & Rattei, T. ProbeBase-an online resource for rRNA-targeted oligonucleotide probes and primers: New features 2016. *Nucleic Acids Res.* **44**, D586–D589 (2016).
 53. Wagner, M., Hornt, M. & Daims, H. Fluorescence in situ hybridisation for the identification and characterisation of prokaryotes. *Curr. Opin. Microbiol.* **6**, 302–309 (2003).
 54. Quast, C. *et al.* The SILVA ribosomal RNA gene database project: Improved data processing and web-based tools. *Nucleic Acids Res.* **41**, 590–596 (2013).
 55. Cole, J. R. *et al.* Ribosomal Database Project: Data and tools for high throughput rRNA analysis. *Nucleic Acids Res.* **42**, 633–642 (2014).
 56. Bäumler, A. J. & Sperandio, V. Interactions between the microbiota and pathogenic bacteria in the gut. *Nature* **535**, 85–93 (2016).
 57. Dejea, C. M. *et al.* Patients with familial adenomatous polyposis harbor colonic biofilms containing tumorigenic bacteria. *Science* **359**, 592–597 (2018).

Supplementary Materials and Methods

- *Composition of acrylamide monomer mix*
- *Tissue preservation and clearing for imaging*
- *HCR staining bacterial 16S rRNA*
- *Media for Bacterial culture*
- *Optimization of lysozyme treatment for HCR*
- *Controls for in situ HCR*
- *In vitro assay to find formamide concentrations for stringent hybridization of taxon-specific HCR probes, as well as to quantify their sensitivity and specificity*

Supplementary Figures S1-S7

Supplementary Video captions S1-S4

Supplementary Tables S1-S2

Supplementary References

Contributions of non-corresponding authors

Composition of acrylamide monomer mix

The following reagents were used for the preservation of exposed intestinal tissue: Acrylamide solution 40% in water (#01697, Sigma Aldrich, Saint Louis, MO, USA), 2% Bis (#1610142, Bio-Rad, Hercules, CA, USA), Paraformaldehyde 32% (#15714-S, Electron Microscopy Sciences, Brisbane, CA, USA), Polymerization thermal initiator VA044 (#NC0632395, Wako Chemicals, Richmond, VA, USA). The acrylamide monomer mix for the protective gel layer on the mucosa requires the crosslinker bis-acrylamide to become rigid. The final concentrations of reagents for the gel layer were: 4% Acrylamide, 0.08% Bis-acrylamide, 4% Paraformaldehyde, 2.5 mg/mL VA044, 1X PBS. The final concentrations of reagents for acrylamide embedding of the rest of the sample were: 4% Acrylamide, 0.0% Bis-acrylamide, 4% Paraformaldehyde, 2.5 mg/mL VA044, 1X PBS.

Tissue preservation and clearing for imaging

To prepare tissue samples for imaging of the mucosal microbiota, C57BL/6J mice of 20–21 weeks of age were euthanized and their GIT tissues harvested. Each mouse received an intraperitoneal injection of 220 μ L of a 10X dilution of the sedative Fatal-Plus (Vortech Pharmaceuticals, Dearborn, MI, USA). Once a mouse was anesthetized, we performed transcardial perfusion with sterile, ice-cold 1X PBS for 20 min at a rate of 4-5 mL/min to euthanize the mouse and clear its vasculature of blood. During perfusion, the exposed viscera were kept wet with sterile 1X PBS, and covered with a small bag of ice. After perfusion, the viscera were quickly removed and kept in a dry, sterile tube on ice. In a biosafety cabinet,

the GIT was isolated from the mesentery, liver, and attached fat. The jejunum and duodenum were also removed and discarded. To preserve the external muscle layer of the intestines in its distended form, we fixed the remaining GIT (from ileum to rectum) for 3 min in ice-cold 4% paraformaldehyde (15714-S Paraformaldehyde 32%, Electron Microscopy Sciences, Hatfield, PA, USA), and then washed it in ice-cold 1X PBS for 3 min to stop fixation. After fixation, the distal colon and the ileum were removed and discarded. The cecum and the proximal colon were separated and kept in sterile containers on ice.

The cecum and the proximal colon were cut open longitudinally and the bulk contents cleared with sterile tweezers. The remainder of the GIT contents were removed by gently dripping sterile, cold 1x PBS across the exposed surfaces. Any intestinal contents that remained attached to the tissue surface after PBS treatment were retained. The proximal colon was then cut into two segments. One contained all the folds and the other segment was a transition from the cecum to the colon and contained no folds. The cecum tissue was split into four segments: the end tip, the middle, the top left, and the top right. Each segment was placed into a pool of PBS (0.5 mL) on a glass slide, which was contained by a silicon isolator (#666503; Grace Bio-Labs, Bend, OR, USA) to keep the tissue in place and prevent tissue desiccation.

Next, in a chemical safety cabinet, tissue samples from each mouse were put in a petri dish, placed in an ice box, and fixed for 1 h by adding 1 mL of ice-cold 4% paraformaldehyde (PFA) to each PBS pool. We replaced spent 4% PFA with fresh 4% PFA every 15 min. After fixation, tissues were flipped over onto the pool of 4% PFA (so that the muscle side was facing up). To increase the volume of the pools in which the tissues were submerged, we stacked onto each slide an additional two silicon isolators. We added more 4% PFA, covered each pool with a silicon membrane to avoid evaporation, placed them in Petri dishes, and transferred the slides into an ice box. The ice box was then placed in an anaerobic chamber along with the bis-acrylamide monomer mix (Supplementary Materials and Methods). In the anaerobic chamber, we removed the 4% PFA in which the tissues were floating, and substituted it with 2 mL of the monomer mix. The tissues were left in the monomer mix on ice for about 15 min so that the components of the mix could penetrate the bacterial biofilms and other contents on the tissues. The monomer mix was removed using a pipette and substituted with 1 mL of fresh mix. Finally, we removed 900 μ L. We covered the pools with plastic membranes (#664475; Grace Bio-Labs), and added a Kimwipe imbibed with PBS to maintain the humidity in the petri dish. We sealed each petri dish with parafilm and put all the Petri dishes into an incubator set to 37 °C in the anaerobic chamber for 3 h to allow the acrylamide layer to form at the glass-tissue interface. We removed the Petri dishes from the incubator and the anaerobic chamber and added a few droplets of 1X PBS onto each tissue to keep them humid. The Petri dishes were refrigerated (4 °C) overnight. The next day, the Petri dishes containing the tissue samples were put in a box with ice and brought back into the anaerobic chamber, where each tissue was embedded in an acrylamide matrix without bisacrylamide. This step is necessary to turn the tissue into a hydrogel. Embedding lasted 3 h, after which the excess acrylamide mix was removed and the tissue was polymerized for 3

h at 37 °C. The tissues were taken out of the incubator and the anaerobic chamber, and stored at 4 °C with a few droplets of sterile PBS.

Tissue samples were removed from the glass slides with a sterile razor-blade and glued (Gluture 503763; World Precision Instruments, Sarasota, FL, USA) onto a piece of semi-rigid plastic (Polypropylene film 160364-46510; Crawford Industries, Crawfordsville, IN, USA) that was previously cleaned of RNase (RNaseZap, AM9780; ThermoFisher Scientific), sterilized with 70% ethanol, and treated with oxygen plasma for 3 min to enhance adherence.

After samples were turned into a hydrogel and before they were passively cleared, we permeabilized bacteria according to the parameters prescribed by the optimization of lysozyme treatment for HCR. Samples were pre-incubated in 10 mM Tris-HCl (#AM9856, Invitrogen, Carlsbad, CA, USA) for 1 h at room temperature, then treated with lysozyme at a concentration of 5 mg/mL in 10 mM Tris-HCl, pH = 7.9, at 37 °C for 7 h for thin samples without much materials left on their surface, and for 13h for samples with abundant contents left on their surface. Lysozyme treatment was stopped by washing excess enzyme overnight in 1X PBS at room temperature with gentle shaking. Permeabilized samples were enclosed in tissue cassettes and cleared for 4 d in 8% w/v sodium dodecyl sulfate (SDS) in PBS, pH = 8.3 at 37 °C. SDS was vigorously stirred. pH was adjusted daily. SDS was removed by washing in 1X PBS with stirring for 2 d at 25 °C. Total DNA was stained with DAPI (3 µg/mL in PBS) for 1 d. Host mucus was stained by submerging samples in a solution of WGA in 1XPBS at a concentration of 50 µg/mL.

Distal ileum samples were obtained from a 9-month-old C57BL/6J male mouse and were processed similarly to tissues from the cecum and proximal colon.

HCR staining of bacterial 16S rRNA

To fluorescently tag 16S rRNA transcripts from mucosal bacteria, we incorporated HCR labeling of RNA to the workflow. HCR is executed in two stages: detection and amplification. In the detection stage, one or multiple HCR probes hybridize to homologous RNA transcripts. In the amplification stage, a unique initiator sequence encoded in each probe selectively hybridizes to matching DNA hairpin pairs. The HCR seeded by the initiator sequence concatenates the matching fluorescently labeled hairpins into a long double-stranded DNA molecule. Independent probes and orthogonal hairpins enable multiplexed fluorescent labeling of RNA markers.

We designed HCR probes (Supplementary Tables S1-S2) and used them to image the location of total bacteria and specific taxa on intestinal tissue. We used the eubacterial probe eub338-B4 and B4-Cy3B hairpins. Samples were pre-hybridized in a solution of 2xSSC (#V4261, saline sodium citrate, Promega Corp., WI, USA) and 10% dextran sulfate sodium (#D8906, Sigma, MO, USA) for 1 h at room temperature. Next, we treated samples for 16 h at 46 °C in a buffer consisting of 2xSSC, 10 %w/v dextran sulfate sodium, 15% formamide (#BP227100, Fisher Scientific, NH, USA) and probe eub338-B4 at a final concentration of

10 nM. The unbound probe was washed off for 1 h in a solution of 2xSSCT (2xSSC, 0.05 % Tween 20) and 30% formamide, followed by another wash in 2xSSCT for 1 h. Samples were pre-amplified in 5xSSC with 10 % w/v dextran sulfate for 1 h. During pre-amplification, the required amount of hairpins was heat-shocked (90 s at 95 °C) and cooled down to room temperature (at least 30 min in the dark). The amplification step was carried out in a buffer that consists of a solution with 5xSSC, 10 % w/v of dextran sulfate, and a final concentration of 120 nM of each hairpin (B4-Cy3B-H1, B4-Cy3B-H2). The amplification reaction lasted 16-20 h at room temperature in the dark. Hairpins that did not participate in the reaction were washed out in 2xSSCT for at least 1 h at room temperature with gentle shaking.

Multiplexed fluorescent labeling of 16S rRNA transcripts of mucosal bacteria by HCR was executed analogously to the monochromatic staining. However, because taxon-specific probes have different melting temperatures, hybridization reactions were executed over 3 d, starting with the probes that required the highest formamide concentration and finishing with the probes that required the least formamide. Because the detection sequence *cfb560* is degenerate and usually produces a low signal, we only considered the sequences (*cfb560a*, *cfb560b*) that target bacteria we found through sequencing. Hybridization reactions were scheduled as follows: *muc1437*-B4 and the suite *Igc354a-b-c*-B5 on day one (10% formamide), *clept1240*-B3 on day two (5% formamide), and *cfb560a*-B2, *cfb560b*-B2 and *lac435*-B1 on day three (0% formamide). Samples were pre-hybridized in a solution of 2xSSC (#V4261, saline sodium citrate, Promega Corporation) and 10% dextran sulfate sodium (#D8906, Sigma) for 1 h at room temperature. Next, samples were treated for 16 h at 46 °C in a buffer consisting of 2xSSC, 10 % w/v dextran sulfate sodium, formamide at the specified concentration (#BP227100, Fisher Scientific) and each probe at a final concentration of 10 nM. Unbound probes were washed off for 1 h in a solution of 2xSSCT (SSC with % Tween 20) and 30% formamide, followed by another wash in 2xSSCT for 1h (or 3 h for the last wash on day 3). Probe *clept1240*-B3 was used at a 2X concentration because it has one degenerate base. After all probes were hybridized to samples, the amplification stage was carried out in a single step. HCR hairpin pairs were assigned to fluorophores as follows: B1-A514, B2-A647, B3-A594, B4-Cy3B, B5-A488. The amplification buffer consisted of a solution of 5xSSC, 10% of dextran sulfate and 120 nM of each hairpin. The amplification reaction was run for 20 h at room temperature in the dark. Hairpins that did not participate in the reaction were washed out in 2xSSCT for 4 h at room temperature with gentle shaking.

HCR probes were ordered as individual 250 nmol scale DNA oligos purified by standard desalting (Integrated DNA Technologies, IA, USA). Hairpins were ordered from Molecular Instruments, a Caltech facility within the Beckman Institute. All the solutions were made with DNase/RNase-free distilled water (#10977023, Invitrogen).

Media for bacterial culture

The following media were used to culture bacteria for *in vitro* assays. *Escherichia coli* was cultured in LB media (LB Broth, #240230, Difco, Becton, Dickinson and Company, NJ, USA) and LB agar. *Clostridium scindens* was cultured in a mix of 50% Shaedler media (#cm0497, Oxoid, ThermoFisher, Waltham, MA, USA) and 50% MRS media (Lactobacilli MRS Broth, #288130, Difco), and in Schaedler agar. *Lactobacillus AN10* was cultured in a mix of 50% Shaedler media and 50% MRS media, and in MRS agar. *Bacteroides fragilis* and *Faecalibacterium prausnitzii* were cultured in LYBHI¹¹ media (brain-heart infusion medium supplemented with 0.5% yeast extract, Difco, Detroit, USA), and in LYBHI agar.

Tissue harvesting for sequencing

Four 4-month-old adult mice were euthanized by CO₂ inhalation according to protocols and guidelines of the Caltech Institutional Animal Care and Use Committee (IACUC). The gastrointestinal tract, from the stomach to the rectum, was dissected and stored in a sterile container on ice. The cecum of mice was cut open with sterile instruments on an ice-cold sterile surface inside a biosafety cabinet. The bulk of cecal contents was removed with sterile tweezers, stored in sterile tubes, and kept at -20 °C. The cecal tissue was kept flat on a cold and sterile surface while it was cleaned with ice-cold and sterile 1X phosphate-buffered saline. PBS 1X was obtained from a 10X dilution of phosphate buffered saline 10X (Corning, 46-013-CM) in UltraPure DNase/RNase-Free Distilled Water (10977023; ThermoFisher, Waltham, MA, USA). After removing contents from the cecum, the cecal mucosa was harvested by scraping it with sterilized microscopy glass plates. Samples were stored in sterile tubes at -20 °C. Cecal contents and tissue scrapings were sent to Zymo Research (Irvine, CA, USA) for 16S rRNA gene sequencing and bioinformatics analyses.

Optimization of lysozyme treatment for HCR

Preparation of acrylamide gel pads with embedded bacteria

Bacteria were cultured to exponential phase at 37 °C in anaerobic conditions. From this culture, a dense (10^9 – 10^{10} cells/mL) suspension of cells was prepared in PBS. This suspension was spiked into the monomer mix with bisacrylamide (see *Composition of acrylamide monomer mix*) to the final cell density of $\sim 5 \times 10^7$ cells/mL. The mix of monomer and cells sat on ice for 15 min before being dispensed into pools made of silicone isolators (13 mm diameter x 0.8 mm depth; #666507; Grace BioLabs) glued to microscope slides. We pipetted 106 μ L into each pool, and polymerized at 37 °C for 3 h in anaerobic conditions. The next day, the original silicone isolators were replaced with larger ones (20 mm diameter x 2.6 mm depth; #666304; Grace-Bio Labs). The new pools with the gels were filled with a monomer mix with no bisacrylamide (see *Composition of acrylamide monomer*) and incubated on ice for 3 h in anaerobic conditions. Next, the monomer mix was removed and the gels were polymerized at 37 °C for 3 h in anaerobic conditions. Bacteria in the gel pads were predigested in lysozyme buffer (10 mM Tris, pH=8.0) at room temperature for 1 h, and then digested with lysozyme (1, 2.5 or 5 mg/mL lysozyme in 10 mM Tris, pH = 8.0) at 37 °C for 6 h. Lysozyme was washed away with PBS at room temperature overnight. The gel

pads were cleared with 8% SDS in 1xPBS, pH = 8.3, at 37 °C for 2 d following a 1x PBS wash at 25 °C for another 2 d. Bacteria were hybridized with a eubacterial HCR probe (eub338-B5) in hybridization buffer (Materials and Methods) with 15% formamide and amplified for 16 h (Materials and Methods). Finally, DNA was stained with DAPI (5 µg/mL) overnight.

Imaging of gel-embedded bacteria

Gel pads were mounted in 1x PBS and imaged with an upright laser-scanning confocal microscope (LSM880, Carl Zeiss AG, Germany) using a long-working-distance water-immersion objective (W Plan Apochromat 20X/1.0 DIC Korr UV Vis IR, #421452-9700; Carl Zeiss AG). Fluorophores were excited using two lasers with $\lambda = 488$ nm and $\lambda = 405$ nm. Imaging settings were the same across all gel pads. Images were processed in commercial software for 3D image analysis (Imaris, Bitplane AG, Switzerland). Cell surfaces were identified by their fluorescence in the 405 nm channel. Finally, for the identified cells, mean cell fluorescence intensity in the 488 nm channel was computed.

Results

The Gram-positive bacterium *Clostridium scindens* was efficiently permeabilized in gel pads subjected to the treatment of 5 mg/mL of lysozyme (Fig. 2b-2c). To assess whether lysozyme treatment may affect HCR staining of Gram-negative bacteria, a lysozyme treatment optimization experiment was carried out using the model Gram-negative bacterium *Bacteroides fragilis*. Exponential phase *B. fragilis* cells were embedded into acrylamide gel pads, treated for 6 h with four concentrations of lysozyme (no lysozyme control, 1.0 mg/mL, 2.5 mg/mL, and 5.0 mg/mL) and cleared with 8% SDS for 2 d. 16S rRNA was stained by HCR using universal detection probe eub338, and DNA was stained with DAPI. Bacteria in gel pads were imaged in a confocal microscope (LSM 880, Carl Zeiss AG) from the surface of the gel down to 600 µm into each gel. Confocal images and the results from image analysis are shown in Supplementary Fig. S1. A 3D rendering of confocal images in the DAPI channel (Supplementary Fig. S1a, S1d, S1g and S1j) shows that DAPI staining did not require permeabilization of the peptidoglycan layer, justifying the choice of using the DAPI channel to define the surface of bacterial cells. When lysozyme treatment was omitted, *B. fragilis* cells at the surface of the gel were stained poorly by HCR (Supplementary Fig. S1b). Image analysis was in agreement with these visual inspections; ECDF curves shifted progressively to higher Signal/Background with depth (Supplementary Fig. S1c). Across all 100-µm thick slices, a substantial fraction of cells (>20%) were fainter than the set background value (Supplementary Fig. S1c). The lowest lysozyme concentration (1 mg/mL) was sufficient to improve HCR staining of *B. fragilis* (Supplementary Fig. S1e-f). Although cells at the surface of the gel pad appeared brighter, >99% of all cells across the entire 600 µm were brighter than the set background value (Supplementary Fig. S1f). Lysozyme concentrations 2.5 and 5.0 mg/mL did not deteriorate HCR staining (Supplementary Fig. S1h-i and S1k-l). These results showed that a treatment of 5 mg/mL of lysozyme for 6 h permeabilized the peptidoglycan layer of Gram-positive and Gram-negative bacterial cells; thus, we used this treatment as a reference for *in situ* experiments.

In vitro assays to find formamide concentrations for stringent hybridization of taxon-specific HCR probes, as well as to quantify their sensitivity and specificity

We created an *in vitro* assay to determine the adequate formamide concentration for the hybridization of each HCR probe to its ideal target (Supplementary Table S1 and Supplementary Fig. S3a), as well as to test the probes' sensitivity and specificity (Supplementary Fig. S3b). The assay consists of regularly spaced shallow acrylamide gels on a glass slide. Bacteria are embedded in the gels, which are then surrounded by individual silicone wells.

Preparation of bacteria embedded in shallow acrylamide gels

Bacteria were grown anaerobically at 37 °C to OD600 0.2–0.24 from overnight cultures (see *Media for bacterial culture*). Cultures were pelleted and resuspended in a preparation of gel mix with bisacrylamide (see *Composition of acrylamide monomer mix*). In anaerobic conditions, 3.8 µL of the acrylamide with bacteria were pipetted into each well of a SecureSeal imaging spacer (#470352; Grace BioLabs) that had been glued to a clean glass slide. Wells were sealed with a silicone membrane (#664475; Grace Bio-Labs). The slide was flipped upside down for 5 min so that bacterial cells could settle on the surface, and then the slide was placed in a sealed petri dish and placed in an anaerobic incubator for 2 h at 37 °C. Once gels solidified, a silicone isolator (#665101; Grace BioLabs) was added to each slide to create a pool around each gel. Next, bacteria were treated with a solution of 1 mg/mL lysozyme in 10 mM Tris balanced to pH = 8 for 2.5 h at 30 °C. Gels were washed twice with 1x PBS for 10 min and 30 min. In agreement with clearing methods, the glass slide was submerged in a solution of 4% SDS in 1x PBS at 37 °C for 2 h. The silicone wells were removed and the SDS solution was gently rinsed with 27 °C 1x PBS. Slides were further washed in 1xPBS for 10 min and overnight at room temperature. Slides were dried out and another silicone isolator was applied around gels. Probes were hybridized in 2x SSC (saline sodium citrate) with 10% dextran sulfate, 0-60% formamide, and final probe concentration of 10 nM. The hybridization buffer was pipetted into the silicone isolator wells, covered with a hybridization film (#716024; Grace BioLabs), and put in a sealed petri dish. Glass slides were incubated at 46 °C for 12 h. Unbound probes were washed three times with 2x SSCT (2x SSC, 0.05% Tween 20), and 30% formamide for 10 min. Three additional 10 min long washes were done in a buffer of 2x SSCT.

In the amplification step, hairpins were heat-shocked at 95 °C for 90 s and cooled down at room temperature for 30 min. Gels were covered with the amplification buffer of 2x SSC, 10 % w/v dextran sulfate and hairpins to a final concentration of 120 nM, and covered with a hybridization film. The amplification reaction was carried out at room temperature for 12 h. Unbound hairpins were washed out in a solution of 2x SSCT three times for 10 min. Three additional 10-min-long washes were done in a buffer of 2x SSC. Finally, bacterial DNA was stained with DAPI for 1 h, followed by a 30 min wash in 1x PBS. Slides were dried out and another imaging spacer was applied around the gels (#654008; Grace BioLabs). Gels were mounted in 1x PBS and covered with a glass coverslip. Bacteria on the upper surface of the gels were imaged with an oil-immersion objective (Plan Apochromat 63X/1.4 Oil DIC,

#420782-9900-799; Carl Zeiss AG) in an upright confocal microscope (LSM 880, Carl Zeiss AG).

Formamide curves

We next established the range of formamide concentrations that would yield stringent hybridization of taxon-specific HCR probes. Two slides of gels were prepared for each target bacterium (Supplementary Fig. S3a). One slide was used to quantify the efficiency of hybridization for concentrations of formamide in 15% steps from 0-60%. The second slide was used to refine the coarse measurements in 5% steps around the maximum of the coarse curve. Each slide was prepared once. We obtained one stack of images from each gel. Stringent hybridization was obtained around the concentration of formamide that produced the strongest average fluorescence.

Sensitivity and specificity of taxon-specific HCR probes

To quantify the sensitivity and specificity of taxon-specific HCR probes, one multi-species glass slide was prepared for each tested probe (Supplementary Fig. S3b). Hybridization was carried out at a formamide concentration within the intervals prescribed by the formamide bar plots (gam42a: 5%, eco630: 10%, lac435 0%, lgc354: 5%, cfb560: 0%, lab158 10%, clept1240 0%) (Supplementary Fig. S3b). Each hybridization experiment was carried out in one gel. One stack of images was acquired for each gel.

Image Processing

Images were analyzed using commercial software (Imaris, Bitplane, Belfast, UK). Image stacks were 3D-rendered and surfaces were created over individual bacteria using the fluorescent signal from the DAPI stain. Because bacterial DNA is found throughout the cell, surfaces derived from DAPI fluorescence encompass entire cells. For each cellular volume, the software computed the average fluorescent intensity for two channels: the eubacterial channel (eub338-B5/Alexa488) and the channel for a taxon-specific sequence (B4/Cy3B). Formamide plots (Supplementary Fig. S4) were obtained by plotting the mean and standard deviation of the fluorescence intensity in the Cy3B channel for each concentration of formamide.

To quantify the sensitivity and specificity of taxon-specific probes (Fig. 5b), images were processed as described in the previous paragraph. For each probe, we set a fluorescence detection threshold such that 85% of the ideal target bacterium was detected (e.g., the lac435 probe's ideal target was *C. scindens*). For each non-ideal target (for example lac435 should not target *B. fragilis* although it may bind to a small number of cells), off-target hybridization is quantified as the fraction of bacteria above the fluorescence detection threshold.

Acquisition, processing, and analysis of in situ imaging

Objectives and laser wavelengths

For large-scale acquisition, we used either of two objectives: Plan-Neofluar 5X/0,15 (#440320, Carl Zeiss AG), or EC Plan-Neofluar 5X/0.16 (#420330-9901, Carl Zeiss AG). For imaging at 20X magnification, we used one CLARITY optimized objective with an adjustable correction collar for compensation of spherical aberrations: Clr Plan-Neofluar 20x/1.0 Corr nd=1.45 M32 85mm (#421459-9970-000, Carl Zeiss AG). Fluorophores were excited with laser light of the following wavelengths: 405 nm, 488 nm, 561 nm, 633 nm. Spectral acquisition was used only for imaging samples with multiplexed HCR.

Imaging of the host-microbiota interface in the proximal colon

In one sample of the proximal colon (Supplementary Fig. S5), four areas corresponding to the tops of intestinal folds were imaged (Materials and Methods). The resulting image stacks contained three channels: one for DNA (DAPI), one for bacteria (HCR staining), and one for mucus (WGA lectin). To quantify the thickness of the layers of mucus at the top of intestinal folds, image stacks were 3D rendered in a commercial software (Vision4D 3.0, Arivis AG, Germany). Next, the maximum intensity projections of two digital cross sections (7 μm), along and across the longitudinal axis of the folds, were obtained. The thickness of the internal mucus layer was measured ($n = 85$) from the edge of the epithelium to the edge of the internal mucus layer. The thickness of the external mucus layer was measured ($n = 75$) from the end of the internal mucus layer to the bright edge of the external mucus layer (Fig. 3b).

Linear unmixing of spectral imaging

Computational linear unmixing of spectral imaging was performed to determine the relative contribution from each fluorophore for every pixel of in situ multiplexed imaging of bacteria. Linear unmixing requires the emission spectrum of every fluorophore that was employed in the staining of samples including DAPI and the suite of Alexa fluorophores of HCR. Spectra were acquired independently but in similar optical conditions as described in our *in situ* imaging of bacteria. We used *E. coli* bacteria embedded in thick acrylamide gels that were prepared with the procedure described in “Optimization of lysozyme treatment for HCR” (Supplementary Materials and Methods). Two gels of 13-mm diameter were split into six smaller gels that were taken through our standard HCR protocol. Each gel with *E. coli* was hybridized with a different probe. Each HCR probe consisted of the eubacterial detection sequence eub338 and a different initiator sequence. Each initiator sequence matched a different hairpin/fluorophore set. Probes: eub338-B1 (A514), eub338-B2 (A647), eub338-B3 (A594), eub338-B4 (A546), eub338-B5 (A488) and eub338-B4 (Cy3B). Bacterial DNA was not stained with DAPI. The emission spectrum of DAPI was acquired directly from the tissue samples. Gels were mounted in a RIMS solution with $n \sim 1.46$. Imaging of bacteria in gels was carried out using a laser-scanning confocal microscope with parallel spectral acquisition (LSM880, Carl Zeiss AG), and with the same objective as imaging of tissue samples (Clr Plan-Neofluar 20x/1.0 Corr nd=1.45 M32, Carl Zeiss AG). We extracted the

spectral references from the imaging of bacteria using commercial software (Zen 2.3 SP1, Carl Zeiss AG). Finally, the spectral references and the same software were used to perform linear unmixing of in situ images.

Multiplexed imaging of cecal crypts

Multiplexed confocal spectral images of cecal mucosa at 20X magnification were taken through linear unmixing (Materials and Methods) and analyzed computationally to measure the abundance and location of bacterial taxa that were labelled by HCR. The resulting data files contained image stacks with seven channels. Five channels corresponded to the probe/fluorophore pairs that were used in HCR (lcg354/A488, lac435/A514, muc1437/Cy3B, clept1240/A594 and cfb560/A647), one channel corresponded to the fluorescent DNA marker DAPI, and one channel stored pixels that were not assigned to any of the other six channels in linear unmixing and thus captured undefined content. Image stacks were uploaded to commercial software Vision4D (Vision4D 3.0, Arivis AG) and saved in the native *sis* format. Because tissue was sometimes not completely parallel to the plane of imaging, image stacks were rotated so that crypts were approximately aligned with the spatial z axis. Rotated stacks were cropped manually to remove areas without data.

The spatial analysis included ~60 crypts from three fields of view obtained from one cluster of crypts in a sample of the cecum. The internal volume of crypts was segmented manually using the “Draw Objects Tool.” The manual segmentation of crypts was guided by the DAPI channel, which showed the location of nuclei on the epithelial wall of crypts. To restrict the analysis to bacteria inside crypts, we used the segmented internal volumes of crypts as a mask on the channels with HCR staining (i.e., the fluorescence intensity value of voxels outside crypts was set to zero in the five HCR channels). Next, bacterial channels were segmented with an “Intensity Threshold” filter. In the output of this operation, a bacterial cell or group of bacteria in each channel (a segment) was defined as a set of contiguous pixels with intensities that fell within a range (minimum and maximum bounds, hereafter Min and Max) where at least one pixel had an intensity equal to a core value (required core intensity, RCI). To guide the definition of parameters (Min, Max, and RCI), we measured the intensity of a subset of pixels in each channel throughout every stack and defined RCI as the mean of pixel intensities, and Min as the difference between the mean and the standard deviation of intensities. Max was set equal to the maximum intensity of bacteria in the channel. Next, we filtered out segments that were ≤ 18 voxels. Channel cfb560/A647 required further manual curation to remove segments that were not likely to be bacteria due to their size and location. Finally, to determine which bacterial segments were located within each crypt, we combined all bacterial segments into a single list and used the “Segment Colocalization” operation. Bacterial segments were considered the “Subjects,” and the manually segmented crypts were used as “References.” The “Colocalization Measure” required that “Subjects” (bacteria) were completely within the “References” (crypts). The identities of bacterial segments and their crypt-specific assignment were stored at the end of the pipeline. The final result of the image-processing pipeline is shown in Supplementary Video S4.

The “Intensity Threshold” filter produced large bacterial segments that spanned multiple fields of view. Because we used the center of mass of segments to measure their location, we were at risk of losing spatial resolution in the location of bacteria along the crypt. To maintain high spatial resolution, we split the bacterial segments manually so they each spanned less than $\sim 10 \mu\text{m}$, and then performed the “Colocalization Measure” operation again. We exported the identity (imaging channel), volume (voxel count), center of mass (z coordinate in μm), and first/last plane of all segments (bacteria and crypts) into a MATLAB-readable file. From this output, we obtained the abundance (voxel count) of bacteria for each crypt, as well as the position (center of mass) of each bacterial segment in the framework of the corresponding crypt. The spatial reference $z = 0 \mu\text{m}$ in each crypt was set at the luminal end of the crypt segment. We obtained the abundance and position of bacteria in 59 crypts. Two crypts surpassed the average abundance per crypt by one order of magnitude, therefore they were considered outliers and excluded from further analysis.

The relationship between the abundance of bacterial taxa (voxel count) across the ensemble of examined crypts was analyzed in two ways. We used a hierarchical clustering analysis over the z-scored abundances of each taxon in each crypt (Materials and Methods), and we calculated the Spearman’s correlation between the abundance of all pairs of taxa in each crypt (Supplementary Fig. S7). Both analyses showed that the correlation between the abundance of Ruminococcaceae and Lachnospiraceae is the strongest across crypts.

Controls for in situ HCR

We performed HCR *in situ* to quantify the intensity of fluorescence due to nonspecific detection and amplification (Fig. 2d). We used an HCR probe with a nonspecific eubacterial detection sequence (non338) (Supplementary Table S1) on one tissue sample from the proximal colon of a mouse with a microbiota (specific pathogen free, SPF), and an HCR probe with a eubacterial detection sequence (eub338) on one tissue sample from the proximal colon of a germ-free (GF) mouse. The HCR reactions for these control experiments followed the same steps as the procedure to stain mucosal bacteria with a single eubacterial probe.

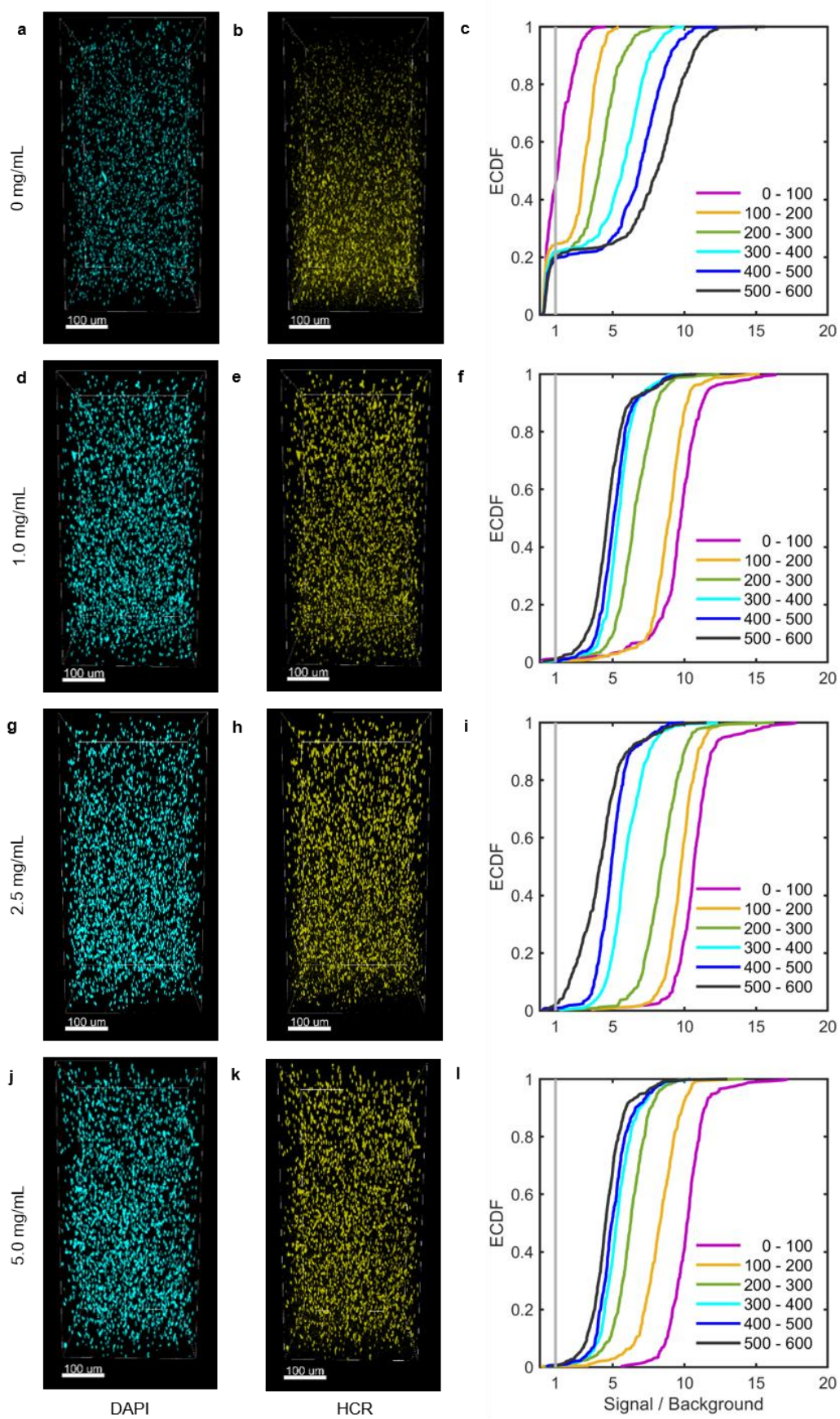


Figure S1. Lysozyme treatment optimization using *Bacteroides fragilis* as a model Gram-negative bacterium. Exponential-phase *B. fragilis* was embedded into four acrylamide gel pads and each pad was treated with lysozyme at a different concentration (**a-c**: no-lysozyme control; **d-f**: 1.0 mg/mL for 6 h, **g-i**: 2.5 mg/mL for 6 h, and **j-l**: 5.0 mg/mL for 6 h). HCR was used to stain 16S rRNA using a eubacterial detection sequence (**a, d, g, j**) and DAPI was used to stain DNA (**b, e, h, k**). In each gel pad, one field of view was imaged from the surface of the gel down to 600 μm . Image stacks were binned in 100 μm slices by depth. In each bin, empirical cumulative distributions functions (ECDF) of HCR-stained *B. fragilis* (**c, f, i, l**) were computed. Cell surfaces were defined by setting a threshold in the DAPI channel, and mean cell fluorescence in the HCR channel was computed for each cell. Cells were binned into six 100- μm thick slices by depth. For each slice, the ECDF of the signal/background ratio was plotted. Signal was defined as the mean cell fluorescence intensity in the HCR channel, and background was defined as the 99th percentile of voxel fluorescence values in the HCR channel from a control gel pad with no bacteria. A given ECDF value on the curve corresponds to the fraction of cells having a signal/background ratio less than or equal to the signal/background ratio specified on the horizontal axis.

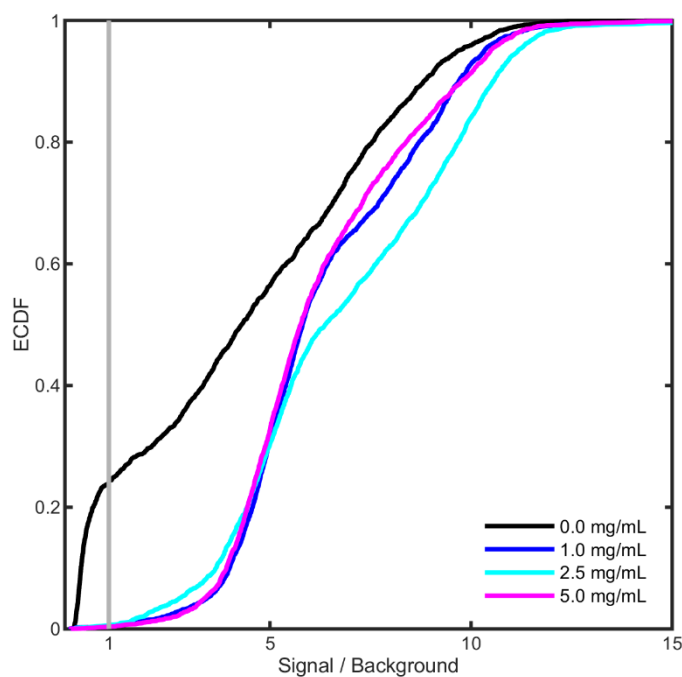


Figure S2. Empirical cumulative distributions functions (ECDF) of HCR staining of *Bacteroides fragilis* over entire image stacks (600 μm deep). Bacteria were embedded in four acrylamide gel pads, each treated with a concentration of lysozyme (0.0, 1.0, 2.5, or 5.0 mg/mL).

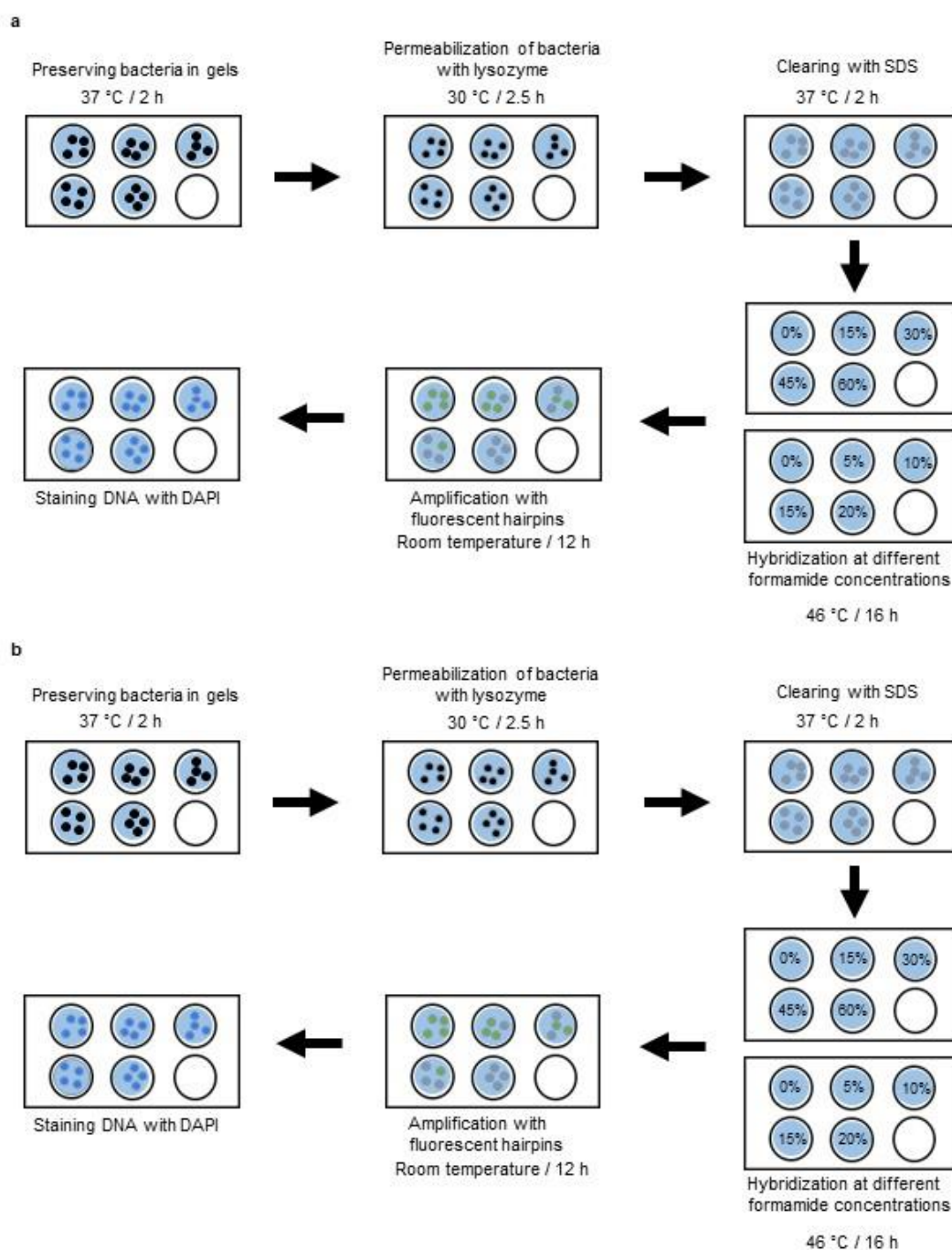


Figure S3. Experimental workflow to obtain the formamide hybridization curves (Supplementary Figure S4) of HCR probes with taxon-specific detection sequences (Supplementary Table S1). (a) Each target bacterium was embedded in shallow acrylamide gels, subjected to a sequence of treatments analogous to the in situ method, and treated with a range of formamide concentrations to determine the optimal concentrations for stringent hybridization to the bacterium's specific detection sequence. (b) To measure the sensitivity and cross reactivity of HCR probes, target bacteria were embedded in shallow acrylamide gels and subjected to a sequence of treatments analogous to the in situ method. The results of these experiments are presented in the main text (Fig. 5b).

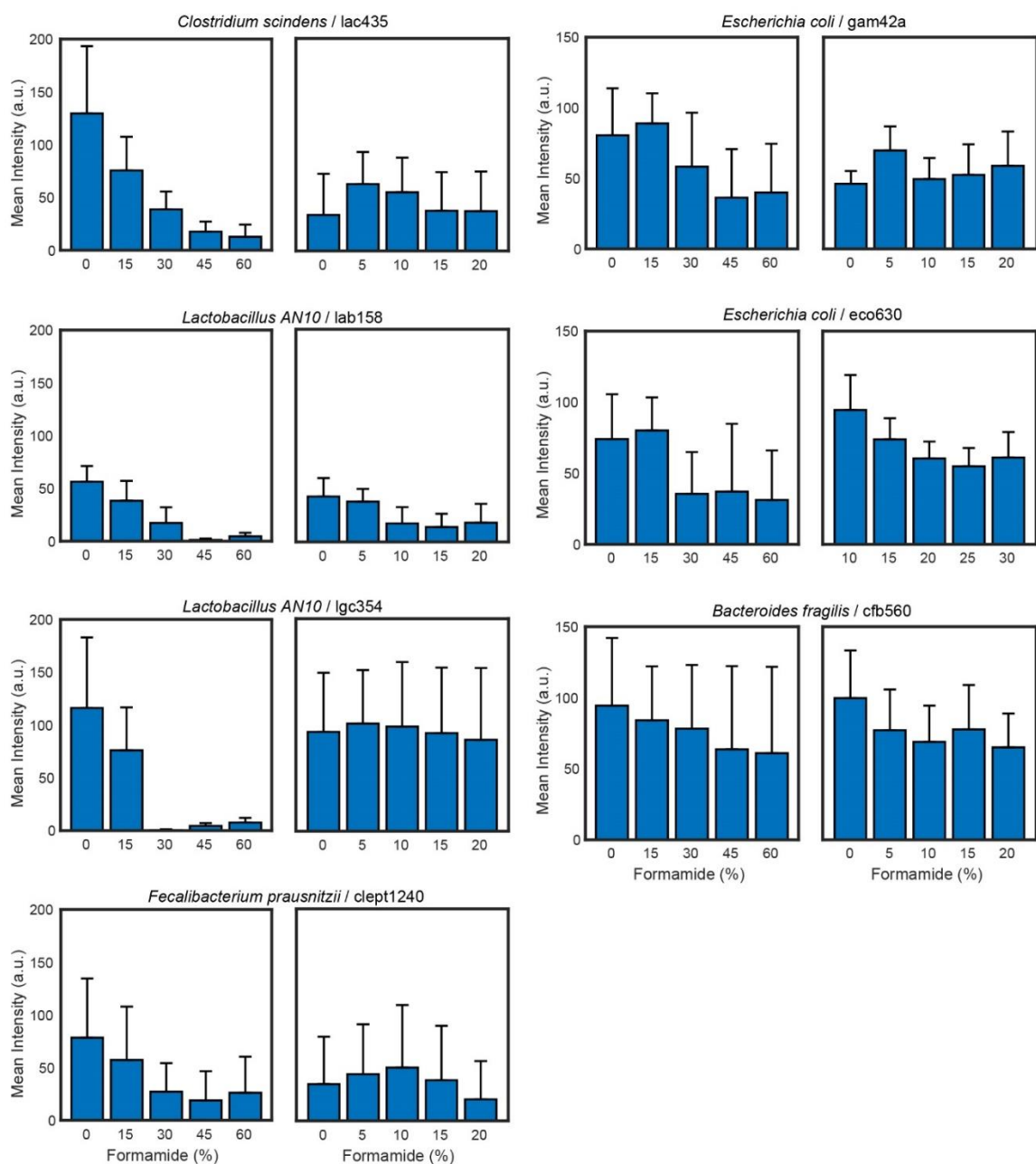


Figure S4. Formamide bar plots for the hybridization of taxon-specific HCR probes to their ideal targets (Supplementary Table S1). From these plots, we estimated the range of formamide concentration to use in the detection step of HCR as follows: gam42a: 5-15%, eco630: 10-15%, lac435 0-10%, lgc354: 0-10%, cfb560: 0-5%, lab158 0-10%, clept1240 0-10%. For the eubacterial detection sequence eub338, we used 15-20% and for muc1437, we used 10% formamide.

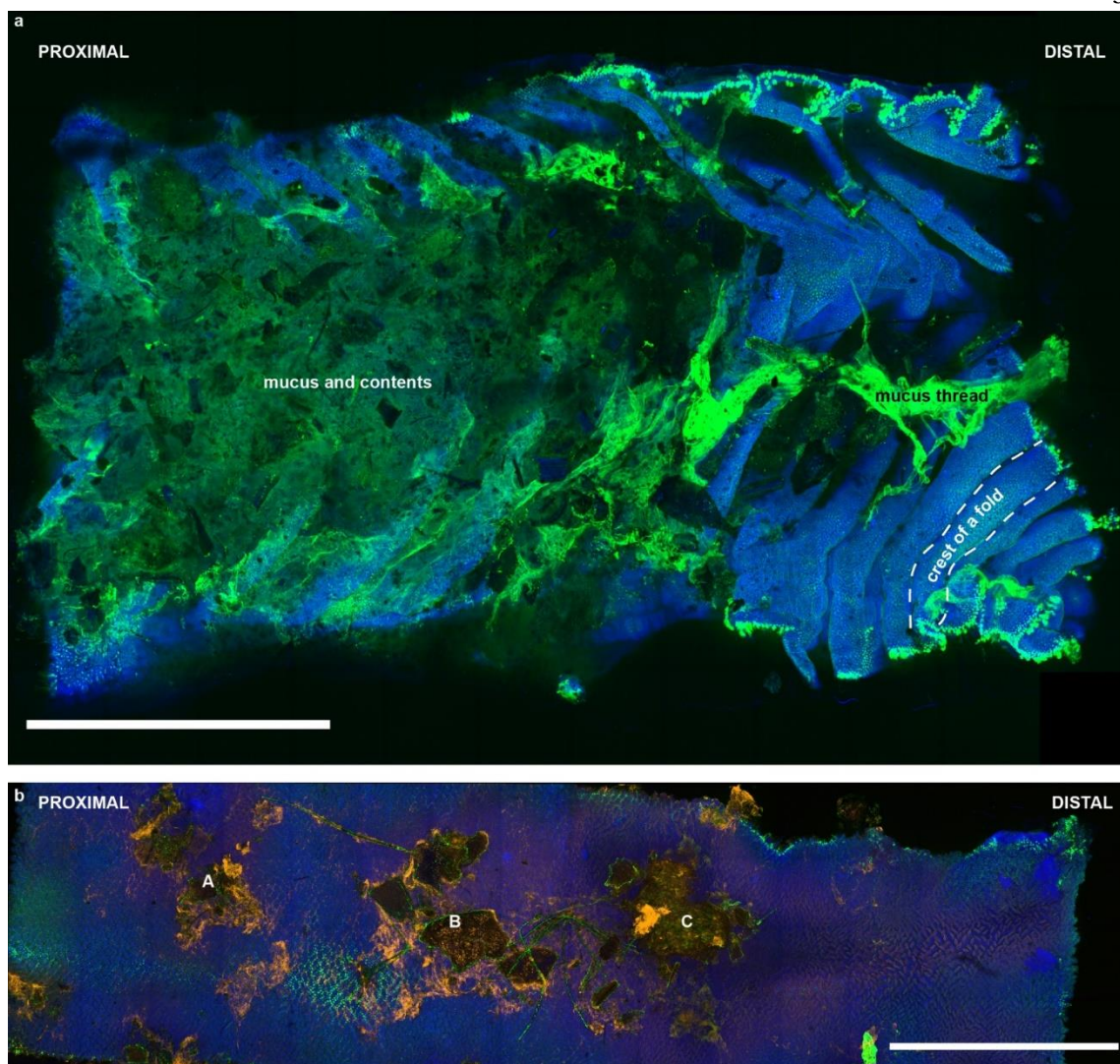


Figure S5. Large-scale imaging of the proximal colon and the distal ileum. (a) Maximum intensity projection of tiled images from the proximal colon of an adult mouse. DNA (blue) was stained with DAPI, and mucus (green) was stained with wheat germ agglutinin lectin conjugated to A488 fluorophore. Bacteria were stained by HCR, but were not imaged at low magnification in this sample. The image was obtained by stitching together multiple fields of view acquired at 5X magnification. The folded topography of the proximal colon is clearly visible near the distal end of the sample, which was not covered by mucus, but merely contained a large mucus thread. The proximal side of the sample was originally covered with luminal contents; these were carefully removed before the application of our method, however some contents remained. Scale bar: 5 mm. (b) Maximum intensity projection of tiled images from the distal ileum of an adult mouse processed by our method. DNA (blue) was stained with DAPI, mucus (green) was stained with wheat germ agglutinin lectin conjugated to A488 fluorophore, and bacteria (orange) were stained by HCR with a eubacterial probe (eub338). The image was obtained by stitching together multiple fields of view acquired at 5X magnification. Particles and materials that adhered to the tissue during cleaning were retained. Labels A-C indicate conglomerates of bacteria-colonized food particles, mucus, and biofilms that adhered to the ileal epithelium. Scale bar: 5 mm.

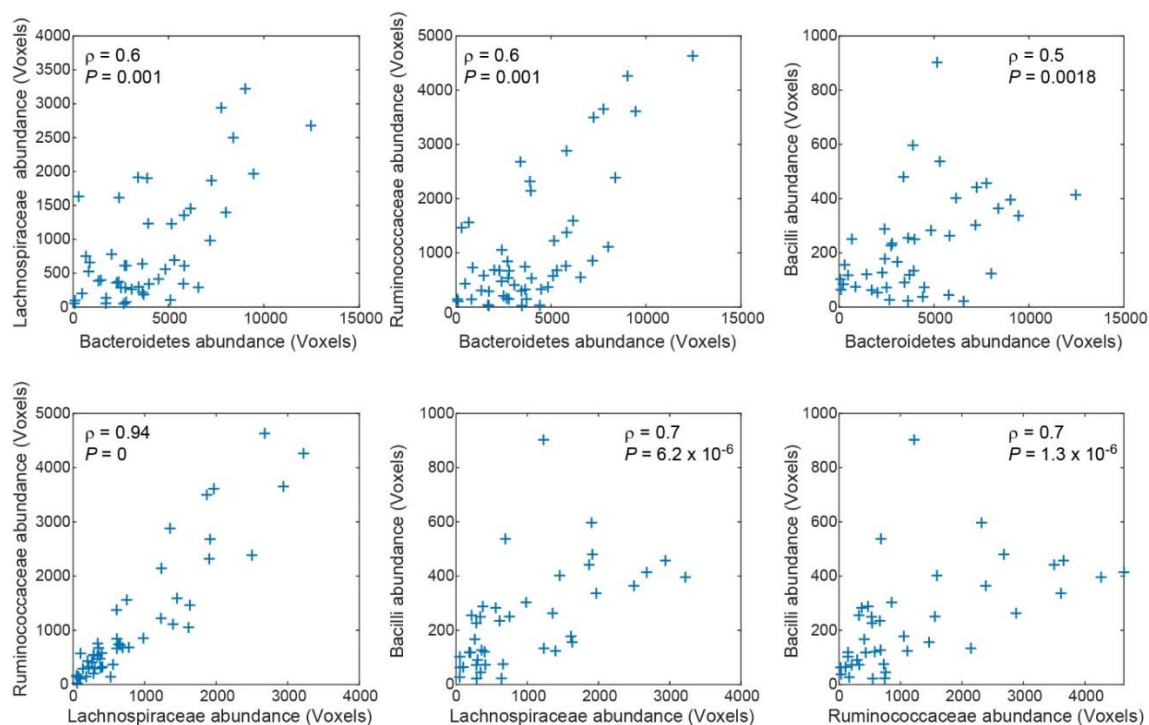


Figure S6. Scatter plots of the abundances (voxel counts) for pairs of bacterial taxa inside crypts, and the value of Spearman's correlation (ρ). Scatter plots and Spearman's correlations showed that the abundance of Lachnospiraceae and Ruminococcaceae track each other closely across the set of crypts. The P-values were smaller than the significance level of 0.05, rejecting the null hypothesis of no correlation ($\rho = 0$).

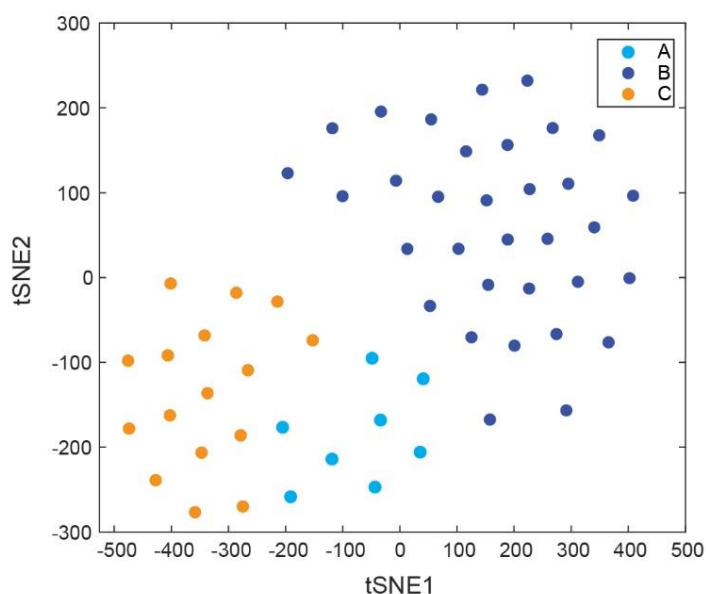


Figure S7. T-distributed stochastic neighbor embedding method (tSNE) for crypt classes identified by a hierarchical clustering analysis. We used t-SNE for dimension-reduction to test the relationship between the branches (A, B, and C) of the hierarchical clustering of crypts (Fig. 6a). The t-SNE clustering algorithm confirmed that the three crypt classes (A, B, and C) identified by HCA form three distinct sets of crypts.

Supplementary Video Captions

Supplementary Video S1. 3D imaging of bacteria in clarified tissues enables the quick exploration of the diverse spatial distribution of bacteria with respect to the host. 3D rendering (volumetric) of confocal imaging (20X) of bacteria (red, eub338 detection sequence) on the cecal mucosa (blue, DAPI staining of DNA). For ease of visualization, the rendered volume is digitally sectioned across the (**X,Y**) and (**X,Z**) planes. The volume is built slice-by-slice starting from the mucosa below the crypts to the lumen and shows that bacteria reached very deep inside some crypts (for example at $(X,Y) = (125, 225)$), and that crevices that ran across some crypts, for example the string of crypts between $300 \mu\text{m} \leq X \leq 450 \mu\text{m}$, enabled the formation of larger colonies than in crypts that are isolated (for example at $(X,Y) = (25, 350)$). Finally, the volume is sliced digitally along the **Y** axis to show that bacteria occupy the luminal and crypt space heterogeneously. Although some crypts were colonized from the top to the bottom, other crypts only had bacteria in the luminal space above the crypts.

Supplementary Video S2. 3D imaging of bacteria in clarified tissues enables the preservation of the rich bacterial colonization at the host-microbiota interface of the colon. 3D rendering (maximum intensity) of confocal imaging (20X) of the host-microbiota interface at the murine proximal colon. 3D rendering showed that bacteria (red) were mixed with mucus (green) in a distinct layer above the colonic mucosa (blue, DAPI staining of DNA). Large mucus threads were clearly observed inside the microbiota-mucus layer. For ease of visualization, the rendered volume is digitally dissected slice-by-slice across the (**X,Z**) plane, first without and then with the mucus layer on display. The thin layer of mucus that divided most bacteria from the epithelium was variable in width and allowed bacteria to reach the epithelium. At time 16 s, bacteria are seen inside a crypt (Fig. 3b) on the right of the image. Although the layer of bacteria was dense, it was discontinuous. Mucus of various densities (as per the intensity of mucus staining) support and segregate bacteria within the layer. Notably, dense mucus threads seem to be impenetrable to bacteria.

Supplementary Video S3. 3D imaging of bacteria in clarified tissues uses multiplexed HCR labelling of bacteria and spectral imaging to provide taxonomic resolution to the spatial order of complex communities. 3D rendering (volumetric) of spectral imaging (20X) of multiplexed HCR labelling of bacteria after linear unmixing. Five channels with bacteria-specific HCR staining (red, magenta, yellow, cyan, and green) and one channel for DAPI staining of DNA (blue) are shown simultaneously. For ease of visualization, the rendered volume was digitally sectioned across the (**X,Y**) and (**X,Z**) planes. The volume was built slice-by-slice from the mucosa below the crypts to the lumen to qualitatively show that crypts of similar sizes hosted different amounts of bacteria. The cfb560a/cfb560b - A647 channel displayed a strong signal from outside the crypts. However, this was likely an artifact of autofluorescence. Finally, the volume was digitally sliced along the **Y** axis to show that different taxa displayed a distinct spatial distribution as discussed in the main text (Fig. 7). Bacteroidetes colonized the full extent of crypts, whereas Firmicutes accumulated around the upper $\sim 15 \mu\text{m}$ layer of each crypt.

Supplementary Video S4. Computerized image processing of 3D imaging of bacteria in clarified tissues enables the simultaneous, *in situ* quantification of the components of crypts. 3D rendering (volumetric) of the host mucosa (blue) obtained by confocal spectral imaging (20X) is superimposed to the segmented bacterial channels (*Processing and analysis of in situ imaging*) and to one segmented crypt. The analysis of the spatial order of bacteria was restricted to bacteria inside crypts. This video shows the same field of view as in Supplementary Video S3.

Supplementary Tables

Table S1. Detection sequences in HCR probes and their ideal bacterial targets. HCR probes were designed by concatenating the desired initiator sequence (Supplementary Table S2) to the 3' end of a detection sequence. The names of the detection sequence and of the initiator sequence are concatenated to designate the HCR probe.

Name of detection sequence	Detection sequence	Rank	Name of ideal target taxon	<i>In vitro</i> target bacteria
eub338 ¹	5'- GCT GCC TCC CGT AGG AGT -3'	Domain	Bacteria	All bacteria
non338 ²	5'- ACT CCT ACG GGA GGC AGC -3'	Domain control	Domain control	none
gam42a ³	5'- GCC TTC CCA CAT CGT TT -3'	Class	<i>Gammaproteobacteria</i>	<i>Escherichia coli</i>
eco630 ⁴ (designed with DECIPHER)	5'- GCT TGC CAG TAT CAG ATG CAG T -3'	Genus	<i>Escherichia/Shigella</i>	<i>Escherichia coli</i>
cfb560 ⁵	5'- WCC CTT TAA ACC CAR T -3'	Phylum	<i>Bacteroidetes</i>	<i>Bacteroides fragilis</i>
lgc354a ⁶	5' - TGG AAG ATT CCC TAC TGC - 3'	Class	<i>Bacilli</i>	<i>Lactobacillus AN10</i>
lgc354b ⁶	5' - CGG AAG ATT CCC TAC TGC - 3'	Class	<i>Bacilli</i>	<i>Lactobacillus AN10</i>
lgc354c ⁶	5' - CCG AAG ATT CCC TAC TGC- 3'	Class	<i>Bacilli</i>	<i>Lactobacillus AN10</i>
clept1240 ⁷	5' - GTT TTR TCA ACG GCA GTC -3'	Family	<i>Ruminococcaceae</i>	<i>Fecalibacterium prausnitzii</i>
lac435 ⁸	5'- TCT TCC CTG CTG ATA GA-3'	Family	<i>Lachnospiraceae</i>	<i>Clostridium scindens</i>
lab158 ⁹	5' - GGT ATT AGC AYC TGT TTC CA- 3'	Genus	<i>Lactobacillus</i>	<i>Lactobacillus AN10</i>
muc1437 ¹⁰	5'- CCT TGC GGT TGG CTT CAG AT -3'	Species	<i>Akkermansia muciniphila</i>	Untested

Table S2. HCR initiator sequences and the corresponding fluorescent hairpins used in this study.

Name of initiator sequence	Initiator sequence	Hairpin pair-Fluorophore
B1	5'- TAT AGC ATT CTT TCT TGA GGA GGG CAG CAA ACG GGA AGA G-3'	B1(H1,H2) – A514
B2	5'- AAA AAG CTC AGT CCA TCC TCG TAA ATC CTC ATC AAT CAT C-3'	B2(H1,H2) – A647
B3	5'- TAA AAA AGT CTA ATC CGT CCC TGC CTC TAT ATC TCC ACT C-3'	B3(H1,H2) – A594
B4	5'- ATT TCA CAT TTA CAG ACC TCA ACC TAC CTC CAA CTC TCA C-3'	B4(H1,H2) – Cy3B
B5	5'- ATT TCA CTT CAT ATC ACT CAC TCC CAA TCT CTA TCT ACC C-3'	B5(H1,H2) – A488

Supplementary References

1. Amann, R. I. *et al.* Combination of 16S rRNA-targeted oligonucleotide probes with flow cytometry for analyzing mixed microbial populations. *Appl. Environ. Microbiol.* **56**, 1919–25 (1990).
2. Wallner, G., Amann, R. & Beisker, W. Optimizing fluorescent in situ hybridization with rRNA-targeted oligonucleotide probes for flow cytometric identification of microorganisms. *Cytometry* **14**, 136–143 (1993).
3. Manz, W., Amann, R., Ludwig, W., Wagner, M. & Schleifer, K.-H. Phylogenetic oligodeoxynucleotide probes for the major subclasses of proteobacteria: Problems and solutions. *Syst. Appl. Microbiol.* **15**, 593–600 (1992).
4. Wright, E. S., Safak Yilmaz, L., Corcoran, A. M., Ökten, H. E. & Noguera, D. R. Automated design of probes for rRNA-targeted fluorescence in situ hybridization reveals the advantages of using dual probes for accurate identification. *Appl. Environ. Microbiol.* **80**, 5124–5133 (2014).
5. O’Sullivan, L. A., Weightman, A. J. & Fry, J. C. New degenerate Cytophaga-Flexibacter-Bacteroides-specific 16S ribosomal DNA-targeted oligonucleotide probes reveal high bacterial diversity in river tuff epilithon. *Appl. Environ. Microbiol.* **68**, 201–210 (2002).
6. Meier, H., Amann, R., Ludwig, W. & Schleifer, K. H. Specific oligonucleotide probes for in situ detection of a major group of gram-positive bacteria with low DNA G+C content. *Syst. Appl. Microbiol.* **22**, 186–196 (1999).
7. Sghir, A. *et al.* Quantification of bacterial groups within human fecal flora by oligonucleotide probe hybridization. *Appl. Environ. Microbiol.* **66**, 2263–2266 (2000).
8. Kong, Y., He, M., McAlister, T., Seviour, R. & Forster, R. Quantitative fluorescence in situ hybridization of microbial communities in the rumens of cattle fed different diets. *Appl. Environ. Microbiol.* **76**, 6933–6938 (2010).
9. Harmsen, H. J. M., Elfferich, P., Schut, F. & Welling, G. W. A 16S rRNA-targeted probe for detection of lactobacilli and enterococci in faecal samples by fluorescent in situ hybridization. *Microb. Ecol. Health Dis.* **11**, 3–12 (1999).
10. Derrien, M., Collado, M. C., Ben-Amor, K., Salminen, S. & De Vos, W. M. The mucin degrader *Akkermansia muciniphila* is an abundant resident of the human intestinal tract. *Appl. Environ. Microbiol.* **74**, 1646–1648 (2008).
11. Martín, R. *et al.* Faecalibacterium prausnitzii prevents physiological damages in a chronic low-grade inflammation murine model. *BMC Microbiol.* **15**, 1–12 (2015).

Contributions of non-corresponding authors

Octavio Mondragon-Palomino

1. **Idea generation.** Conceived the project with R.F.I. Contributed financially to the project.
2. **Preliminary experimental work.** Demonstrated the feasibility of the project in preliminary experiments. Learned necessary technologies that were originally unavailable in the lab. Literature search and *in silico* testing of probes. Tested multiple tissue sample preservation strategies.
3. **Method development.** Conceived and developed the method’s workflow. Conceived and supervised the development of *in vitro* hybridization assays in shallow gels. Conceived lysozyme treatment optimization in gels.
4. **Data accumulation.** Planned and performed all tissue sample preparation and *in situ* microscopy. Trained and advised R.P. and J.G. in microscopy for *in vitro* hybridization assays. Performed and analyzed controls for *in situ* HCR. Obtained spectral references and executed spectral imaging strategy. Collected samples for sequencing with RP.

5. **Data analysis.** Processed all *in situ* imaging, extracted all data from *in situ* imaging, conceived and executed spatial analysis in crypts, conceived statistical analysis across crypts (HCA) with AL, calculated population correlations across crypts. Made measurements of mucus layers of the proximal colon. Analyzed *in situ* HCR controls. Conceived and supervised data analysis for *in vitro* hybridization assays in shallow gels.
6. **Outline writing.** Conceived and wrote outlines.
7. **Figure generation.** Created the figures for the main text except Fig. 2c and Fig. 6. Created early versions of Fig. 5b with data by J.G. Created Supplementary Figs. S5-S6, and created Supplementary Figs. S3-S4 with materials provided by J.G. and R.P. Created Supplementary Table S2. Created Supplementary Table S1 with material provided by J.G. Created Supplementary Videos.
8. **Manuscript writing.** Wrote the manuscript.

Roberta Pocevičiute

1. **Method development.** Major contributor to the development of the sample preparation method. Developed the assay for the optimization of lysozyme treatment.
2. **Data accumulation.** Collected all data of lysozyme treatment optimization. Collected samples for sequencing with O.M.P.
3. **Data analysis.** Analyzed all data of lysozyme treatment optimization experiments in coordination with O.M.P. Contributed to the analysis of data from *in vitro* hybridization assays in shallow gels.
4. **Figure generation.** Created Fig. 2c and Supplementary Figs. S1-S2. Supplied plots for Supplementary Fig. S4, and color intensity plot for final version of Fig. 5b.
5. **Manuscript writing.** Wrote methods and results/discussion of lysozyme treatment optimization.

Antti Lignell

1. **Idea generation.** Conceived quantitative multiplexing of bacteria by HCR staining together with O.M.P. Conceived the idea of hierarchical clustering analysis (HCA) approach to describe bacterial colonization patterns in strong collaboration with O.M.P. Contributed financially to the project.
2. **Preliminary experimental work.** Participated in preliminary experiments regarding HCR staining of bacteria.
3. **Method development.** Developed the HCR staining protocol together with O.M.P. Advised on the development of sample mounting protocol.
4. **Data analysis.** Developed the code and performed the HCA and tSNE analyses, as well as mapping crypt states to the physical space.
5. **Figure generation.** Generated plots for Fig. 6 and Supplementary Fig. S7.

6. **Manuscript writing.** Contributed to main text related to HCA and tSNE analyses. Edited late versions of the text.

Jessica Griffiths

1. **Idea generation.** Contributed to the conception of *in vitro* hybridization assays in shallow gels.
2. **Preliminary experimental work.** Researched and selected bacterial species for positive controls of clept1240 detection sequence.
3. **Method development.** Developed and troubleshot *in vitro* hybridization assays in shallow gels.
4. **Data accumulation.** Performed all microscopy for *in vitro* hybridization assays in shallow gels (Fig. 5b and Supplementary Fig. S3-S4).
5. **Data analysis.** Developed a computational image processing pipeline in commercial software (Imaris) for the quantification of *in vitro* hybridization assays in shallow gels. Analyzed the resulting data (Supplementary Fig. S4). Analyzed data for Fig. 5b.
6. **Figure generation.** Provided early versions of Fig. 5b, Supplementary Fig. S3-S4.
7. **Manuscript writing.** Provided written summary of the methods, data collection, and data analysis for *in vitro* hybridization assays in shallow gels.

TRANSLATION OF 3D MUCOSAL IMAGING TO PARTICULARLY THICK MOUSE JEJUNUM AND HUMAN GUT SAMPLES

Introduction

Host-microbe interactions in the gut have been shown to play a role in cancer¹⁻³, metabolic syndrome^{4,5}, neurodegenerative disease^{6,7}, neurological⁸, and psychological disorders⁹. Although the host-microbe mucosal interface may be pivotal in many disorders, in this work we have focused on inflammatory bowel disease (IBD) as one important example. Recent studies into the pathogenesis of IBD, primarily ulcerative colitis (UC) and Crohn's disease (CD), have established that disrupted host-microbe homeostasis in the gut is the hallmark of IBD. On the host side, genetic susceptibility loci have been implicated in the maintenance of host-microbe homeostasis, including genes associated with barrier function, microbial recognition, immune system regulation, and the function of both pro- and anti-inflammatory arms of the immune system¹⁰, suggesting that host response towards commensals is altered in IBD. As expected, such altered responses by the host are accompanied by changes in gut microbiota structure, with reduced community diversity being the most widely supported signature of IBD^{11,12}. Furthermore, manifestation of the IBD phenotype requires microbiota: germ-free mice (even those genetically susceptible to IBD) develop a less severe phenotype than microbiota-competent specific-pathogen free (SPF) mice¹³, and antibiotics temporarily alleviate IBD symptoms in humans¹⁴, although in the long run they may further disrupt microbiota structure¹⁵. It has long been recognized that environment plays a role in the pathogenesis of IBD¹⁶, however, whether a subset of microbiota members proactively drives disease remains an active area of research.

To better understand the role of microbiota in IBD, the focus has shifted towards the analysis of mucosal microbes^{15,17} which are compositionally distinct from microbes in the stool or lumen¹⁸⁻²⁰ and may interact with the host not only through diffusible signals but also through direct contact. Indeed, the comparison of mucosal microbes has outperformed the

comparison of luminal microbes in classification of CD-positive and CD-negative patients¹⁵, supporting the hypothesis that mucosal microbiota are more pivotal in the pathogenesis of IBD. Palm et al.²¹ sorted fecal bacteria from IBD patients based on the degree of IgA coating and determined that the highly IgA-coated fraction induced a stronger IBD phenotype in mice and that these coated bacteria also penetrated the normally sterile inner mucus layer^{22,23}, further suggesting that ability to colonize mucosa may discriminate IBD drivers from other commensals. Moreover, an analysis of mucosa-adherent fungi, such as *Malassezia restricta*, determined that mucosal fungi drive inflammation in a subset of CD patients with genetic susceptibility in the *CARD9* gene²⁴. Curiously, *M. restricta* persisted in the mucosa despite the heightened immune response, implying that either microbial clearance was insufficient or that *M. restricta* successfully persisted despite mucosal inflammation. Adherent mucosal biofilms visualized by fluorescence in situ hybridization (FISH) have been documented in CD patients^{25,26}, however, their exact spatial location and structure in the gut and their functional significance are not fully characterized or understood.

When confined to a different spatial structure, a synthetic community has been shown to exhibit a different phenotype²⁷, suggesting that the reverse also holds merit: the spatial structure of a microbial community may influence its phenotype and function. However, commonly used methods, such as sequencing, normally require sample homogenization and, as result, report average levels of target analyte, e.g. bacterial load or host marker expression, across space. Such averaging may be suitable in the study of luminal and fecal microbiota because microbiota in these locations have been shown to be well-mixed^{28,29}; however, averaging is not appropriate in the study of mucosal microbiota because the mucosal landscape of the host is complex, and villi, crypts, and epithelial folds prevent thorough mixing. Imaging of two-dimensional (2D) thin sections has been the gold standard, however, because host-microbe and microbe-microbe interactions are not confined to two dimensions, imaging of thin sections inevitably loses precious information and biases the perception of the full three-dimensional (3D) structure, unless a laborious 3D reconstruction from many separate sections is performed. Although attempts have been made to image thicker sections, imaging has been limited to a depth of only 12.5 μm ³⁰.

CLARITY, a method for 3D imaging of tissues, was a key breakthrough in the field of neuroscience³¹⁻³⁴. In neuroscience, 2D imaging was particularly limiting because 3D information is necessary to map complex neuronal networks. This need motivated the development of various hydrogel tissue stabilization, lipid clearing, and refractive index matching modalities for reduced light scattering and increased imaging depth for 3D imaging³²⁻³⁴. Steps have been taken towards translating CLARITY to 3D imaging host-microbe interface in the gut. For example, in combination with sensitive detection of bacteria by hybridization chain reaction (HCR v2.0^{35,36}), CLARITY has been used to visualize bacteria in the sputum of cystic fibrosis patients and their location relative to secreted mucus and free host cells³⁷. However, host epithelium was not captured by this method. CLARITY has also been used to preserve and clear intact mouse gut tissue^{38,39}; however, neither bacteria nor mucus were visualized by these methods.

Imaging of thin sections has exposed challenges associated with preservation of loosely adherent bacteria and mucus^{26,40,41}. Carnoy and methanol-Carnoy fixatives have been the fixatives of choice as loosely adherent bacteria and mucus could not be robustly visualized in paraformaldehyde (PFA) or formalin-fixed samples^{26,40,41}. However, PFA is a desirable fixative because it is part of various 3D imaging protocols³³. Curiously, novel preservation protocols that rely on PFA fixation in combination with a hydrogel³⁷ [Chapter 2] or resin embedding³⁰ report successful visualization of bacteria and mucus, suggesting that it is not PFA but rather other components in the fixative solution, e.g. solvent or buffer, that are problematic. PFA and Carnoy fixatives are formulated in aqueous and organic solvents, respectively, whereas mucus is a biological hydrogel with high affinity for water⁴². Therefore, mucus may disperse into the aqueous fixative unless it is physically protected by a hydrogel or resin^{30,37}, explaining the recent successes in mucus preservation even in PFA-fixed samples.

In Chapter 2, we presented a novel implementation of CLARITY for 3D imaging of delicate mucosa over large areas of mouse gut tissue. However, labeling and 3D imaging of particularly thick samples presented challenges, such as low signal-to-background deep in

the hydrogel-tissue hybrid due to poor reagent penetration during staining and poor removal during washing. Outside the fields of microbiology and microbiota, transport limitations have been met by elegant solutions, such as tuning hydrogel porosity for improved transport of large molecules⁴³, strategies to turn probe-target binding on or off in recognition that binding slows down probe transport⁴⁴, utilization of stochastic electrical fields for accelerated diffusion⁴⁵, and inclusion of an AND gate in the design of HCR probes for automatic background suppression⁴⁶. Moreover, as modern imaging gained momentum, the number of imaging targets quickly exhausted the number of fluorophores with non-overlapping spectra. In response, multiplex imaging is accomplished by multiple rounds of staining/destaining followed by image re-alignment^{44,47} or spectral imaging followed by unmixing of fluorescence spectra^{29,48,49}. However, these advances have not yet been adapted to investigate microbial communities in clinical samples, such as resected human gut samples from IBD patients. These samples offer ample material for spatial structure interrogation into the host-microbe relationship in IBD that is critical to better understanding this disease.

Acknowledging the importance of host-microbe interactions on mucosal surfaces in IBD, yet the limited understanding of their spatial structure, we leverage recent advances in fluorescence microscopy for imaging particularly thick samples, specifically resected human gut samples from IBD patients. Here we present an improved design of our previously described [Chapter 2] two-step acrylamide hydrogel for stabilization of both fragile mucosa and the underlying tissue. Previously [Chapter 2], we stabilized fragile mucosa with a high-density surface hydrogel, however, we observed that this hydrogel created an additional transport barrier. We predicted that this high-density surface hydrogel was essential for preservation of fragile mucosa and that the previously reported loss of bacteria and mucus in PFA-fixed samples^{26,40,41} was the result of exposing hydrophilic mucosa to an aqueous fixative solution. Therefore, we have further optimized our two-step hydrogel chemistry such that it continues to retain loosely adherent bacteria and mucus, but now also permits the entry of large probes, such as antibodies. Furthermore, to mitigate the problem of unwashed HCR probes deep in the hydrogel, we have integrated the concept of split HCR v3.0 probes, originally designed for mRNA staining with automatic background suppression⁴⁶, to

visualize mucosal colonizers with taxonomic resolution, high signal-to-background ratio and low false positive rate deep into hydrogel-tissue hybrids. Finally, we aimed to combine these advances to simultaneously visualize bacteria with HCR v3.0, mucus with lectins and host cells with antibodies in a mouse and present preliminary validation of these advances using resected human gut samples of IBD patients to show that our technology preserves and retained loosely adherent mucus.

Results

Protective surface gel retains loosely adherent bacteria and mucus

To validate that our previously used high acrylamide concentration surface hydrogel was necessary to preserve and retain mucus and the associated bacteria, we compared the preservation of bacteria and mucus in mouse proximal colon samples with or without A4B.08P4 (4% acrylamide, 0.08% bis-acrylamide and 4% PFA) protective surface gel described in Chapter 2 (Fig.3.1). To protect fragile mucosa as soon as possible and minimize mucus and bacteria losses, the surface gel was polymerized before tissue infusion with tissue gel monomer mix (Fig.3.2). Both tissues shown in Figure 1 were fortified with a low-density (i.e. low acrylamide content, in this case, A1B.01P1) liquid hydrogel that is not expected to offer sufficient protection to the loosely adherent mucosal matter. After a multi-step processing and staining procedure that involved shaking the tissues in various aqueous solutions and harsh clearing in sodium dodecyl sulfate (SDS) (see Methods), bacteria were scarce, and the mucus appeared to be lost from the crypts when a protective surface gel was omitted (Fig.3.1, A and C). However, when the mucosa was protected by a high-density surface hydrogel (A4B.08P4), mucus and bacteria were successfully retained (Fig.3.1, B and D). This experiment supports the hypothesis that the previously reported loss of bacteria and mucus in PFA-fixed samples^{26,40,41} was the result of using an aqueous solution on a hydrophilic tissue.

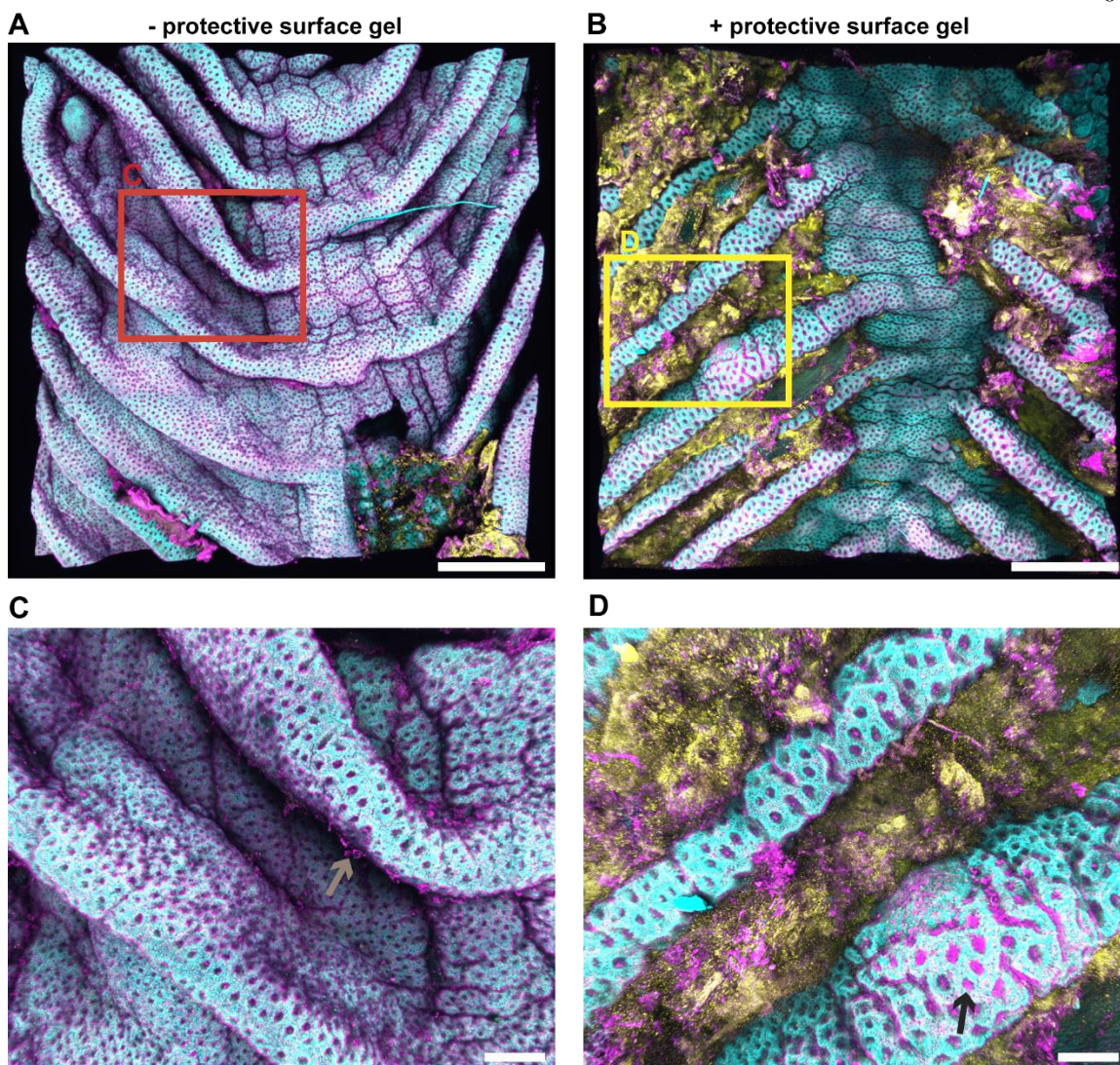


Figure 3. 2. A protective surface hydrogel retains loosely adherent bacteria and mucus in a mouse proximal colon. (A and C) A mouse proximal colon preserved with (A and C) or without (B and D) a protective surface hydrogel. The tiles were scanned with a 10x objective on Zeiss LSM 880 confocal microscope for DAPI staining of epithelium (cyan), WGA staining of mucus (magenta) and HCR v2.0 staining of bacteria with a universal bacterial EUB338 probe. In panel (C), grey arrow points to areas where mucus appeared to sheered and lost from the crypts. In panel (D), black arrow points to a crypt that was filled with mucus, which was not lost during the procedure. Both tissues were fortified with the same low-density hydrogel and were permeabilized, cleared, stained, and imaged following identical protocols. Scale bars: (A and B) 1 mm and (C and D) 200 μm .

Protective surface gel creates an additional transport barrier; changing hydrogel chemistry improves transport

Next, we sought to address transport limitations posed by the protective surface gel. As expected, the protective surface gel created an additional transport barrier, especially for large molecules with a large hydrodynamic radius⁵⁰. For example, our previously reported hydrogel chemistry impeded lysozyme diffusion, requiring us to increase lysozyme concentration from the standard 1 mg/mL to 5 mg/mL [Chapter 2], and almost completely prohibited antibody entry (Fig.3.3B, left). In other applications, permeability problems posed by a firm hydrogel surrounding soft tissues were addressed by polymerizing a liquid hydrogel around them⁴³, however, our previous experiment showed that a firm surface hydrogel was necessary for preservation of fragile mucosa (Fig.3.1). Our previously observed severe transport limitations may be explained by the two-step hydrogel embedding protocol (Fig.3.2). Briefly, to protect fragile mucosa as soon as possible and minimize mucus and bacteria losses, the surface gel is polymerized before tissue infusion with tissue gel monomer mix (Fig.3.2D). In this step, elevated temperature (37 °C) destabilizes the thermal initiator and speeds up reaction initiation and propagation, and high acrylamide concentration further increases propagation rate, such that hydrogel monomers preferentially polymerize into a surface gel rather than diffuse into the tissue. Because this polymerization is performed first, the tissue-gel-monomer mix may further fortify the protective surface gel and reduce its permeability in the next step (Fig.3.2E). Specifically, in the next step, the tissues are first infused with the tissue-gel-monomer mix on ice to slow down thermal initiator decomposition and reaction initiation so that hydrogel monomers preferentially diffuse through the tissue and, unavoidably, through the surface gel. The infused tissue-gel-monomer mix is then polymerized at 37°C. We predicted that when high acrylamide concentration is used in both steps, the resulting small pore size of the surface gel (Fig.3.3A, left) severely reduces antibody diffusion rate, increasing Damköhler number and leading to reagent accumulation at the surface and weak staining deep in the hydrogel-tissue hybrid⁴⁵. To improve permeability of these firm gels, we switched from the A4B0P4 (4% acrylamide and 4% PFA) [Chapter 2] to an A1B.01P4 (1% acrylamide, 0.01% bis-acrylamide and 4%

PFA) tissue gel formulation to not over-polymerize the surface gel (Fig.3.3A). Although both A4B0P4 and A1B.01P4 formulations form soft or liquid hydrogels upon polymerization⁴³, the chemistry of the gel with lower acrylamide content (A1B.01P4), substantially improved transport of large molecules, such as antibodies (Fig.3.3, B-C), without increasing net protein loss during clearing (Fig.3.3D) or affecting the final tissue transparency after clearing (Fig.3.3E). Because the tissues are only briefly fixed in 4% PFA before surface-gel polymerization (Fig.3.2C), PFA concentration in the tissue gel formulation had to be maintained at the standard 4% concentration to ensure thorough fixation. Importantly, PFA in the surface gel formulation improved its bonding to tissues without affecting the gel's final firmness, suggesting that PFA in the surface gel formulation could be reduced or excluded for best transport properties. The final surface and tissue gel formulations were chosen to be A4B.08P1 and A1B.01P4, respectively.

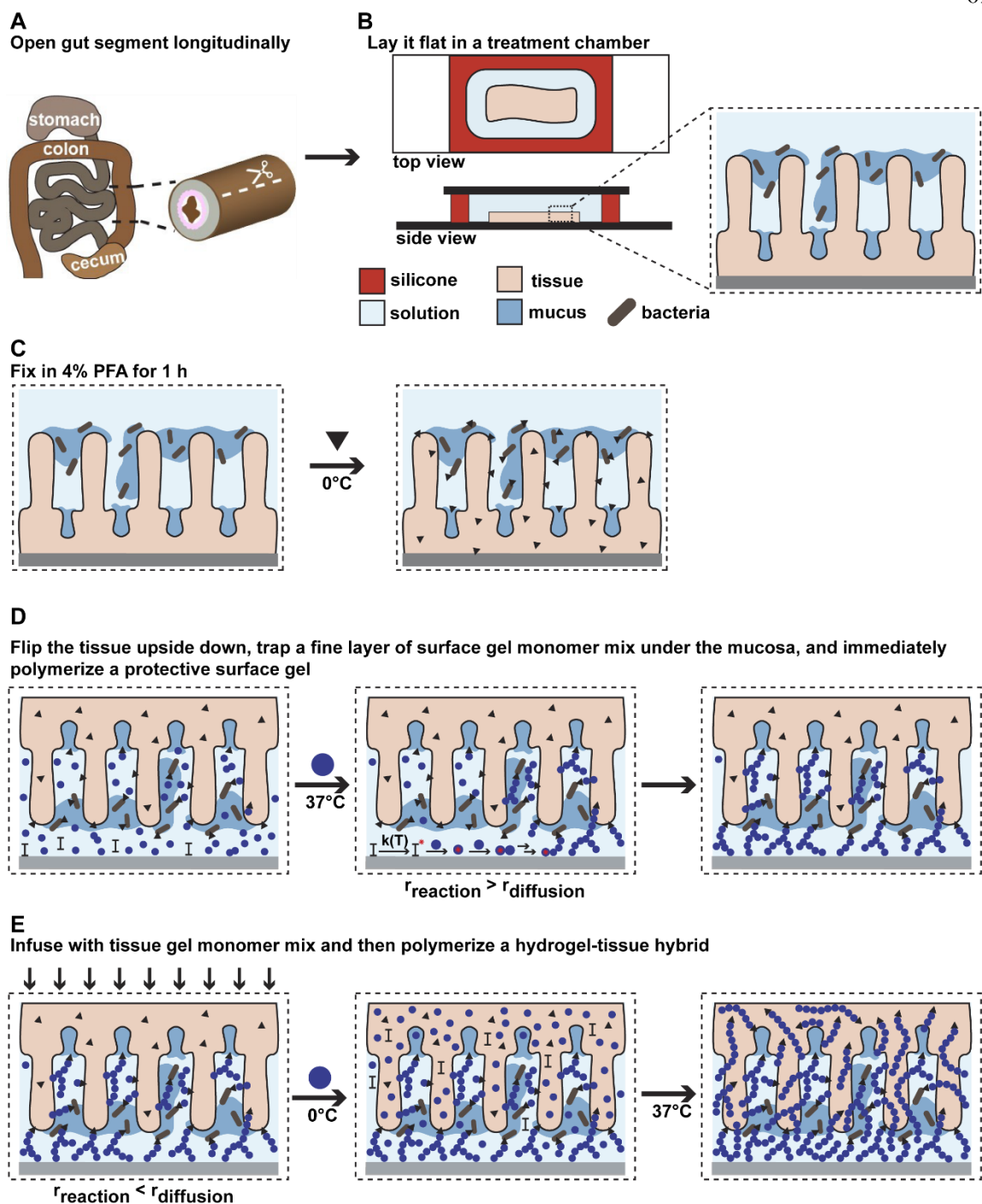


Figure 3. 3. Schematic of a general two-step hydrogel embedding protocol for prompt hydrogel fortification of the fragile mucosa and the subsequent hydrogel embedding of the underlying tissue with surface and tissue hydrogel formulations. After mouse dissection, a short gut segment is (A) opened longitudinally, (B) placed into a processing chamber, (C) fixed for 1 h in 4% PFA on ice, and (D) polymerized with a high density (i.e. high acrylamide content) surface hydrogel. A fine surface hydrogel layer is created by trapping surface-gel-monomer mix under the mucosa and in between mucosal crevices, and then immediately raising the temperature to 37 °C in favor of monomer reaction. (E) The tissue is infused with tissue-gel-monomer mix on ice in favor of monomer diffusion followed by a second hydrogel polymerization.

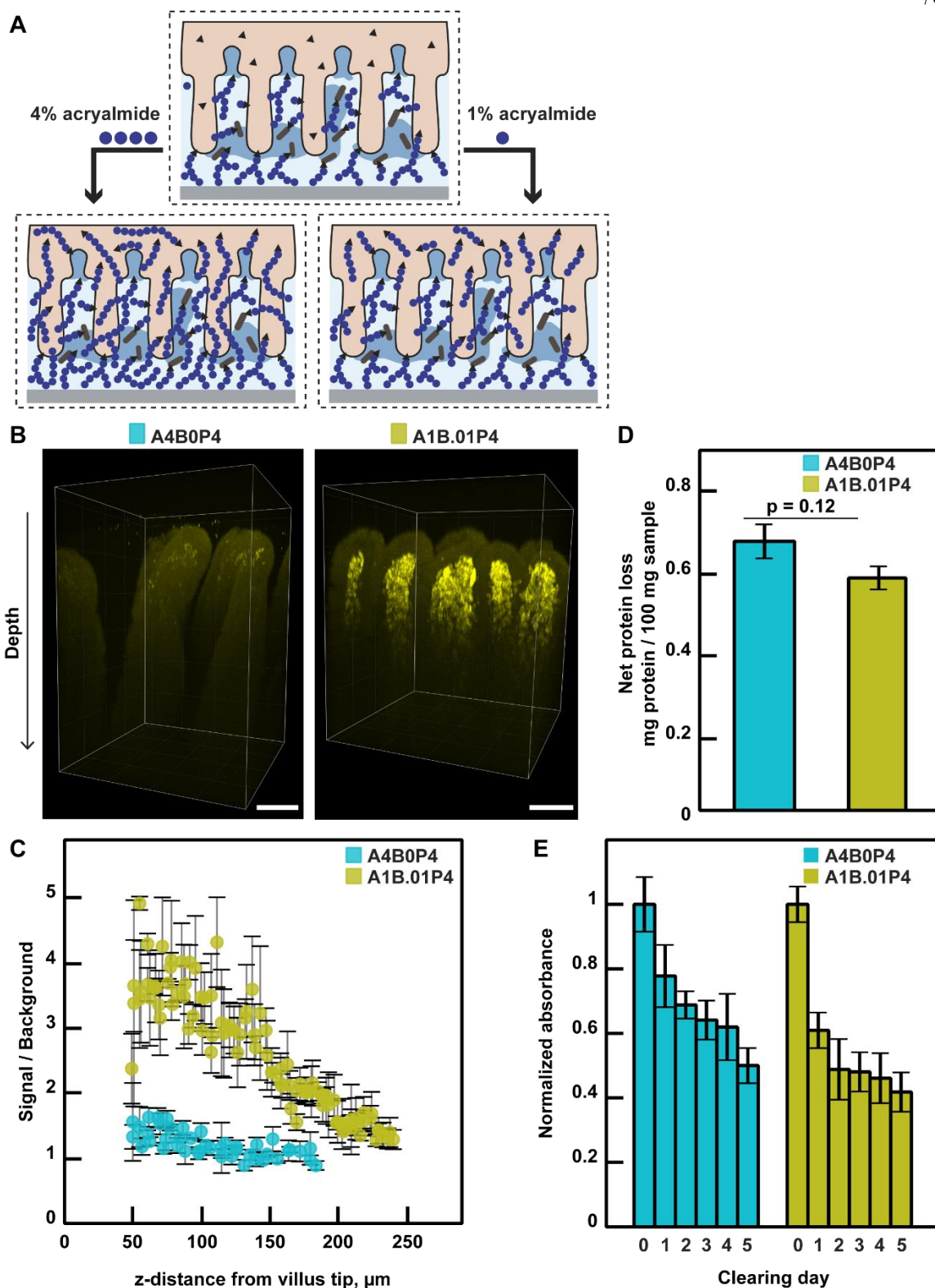


Figure 3. 4. Optimization of hydrogel chemistry improves antibody penetration into a hydrogel. (A) Cartoon representation of the effect of acrylamide concentration in the tissue-gel-monomer mix on the pore size

of the protective surface gel. (B) 3D imaging z-stacks of anti-CD45 antibody staining of total immune cells (yellow) in a mouse small intestine. In both images, the mucosa was protected by the same surface hydrogel, but the tissues were additionally fortified with either a 4% acrylamide + 4% paraformaldehyde formulation (A4B0P4) (left) or a 1% acrylamide + 0.01% bis-acrylamide + 4% paraformaldehyde (A1B.01P4) hydrogel formulation (right). Scale bars = 100 μm . (C) Quantification of antibody penetration into the hydrogel-tissue hybrids shown in panel (B), demonstrating that A1B.01P4 chemistry increases the antibody signal/background ratio deep in the sample. (D) Net protein loss during clearing shows that a lower percentage of acrylamide hydrogel did not increase protein loss. (E) Normalized tissue absorbance during clearing shows that tissue clarity was similar for both hydrogel formulations.

Although physical barriers, such as small pore size, reduce diffusion rate directly, chemical interactions with the target and the hydrogel-tissue matrix slow transport indirectly by increasing the ratio of reaction rate to diffusion rate⁴⁴, i.e. Damköhler number. In standard imaging of thin sections, blocking agents, such as serum, and surfactants, such as TritonX, have been used to reduce antibody interactions with the sample matrix, which can result in background staining⁵¹ whereas more recently SDS has been used to turn on/off antibody interactions with the sample matrix, which enables faster and more uniform antibody staining⁴⁴. Although non-specific antibody interactions with endogenous biomolecules in tissue samples are expected in a hybrid of acrylamide hydrogel and tissue, we additionally questioned the possibility of antibody interactions with the hydrogel components (that is, acrylamide, bis-acrylamide and PFA). The typical components of an acrylamide hydrogel are acrylamide, PFA (which depolymerizes into reactive formaldehyde monomers), and bis-acrylamide, which can be regarded as acrylamide dimer crosslinked by formaldehyde. According to the proposed mechanism of tissue embedding into acrylamide hydrogel^{31,52}, formaldehyde fixative first crosslinks biomolecules to each other as well as acrylamide to biomolecules. This crosslinking anchors acrylamide to the tissue and prepares the tissue for the second step, acrylamide polymerization. Acrylamide and bis-acrylamide polymerize to form a hydrogel-tissue hybrid. Although polymerization of alkene functional groups of acrylamide and bis-acrylamide yields stable, non-reactive alkane bonds, formaldehyde crosslinks are reversible and may form reactive Schiff base intermediates⁵³. Furthermore, formaldehyde reverse-crosslinking increases with temperature⁵⁴, which may explain reports that acrylamide hydrogel does not withstand clearing at elevated temperatures^{44,55}. This has been used to quench unreacted formaldehyde⁵³, so we hypothesized that a Tris wash of hydrogel-tissue hybrids before antibody staining may increase antibody penetration and the

signal-background ratio by reacting with free formaldehyde and Schiff bases (Fig.3.S1).

We found that although Tris wash did not improve antibody staining closer to the surface of the gel, >50% increase in signal/background ratio could be measured 200 μm deep into the tissue (Fig.3.S1C). Therefore, washing a sample with Tris prior to antibody staining may be a simple strategy to improve antibody staining in PFA-fixed samples. The results suggest the possibility that acrylamide hydrogel-tissue hybrids are not inert, although future studies should investigate the mechanism behind this improved antibody staining.

We next wished to test whether the protective surface gel acts as a reagent sink, potentially exposing reagent incompatibilities and further reducing hydrogel pore size. For example, despite thorough washes, SDS micelles can remain in the surface gel, seen as white SDS-lysozyme co-precipitate⁵⁶ when lysozyme treatment is performed after SDS clearing (Fig.3.S2A). Although an individual SDS molecule is small and should diffuse freely even through dense hydrogels, mixed SDS-lipid micelles can be as large as antibodies and even larger, reaching as much as 100 nm hydrodynamic radius^{57,58}. Similarly, the surface gel may also trap antibodies, which would be indicated by strong fluorescence after antibody staining (Fig.3.S2B). Curiously, we observed that when dextran sulfate of high molecular weight (>500,000 Da) is used as a crowding agent during HCR tagging of bacteria, it exacerbated antibody retention in the surface gel, whereas this did not occur when we used dextran sulfate of intermediate molecular weight (<40,000 Da) (Fig.3.S2B). Overall, such observations supported the notion that reagents with large molecular weights may be retained in the hydrogel and interfere with subsequent steps. In addition to SDS micelles and dextran sulfate, other molecules may also be retained in the surface gel, such as lysozyme, HCR probes and amplifiers, and even proteins lost during clearing. Acknowledging that reagents can remain in the hydrogel despite thorough washes, we carefully considered reagent compatibility when designing the multi-step process of permeabilizing the tissue, clearing it, and staining it. For example, we opted to perform lysozyme permeabilization of bacterial peptidoglycan layer before SDS clearing to prevent potential lysozyme inactivation by SDS [Chapter 2]. If experimental design required antibody staining to be performed after HCR (e.g., in the case

of antibody staining described in Chapter 4), we opted to use low molecular weight dextran sulfate in HCR.

HCR v3.0 16S rRNA probes enable sensitive and specific visualization of bacteria at depth

Next, we sought to improve the specificity of bacterial tagging by HCR. In conventional fluorescence in situ hybridization (FISH), autofluorescence and light scattering may obscure the relatively weak signal, motivating the development and adoption of hybridization chain reaction (HCR) that amplifies signal above background noise^{35,37,59} [Chapter 2]. However, because the original HCR design (HCR v2.0) requires only a single probe to initiate signal amplification, non-specifically bound probes give rise to amplified background⁴⁶. In thick samples subject to 3D imaging, unbound probes deep in the sample are particularly challenging to wash away, and amplified background increases with depth. Additionally, in discrimination of bacteria with taxonomic resolution, taxon-specific probes may bind off-targets with high degree of homology in the 16S ribosomal RNA (rRNA) sequence and may not be properly removed from deep in the hydrogel during washing, such that amplified false positive signal also increases with depth. We have previously reported weak cross-reactivity of *Bacteroidetes*-specific CFB560 HCR v2.0 probe towards *E. coli* in thin hydrogel slabs [Chapter 2]. However, such cross-reactivity increased sharply with depth in thick hydrogel slabs (Fig.3.3, A-B). To decrease the likelihood of non-specific amplification, we selected HCR v3.0 probes (designed by Molecular Instruments) that require two split probes bound to the target for HCR initiation and, in so doing, reduce false positive signal⁴⁶. For example, *Bacteroides/Parabacteroides*-specific HCR v3.0 probe that binds 16S rRNA molecule in the same region as CFB560 HCR v2.0 probe amplified signal in *Bacteroides fragilis* (*B. fragilis*) but not *E. coli* hydrogel slabs (Fig.3.3, C-D). In the case of *B. fragilis*, a high signal-background ratio was achieved partially because background amplification was also suppressed (Fig.3.3D). Therefore, HCR v3.0 outperforms HCR v2.0 at specific detection of bacteria with taxonomic resolution deep in particularly thick hydrogel-tissue hybrids.

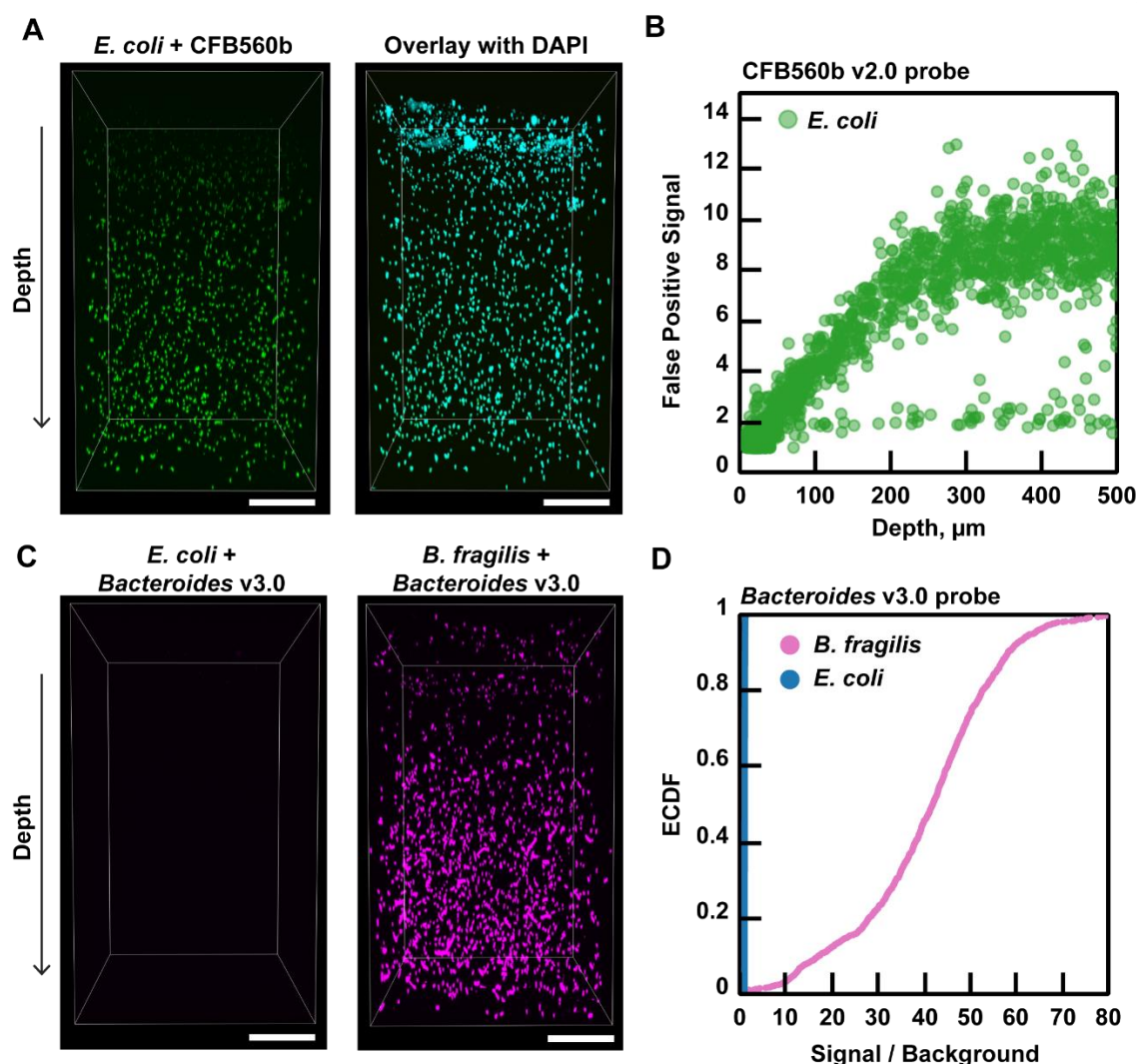


Figure 3. 4. Adoption of HCR v3.0 mitigates false positive signal amplification at depth *in vitro*. (A) HCR v2.0 staining of *E. coli* with the *Bacteroidetes*-specific CFB560 probe. Left: HCR v2.0 with CFB560 probe (green); right: overlay with DAPI staining of DNA (cyan). (B) Quantification of false-positive fluorescence signal in panel (A) as a factor of depth into the *in vitro* hydrogel. Each data point represents the ratio of average fluorescence in a cell to the average background fluorescence. (C) HCR v3.0 staining of *E. coli* (left) and *Bacteroides fragilis* (right) with a *Bacteroides/Parabacteroides*-specific probe, referred to in the figure as *Bacteroides* probe, (magenta) that binds in the same region as the CFB560 probe. (D) Quantification of the fluorescence signal in panel (C) is expressed as an empirical cumulative distribution function (ECDF), which shows what fraction of cells in panel (C) (y-axis) had a particular or lower signal/background ratio (x-axis). For the *Bacteroides/Parabacteroides*-specific HCR v3.0 probe, *B. fragilis* is the true target and *E. coli* is the false target. All scale bars = 100 μm .

Split HCR v3.0 probes span a wider region than standard probes, complicating the design of broad coverage 16S rRNA probes, such as the universal bacterial EUB338 probe. The EUB338 probe is only 18 base pairs (bp) long, whereas split HCR v3.0 probes cover a region

of 52 bp⁴⁶. The EUB338 probe covers >95% of all known bacterial 16S rRNA sequences without a mismatch, however no single 52 bp region is shared among >95% of sequences. We hypothesized that degenerate probes would increase coverage and designed a degenerate universal HCR v3.0 probe set to cover bacterial orders common in both the mouse and human gut (Fig.7, A-B). Briefly, a 52 bp region around the EUB338 probe binding site compatible with the HCR v3.0 reaction mechanism was selected by Molecular Instruments Corporation. Considering only the most prevalent bacterial orders in mouse and human gut, we aligned the selected 52 bp region to 16S rRNA sequences in SILVA database (Fig.3.5). After alignment, we selected the most frequent hits that maximized coverage. The degenerate universal HCR v3.0 probe set was narrowed down to 17 52-bp-long probes, however, different combinations of split probes further increased coverage. The exact location of the split is proprietary (Molecular Instruments Corp.), therefore, we assessed the coverage of the hypothetical 26 bp long probes (Fig.3.5). For most bacterial orders under consideration, both split degenerate probe sets covered >80% 16S rRNA sequences in SILVA database without mismatch (Fig.3.5). The probes are not expected to differentiate between sequences with zero or one mismatch; therefore, in practice, our designed degenerate universal HCR v3.0 probes are expected to cover nearly all bacteria in the bacterial orders of interest.

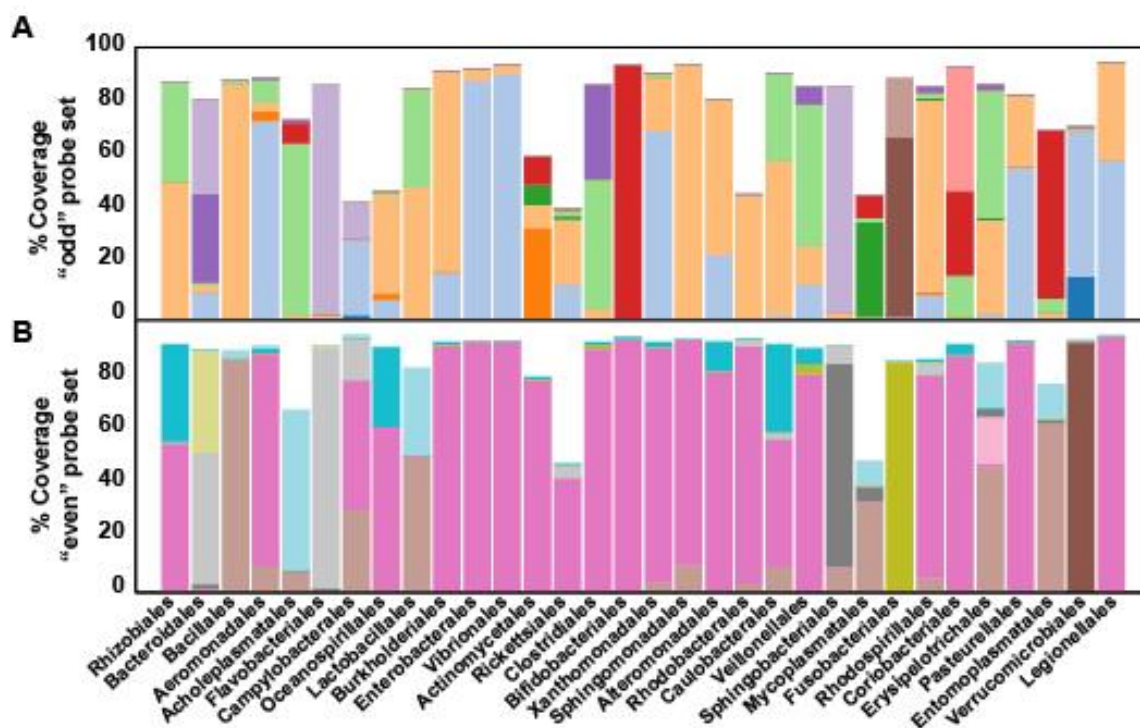


Figure 3.5. Design of the universal degenerate split HCR v3.0 probe set. A 52-bp region around EUB338 binding site was selected by Molecular Technologies. To improve coverage, we expanded to 17 full degenerate probes, and analyzed the coverage of 10 and 12 split probes split in the center, referred here as “odd” (A) and “even” (B). The location of the split is proprietary (and it actually yields 7 and 12 probes); therefore, we analyzed the coverage of the hypothetical 26-bp-long split probes. The height of each colored bar represents the percentage of coverage without a mismatch by one degenerate split probe, and the net bar height represents cumulative coverage by the degenerate probe set of the bacterial order of interest. Coverage is defined as % of order-specific 16S rRNA sequences in the SILVA 138 NR99 database that align with the probe without a mismatch. Only bacterial orders common to mouse and human gut were considered in the analysis.

The degenerate universal HCR v3.0 probe set was compared against EUB338 HCR v2.0 experimentally in a proximal colon tissue from a specific pathogen free (SPF) mouse (Fig.3.6). Because both probes competed for the same binding site, their concentrations were matched to avoid out-competition. Both probes successfully visualized abundant bacteria in between two proximal colon folds (Fig.3.6, A-C), but only EUB338 HCR v2.0 probe gave amplified background in the tissue (Fig.3.6, A, D and J). In contrast, degenerate universal HCR v3.0 probe set effectively suppressed background amplification in the tissue (Fig.3.6, B, D and K). The signals overlapped well (Fig.3.6, C and I) and were positively correlated (Fig.3.6L, $\rho = 0.6$) in between two proximal colon folds. The probes competed for the same binding site, partially explaining the lower than 1 Pearson's correlation coefficient. To assess the coverage of the degenerate universal HCR v3.0 probe set, we attempted to quantify the fraction of HCR v2.0 positive voxels that are also positive for HCR v3.0. However, because HCR v2.0 showed strong amplified background, the full HCR v2.0 positive population could not be clearly defined. Therefore, we only considered voxels brighter than 500 in HCR v2.0 channels because we were confident they did not co-localize with DAPI staining. In this select voxel population, 85% of voxels were also HCR v3.0 positive, suggesting that broad coverage of the degenerate universal HCR v3.0 probe set was achieved. Furthermore, consistent with the commonly reported bacterial colonization of mucus⁴⁰, bacteria labeled by the degenerate universal HCR v3.0 probe set co-localized with mucus staining (Fig.3.6, E and F). Thus, the results suggested that degenerate HCR v3.0 probes can also be designed to cover broad bacterial groups while continuing to suppress non-specific amplification.

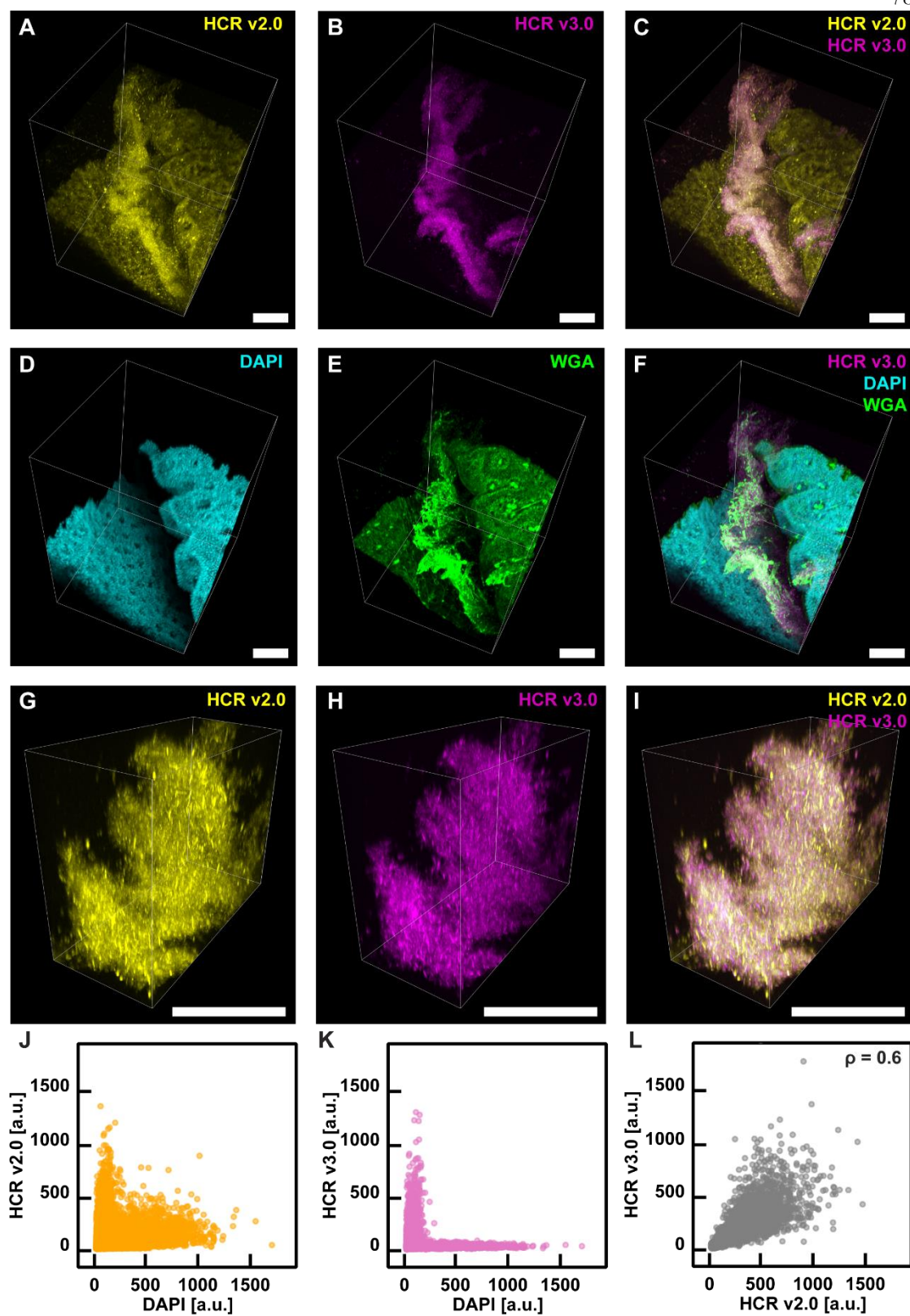


Figure 3. 6. Comparison of the degenerate universal HCR v3.0 probe set and EUB338 HCR v2.0 probe in a mouse proximal colon. (A-I) CLARITY imaging of a mouse proximal colon with the full acquired z-stack shown in (A-F) and the zoomed in portions focused on bacteria shown in (G-I). All scale bars = 100 μ m. (A) Bacteria tagging with EUB338 HCR v2.0 probe (yellow). (B) Bacteria tagging with the degenerate universal HCR v3.0 probe set (magenta). (C) Overlay of A and B showing that the signals overlap in the center of the image, i.e. in between two proximal colon folds. (D) Epithelium staining with DAPI (cyan) showing proximal colon folds and a void in between. (E) Mucus staining with WGA lectin (green) showing mucus filled goblet cells in the tissue and secreted mucus in between proximal colon folds. (F) Overlay of (B), (D), and (E) showing spatial structure of tissue, secreted mucus and bacteria tagged by HCR v3.0. (J-K) Voxel intensity analysis of a sub-sampled voxel population in panels (A-F). (J) HCR v2.0 signal vs DAPI signal, showing that voxels well-stained by DAPI also had elevated HCR v2.0 signal. (K) HCR v3.0 signal vs DAPI signal, showing that voxels well-stained by DAPI segregate from voxels well-stained by HCR v3.0. (L) Voxel intensity analysis of the zoomed in images shown in (G-I), showing that HCR v3.0 signal positively correlated with HCR v2.0 signal (Pearson's correlation coefficient = 0.6). These probes compete for the same binding site, partially explaining the <1 correlation coefficient.

Bacteria, mucus, and host cells can be simultaneously imaged in 3D in mouse jejunum

Finally, we asked whether our technological advances enabled simultaneous visualization of bacteria, mucus, and host immune cells in 3D (Fig.3.8). In a mouse jejunum, we were able to capture long intestinal villi from their tip to the base (Fig.3.8A), although imaging depth varied across the sample. Mucus was successfully preserved, and WGA staining detected abundant mucus-filled goblet cells in the epithelial lining (Fig.3.8B). Bacteria were retained and detected with low background by HCR v3.0 (Fig.3.8.C). More permeable hydrogel-tissue hybrids also facilitated antibody transport deep into the hydrogel and across the epithelial layer, visualizing immune cells densely packed in the core of the villi (Fig.3.8D). Therefore, our technological advances offer a versatile tool for the interrogation of host-microbe interface in the mucosa.

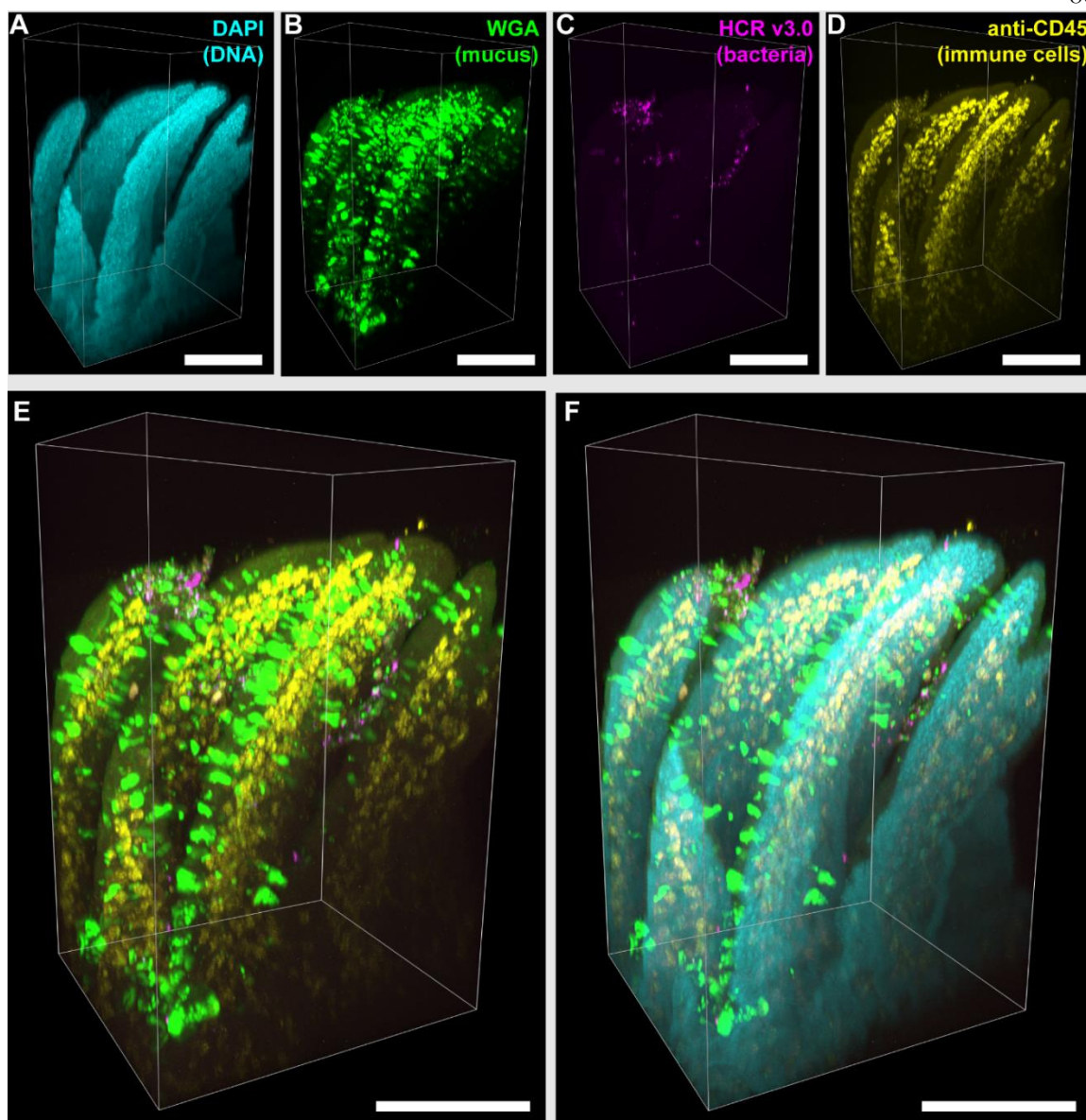


Figure 3. 7. Multi-modal staining of mouse small intestinal tissue. (A) DAPI staining of DNA marks the tissue (cyan); (B) WGA lectin stains mucus and other glycans (green); and (C) HCR v3.0 stains total bacteria with the universal degenerate probe set presented in Fig.3.5 and Fig.3.6 (magenta). (D) Antibody staining of total immune cells clustered in the core of the villi with anti-CD45 antibody (yellow). (E) Overlay of lectin staining of mucus, HCR v3.0 staining of bacteria, and antibody staining of immune cells. (F) Additional overlay with DAPI staining of DNA. Scale bars = 200 μ m.

Two-step hydrogel polymerization retains mucus in resected human gut samples

Continued retention of bacteria and mucus along with improved specificity of bacterial labelling and improved antibody transport for characterization of the host (Fig.3.7) hold promise in elucidating the spatial structure of the host-microbe interface in IBD. However, the gut wall of humans is much thicker than that of mice, requiring further optimization and validation of reagent concentrations, volumes, and incubation durations. Furthermore, the gastrointestinal tract of humans affected by IBD can be fibrotic⁶⁰, which might make it denser and less permeable to reagents. To translate our two-step hydrogel embedding protocol to human gut, we collaborated with researchers at Cedars-Sinai Medical Center in Los Angeles. Remnant resected human gut samples from patients undergoing surgery for Crohn's disease (CD) were provided under exempt Caltech IRB protocol 19-0915. Immediately after surgery, the samples were dissected at Cedars-Sinai hospital and fixed in 4% PFA during their transportation to Caltech located 15 miles, or up to 1 h, away from Cedars-Sinai Medical Center. At Caltech, the samples were immediately subjected to surface-gel polymerization to minimize mucus and bacteria losses, followed by tissue infusion with tissue gel monomer mix and polymerization. In the first validation experiment, involved (i.e. affected by CD) and uninvolved (i.e. not affected by CD) ileum segments from a single IBD patient were stained with DAPI for DNA and wheat germ agglutinin (WGA) for mucus and other glycans (Fig.3.8). Uninvolved segment is expected to appear like healthy tissue; indeed, 3D images show intact, vertically aligned villi, suggesting that the samples were not damaged during surgery, dissection, or transportation. Furthermore, 3D images of uninvolved segment show mucus surrounding the villi, suggesting that mucus was successfully preserved and retained. In contrast, involved segment shows damage to the epithelium and depletion of secreted mucus. Given that no epithelial damage or absence of mucus was observed in the uninvolved segment, we assume that the morphology observed in the involved segment arises from tissue inflammation rather than sample handling.

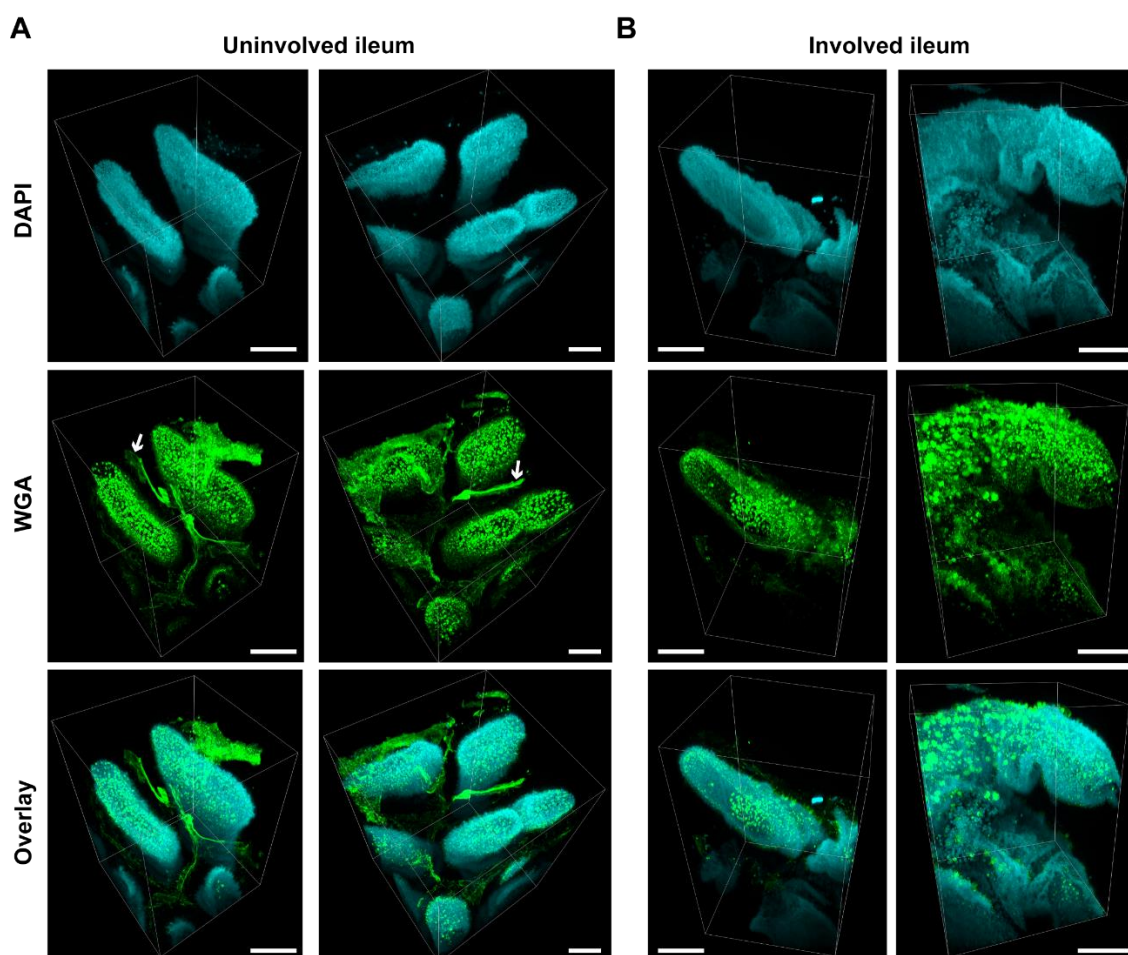


Figure 3.8. 3D imaging of resected human gut from one IBD patient using optimized hydrogel chemistry. (A) 3D imaging of uninvolved, healthy-like ileum showing intact, vertically aligned villi surrounded by secreted mucus (white arrows). (B) 3D imaging of involved ileum affected by CD showing irregular villi and absence of secreted mucus. Cyan: DAPI staining DNA that marks epithelial boundary. Green: WGA staining of mucus. Scale bars = 200 μm .

Discussion

In Chapter 3 of this thesis, we describe our advanced technology for 3D imaging of the intestinal mucosa that continues to retain loosely adherent bacteria and mucus, but improves signal-to-background ratio deep in particularly thick samples. Having observed slow reagent transport into the hydrogel during incubation and out of the hydrogel during wash (which reduces signal-to-background ratio at depth), we sought to mitigate both physical and chemical transport barriers and achieve a lower Damköhler number for more uniform staining. Specifically, we recognized that our two-step hydrogel polymerization protocol that

stabilizes loosely adherent bacteria and mucus promptly in the first step and the underlying tissue in the second step can result in particularly small pore sizes. Therefore, to both retain loosely adherent mucosal matter and maintain sufficient pore sizes for antibody transport, we did not alter the acrylamide concentration in the first polymerization step, but reduced its concentration in the second step. Furthermore, we recognized that reversible PFA crosslinking may generate Schiff bases, which may react with antibodies, further slowing antibody transport and increasing background staining. To mitigate this chemical transport barrier, we incorporated a wash step with a formaldehyde scavenger prior to antibody staining. Future technological developments will aim to further improve transport by incorporating SWITCH⁴⁴, stochastic electro-transport⁴⁵, or eFLASH⁶¹. These methods accelerate antibody transport by switching off its interactions with the hydrogel-tissue matrix during the incubation step⁴⁴, using stochastic electric fields for faster transport⁴⁵, or both⁶¹. Nonetheless, we reasoned that for these approaches to work in future developments of our technology, the pore size has to be sufficiently large such that antibody entry into the hydrogel is possible.

To improve the specificity of HCR tagging of bacteria in particularly thick samples, we adopted HCR v3.0 that offers automatic suppression of non-specific signal amplification⁴⁶. Although HCR v2.0 amplifies RNA signal and improves sensitivity at depth³⁶, it suffers from false positive signal amplification and low specificity deep in the hydrogel-tissue hybrids where the wash of non-specifically bound probes is not effective. In this work, we demonstrate that taxon-specific HCR v3.0 probes resolve false positive signal amplification and maintain probe specificity in particularly thick samples. However, split HCR v3.0 probes bind a 52 bp long region; as a result, broad coverage 16S rRNA probes require degenerate probe design. In this work, we designed a universal bacterial HCR v3.0 degenerate probe set composed of 17 full degenerate probes (7 and 12 split degenerate probes). In silico alignment of these probes to 16S rRNA sequences in SILVA database predicted that they should cover >80% of bacterial species without a mismatch among bacterial orders common to mouse and human gut. The use of degenerate probes increased the net probe concentration, increasing

the risk of background amplification. However, we demonstrated that our universal bacterial HCR v3.0 degenerate probe set continued to suppress background amplification.

In this work, we relied on acrylamide hydrogel chemistry in combination with PFA fixative. PFA performs two functions: it fixes biomolecules and anchors acrylamide to them. However, as previously recognized, PFA is a problematic fixative. First, it can overfix staining targets⁵⁵; second, PFA-fixed acrylamide hydrogel are unstable at elevated temperatures^{44,55}, and we have reasoned that reversibility of PFA crosslinking^{53,54} may explain the previously reported instabilities. Novel fixatives, e.g. polyepoxides used in SHIELD⁵⁵, have been reported to maintain tissue stability at elevated temperatures without overfixing. However, to the best of our understanding, the previously reported polyepoxides would not anchor acrylamide to the tissue nor would they form a firm hydrogel on their own, which is required to stabilize fragile mucosa. Therefore, exciting future technological developments will also consider the design of novel fixatives superior to PFA but still compatible with stabilization of loosely adherent bacteria and mucus.

Suspension of elective surgeries due to Covid-19 pandemic also suspended further technological translation and application to resected human gut samples from IBD patients. However, in Chapter 4 of this thesis, we demonstrate that technological developments described in Chapters 2 and 3 have been essential to dissecting the dynamics of *Enterobacteriaceae* – *Bacteroidaceae* association in the small intestine. For example, the capability of our technology to scan large areas of mucosal surface described in Chapter 2 enabled to detect rare events of bacteria remaining in the SI after digesta passage, whereas adoption of HCR v3.0 for specific labelling of bacteria in particularly thick samples described in Chapter 3 additionally enabled to detect bacteria deep in the SI mucosa. Furthermore, HCR v3.0 allowed us to conclude that, in the SI mucosa, *Bacteroidales* were abundant and associated with sparse *E. coli* cells. Finally, improved antibody staining described in Chapter 3 allowed to conclude that free mammalian nuclei not integral to the epithelium were epithelial cells, suggestive of epithelial damage due to bacterial colonization

of the mucosa. Thus, our novel technology also holds promise in elucidating host-microbe interactions in human gut as well.

Materials and Methods

Mice

All animal husbandry and experiments were approved by the Caltech Institutional Animal Care and Use Committee (IACUC protocol #1646). Male and female, 2–4 month-old CHOW-fed C57BL/6J mice were purchased from Jackson Laboratory (JAX) or bred at the Caltech animal facilities.

General protocol for mouse GIT preservation for imaging

With modifications, the protocol described in Chapter 2 was followed. The mice were euthanized by euthasol injection (250 μ L of 10x Euthasol dilution in saline per mouse). In a subset of mice, euthasol-injected anesthetized mice were transcidentally perfused with ice-cold hPBS (0.5 w/v% sodium nitrite and 10 U/mL heparin in PBS) at 5 ml/min rate for 10 min. The gut was excised and quick-fixed in an excess (40 mL) of ice-cold 4% PFA for 2–3 min (alternatively, if quick fixation was performed on short ~1-inch segment, 5 mL of 4% PFA was used); we observed that rapid fixation of the outer muscle layer reduces tissue warping during the subsequent preservation protocol. The gut was then rinsed in ice-cold PBS and further dissected on an ice-cold dissection stage in a biosafety cabinet (BSC). The gut was untangled and the mesentery was removed. An approximately 1-inch-long segment of interest (e.g. proximal colon or jejunum) was excised. The segment was placed on a microscope slide that had a thin (1 mm thick) silicone isolator glued to it (666103; Grace Biolabs). The segment was opened longitudinally using fine dissection scissors (504024; World Precision Instruments) and laid out flat on the slide with the mucosa facing up. If luminal contents were present, they were carefully removed by picking them up with tweezers and/or gently applying PBS to wash them off. Two additional thick (1.8 mm thick) silicone isolators (666203; Grace Biolabs) were stacked on top of the bottom isolator to

create a ~2.5 mL reservoir for subsequent incubations. The reservoir was first filled with 4% PFA, covered with another microscope slide to prevent PFA evaporation, and the slide was placed on ice for 1 h to fix the tissue. After fixation, the tissues were flipped upside down so the mucosa faced the glass slide (we have observed that the most convenient way to flip the tissues is to drag them over a cover slip, flip the cover slip upside down, and drag the tissue back to the liquid-filled reservoir).

Flipped tissue was moved to an anaerobic chamber (Coy Labs) where an oxygen-sensitive polymerization of acrylamide hydrogel was performed. In the anaerobic chamber, the isolator was first vacuum-degassed and argon-purged and then filled with surface-gel-monomer mix (see Table 3.1 for compositions) and the tissue was incubated on ice for 15 min to allow the monomer mix to displace liquid in tissue crevices. Then, spent surface-gel-monomer mix was exchanged with clean surface-gel-monomer mix, and most of the monomer mix was again removed to leave only a fine layer under the mucosa – this fine layer ultimately polymerizes into a protective surface gel. The isolator was covered with a silicone sheet (664475; Grace Biolabs) to allow for gas exchange, and the surface gel was polymerized at 37 °C for 3 h in a humid environment (humidity was maintained by placing either an open container with water in the 37 °C incubator or wet tissue directly in a petri dish with tissue samples). After surface gel polymerization, the tissue proceeded to hydrogel tissue embedding either immediately or within 1 week; if hydrogel tissue embedding was not performed immediately, the tissues were stored at 4 °C in the meantime.

Tissue embedding into a hydrogel was also performed in the anaerobic chamber. The reservoirs were filled with vacuum-degassed and argon-purged tissue-gel-monomer mix, and hydrogel monomers were infused on ice for 3 or 18 h, as specified below. After infusion, the tissue-gel-monomer mix was removed, the reservoirs were covered with silicone sheets for gas exchange, and hydrogel-tissue hybrids were polymerized at 37 °C in a humid environment for 3 or 5 h as specified below. Finally, hydrogel-tissue hybrids were removed from the anaerobic chamber, the muscle side of the tissue was glued to a solid support using GLUture tissue glue (10014489; Zoetis), and the tissue was dislodged from the glass slide.

The tissues were then stored in 0.025% sodium azide in PBS until lysozyme permeabilization.

Table 3.1. Surface-gel and tissue-gel monomer mix chemistries. Acrylamide was acquired from Sigma (01697), bis-acrylamide – BioRad (161-0142), PFA – Electron Microscopy Sciences (100504), and VA044 thermal initiator (CAS NO. 27776-21-2) – Wako (011-193365).

	Total % and amount	Acrylamide, 40%	Bis-acrylamide, 2%	PFA, 32%	PBS, 10x	UltraPure Water	VA044
Surface-gel-monomer mix chemistries							
A4B.08P4	100%	4%	0.08%	4.05%	NA	NA	0.25 w/v%
	30 mL	3 mL	1.2 mL	3.8 mL	3 mL	19 mL	75 mg
A4B.08P1	100%	4%	0.08%	1.07%	NA	NA	0.25 w/v%
	30 mL	3 mL	1.2 mL	1 mL	3 mL	21.8 mL	75 mg
A4B.08P0	100%	4%	0.08%	0%	NA	NA	0.25 w/v%
	30 mL	3 mL	1.2 mL	0 mL	3 mL	22.8 mL	75 mg
Tissue-gel-monomer mix chemistries							
A4B0P4	100%	4%	0%	4.05%	NA	NA	0.25 w/v%
	30 mL	3 mL	0 mL	3.8 mL	3 mL	20.2 mL	80 mg
A1B.01P1	100%	1.25%	0.0125%	1%	NA	NA	0.25 w/v%
	32 mL	1 mL	0.2 mL	1 mL	3.2 mL	26.6 mL	80 mg
A1B.01P4	100%	1.25%	0.0125%	4%	NA	NA	0.25 w/v%
	32 mL	1 mL	0.2 mL	4 mL	3.2 mL	23.6 mL	80 mg

Experiment-specific protocols for mouse GIT preservation for imaging

Tissue-preservation protocols were optimized using mouse GIT samples. To better mimic resected human gut samples that cannot be perfused and thus contain blood, we opted to perform all optimization experiments using GIT tissue from mice euthanized by standard euthasol injection and not transcardial perfusion.

Fig.3.1. Two mice were euthanized one day apart without transcardial perfusion for preservation of proximal colon tissues. On the first day of the experiment, A4B.08P4 surface gel was polymerized over the mucosa of the first proximal colon tissue. After polymerization, the sample was stored overnight in the fridge. The next day, surface gel polymerization was omitted for the proximal colon tissue from the second mouse and was immediately embedded in hydrogel. Tissues from both mice were infused with A1B.01P1 tissue-gel-monomer mix for 3 h, and then polymerized for 5 h.

Fig.3.3. One mouse was euthanized without transcordial perfusion. A4B.08P4 hydrogel was polymerized over the mucosa of two small intestinal segments. After surface gel polymerization, tissue samples were stored in the fridge overnight. The next day, one sample was infused with A4B0P4 tissue-gel-monomer mix and one with A1B.01P4 tissue-gel-monomer mix. After infusion, the first tissue with high acrylamide concentration tissue hydrogel was polymerized for 3 h, whereas the second tissue with low acrylamide concentration tissue hydrogel was polymerized for 5 h.

Fig.3.4. *E. coli* and *B. fragilis* were cultured anaerobically at 37 °C. First, frozen bacterial stocks were plated on Brucella blood agar plates (A30; Hardy Diagnostics) and cultured for 1-2 days. The night before bacterial embedding into hydrogel slabs, single colonies were inoculated in 5 mL of brain heart infusion (BHI) medium supplemented with 5 µg/mL hematin, 1 µg/mL vitamin K1 and 250 µg/mL L-cysteine (BHI-SS) and cultured overnight for 14 h. The next day, stationary overnight cultures were re-inoculated into fresh 5 mL of BHI-SS; the inoculum volume was such that all bacterial isolates reached mid-exponential phase (OD = 0.7-1.0 as measured in transparent 14 mL round-bottom culture tubes) within 2-2.5 h (50 µL for *E. coli* and 300 µL for *B. fragilis*). Pelleted cells were re-suspended in PBS, mixed with 8% PFA in 1:1 ratio and fixed on ice for 1 h. Fixed cells were spiked into A4B.08P1 surface gel monomer mix at $\sim 5 \cdot 10^7$ cells/mL density and polymerized into hydrogel slabs. After surface gel polymerization, hydrogel slabs were infused overnight with A1B.01P4 tissue gel monomer mix and polymerized for 5 h.

Figs 3.6, 3.7, 3.S1, 3.S2. Five mice were euthanized without transcordial perfusion. A4B.08P1 hydrogel over the mucosa of intestinal segments of interest (either proximal colon or small intestine). After surface gel polymerization, the tissue sample proceeded immediately to overnight infusion with A1B.01P4 tissue gel monomer mix. The next day, the tissue hydrogel was polymerized for 5 h. In Figure3.S2B, a malnourished mouse gavaged with PBS (as described in Chapter 4) was used instead.

Preservation of resected human gut tissues for imaging

Remnant resected human gut samples from patients undergoing surgery for Crohn's disease (CD) were provided under exempt Caltech IRB protocol 19-0915. In the morning of the gastrointestinal surgeries, resected human gut samples were stored at 4 °C and dissected within a few hours in a BSC. Dissected tissue samples (approximately 0.5 cm wide and up to 2 cm long) were immobilized in tissue cassettes, submerged in 50 mL of 4% PFA, and transported on ice from Cedars-Sinai Medical Center to Caltech located up to 1 h away. To equilibrate thick human tissue to an anaerobic environment, fixation was continued in an anaerobic chamber in anaerobic-environment equilibrated 4% PFA on ice for another 2 h. Fixed tissues were transferred to reservoirs built by stacking adhesive silicone isolators (Grace Biolabs) on a microscope slide and incubated with A4B.08P0 surface-gel-monomer mix on ice for 30 min. The surface-gel-monomer mix was then exchanged and removed again, leaving only a fine layer under the tissue. The polymerization was carried out at 37 °C for 3 h in a humid environment. After surface-gel polymerization, the tissues proceeded immediately to overnight infusion with A1B.01P4 tissue-gel-monomer mix. The next day, they were polymerized at 37 °C for 5 h in a humid environment.

Bacterial peptidoglycan permeabilization with lysozyme

On the day of lysozyme treatment, hydrogel-tissue hybrids were incubated in lysozyme treatment buffer (10 mM Tris-HCl, pH=8.0 (AM9856; Ambion)) at room temperature (RT) for 1 h before treatment. Bacterial peptidoglycan layer was then permeabilized. For mouse gut samples, permeabilization was with 1 mg/mL lysozyme (90082; ThermoFisher Scientific) in 10 mM Tris HCl, pH=8.0, at 37 °C for 6 h with shaking. After treatment, the hydrogels were rinsed in PBS and then washed three times in excess of PBS (~50 mL) over the course of one day.

For ~5mm thick human gut samples, hydrogel-tissue hybrids were incubated in lysozyme treatment buffer for 5 h, infused with 1 mg/mL lysozyme in 10 mM Tris HCl, pH=8.0,

overnight at 4 °C, and permeabilized the next day at 37 °C for 6 h. After lysozyme treatment, the samples were washed three times in excess PBS at RT over the course of a day.

SDS clearing

Each piece of tissue was cleared in a separate 50 mL tube filled with 4% SDS (51213; Lonza) in PBS, pH=8.5, at 37 °C and 180 rpm. Mouse tissues were cleared for 3-5 days with daily clearing solution changes, whereas human tissues were cleared for 10 days with solution changes every other day. After clearing, the samples were washed for one day at 37 °C in PBS, and then for an additional day at RT in PBS. Two washes were performed each day, with 50 mL of wash solution per sample per wash.

General antibody staining protocol

Before antibody staining, the samples were blocked overnight in 2% serum (100487-948; Electron Microscopy Sciences) in PBST buffer (0.1% TritonX-100, 0.01% sodium azide in PBS) at RT. The next day, antibody (and optionally lectin) stocks were centrifuged at 10,000 g and 4 °C for 10 min to pellet large aggregates. Antibody staining solution contained 2% serum, 5 ug/mL of anti-CD45-AlexaFluor546 antibody (sc-53665 AF546; Santa Cruz Biotechnology), 5 ug/mL DAPI (ThermoFisher Scientific) and, optionally, 1-5 ug/mL WGA conjugated with either AlexaFluor488 (W11261; ThermoFisher Scientific) or AlexaFluor647 (W32466; ThermoFisher Scientific) fluorophores. Hydrogel-tissue hybrids were stained for 1–3 days at RT with gentle shaking. After staining, they were rinsed in PBST, and then washed 3 times in excess of PBST (20–30 mL per sample) over the course of one day.

Experiment-specific antibody staining protocols

Fig.3.3. Hydrogel-tissue hybrids were stained with 5 ug/mL anti-CD45-AlexaFluor546 and 5 ug/mL of DAPI, 0.5 mL of staining solution per sample. The staining was carried out for 24 h. Otherwise, the general antibody staining protocol was followed.

Fig.3.S1- S2. Hydrogel-tissue hybrids were stained with 5 $\mu\text{g}/\text{mL}$ anti-CD45-AlexaFluor546 and 5 $\mu\text{g}/\text{mL}$ of DAPI, 0.5 mL of staining solution per sample. The staining was carried out for 3 days. Otherwise, the general antibody staining protocol was followed.

General HCR v2.0 protocol

Hybridization solution consisted of 10 nM of each probe in hybridization buffer (15% v/v% formamide, 10 w/v% high molecular weight dextran sulfate in 2xSSC (Sodium Saline Citrate) buffer). Probe sequences are provided in Table 3.S1, and HCR initiator sequences are provided in Table S2. Hydrogel-tissue hybrids were hybridized at 46 °C for 16 h. After hybridization, they were rinsed in 2xSSCT buffer (0.1% Tween20 in 2xSSC) and then washed for 2 h in 30 mL of 30% formamide in 2xSSCT buffer, 2 h in 30 mL of 2xSSCT, and 2 h in PBS. Amplification solution consisted of 0.12 μM of each amplifier in amplification buffer (10 w/v% high molecular weight dextran sulfate in 2xSSC buffer). Prior to combining all amplifiers in the amplification solution, they were heat-shocked at 95 °C for 90 s and cooled to RT for 30 min. Hybridized probes were amplified at RT for 16 h. After amplification, each hydrogel-tissue hybrid was first rinsed in 5xSSCT, washed twice with shaking in 30 mL of 5xSSCT for 2 h, and then in 30 mL of PBS for 2 h. All washes were performed at RT and with shaking.

General HCR v3.0 protocol

Before hybridization, samples were pre-hybridized in 30% formamide in 5xSSCT at 37 °C for 2 h. Pre-hybridized samples were then hybridized at 37 °C for 20 h in hybridization solution containing either 4 nM of each degenerate universal HCR 3.0 probe or 10 nM of taxon-specific non-degenerate HCR v3.0 probe as specified below. Probe sequences are provided in Table 3.S1. Hybridization solution was prepared in probe hybridization buffer for tissues in whole-mount (Molecular Technologies). After hybridization, the hydrogel-tissue hybrids were first rinsed in warm (equilibrated to 37 °C) probe wash buffer (Molecular Technologies), and then a series of washes was performed in 20 mL of wash buffer per sample per wash at various volumetric ratios of Probe Wash Buffer (Molecular

Technologies) and 5xSSCT: 3:0 for 30 min, 2:1 for 30 min, 1:2 for 60 min, and 0:3 for 60 min. All washes were performed at RT and with shaking.

Hybridized probes were amplified at RT for 20 h in an amplification solution containing 0.12 μ M of each amplifier. The amplification solution was prepared in amplification buffer for tissues in whole-mount (Molecular Technologies). Prior to combining all amplifiers in the amplification buffer, they were heat-shocked at 95 °C for 90 s, and then cooled down at RT for 30 min. After amplification, each hydrogel-tissue hybrid was first rinsed in 5xSSCT, and then washed twice in 20 mL of 5xSSCT for 30 min each time and twice in 20 mL of 5xSSCT for 60 min each time. Finally, the samples were washed in 20 mL of PBS for 1 h. All washes were performed at RT with shaking.

Experiment-specific HCR tagging of bacteria

Fig.3.1. Each hydrogel-tissue hybrid was hybridized with EUB338 probe linked to B5 initiator in 5 mL of hybridization solution and then amplified with B5-AlexaFluor488 amplifier pair in 1.5 mL of amplification buffer. Otherwise, the general HCR v2.0 protocol was followed. After HCR v2.0 tagging of bacteria, hydrogel-tissue hybrids were stained with 5 μ g/mL DAPI and 1 μ g/mL WGA-AlexaFluor647 in 5 mL of PBS at RT for 36 h. After staining, the samples were washed in excess of PBS for 4 hours prior to imaging.

Fig3.7. (HCR v3.0). The hydrogel-tissue hybrid was hybridized with the degenerate universal HCR 3.0 probe set linked to B2 initiator in 1 mL of hybridization solution and amplified with B2-AlexaFluor647 amplifier pair (Molecular Technologies) in 0.5 mL of amplification solution. Otherwise, the general HCR v3.0 protocol was followed. After HCR v3.0 tagging of bacteria, the hydrogel-tissue hybrid proceeded to a 3-day antibody staining with 5 μ g/mL of anti-CD45-AlexaFluor546, 5 μ g/mL WGA-AlexaFluor488, and 5 μ g/mL DAPI. Otherwise, the general antibody staining protocol was followed.

Fig.3.4. (in vitro HCR v2.0 vs HCR v3.0 with non-degenerate taxon-specific probes). *E. coli* and *B. fragilis in vitro* hydrogels were hybridized following the general HCR v3.0 protocol

with the following specifications: hydrogels were hybridized with the CFB560b-B5 HCR v2.0 probe and *Bacteroides*-B2 HCR v3.0 probe, each at 10 nM in 1 mL of hybridization solution. Then the hydrogels were amplified with B5-AlexaFluor488 and B2-AlexaFluor647 amplifiers in 0.5 mL of amplification solution. After HCR tagging of bacteria, the hydrogels were counterstained with 5 µg/mL of DAPI overnight.

Fig.3.6. (in vivo HCR v2.0 vs HCR v3.0 with degenerate universal HCR v3.0 probe set). The general HCR v3.0 protocol was followed in this experiment. The hydrogel-tissue hybrid was hybridized with the EUB338-B4 HCR v2.0 probe and the degenerate universal HCR v3.0 probe set linked to the B2 initiator in 3 mL of hybridization solution. The concentration of each degenerate universal HCR v3.0 probe was 4 nM; considering that each arm of the split universal HCR v3.0 probe set contains ~10 probes (7 and 12 to be exact), we set EUB338-B4 concentration to 40 nM to avoid out-competition. The hydrogel-tissue hybrid was then amplified with B4-AlexaFluor546 and B2-AlexaFluor647 amplifier pairs in 1.5 mL of amplification solution. Finally, before imaging, the sample was stained overnight at RT with 5 µg/mL DAPI and 5 µg/mL WGA-AlexaFluor488 in 5 mL of PBS.

Design of the degenerate universal HCR v3.0 probe set

Split v3.0 16S rRNA probes were designed in collaboration with and synthesized by Molecular Technologies. First, Molecular Technologies selected a 52 bp region around EUB338 binding site that was compatible with HCR v3.0 mechanism. We then aligned this selected region to nearly 200,000 16S rRNA sequences in SILVA 138 NRPP database only considering bacterial orders relevant to mouse and human gut microbiomes and selected the most common hits that maximized coverage. The selection of degenerate probes can be performed on either full or split probes; we opted to work with split probes because we noted that the search space was smaller (different combinations of split probes further increase diversity and increase search space when degenerate probe design is performed on full probes). Nonetheless, because the exact location of the split is unknown to us (proprietary to Molecular Technologies), we designed 30-bp-long split probes that shared 8 bp of overlap in the center. In the end, we merged split degenerate probes based on the perfect overlap in the

center. We obtained 17 full degenerate probes (Table 3.S1); splitting of these probes by Molecular Technologies yielded 7 and 12 split degenerate probes.

For each split degenerate probe and bacterial order combination, coverage was defined as percentage of 16S rRNA gene sequences in the SILVA 138 NR99 database that aligned with the probe without a mismatch.

Imaging

All images were acquired on a Zeiss LSM880 confocal microscope.

10x Water Immersion Objective. Images presented in Fig.3.1 were tile-scanned with a 10x water immersion objective with 10% overlap in channel mode for DAPI staining of epithelium, WGA staining of mucus, and HCR v2.0 tagging of bacteria. Tiles were stitched in Zen software. All imaging and display metadata are provided in the SI.

20x Water Immersion Objective. Images presented in Fig.3.4 were imaged with a 20x water immersion objective in channel mode for DAPI staining of DNA, CFB560b HCR v2.0, and *Bacteroides* HCR v3.0 tagging of bacteria. All imaging and display metadata are provided in the SI.

20x CLARITY objective. The rest of the images were acquired with a 20x CLARITY objective. Samples were mounted in RIMS (600 mL of 0.02 M phosphate buffer (P5244; MilliporeSigma) + 800 g of Histodenz (CAS #: 66108-95-0; JINLAN Pharm-Drugs Technology Co.) supplemented with 0.01% sodium azide, pH=7.5, RI=1.47) and incubated overnight. To prevent RIMS dehydration during imaging, RIMS was covered with a layer of Immersion Oil (Type FF, 16916-04; Electron Microscopy Sciences). All images were acquired in channel mode. All imaging and display metadata are provided in the SI.

Image analysis

Antibody penetration (Figs.3.3 and 3.S1). Antibody penetration was quantified in FIJI. Briefly, a region of interest (ROI) was first drawn to mark the tip of a villus so that the z-distance from the villus tip can later be quantified. Then, at various planes along the villus, 4 ROIs were selected: three marking immune cells in the core of the villus (signal) and one marking epithelial cells (background). Average ROI fluorescence was calculated in FIJI, and the results were exported for further analysis in Python. In Python, the signal-background ratio was calculated as the ratio of average fluorescence in signal ROI to average fluorescence in background ROI at the same z-plane. Each data point in Fig.3.3B and Fig.3.S1B represents signal-background ratio averaged over three signal ROIs at the same plane. For each z-stack, three villi were analyzed; for Fig.3.3B, one z-stack was considered for each condition, whereas for Fig.3.S1B, two z-stacks were considered for each condition.

HCR v2.0 vs HCR v3.0 tagging of bacteria *in vitro* (Fig.3.4). Bacterial cells were segmented based on DAPI staining of DNA in Imaris. Object parameters (object size, position, and average fluorescence in each channel) were exported for further analysis in Python. In Python, signal-background ratio was calculated as object average fluorescence intensity over average background fluorescence intensity.

HCR v2.0 vs HCR 3.0 background amplification in *in vivo* hydrogel-tissue hybrids (Fig.3.6). Voxel fluorescence intensity was analyzed in Python. Three major populations of voxels were identified: dark voxels peaking at ~0 a.u., background voxels peaking at ~50 a.u., and signal voxels that spread into the rest of the range. First, dark voxels dimmer than 22 a.u. were removed based on signal in EUB338 channel (notably, background voxels were not removed). Due to the size of the data, voxels sub-sampled for plotting.

Statistical analyses

Statistical significance was evaluated using the Kruskal-Wallis test.

References:

1. Dejea, C. M. *et al.* Patients with familial adenomatous polyposis harbor colonic biofilms containing tumorigenic bacteria. *Science (80-.)*. **359**, 592–597 (2018).
2. Park, C. H. *et al.* Role of Fusobacteria in the serrated pathway of colorectal carcinogenesis. *Sci. Rep.* **6**, 1–8 (2016).
3. Brennan, C. A. & Garrett, W. S. Fusobacterium nucleatum — symbiont, opportunist and oncobacterium. *Nat. Rev. Microbiol.* **17**, 156–166 (2019).
4. Ridaura, V. K. *et al.* Gut microbiota from twins discordant for obesity modulate metabolism in mice. *Science (80-.)*. **341**, (2013).
5. Wang, J. *et al.* A metagenome-wide association study of gut microbiota in type 2 diabetes. *Nature* **490**, 55–60 (2012).
6. Blacher, E. *et al.* Potential roles of gut microbiome and metabolites in modulating ALS in mice. *Nature* **572**, 474–480 (2019).
7. Sampson, T. R. *et al.* A gut bacterial amyloid promotes a-synuclein aggregation and motor impairment in mice. *Elife* **9**, 1–19 (2020).
8. Olson, C. A. *et al.* The gut microbiota mediates the anti-seizure effects of the ketogenic diet. *Cell* **173**, 1728-1741.e13 (2018).
9. Sharon, G. *et al.* Human gut microbiota from autism spectrum disorder promote behavioral symptoms in mice. *Cell* **177**, 1600-1618.e17 (2019).
10. Khor, B., Gardet, A. & Xavier, R. J. Genetics and pathogenesis of inflammatory bowel disease. *Nature* **474**, 307–317 (2011).
11. Manichanh, C., Borruel, N., Casellas, F. & Guarner, F. The gut microbiota in IBD. *Nat. Rev. Gastroenterol. Hepatol.* **9**, 599–608 (2012).
12. Wright, E. K. *et al.* Recent advances in characterizing the gastrointestinal microbiome in Crohn's disease: A systematic review. *Inflamm. Bowel Dis.* **21**, 1219–1228 (2015).
13. Sellon, R. K. *et al.* Resident enteric bacteria are necessary for development of spontaneous colitis and immune system activation in interleukin-10-deficient mice. *Infect. Immun.* **66**, 5224–5231 (1998).
14. Lal, S. & Steinhart, A. H. Antibiotic therapy for Crohn's disease: A review. *Can. J. Gastroenterol.* **20**, 651–655 (2006).
15. Gevers, D. *et al.* The treatment-naive microbiome in new-onset Crohn's disease. *Cell Host Microbe* **15**, 382–392 (2014).
16. Ananthakrishnan, A. N. Epidemiology and risk factors for IBD. *Nat. Rev. Gastroenterol. Hepatol.* **12**, 205–217 (2015).
17. Frank, D. N. *et al.* Molecular-phylogenetic characterization of microbial community imbalances in human inflammatory bowel diseases. *Proc. Natl. Acad. Sci. U. S. A.* **104**, 13780–13785 (2007).
18. Paul B. Eckburg *et al.* Diversity of the human intestinal microbial flora. *Science*. **308**, 1635–38 (2005).
19. Yasuda, K. *et al.* Biogeography of the intestinal mucosal and luminal microbiome in the rhesus macaque. *Cell Host Microbe* **17**, 385–391 (2015).
20. Li, H. *et al.* The outer mucus layer hosts a distinct intestinal microbial niche. *Nat. Commun.* **6**, 1–13 (2015).
21. Palm, N. W. *et al.* Immunoglobulin A coating identifies colitogenic bacteria in inflammatory bowel disease. *Cell* **158**, 1000–1010 (2014).
22. Hansson, G. C. & Johansson, M. E. V. The inner of the two Muc2 mucin-dependent mucus layers in colon is devoid of bacteria. *Gut Microbes* **1**, 51–54 (2010).
23. Johansson, M. E. V *et al.* Bacteria penetrate the normally impenetrable inner colon mucus layer in both murine colitis models and patients with ulcerative colitis. *Gut* **63**, 281–291 (2014).
24. Limon, J. J. *et al.* Malassezia is associated with Crohn's Disease and exacerbates colitis in mouse models. *Cell Host Microbe* **25**, 377-388.e6 (2019).
25. Swidsinski, A. *et al.* Mucosal flora in inflammatory bowel disease. *Gastroenterology* **122**, 44–54 (2002).
26. Swidsinski, A., Weber, J., Loening-Baucke, V., Hale, L. P. & Lochs, H. Spatial organization and composition of the mucosal flora in patients with inflammatory bowel disease. *J. Clin. Microbiol.* **43**, 3380–3389 (2005).

27. Kim, H. J., Boedicker, J. Q., Choi, J. W. & Ismagilov, R. F. Defined spatial structure stabilizes a synthetic multispecies bacterial community. *Proc. Natl. Acad. Sci. U. S. A.* **105**, 18188–18193 (2008).
28. Cremer, J. *et al.* Effect of flow and peristaltic mixing on bacterial growth in a gut-like channel. *Proc. Natl. Acad. Sci. U. S. A.* **113**, 11414–11419 (2016).
29. Welch, J. L. M., Hasegawa, Y., McNulty, N. P., Gordon, J. I. & Borisy, G. G. Spatial organization of a model 15-member human gut microbiota established in gnotobiotic mice. *Proc. Natl. Acad. Sci. U. S. A.* **114**, E9105–E9114 (2017).
30. Hasegawa, Y., Welch, J. L., Rossetti, B. J. & Borisy, G. G. Preservation of three-dimensional spatial structure in the gut microbiome. *PLoS One* **12**, 1–16 (2017).
31. Chung, K. *et al.* Structural and molecular interrogation of intact biological systems. *Nature* **497**, 332–7 (2013).
32. Richardson, D. S. & Lichtman, J. W. Clarifying tissue clearing. *Cell* **162**, 246–257 (2015).
33. Tainaka, K., Kuno, A., Kubota, S. I., Murakami, T. & Ueda, H. R. Chemical principles in tissue clearing and staining protocols for whole-body cell profiling. *Annual Review of Cell and Developmental Biology* **32**, (2016).
34. Gradinaru, V., Treweek, J., Overton, K. & Deisseroth, K. Hydrogel-tissue chemistry: Principles and applications. *Annu. Rev. Biophys.* **47**, 355–76 (2018).
35. Choi, H. M. T. *et al.* Programmable in situ amplification for multiplexed imaging of mRNA expression. *Nat. Biotechnol.* **28**, 1208–1212 (2010).
36. Shah, S. *et al.* Single-molecule RNA detection at depth by hybridization chain reaction and tissue hydrogel embedding and clearing. *Development* **143**, 2862–2867 (2016).
37. DePas, W. H. *et al.* Exposing the three-dimensional biogeography and metabolic states of pathogens in cystic fibrosis sputum via hydrogel embedding, clearing, and rRNA labeling. *MBio* **7**, 1–11 (2016).
38. Neckel, P. H., Mattheus, U., Hirt, B., Just, L. & Mack, A. F. Large-scale tissue clearing (PACT): Technical evaluation and new perspectives in immunofluorescence, histology, and ultrastructure. *Sci. Rep.* **6**, 1–13 (2016).
39. Yang, B. *et al.* Single-cell phenotyping within transparent intact tissue through whole-body clearing. *Cell* **158**, 945–958 (2014).
40. Johansson, M. E. V., Holmén Larsson, J. M. & Hansson, G. C. The two mucus layers of colon are organized by the MUC2 mucin, whereas the outer layer is a legislator of host-microbial interactions. *Proc. Natl. Acad. Sci. U. S. A.* **108**, 4659–4665 (2011).
41. Earle, K. A. *et al.* Quantitative imaging of gut microbiota spatial organization. *Cell Host Microbe* **18**, 478–488 (2015).
42. Lieleg, O. & Ribbeck, K. Biological hydrogels as selective diffusion barriers. *Trends Cell Biol.* **21**, 543–551 (2011).
43. Hsueh, B. *et al.* Pathways to clinical CLARITY: Volumetric analysis of irregular, soft, and heterogeneous tissues in development and disease. *Sci. Rep.* **7**, 1–16 (2017).
44. Murray, E. *et al.* Simple, scalable proteomic imaging for high-dimensional profiling of intact systems. *Cell* **163**, 1500–1514 (2015).
45. Kim, S.-Y. *et al.* Stochastic electrotransport selectively enhances the transport of highly electromobile molecules. *Proc. Natl. Acad. Sci.* **112**, E6274–E6283 (2015).
46. Choi, H. M. T. *et al.* Third-generation in situ hybridization chain reaction: Multiplexed, quantitative, sensitive, versatile, robust. *Dev.* **145**, 1–10 (2018).
47. Lignell, A., Kerosuo, L., Streichan, S. J., Cai, L. & Bronner, M. E. Identification of a neural crest stem cell niche by Spatial Genomic Analysis. *Nat. Commun.* **8**, (2017).
48. Valm, A. M., Oldenbourg, R. & Borisy, G. G. Multiplexed spectral imaging of 120 different fluorescent labels. *PLoS One* **11**, 1–17 (2016).
49. Welch, J. L. M., Rossetti, B. J., Rieken, C. W., Dewhirst, F. E. & Borisy, G. G. Biogeography of a human oral microbiome at the micron scale. *Proc. Natl. Acad. Sci. U. S. A.* **113**, E791–E800 (2016).
50. Pluen, A., Netti, P. A., Jain, R. K. & Berk, D. A. Diffusion of macromolecules in agarose gels: Comparison of linear and globular configurations. *Biophys. J.* **77**, 542–552 (1999).
51. R&D Systems. Preventing non-specific staining. Available at: <https://www.rndsystems.com/resources/protocols/preventing-non-specific-staining>. (Accessed: 27th June 2020)

52. Tomer, R., Ye, L., Hsueh, B. & Deisseroth, K. Advanced CLARITY for rapid and high-resolution imaging of intact tissues. *Nat. Protoc.* **9**, 1682–97 (2014).
53. Hoffman, E. A., Frey, B. L., Smith, L. M. & Aulsebrook, D. T. Formaldehyde crosslinking: A tool for the study of chromatin complexes. *J. Biol. Chem.* **290**, 26404–26411 (2015).
54. Kennedy-Darling, J. & Smith, L. M. Measuring the formaldehyde protein-DNA cross-link reversal rate. *Anal. Chem.* **86**, 5678–5681 (2014).
55. Park, Y. G. *et al.* Protection of tissue physicochemical properties using polyfunctional crosslinkers. *Nat. Biotechnol.* **37**, 73 (2019).
56. Morén, A. K. & Khan, A. Phase equilibria of an anionic surfactant (sodium dodecyl sulfate) and an oppositely charged protein (lysozyme) in water. *Langmuir* **11**, 3636–3643 (1995).
57. Christov, N. C., Denkov, N. D., Kralchevsky, P. A., Ananthapadmanabhan, K. P. & Lips, A. Synergistic sphere-to-rod micelle transition in mixed solutions of sodium dodecyl sulfate and cocoamidopropyl betaine. *Langmuir* **20**, 565–571 (2004).
58. Hartmann, W. K., Saptharishi, N., Yang, X. Y., Mitra, G. & Soman, G. Characterization and analysis of thermal denaturation of antibodies by size exclusion high-performance liquid chromatography with quadruple detection. *Anal. Biochem.* **325**, 227–239 (2004).
59. Shah, S. *et al.* Single-molecule RNA detection at depth via hybridization chain reaction and tissue hydrogel embedding and clearing. *Development In Review*, 2862–2867 (2016).
60. Mao, R. *et al.* The mesenteric fat and intestinal muscle interface: Creeping fat influencing stricture formation in Crohn's Disease. *Inflamm. Bowel Dis.* **25**, 421–426 (2019).
61. Yun, D. H. *et al.* Ultrafast immunostaining of organ-scale tissues for scalable proteomic phenotyping. *bioRxiv* (2019).

Supplementary Information

Contributions of non-corresponding authors

- Roberta Pocevičiute (R.P.) designed the study, performed all experiments (except for protein loss measurements during clearing and preliminary HCR v2.0 cross-reactivity experiments), collected and analyzed the data, made figures and wrote the manuscript. In the design of the universal degenerate HCR v3.0 probe set, R.P. expanded a single 52 bp long region in 16S rRNA molecule (selected by M.S.) into 17 degenerate universal probes.
- Amanda Hazel Dilmore (A.H.D.) measured protein loss during clearing.
- Heli Takko (H.T.) performed preliminary HCR v2.0 cross-reactivity experiments (not displayed here).
- Suzanne Devkota (S.D.) provided resected human gut samples.
- Maayan Schwarzkopf (M.S.) selected 52 bp regions in 16S rRNA sequences compatible with HCR v3.0 mechanism.

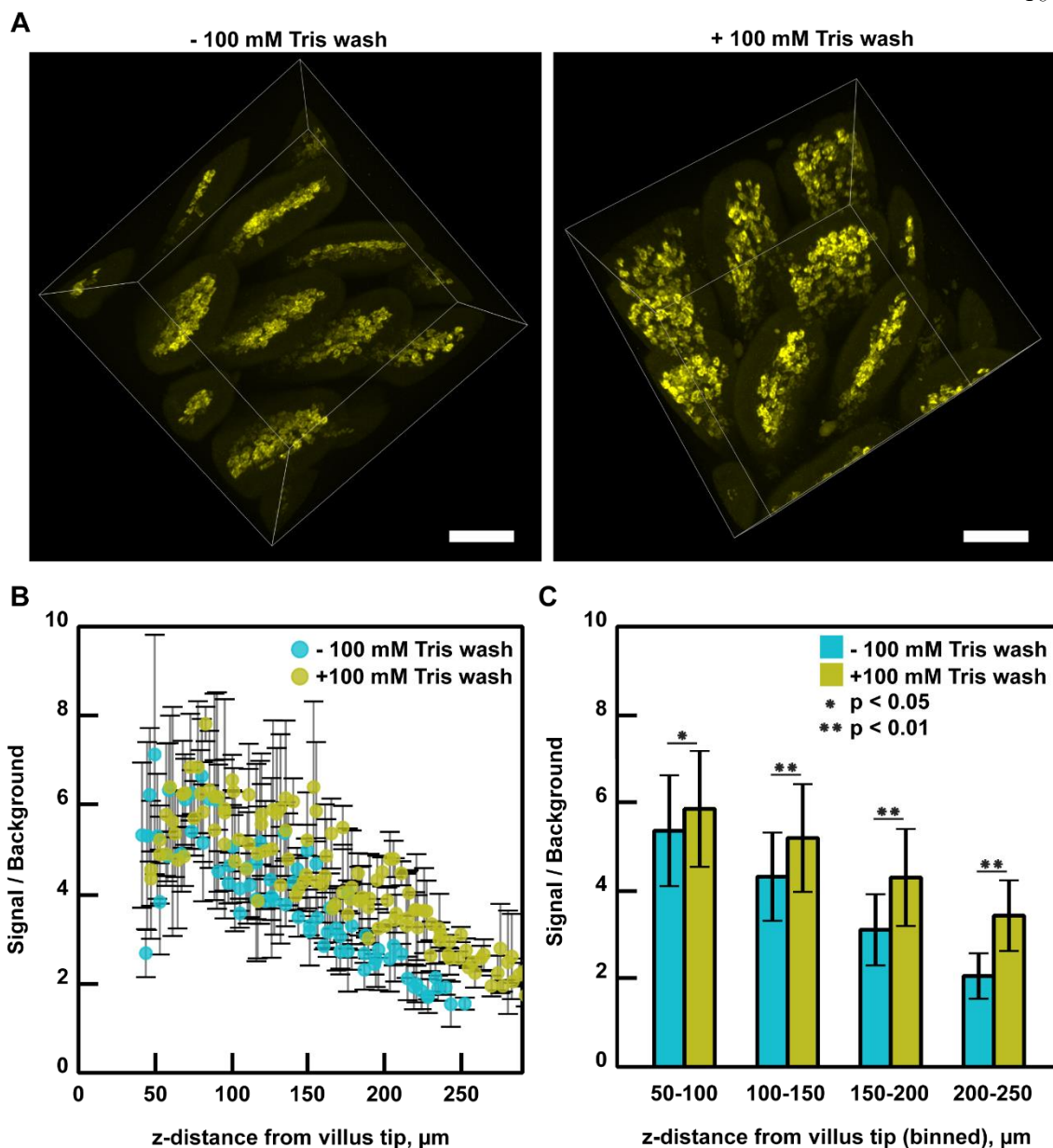


Figure 3. S1. Hydrogel-tissue hybrid wash with a formaldehyde scavenger improves antibody staining. (A) Antibody staining of a mouse small intestine hydrogel-tissue hybrid divided into two pieces, but only one piece (right) washed with 100 mM Tris-HCl, pH=8.0, prior to antibody staining. Yellow: anti-CD45 staining of immune cells centered in the core of the villi. Scale bar = 100 μ m. (B) Quantification of antibody signal/background ratio with depth for the images shown in panel (A). (C) The same quantification as in (B), but now signal/background ratios are binned by depth into 50 μ m thick bins.

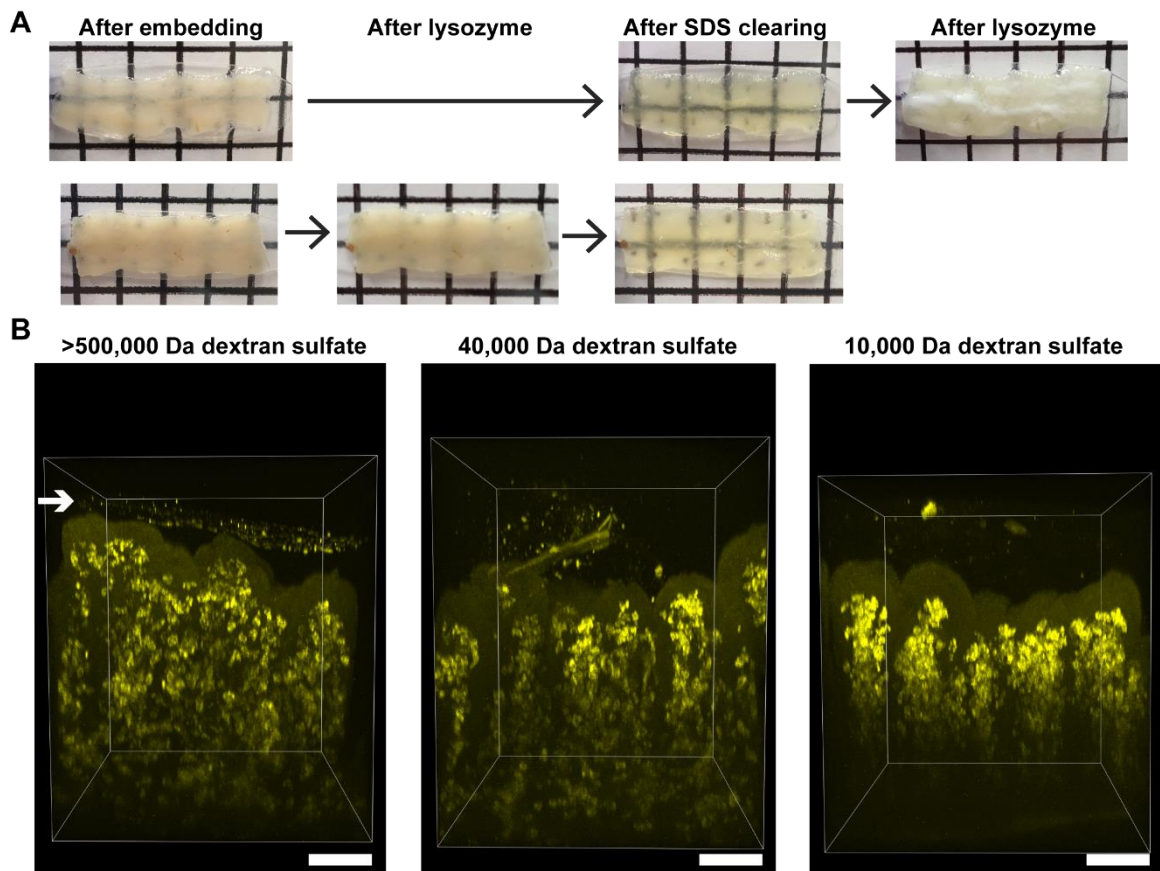


Figure 3. S2. Protective surface gel can act as a reagent sink. (A) Lysozyme treatment after (top) but not before SDS clearing produces white precipitate in the surface gel. Grid size = 6 mm. (B) Antibody retention at the very surface of the gel (white arrow) correlates with the use of high (left) but not the intermediate (center and right) molecular weight dextran sulfate in the preceding HCR tagging of bacteria. Scale bar = 100 μ m).

Table 3.S1. HCR v2.0 and HCR v3.0 probe sequences. Probe sequences are provided in 5' >>> 3' orientation. For HCR v3.0 probes, the regions that align with HCR v2.0 probes are underscored.

Probe name	HCR version	Probe sequence (5' >>> 3')
EUB338 16S rRNA	v2.0	GCTGCCTCCCGTAGGAGT
CFB560 16S rRNA	v2.0	WCCCTTTAAACCCART
GAM42a 23S rRNA	v2.0	GCCTTCCCACCTTCGTTT
Degenerate Universal 16S rRNA	v3.0	CTCGACT <u>GCTGCCACCCGTAGG</u> TGICTGGACCGTGTCTCAGTTCAGTGTGC CTCGACT <u>GCTGCCACCCGTAGG</u> TGICTGGACCGTGTCTCAGTTCAGTGTGG CCCTACT <u>GCTGCCTCCCGTAGG</u> AGICTGGGCCGTGTCTCAGTCCCAGTGTGA CCCCACT <u>GCTGCCTCCCGTAGG</u> AGICTGGGCCGTGTCTCAGTCCCAGTGTGG CCCTACT <u>GCTGCCTCCCGTAGG</u> AGICTGGGCCGTATCTCAGTCCCAGTGTGG CCCTACT <u>GCTGCCTCCCGTAGG</u> AGICTGGGCCGTGTCTCAGTCCCAGTGTGG CCCTACT <u>GCTGCCTCCCGTAGG</u> AGICTGGGCCGTATCTCAGTCCCAGTGTGG CCCCACT <u>GCTGCCTCCCGTAGG</u> AGICTGGGCCGTATCTCAGTCCCAGTGTGG CCCTACT <u>GCTGCCTCCCGTAGG</u> AGICTGGGCCGTGTCTCAGTCCCAGTGTGG CCCCACT <u>GCTGCCTCCCGTAGG</u> AGICTGGGCCGTATCTCAGTCCCAGTGTGG CCCTACT <u>GCTGCCTCCCGTAGG</u> AGICTGGGCCGTGTCTCAGTCCCAGTGTGG CCCCACT <u>GCTGCCTCCCGTAGG</u> AGICTGGGCCGTATCTCAGTCCCAGTGTGG CCCTACT <u>GCTGCCTCCCGTAGG</u> AGICTGGGCCGTGTCTCAGTCCCAGTGTGG CCCCACT <u>GCTGCCTCCCGTAGG</u> AGICTGGGCCGTATCTCAGTCCCAGTGTGG CCCTACT <u>GCTGCCTCCCGTAGG</u> AGICTGGGCCGTGTCTCAGTCCCAGTGTGG CCCCACT <u>GCTGCCTCCCGTAGG</u> AGICTGGGCCGTATCTCAGTCCCAGTGTGG CCCTACT <u>GCTGCCTCCCGTAGG</u> AGICTGGGCCGTGTCTCAGTCCCAGTGTGG
<i>Bacteroides / Parabacteroides</i> 16S rRNA	v3.0	<u>CCCTTTAAACCCAATAAATCCGGATAACGCTCGGATCCTCCGTATTACCGCG</u>
<i>E. coli</i> 16S rRNA	v3.0	GATAACTACTGGAAACGGTAGCTAATACCGCATAACGTCGCAAGACCAAAGA

APPLICATION OF 3D IMAGING TOOLS TO *ENTEROBACTERIACEAE* – *BACTEROIDACEAE* INTERACTIONS IN THE SMALL INTESTINE

Introduction

Members of the *Enterobacteriaceae* family can cause severe, drug-resistant urinary tract, lung and blood infections¹, and they are also thought to drive dysbiosis in the gut^{2,3}. Curiously, *Enterobacteriaceae* co-occur with *Bacteroidaceae* in several clinical contexts of the gastrointestinal tract (GIT), raising the hypothesis that such association may not be random, but rather indicative of potential synergy. For example, the canonical pair *Escherichia coli* and *Bacteroides fragilis* has been shown to co-localize in mucosal biofilms in the colon and act synergistically to promote tumor development in a genetically susceptible host⁴. Similarly, shotgun metagenomic sequencing of stool has revealed that the relative abundance of *Bacteroides vulgatus*, *B. fragilis*, and *Escherichia/Shigella* species increases in Crohn's disease (CD)⁵, and imaging of CD-affected colon tissue has revealed abundance of *B. fragilis* and sporadic presence of *E. coli* in mucosal biofilms⁶. *Enterobacteriaceae* and *Bacteroidaceae* have also been implicated in dysbiosis of the small intestine (SI), where higher oxygen levels than in the colon⁷ should inhibit the growth of strictly anaerobic *Bacteroides* spp. For example, in small intestinal bacterial overgrowth (SIBO) both facultative anaerobes, such as *Klebsiella* and *Escherichia*, and strict anaerobes, such as *Bacteroides*, are commonly detected in the upper SI³. Here, the unexpected presence of anaerobes has motivated the suggestion to refine SIBO diagnosis to include not only quantitative increases in total bacterial load, but also qualitative changes marked by the presence of colonic anaerobes even if total bacterial load does not increase⁸. Although such associations hold promise in understanding and eventually controlling host-microbe and microbe-microbe interactions, in most cases the significance and mechanism of these associations remain elusive.

Studies of dysbiosis in different contexts have broadened our awareness of factors that may mediate possible interactions between *Enterobacteriaceae* and *Bacteroidaceae*. For example, in wound infections where disruption of the protective skin barrier exposes a moist and nutrient-rich environment suitable for microbial growth, both facultative anaerobes (aerobes that can switch their metabolism to fermentation in the absence of oxygen) and strict anaerobes are detected, including *E. coli* and *Bacteroides* spp., respectively⁹. Although disrupted blood and oxygen supply may explain the growth of anaerobes in wounds, it has also been hypothesized that oxygen consumption by the aerobes and facultative anaerobes further reinforces an anaerobic environment⁹. Genome-scale metabolic models and *in vitro* bioreactor studies further support the role of oxygen consumption in maintaining the synergy between aerobes and anaerobes¹⁰. In one study, oxygen consumption by a model facultative anaerobe *Klebsiella pneumonia* was sufficient to permit the growth of a model strict anaerobe *Bacteroides thetaiotaomicron* (*B. theta*) under microoxic conditions. Furthermore, the role of oxygen in wound infections is multifaceted: insufficient oxygen supply also slows down the oxygen-dependent healing process⁹ and reduces the production of antimicrobial reactive oxygen species (ROS)¹¹. In addition to oxygen, pH and metabolites may also play a role, such as short chain fatty acids (SCFA). In the aforementioned genome-scale metabolic models and bioreactor experiments, degradation of complex carbohydrates and production of SCFA by the strict anaerobe supported the growth of the facultative aerobe¹⁰, whereas in a separate study, succinate production and environment acidification by *B. fragilis* impaired neutrophil response towards *E. coli ex vivo*¹². Although the mechanisms of microbial interactions are diverse and likely variable across systems, the unifying theme is that environmental variables, such as oxygen flux, nutrient availability, and host immune response, shape microbial interactions and these variables must be characterized to fully explain the mechanisms behind their interactions.

Although bulk analyses can profile average microbial community composition and correlate it to average environmental variables with great sensitivity and accuracy, imaging uniquely captures community spatial structure and correlate it to its immediate environment. For example, imaging of supragingival dental plaque with taxon-specific 16S rRNA FISH probes

at micron-scale resolution has exposed the complex structure of these microbial communities with filamentous bacteria structuring the entire community and anchoring it to a solid support, anaerobes preferentially partitioned in the core and aerobes on the outer shell¹³. In the gastrointestinal tract, imaging of host-secreted mucus has suggested that mucus is an important environmental variable modulating host-microbe homeostasis. In healthy humans, mucus secretions in the colon form a physical barrier that segregates bacteria from the host¹⁴, whereas in ulcerative colitis and mouse models of colitis, this mucosal layer is disrupted, allowing bacteria to become closer to the host¹⁵. Imaging has also revealed ways that diet can modulate mucus structure. For example, long dietary fibers have been shown to compress mucus in mice¹⁶, and diets deficient in microbiota-accessible carbohydrates have been shown to promote mucus thinning, possibly by shifting bacterial metabolism towards utilization of mucus as a carbon source¹⁷. Finally, imaging that captures the biogeography of stationary and migratory host cells may shed light on host-microbe interactions, as illustrated by a study investigating neutrophil infiltration and intraluminal cast formation in the SI in response to post-infectious overgrowth of *Enterobacteriaceae*¹⁸.

In this work, we investigated the surprising co-existence of *Enterobacteriaceae* and *Bacteroidaceae* in the small bowel by applying novel 3D imaging tools [Chapters 2 and 3] to a previously published mouse model wherein the combination of a malnutrition diet and co-gavage with both *E. coli* and *Bacteroides/Parabacteroides* spp. induced features of environmental enteropathy (EE)¹⁹. Although microbial load in the human SI, particularly duodenum and jejunum, is orders of magnitudes lower than in the human colon²⁰, we focused on the SI because its unique architecture and function warrant more attention from microbiome researchers. The surface area of the SI is 15 times larger than that of the colon²¹ and the SI is not covered by a continuous dense layer of mucus²², possibly providing opportunities for bacteria to directly contact host cells as well as enable greater flux of microbial metabolites to the host. Elevated microbial loads have been observed in the SI (e.g. in SIBO³), however, these bacteria were measured in the SI fluid; it is not known whether high bacterial loads are maintained deep in the mucosa of the SI. Moreover, the hypothesized bacterial colonization of SI mucosa is challenging to study

because mucosal immunity, digestive secretions, and intestinal motility effectively clear mucosal invaders^{20,23,24}: even if colonization of SI mucosa occurs, it is likely rare, transient, and elusive to observation. We hypothesized that, in a host weakened by malnutrition and challenged with oral exposure to the synergistic *Enterobacteriaceae*–*Bacteroidaceae* pair, the likelihood of this rare co-colonization event increases such that now it can be captured. Even if rare and transient, bacterial colonization of the SI mucosa would be significant because, unlike the colon, the SI performs the essential function of food digestion and nutrient absorption, so dysbiosis in the SI may be more detrimental to the host than dysbiosis in the large intestine. The importance of the SI is emphasized in EE, a subclinical disorder of the SI common in the developing world and characterized by altered epithelial morphology, such as villus blunting, increased intestinal inflammation, and permeability²⁵. EE can be particularly detrimental to children because impaired digestive and absorptive function of the SI can lead to growth stunting, wasting, and impaired development²⁵. EE is thought to be caused by ingestion of food and water contaminated with fecal bacteria²⁵, however, it remains poorly understood not only because it occurs in resource-limited settings, but also because it is subclinical and does not present with overt²⁵ or persistent²⁶ gastrointestinal symptoms.

Results

To test the hypothesis that the rare event of bacterial colonization of SI mucosa can be observed in malnourished mice challenged with the likely synergistic *Enterobacteraceae* and *Bacteroidaceae* pair, we set up an experiment to recapitulate the published mouse model of environmental enteropathy (EE)¹⁹. Briefly, at 21 days of age, mice were placed on either malnourishing (MAL) or complete control (COM) diet (Fig.4.1A). Diet formulations were identical to those in the EE study¹⁹ except that food dyes were omitted to minimize sample autofluorescence during imaging. All the human gut bacterial isolates – *Bacteroides dorei*, *Bacteroides fragilis*, *Bacteroides ovatus*, *Bacteroides vulgatus*, *Parabacteroides distasonis*, and *E. coli* – were identical to the previously used isolates¹⁹. During the third week on the experimental diets, mice were orally gavaged three times (once every other day) with one of

the bacterial cocktails (*E. coli* and *Bacteroides/Parabacteroides* spp. mixture (EC&BAC), *E. coli* only (EC), *Bacteroides/Parabacteroides* spp. only (BAC), or PBS control) (Fig.4.1A). During the fifth week, mice were euthanized, and small and large intestines were considered in the analyses because colonic microbiota may impact SI microbiota by retrograde transport from cecum to ileum²⁷ and as a result of coprophagy (fecal ingestion)²⁸. Therefore, to more fully understand any potential changes to SI microbiota, information on colonic microbiota may be necessary. Consistent with the previous EE study¹⁹, malnutrition retarded growth, however, in contrast to the previous report¹⁹, oral gavage of bacteria did not further slow weight gain or lead to weight loss (Fig.4.1B). Furthermore, we detected only slight differences in gastrointestinal inflammation. For example, fecal lipocalin-2 was 2-folds greater in MAL+EC&BAC compared with MAL+PBS mice, however, this increase was not statistically significant (Fig.4.1C). Additionally, differences in the transcription of inflammatory cytokines TNF- α and IL-6 in jejunal, ileal, and colonic tissues among treatments were also modest and non-significant (Fig.4.1 D-E). Therefore, the previously reported wasting and intestinal inflammation characteristics of EE were not reproduced.

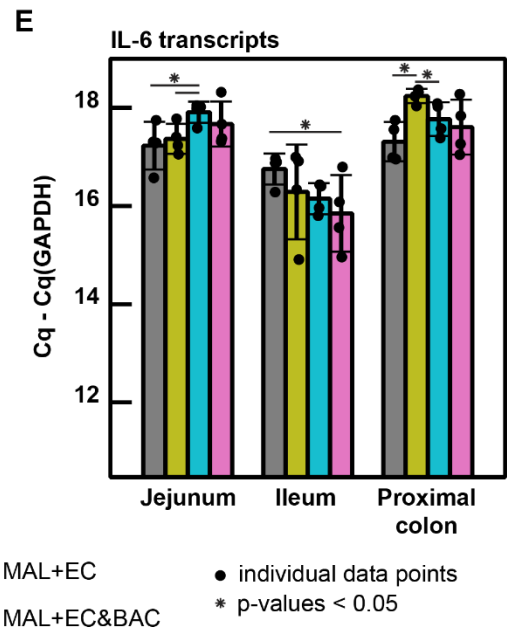
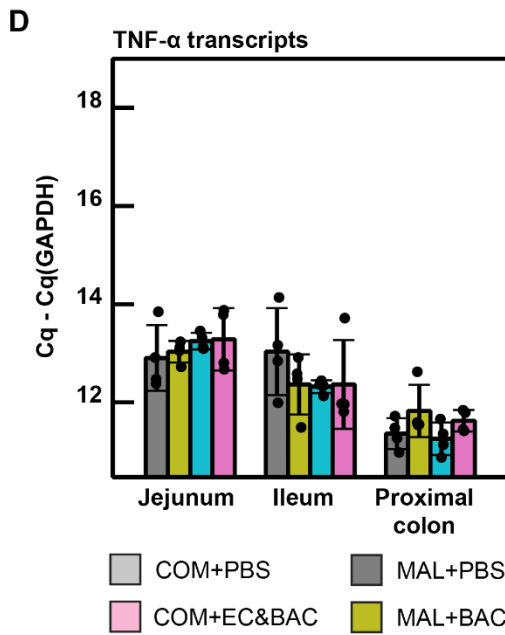
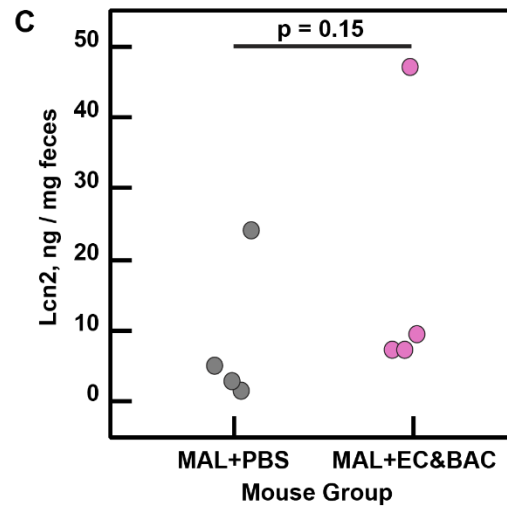
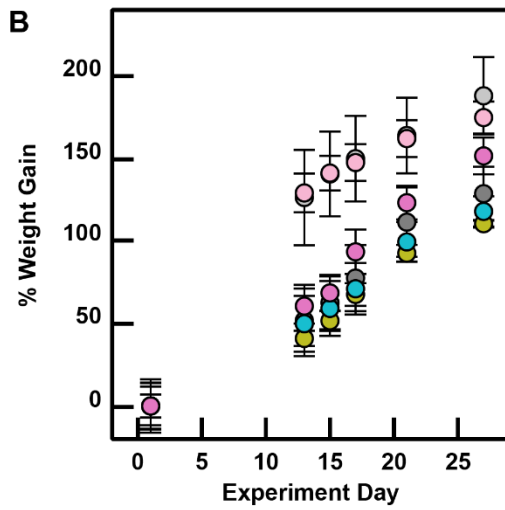
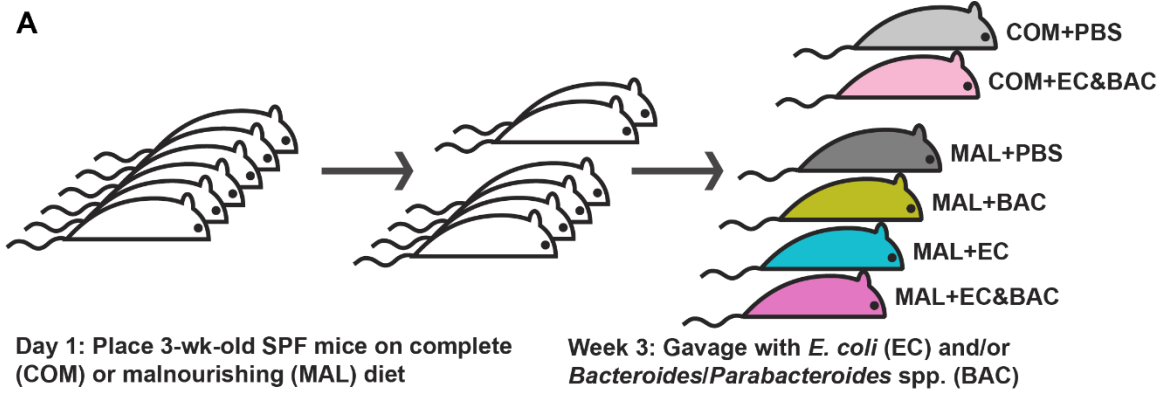


Figure 4. 1. Experiments aiming to reproduce the published EE mouse model¹⁹. (A) The setup of the animal experiment. COM: complete, well-nourishing diet. MAL: malnourishing diet low in protein (7%) and fat (5%), but containing the same amounts of calories, vitamins, and minerals on the basis of mass. PBS: no bacteria gavage control. BAC: gavage with five *Bacteroides/Parabacteroides* spp. isolates. EC: gavage with two *E. coli* isolates. EC&BAC: gavage with all seven bacterial isolates. The mice were gavaged with bacterial cocktails or PBS control on the third week of the experiment, on days 14, 16, and 18. The mice were euthanized for examination on the fifth week of the experiment, on days 28, 29, 30, and 31. (B) Growth curves showing how malnutrition and bacterial gavage affect animal growth. (C) Preliminary fecal lipocalin-2 measurement in feces of MAL+PBS and MAL+EC&BAC mice on Day 27 of the experiment. (D – E) TaqMan quantification of TNF- α (D) and IL-6 (E) transcripts and normalized to GAPDH housekeeping gene. Transcripts were quantified in jejunum (2nd quartile of the SI), ileum (4th quartile of the SI), and proximal colon tissues in malnourished mice only (3rd quartile was used in imaging experiments). Each group contained 4 mice, which were euthanized over the course of 4 days, one mouse per group per day. Statistical significance was evaluated using the Kruskal-Wallis test.

Malnutrition and co-gavage with E. coli and Bacteroides/Parabacteroides spp. uniquely impact relative microbiota composition

Although the reported EE phenotype was not induced in our experiment, we wanted to test whether the gavaged bacterial isolates persisted in the gut and, if so, whether they altered resident microbiota composition relative to non-gavaged mice (Fig.4.2). We performed 16S rRNA gene amplicon sequencing and found that, most remarkably, *Enterobacterales*, the order of the gavaged *E. coli*, was only detected in MAL+EC&BAC mice. *E. coli* was detected in both feces and jejunum luminal contents (hereafter jejunum digesta) in all three replicates of the MAL+EC&BAC group (Fig.4.3B). In fact, all *Enterobacterales* reads in the MAL+EC&BAC mice corresponded to the *Enterobacteriaceae* family (Fig.4.2B) and specifically the *Escherichia-Shigella* genus (Fig.4.S1). Furthermore, the detected reads aligned perfectly with the complete 16S rRNA gene sequences of the gavaged *E. coli* isolates. In contrast, *Bacteroidales* were abundant in all experimental animals, including the PBS-gavaged mice and the mice on the COM diet (Fig.4.2A). In feces, the relative abundance of *Bacteroidales* was ~40% across all experimental conditions evaluated, whereas in jejunum digesta there was a trend towards a higher relative abundance in response to malnutrition and/or gavage. Three *Bacteroidales* families could be identified: *Muribaculaceae*, *Bacteroidaceae* (the family of *Bacteroides* genus), and *Tannerellaceae* (the family of *Parabacteroides* genus) (Fig.4.2B), with *Muribaculaceae* being the dominant family in both feces and, even more prominently, in jejunum digesta (Fig.4.2B). In feces, *Bacteroidaceae*,

solely represented by *Bacteroides* genus (Fig.4.S1), were present in non-gavaged mice, and their relative abundance was greater in well-nourished mice gavaged with EC&BAC as well as malnourished mice gavaged with either BAC or EC&BAC gavage (Fig.4.2B). In contrast, *Tannerellaceae*, solely represented by *Parabacteroides* genus (Fig.4.S1), could be detected in feces only in mice exposed to *Bacteroides/Parabacteroides* spp. (Fig.4.2B). In jejunum digesta, the relative abundance of both *Bacteroidaceae* and *Tannerellaceae* was low across all mouse groups (Fig.4.2B). The reads assigned to *Parabacteroides* genus aligned perfectly with the complete 16S rRNA sequence of the gavaged *P. distasonis* isolate, whereas the reads assigned to *Bacteroides* genus aligned perfectly to the full 16S rRNA sequences of gavaged *Bacteroides* spp. isolates. Additionally, one resident *Bacteroides* species, *B. theta*, was identified. Finally, malnutrition and oral challenge with human gut bacterial isolates shifted the relative composition of the resident microbiota (Fig.4.2). For example, compared with well-nourished controls, *Coriobacteriales* were depleted in malnourished mice (Fig.4.2A). However, staggering of experimental conditions and using mice from different litters may partially contribute to the apparent shifts in the resident microbiota composition. Overall, the analysis of relative abundance concluded that, although gavaging bacterial isolates did not induce EE in malnourished mice, these bacteria colonized and likely shifted resident microbiota composition.

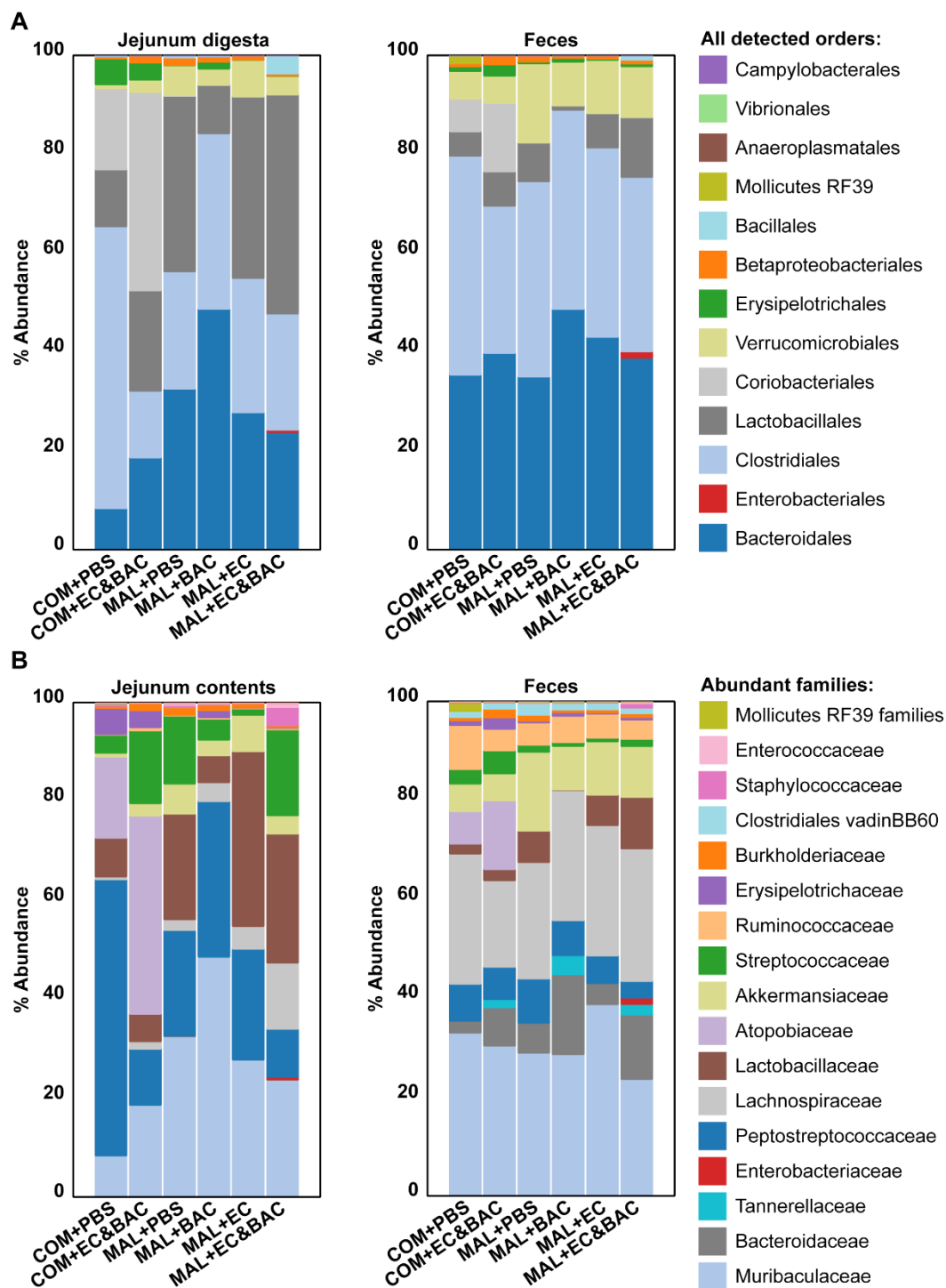


Figure 4. 2. Relative abundance of major bacterial taxa in jejunum digesta and feces assessed by 16S rRNA gene amplicon sequencing. (A) Composition at the order level with all orders detected specified in the legend and (B) composition at the family level with only the 17 most abundant families specified in the legend. The analysis consisted of six groups: well-nourished control mice not exposed to bacteria (COM+PBS), well-nourished control mice exposed to *E. coli* and *Bacteroides/Parabacteriodes* spp. cocktail (COM+EC&BAC), malnourished mice not exposed to bacteria (MAL+PBS), malnourished mice exposed to

Bacteroides/Parabacteroides spp. isolates only (MAL+BAC), malnourished mice exposed to *E. coli* isolates only (MAL+EC), and malnourished mice exposed to the full bacterial cocktail (MAL+EC&BAC). Each group contains three mice euthanized during the fifth week of the experiment, on days 28, 29, and 30, with one mouse per group per day.

Absolute quantification reveals bias of relative abundance analysis

Relative abundance can be misleading because changes in absolute abundance of unrelated taxa may produce apparent changes in the taxon of interest²⁹; therefore, we also evaluated whether the absolute abundances of bacterial taxa were different among the six treatments. Following our lab's previously published quantitative sequencing protocol²⁸⁻³⁰, the fractional composition obtained by 16S rRNA gene amplicon sequencing was anchored by the absolute load of total bacterial 16S rRNA gene copy numbers in each sample. Notably, the sequencing library presented in Fig.4.2 was amplified following protocols that have been shown to minimize amplification bias²⁸⁻³⁰. Figure 4.3A first presents total bacterial 16S rRNA gene copy load in jejunum contents and feces. Consistent with previous reports, total bacterial loads were lower in the SI than in feces, presumably due to the fast transit time and abundance of digestive secretions and antimicrobial compounds in the SI^{20,31}. However, bacterial loads in the SI were orders of magnitude higher than in humans²⁰, likely due to coprophagy²⁸, a common behavior in lab mice. Among fecal samples, total 16S rRNA gene copy loads were consistent across groups and only the MAL+BAC group displayed a modest 4-fold decrease with respect to the COM+EC&BAC and MAL+EC groups (Fig.4.3A). Most noteworthy, in the jejunum of well-nourished mice, EC&BAC gavage reduced total 16S rRNA gene copy load 10-fold (Fig.4.3A). However, such decrease in response to EC&BAC gavage was not mirrored in feces of well-nourished controls nor in the feces or jejunum contents of malnourished mice (Fig.4.3A). Accounting for these differences in total bacterial 16S rRNA gene copy abundance enabled us to correct bias in taxon-specific 16S rRNA gene copy abundance. For example, absolute abundance quantification captured that *Muribaculaceae* load in the SI was orders of magnitude lower than in feces (Fig.5.3F). Furthermore, while relative abundance analysis suggested that, in jejunum digesta, *Muribaculaceae* were least abundant in the COM+PBS group and most prevalent in the MAL+BAC group (Fig.4.2A), quantification of absolute abundance concluded that

Muribaculaceae were consistent between these two groups (Fig.4.3F). Therefore, because absolute quantification of bacterial abundance more objectively compares bacterial colonization across the mouse groups and along the GIT, it is more suitable in this study to understand how gavaged bacterial isolates colonize the GIT.

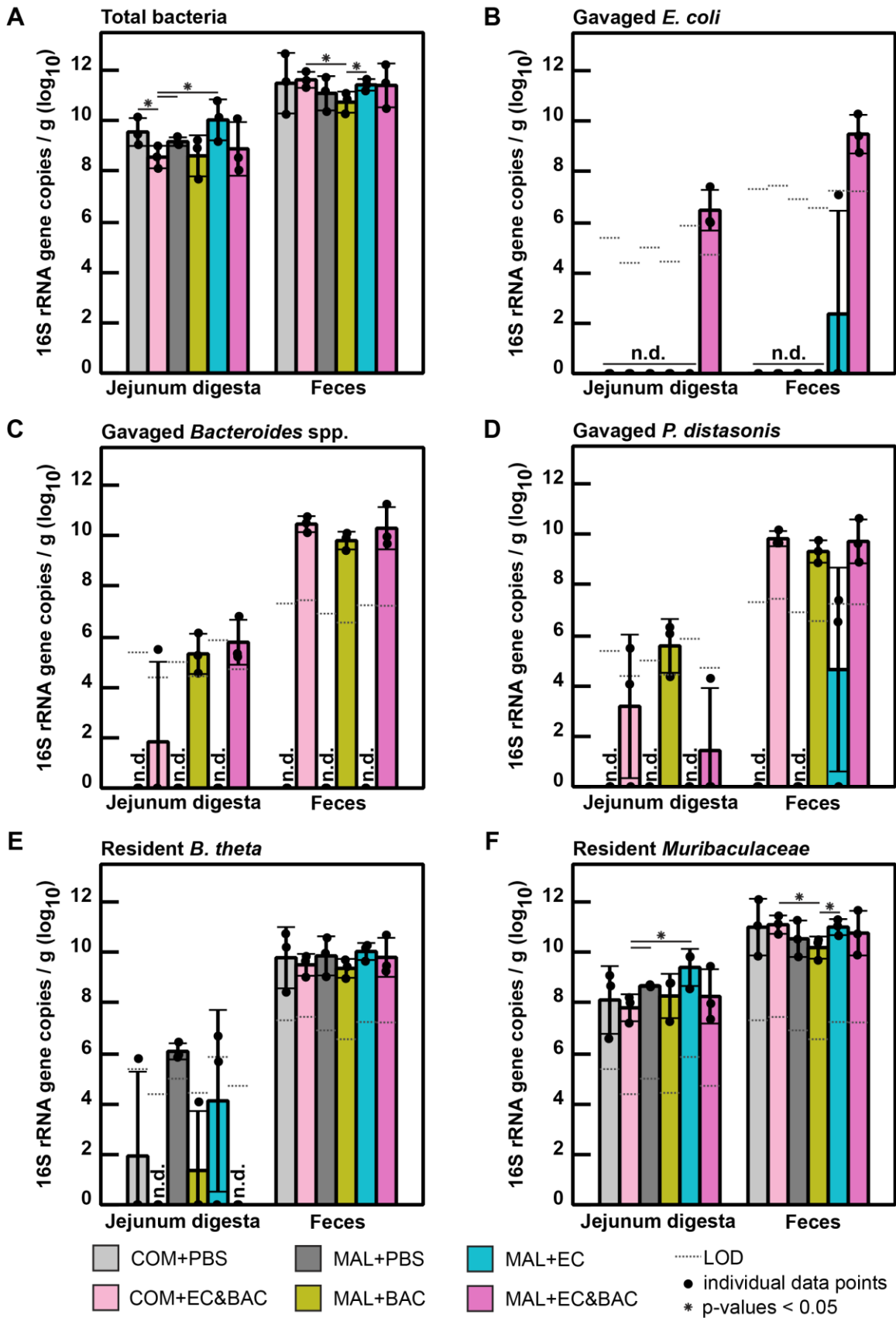


Figure 4.3. Absolute quantification of gavaged and selected resident bacteria in jejunum digesta and feces across six mouse groups as assessed by 16S rRNA gene amplicon sequencing. Absolute abundance is plotted on a log scale for (A) total bacteria, (B) gavaged *E. coli* isolates, (C) gavaged *Bacteroides* spp. composed of *B. fragilis*, *B. dorei*, *B. ovatus* and *B. vulgatus*, (D) gavaged *Parabacteroides* solely represented by *P. distasonis*, (E) resident *Bacteroides* solely represented by *B. theta*, and (F) resident *Muribaculaceae* family. The only three families in the Bacteroidales order that were detected in the experimental animals were Muribaculaceae, Bacteroidaceae (a.k.a. *Bacteroides* family), and *Tannerellaceae* (a.k.a. *Parabacteroides* family). *E. coli* was the only species in the *Enterobacteriales* order that was detected in experimental animals. Each group contained 3 mice euthanized over the course of 3 consecutive days (28, 29, and 30), one mouse per group per day. COM: complete, well-nourishing diet. MAL: malnourishing diet low in protein and fat but containing the same amount of calories, vitamins, and minerals on the mass basis. PBS: no bacteria gavage control. BAC: gavage with five *Bacteroides/Parabacteroides* spp. isolates. EC: gavage with two *E. coli* isolates. EC&BAC: gavage with all seven bacterial isolates. LOD: limit of detection expressed as group average. Statistical significance was evaluated using Kruskal-Wallis test.

To expand in the jejunum, Bacteroides/Parabacteroides spp. only required malnutrition, whereas E. coli required both malnutrition and co-gavage with Bacteroides/Parabacteroides spp.

Relying on absolute abundance quantification, we investigated how malnutrition and co-gavage affected the loads of the gavaged bacteria in the jejunum. Although 16S rRNA gene amplicon sequencing is generally not suitable for species level analysis³², the well-defined *Bacteroides* pool in non-gavaged mice and the availability of complete 16S rRNA gene sequences of gavaged isolates permitted it in this situation. We found that MAL diet was required for *Bacteroides/Parabacteroides* spp. to colonize mice and reach $\sim 10^6$ 16S rRNA gene copies per gram of jejunum digesta whereas co-gavage with *E. coli* was not required (Fig.4.3, C-D). Among the gavaged *Bacteroides/Parabacteroides* spp. isolates, only *B. fragilis* was detected in all three replicates of both MAL+BAC and MAL+EC&BAC mice, whereas other *Bacteroides/Parabacteroides* spp. were primarily detected in MAL+BAC mice (Fig.4.S2). In contrast, both the MAL diet and co-gavage with *Bacteroides/Parabacteroides* spp. were required for *E. coli* to colonize the mice and reach $10^6 - 10^7$ 16S rRNA gene copies per gram of jejunum digesta (Fig.4.3B). The co-gavage was also required for *E. coli* to increase in other locations in the gastrointestinal tract (GIT) (Fig.4.3B). We confirmed these findings using quantification by digital PCR with *Enterobacteriaceae* primers, demonstrating a significant ~ 100 -fold increase of *Enterobacteriaceae* load in the GIT of mice on the MAL diet and co-gavaged with

Bacteroides/Parabacteroides spp. (Fig.4.S3B). In contrast, consistent with the analysis of relative abundance, neither the MAL diet nor co-gavage with *E. coli* were required for *Bacteroides/Parabacteroides* spp. to increase to the colon at loads comparable to resident *B. theta* (Fig.4.3, C-E). Therefore, we identified two dependencies in the increase of the gavaged isolates in the SI: *Bacteroides/Parabacteroides* spp. required malnutrition, whereas *E. coli* required both malnutrition and co-gavage with *Bacteroides/Parabacteroides* spp., suggesting that *Bacteroides/Parabacteroides* spp. expansion in the SI led to *E. coli* expansion.

The effect of *Bacteroides/Parabacteroides* spp. on *E. coli*'s increase in the jejunum digesta of malnourished mice was reproducible. For example, in two independent experiments separated by more than one year, we detected orders of magnitude higher *Enterobacteriaceae* 16S rRNA gene copy loads in the jejunum digesta of MAL+EC&BAC than in the jejunum digesta of MAL+EC mice (Fig4.S3C). The only single experiment in which this effect was not reproduced and *E. coli* was not detected to increase in the MAL+EC&BAC treatment was an experiment where we deviated from the normally followed *E. coli* culture conditions (Fig4.S2D) and subjected it to aerobic culture with shaking. Specifically, in all experiments where the effect was reproduced, *E. coli* isolates were cultured anaerobically without shaking. We suspect that aerobic culture of *E. coli* with shaking disrupted colonization of GIT. Curiously, shaking has been reported to disrupt pili formation³³, and pili were required for colonization by the uropathogenic *E. coli*³⁴. Thus, these data suggest a hypothesis that our observed enhanced *E. coli*'s colonization of the malnourished GIT by co-gavage with *Bacteroides/Parabacteroides* spp. may rely on *E. coli*'s expression of pili. However, testing this hypothesis is outside the scope of this study.

We addressed the surprising conclusion that, although *Bacteroides/Parabacteroides* spp. effectively colonized only the colon, they enhanced *E. coli* expansion in both the small and the large intestines. Several hypotheses may explain the observation. For example, although *Bacteroides/Parabacteroides* spp. loads in the SI are only 10^6 16S rRNA gene copies/g, four orders of magnitude lower than in the colon, such relatively low loads may be significant.

For example, in humans, SIBO is diagnosed when total bacterial load in the upper SI reaches 10^5 colony forming units (CFUs)/g⁸. Alternatively, the events that determined successful *E. coli* expansion in the SI may have taken place at the time of bacterial gavage, whereas samples for analyses were collected one week after the last gavage. Finally, *Bacteroides/Parabacteroides* spp. in feces may have increased *E. coli* load in the SI due to fecal reingestion. Indeed, feces, now colonized by *E. coli* and *Bacteroides/Parabacteroides* spp., may have a similar effect as the gavage itself. To test, we have performed the following experiment, the analysis of which awaits the end of the COVID-19 quarantine. MAL+EC&BAC were split across two groups after the gavage: one group received functional tail cups that prevented fecal reingestion, whereas the other group received mock tail cups that permitted coprophagy, but recapitulated the stress of wearing them²⁸. If *E. coli* loads in the SI decrease in the functional tail cup group, we will conclude that continuous re-exposure to *E. coli* and *Bacteroides/Parabacteroides* spp. is required for *E. coli* to persist in the SI.

Pilot experiment shows that more bacteria remained in the SI after digesta passage in the MAL+EC&BAC group

Having established that gavaged bacteria expanded in the jejunum digesta, we asked whether they remained in the SI after digesta passage or whether they were cleared. Potential mechanisms behind the enhanced *E. coli* expansion of the SI by *Bacteroides/Parabacteroides* spp. in malnourished mice include metabolic coupling between the two bacterial taxa^{10,35}, bacterial modulation of the host's immune system^{12,36}, or bacterial adherence to the mucosa^{4,37}. The last mechanism is particularly interesting because the SI is a high-flux environment with fast digesta-transit times³⁸⁻⁴⁰; thus, the ability of bacteria to adhere to the mucosa and resist washout would provide an important advantage in their colonization of the SI. We recognize that the SI is not continuously filled with digesta, that is, stretches of the SI with digesta are separated by stretches of the SI without digesta; potentially, this digesta separation marks meals ingested at different times. We hypothesized that if bacteria have fitness to resist washout, we would be able to detect them in the empty

segments of the SI (whereas in segments containing digesta it would be difficult to differentiate bacteria moving with the digesta from those retained in the SI). Furthermore, although simple nutrients (e.g. simple sugars, amino acids, and their short oligomers) from food released during host digestion are abundant in segments full of digesta, only complex nutrients (e.g. mucus, cellular debris, undigested food such as fiber) may be available in empty segments. Therefore, metabolic coupling between bacterial taxa would also be more likely to be detectable in empty segments.

Imaging tools are best suited to analyze the hypothesized bacterial adherence to the mucosa because they allow to simultaneously visualize bacteria, mucus, and host cells and to map the exact bacterial location with respect to the complex mucosal landscape of the host [Chapters 2 and 3]. The results from a pilot imaging experiment that included one tissue sample from one mouse in each malnourished group are shown in Figure 4.4. Briefly, empty jejunum segments identified approximately in the middle along the SI (hereafter mid SI) were preserved in whole-mount, permeabilized with lysozyme for bacterial staining, and cleared with SDS for 3D imaging. Processed samples were stained with DAPI for DNA, which marks epithelium, and HCR v2.0 for total bacteria, *Bacteroidales*, and *Enterobacteriales* using the EUB338, CFB560, and GAM42a probes, respectively (see Methods for details). First, the tissues were tile-scanned for DAPI staining of epithelium and hybridization chain reaction (HCR) staining of total bacterial (Fig.4.4A). Despite high total bacterial loads in jejunal contents of full segments, reaching 10^8 - 10^{10} 16S rRNA gene copies per gram (Fig.4.3A), empty segments appeared remarkably void of bacteria, emphasizing the effectiveness of bacterial clearance after food digestion. In an empty jejunum section from a MAL+EC&BAC mouse, a handful of large surface aggregates could be detected. The mechanism forming these aggregates is unknown; they may represent bacterial self-aggregation for improved colonization, such as biofilm formation^{4,6}, or bacterial aggregation by the host for increased bacterial retention⁴¹ or expulsion⁴²⁻⁴⁴, or the aggregation may be caused by the presence of dietary polymers⁴⁵. Furthermore, the observed aggregates could be the product of multiple processes, for instance, the host may aggregate undigested food, cellular debris, and bacteria to expel these materials, whereas some bacterial communities

may actually thrive in these aggregates. Regardless of the mechanism, the presence of bacterial aggregates in the empty jejunum segment was indicative of bacterial resistance to washout.

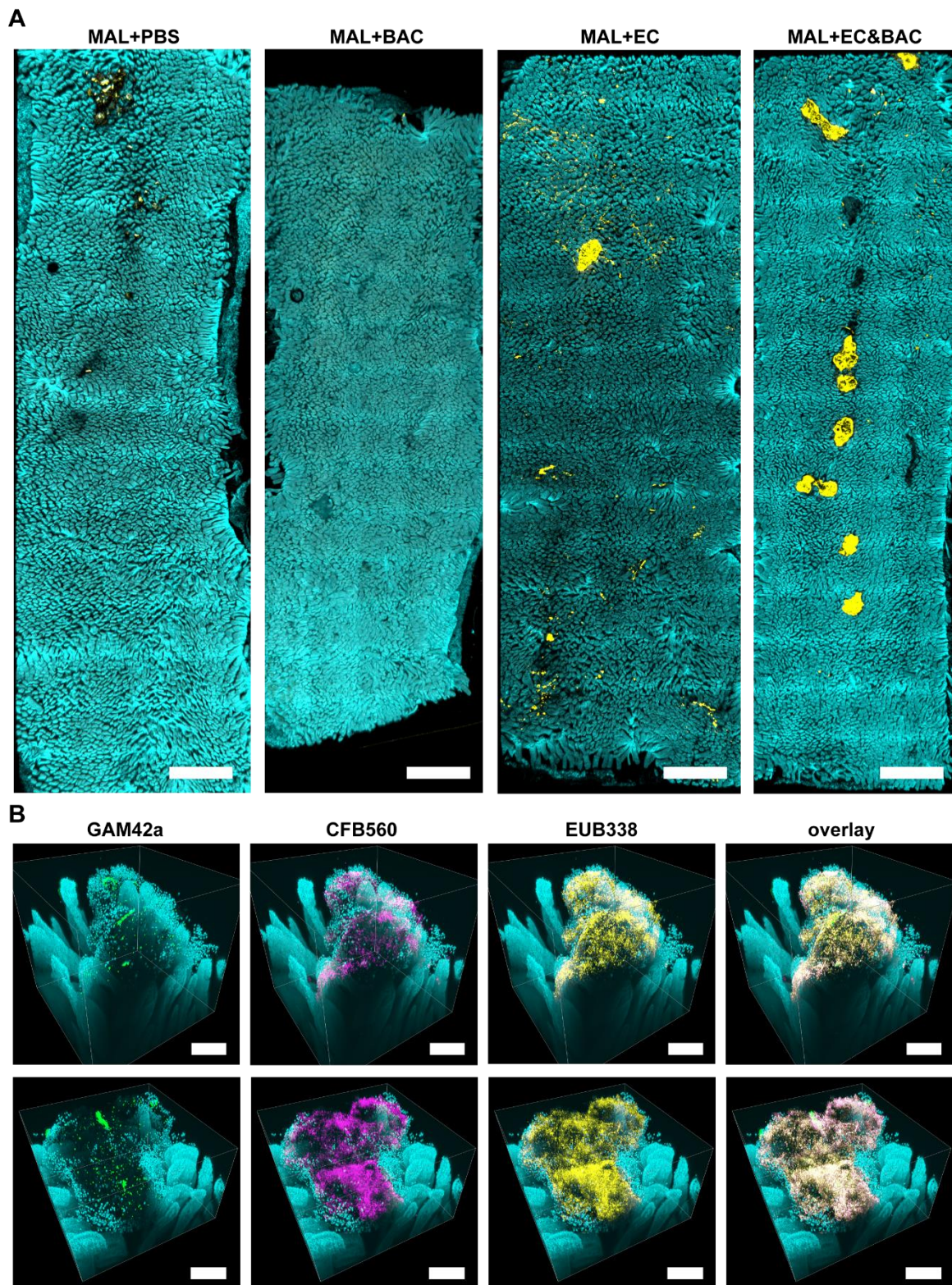


Figure 4. 4. Pilot experiment showing empty jejunum segments of malnourished mice without fasting. (A) 5x tile scans showing DAPI staining of epithelium (cyan) and HCR v2.0 staining of total bacteria with

EUB338 probe (yellow). All scale bars 2 mm. (B) 20x CLARITY images of bacterial aggregates detected in MAL+EC&BAC mouse also showing *Enterobacterales* stained with GAM42a HCR v2.0 probe (green) and *Bacteroidales* stained with CFB560 HCR v2.0 probe (magenta). A single mouse was imaged in each group. All scale bars 200 μ m.

Next, we wanted to investigate whether the bacterial taxa of the gavaged isolates were present in these bacterial aggregates in the MAL+EC&BAC mouse. For this purpose, two bacterial aggregates were imaged at higher magnification and with taxonomic resolution for EUB338, CFB560 and GAM42a HCR v2.0 staining (Fig.4.4B). In our study, CFB560 only targeted the *Bacteroidales* order, including *Bacteroides*, *Parabacteroides* and *Muribaculaceae*, without a mismatch, whereas GAM42a only targeted the *Enterobacterales* order, solely represented by *E. coli*, without a mismatch and had only one mismatch with the resident *Betaproteobacterales* order. To quantify abundance of each taxon, the images were segmented in Imaris to obtain EUB338, CFB560, and GAM42a positive objects. After segmentation, candidate bacterial objects were additionally filtered to remove false positives (objects with weak EUB338 staining), double positives (objects with strong GAM42a and CFB560 staining), as well as small-size outliers and objects inside the villi (which in our experience were autofluorescence in blood capillaries). In both of the examined aggregates (Fig.4.4B), *Enterobacterales* volume fraction was 2%, whereas *Bacteroidales* volume fraction was 40% and 70% in the first and second aggregate, respectively. Therefore, consistent with visual inspection, *Bacteroidales* were abundant in bacterial aggregates, whereas *Enterobacterales* were sparse. Based on 16S rRNA gene amplicon sequencing, *Enterobacterales* relative abundance was in the range of 0.1-1% in jejunum digesta of the MAL+EC&BAC mouse; therefore, *Enterobacterales* volume fraction of 2% in bacterial aggregates suggested that *Enterobacterales* were fractionally enriched, that GAM42a probe also recognized *Betaproteobacterales* (which amounted to <0.5% of total 16S rRNA gene copies and only had one mismatch with GAM42a probe), or that there was a discrepancy between the imaging and sequencing methods. *Bacteroidales* amounted to 20-30% of total 16S rRNA gene copies, also suggestive of fractional *Bacteroidales* enrichment in bacterial aggregates. Therefore, imaging with taxonomic resolution suggested that *Enterobacterales* and *Bacteroidales* orders of the gavaged bacterial isolates were present in bacterial

aggregates and suggested that they may be found at greater relative abundance than in the digesta.

To determine whether *Enterobacterales* within bacterial aggregates are structured or well-mixed, we quantified bacterial spatial structure in the aggregates (Fig.4.5). *Enterobacterales* existed predominantly as single cells separated from each other by a distance larger than the estimated cell diameter (Fig.4.5C). In contrast, *Bacteroidales* were so tightly packed that they could not be segmented into individual cells. Furthermore, *E. coli* associated more closely with *Bacteroidetes* than with each other (Fig.4.8D), with 80% of *Enterobacterales* cells located less than 1 μm away from *Bacteroidetes* and all *Enterobacterales* cells within 30 μm of at least one *Bacteroidetes* cell (Fig.4.8E). Such close association of *Enterobacterales* with *Bacteroidales* suggested metabolic coupling. Alternatively, existence of *E. coli* as single scattered cells could be due to motility of *E. coli* (unlikely in aggregates), or that *E. coli* had not divided within the aggregates prior to sample collection. The latter could arise, for example, as the product of either aggregation of well-mixed luminal contents^{46,47} dominated by *Bacteroidales* or the initial growth of *Bacteroidales* followed by arrival or adhesion of *Enterobacterales*. We have not investigated these possibilities here.

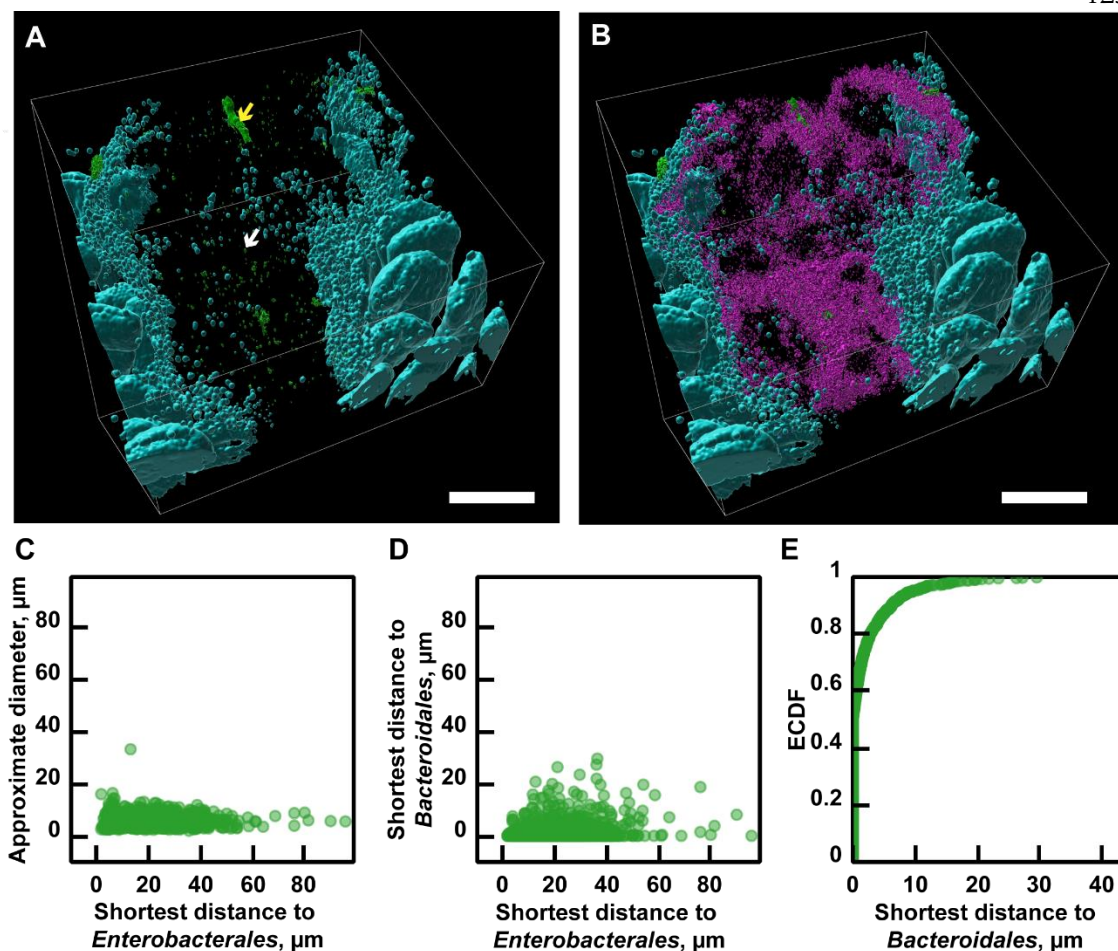


Figure 4. 5. Image analysis of bacterial aggregates shown in Fig.4.4B. (A-B) Image segmentation in Imaris marks the boundaries of DAPI+ objects (cyan), GAM42a+ objects (green), and CFB560+ objects (magenta). Scale bar = 200 μm . After segmentation in Imaris, candidate objects were additionally filtered to remove false positives (objects with weak EUB338 staining), double positives (objects with strong GAM42a and CFB560 staining), as well as small-size outliers and objects inside the villi. Although both true-positive (white arrow) and false-positive (yellow arrow) objects are displayed in the images in panels (A-B), only true-positive bacterial cells and clusters are analyzed in panels (C-E). (C) *Enterobacteriales* diameter as a function of distance to the nearest like-neighbor. (D) *Enterobacteriales* shortest distance to *Bacteroidales* as a function of their shortest distance to the like-neighbor. (E) Empirical cumulative distribution function (ECDF) showing the fraction of *Enterobacteriales* cells (y-axis) that are separated from *Bacteroidales* cells at a particular or smaller distance (x-axis). For instance, most *Enterobacteriales* cells are located within 10 μm of *Bacteroidales*. Both aggregates (A-B) were quantified in (C-E).

In MAL+EC&BAC mice, more bacteria remained in the SI after a 1-hour fast

To answer our next three questions – (1) are gavaged isolates retained in empty segments of the SI? (2) which host cells surround bacterial aggregates?, and (3) what is the significance of bacterial retention? – we had to further develop tools and approaches. For

example, the significance of bacterial presence in empty segments was challenging to evaluate because it may have reflected the timing of sampling with respect to food ingestion and transit through the GIT (Fig.4.4A). Furthermore, mammalian nuclei in association with bacterial aggregates (Fig.4.4B, Fig.4.5 A-B) could not be identified by antibody staining because hydrogel chemistry severely limited antibody entry [Chapters 2 and 3]. Finally, previously used HCR v2.0 CFB560 and GAM42a probes targeted resident bacteria and suffered from increasing false positive signal with depth [Chapter 3]. Therefore, new methods and approaches were adopted in the subsequent imaging experiments. For instance, to address bias arising from different timing of sampling with respect to food ingestion and transit through the GIT, the mice were briefly fasted for 1 h prior to euthanasia and sample collection. Furthermore, we adapted a new hydrogel chemistry more permeable to antibodies [Chapter 3], and we designed new HCR v3.0 probes to target the gavaged *E. coli* or *Bacteroides/Parabacteroides* spp. isolates without a mismatch using their full 16S rRNA sequences (Fig.4.S5). Compared to HCR v2.0 probes employed previously, HCR v3.0 probes also reduced false positive signals and background amplification, increasing the true positive signal to background ratio at depth ⁴⁸ [Chapter 3]. Potential cross-reactivity of these probes towards resident bacterial orders (Fig.4.2) was assessed by aligning them to 16S rRNA sequences in SILVA database (Fig.4.S5, A-B). *E. coli* and *Bacteroides/Parabacteroides* spp. HCR v3.0 probes only recognized *Enterobacterales* and *Bacteroidales* orders, respectively, even when one mismatch was allowed. Among the relevant families of the *Bacteroidales* order, the *Bacteroides/Parabacteroides* spp. probe only recognized *Bacteroidaceae* (the family of gavaged *Bacteroides* spp. and resident *B. theta*) and *Tannerellaceae* (the family of gavaged *P. distasonis*) families without a mismatch and recognized *Muribaculaceae* family with one mismatch (Fig.4.S5B). The designed probes were also validated *in vitro* using *B. fragilis* and one of the *E. coli* isolates: the probes recognized their targets, but did not cross-react (Fig.4.S5C).

Next, we asked whether large surface bacterial aggregates were still detected in fasted mice (with more of the SI now empty) and whether these rare events were more common in the

MAL+EC&BAC treatment. Indeed, after a brief fast, large surface aggregates were still present in the empty segments of the mid SI, and were most common in the MAL+EC&BAC group (3 out of 4 mice had aggregates), followed by MAL+BAC group (1 out of 4 mice had aggregates); none of the mice in the MAL+PBS or the MAL+EC groups had aggregates (Fig.4.6A, Fig.4.S6 and Fig.4.S7). Notably, these aggregates were opaque and large enough so that they were visible to the naked eye after tissue clearing (Fig.4.6A). To confirm these aggregates were bacteria, cleared hydrogel-tissue hybrids from two mice per group were stained with DAPI for epithelium and with HCR v3.0 for total bacteria, *Bacteroides/Parabacteroides* spp. and *E. coli*. Tile-scanning for epithelium and total bacteria at low magnification detected bacteria only in samples with large surface aggregates (Fig.4.6A, Fig.4.S7). Furthermore, bacteria were predominantly found in large surface aggregates; only MAL+EC&BAC day 28 sample showed small bacterial clusters on the tissue (Fig.4.6A). Therefore, low magnification imaging suggested that, in malnourished mice not exposed to bacterial isolates, SI mucosa is void of bacteria after a 1 h fast, whereas in the gavaged malnourished mice, the EC&BAC bacterial cocktail resulted in bacterial retention, suggestive of bacterial resistance to washout by adhesion to mucosa and/or continued growth in the absence of digesta.

Bacterial retention in the MAL+EC&BAC group after a 1-h fast was then visualized at higher magnification and with taxonomic resolution (Fig.4.6B). Consistent with the pilot experiment, *Bacteroides/Parabacteroides* spp. were abundant but only in two (of three imaged) mice where large surface aggregates were detected (one MAL+BAC day 29 mouse and one MAL+EC&BAC day 28 mouse) whereas *E. coli* were sparse in these two mice and absent in all other treatments (Fig.4.6B). After segmentation in Imaris, candidate objects were again quality-filtered to remove false positives (objects with weak total bacterial staining), double positives (objects with strong *E. coli* and *Bacteroides/Parabacteroides* spp. staining) as well as size outliers and objects inside the villi. Consistent with low-magnification imaging, bacteria were not detected in samples where large surface aggregate were not detected (Fig.4.7, Fig.4.S7). In the two mice where *Bacteroides/Parabacteroides* spp. were abundant, they amounted to between 10% and 76% of total bacteria (Fig.4.7, A-

B), whereas 16S rRNA gene copy analysis by sequencing detected *Bacteroides/Parabacteroides* spp. at only $\sim 10^6$ 16S rRNA gene copies per gram of digesta, which is equivalent to the order of 0.1% of total 16S rRNA load (Fig.4.3, A, C and D). This difference in relative abundance between empty segments and digesta suggested that *Bacteroides/Parabacteroides* spp. were fractionally enriched in empty segments, or that their HCR v3.0 probe cross-reacted with *Muribaculaceae* and labeled the entire *Bacteroidales* order. In contrast, *E. coli* were less prevalent and amounted to on the order of 0.1% of total bacteria in empty segments (Fig.4.7C), which was consistent with *E. coli* load in the digesta measured at $\sim 10^6 - 10^7$ 16S rRNA gene copies per gram of digesta and equivalent to 0.1-1% of total bacteria (Fig.4.3, A-B). Consistent with 16S rRNA gene copy quantification (Fig.4.3B), *E. coli* could not be detected on the mucosa of any of the MAL+EC mice (Fig.4.7C). These results suggested that, in malnourished mice, EC&BAC cocktail increased bacterial retention in the SI after a 1-h fast and that gavaged *E. coli* could be detected among these retained taxa. Furthermore, it suggested that *Bacteroides/Parabacteroides* spp. not only remained, but may also have been found at greater relative abundance compared with the digesta.

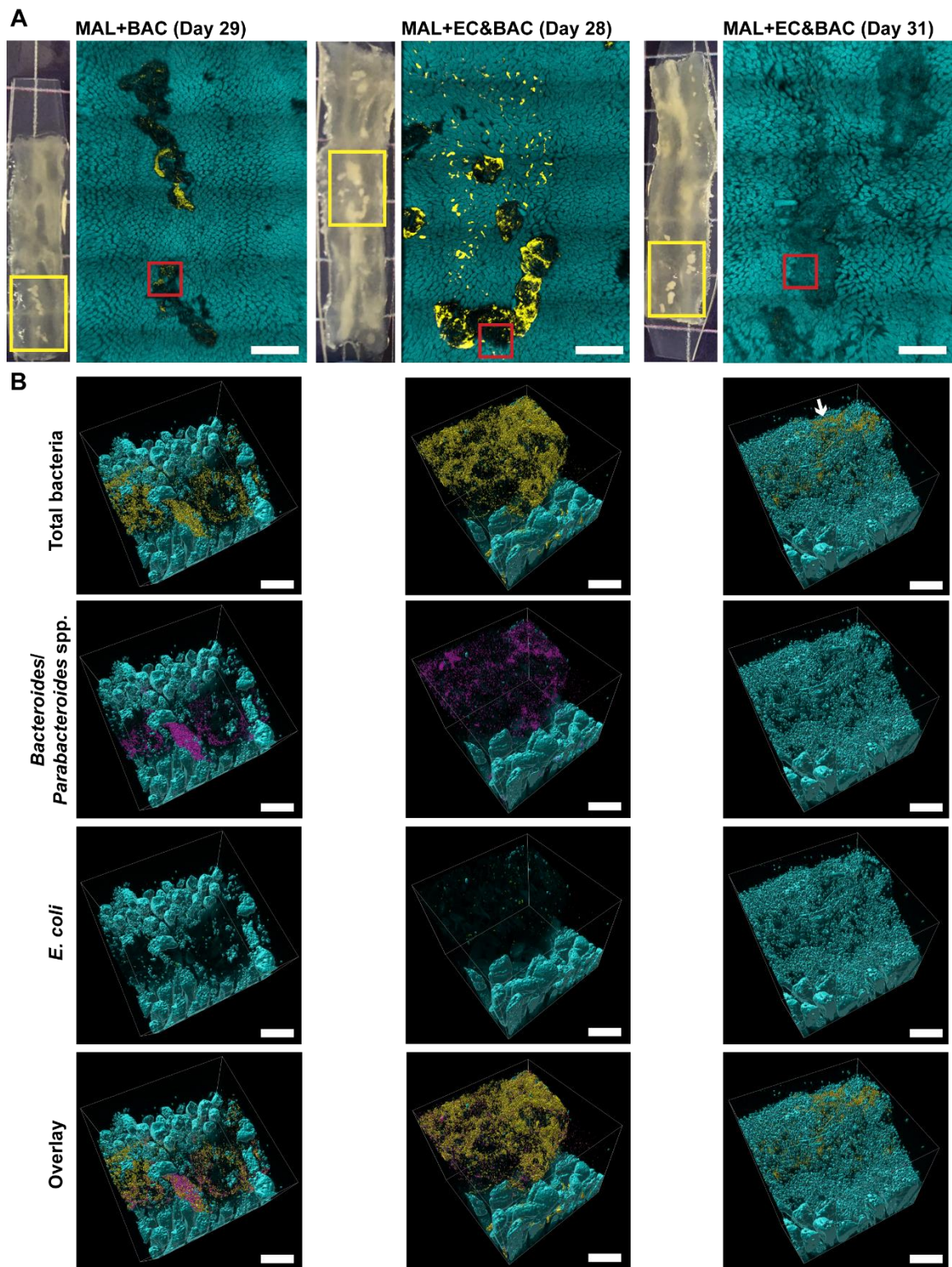


Figure 4. 6. Inspection of large opaque surface aggregates detected in fasted mice by eye and their imaging by microscopy. (A): Images of cleared tissues showing opaque large surface aggregates and their tile-scanning at low magnification for DAPI staining of epithelium (cyan) and HCR v3.0 staining of total bacteria

(yellow). Yellow boxes mark the areas presented in low magnification tile scans. In aggregates where bacteria are sparse, they are not clearly visible due to low magnification and image thresholding. Images of cleared tissues and full low magnification tile scans of all other mice are provided in Fig.4.S6 and Fig.4.S7. The grid size in photos is 6 mm, and the scale bar in tile scans is 1 mm. (B) CLARITY imaging of large aggregates shown in panel (A, red boxes) for DAPI staining of mammalian nuclei / epithelium (cyan), total bacteria (yellow), *Bacteroides/Parabacteroides* spp. (magenta), and *E. coli* (green) followed by object segmentation in Imaris. Sparse *E. coli* cells are hard to see at this resolution, but they are quantified in Fig.4.7. In MAL+EC&BAC day 31 mouse, free mammalian nuclei surround and obscure bacteria (white arrow). Each image is composed of 4 fields of view stitched together. For each sample, large surface aggregates were imaged at three locations. The same amount of data was collected from the remaining stained samples, and the analysis of all data is shown in Fig.4.7. One piece of tissue from each of two mice in each mouse group were imaged. Scale bar = 200 μm .

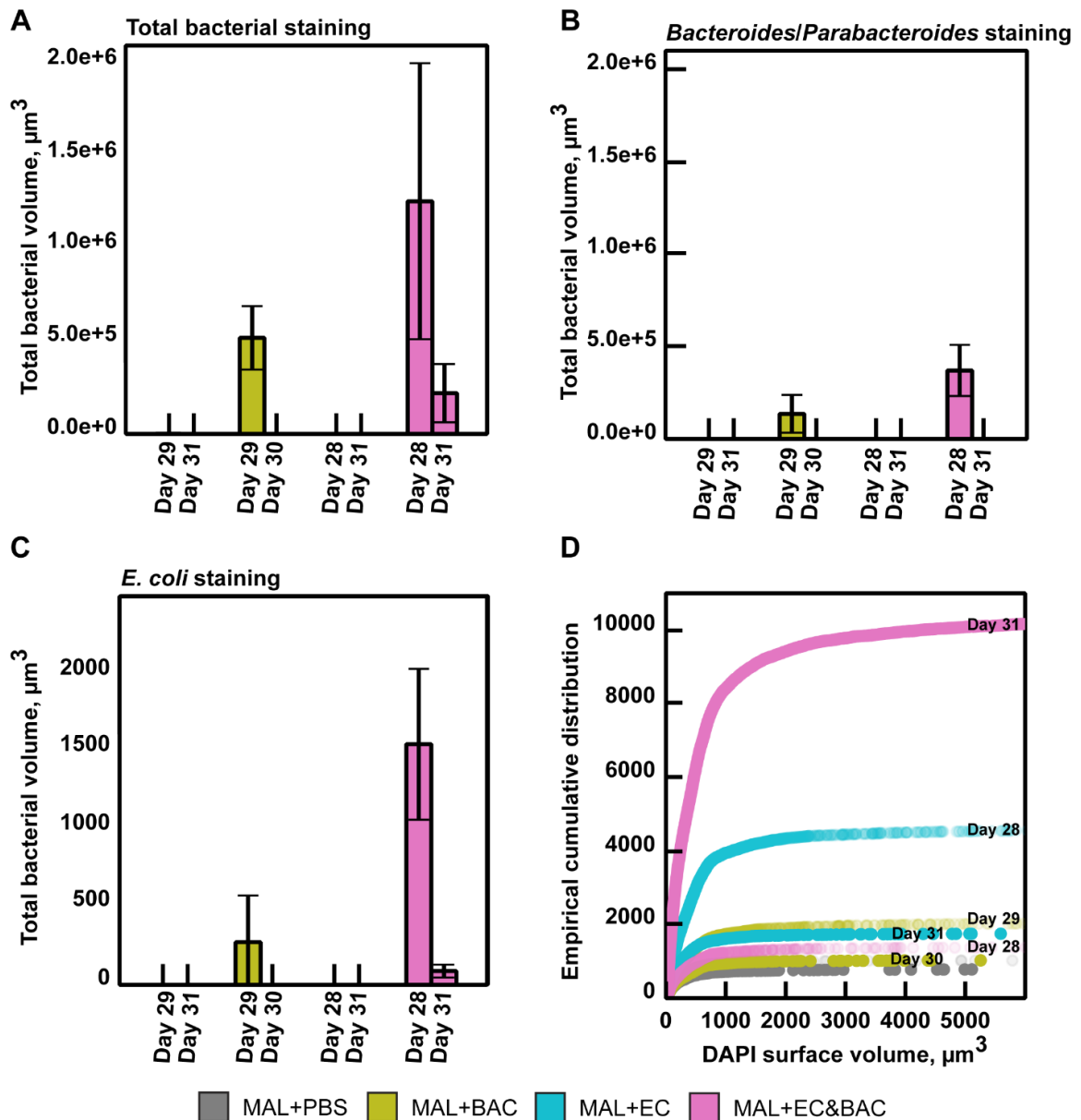


Figure 4.7. Image analysis of CLARITY-processed tissues displayed in Fig.4.6 and Fig.4.S7 with two mice per group and one tissue per mouse. The experiment days when the mice were euthanized are specified in the plots. All images were stained, imaged, and analyzed following identical protocols. (A) Total bacterial volume averaged over three images, each imaging containing 4 fields of view. Bacteria could be reliably detected only in three mice that had large surface aggregates. (B) *Bacteroides/Parabacteroides* spp. volume with only two mice showing detectable levels of *Bacteroides/Parabacteroides* spp. (C) *E. coli* volume, which was lower than that of total bacteria or *Bacteroides/Parabacteroides* spp. and was close to background signal seen as false positive signal in one MAL+BAC mouse. (D) Empirical cumulative distribution of DAPI objects based on their size, with smaller objects representing free nuclei and larger objects representing intact villi. Each curve represents one mouse with distribution calculated over three image files.

In MAL+EC&BAC group, bacteria are detected to colonize the mucosa

We hypothesized that, in the MAL+EC&BAC group, the observed bacterial aggregates retained in the mid SI after a 1 h fast correlated with the increased likelihood of bacterial colonization of the SI mucosa, and that our imaging technology would allow to detect these rare events and visualize them in 3D, which has never been done. Previously, 2D imaging detected bacteria in between the villi in the jejunum¹⁹, however, it was unclear whether those images were acquired at locations with or without digesta. Where digesta is present, bacterial detection in between the villi could also be explained by partial partitioning of luminal bacteria to the mucosa, therefore, our study design offers a unique opportunity to visualize bacteria in the intervillus spaces not biased by the presence of digesta. To test whether bacteria can be detected as colonizers of the intervillus space in MAL+EC&BAC group, we examined a MAL+EC&BAC day 28 mouse that showed small bacterial clusters in addition to large surface bacterial aggregates (Fig.4.6A, Fig.4.8A). To sensitively and specifically visualize bacteria deep in the mucosa required the adoption of the HCR v3.0 probes (Chapter 3) to stain bacteria because the previously used HCR v2.0 probes (Chapter 2) were prone to giving amplified background and false positive signal at these depths. In MAL+EC&BAC day 28 mouse, small bacterial clusters detected at low magnification were observed to penetrate deep in between the villi at higher magnification (Fig.4.8, B-E). Bacterial density varied in the intervillus spaces, with some areas showing tightly packed bacteria (Fig.4.8, B-E). Furthermore, bacteria appeared to be anchored to and wrapped around the villi (Fig.4.8, C and E). Although this single event does not convey the prevalence of mucosal colonization, it shows that bacteria can be retained in the intervillus spaces (independent of digesta) and that this potentially rare event can be detected using our experimental design and imaging technology.

We next tested whether gavaged bacteria or their higher order taxonomic groups were present in the detected mucosal bacterial communities between the villi (Fig.4.8F). Like in large surface aggregates, *Bacteroides/Parabacteroides* spp. were abundant and amounted to 35–100% of total bacteria across different images of the same sample. Such high fractional

Bacteroides/Parabacteroides spp. abundance suggested they were enriched in the mucosa compared to the digesta, or that the probe cross-reacted with other resident bacteria, in particular the most abundant family of *Bacteroidales* order, *Muribaculaceae*, which had only one mismatch with the probe. Again, *E. coli* were sparse, but could be detected to associate with *Bacteroides/Parabacteroides* spp. (Fig.4.8F). The observed spatial structure was consistent with the 16S rRNA gene copy analysis, which demonstrated that *Bacteroides/Parabacteroides* spp. did not require gavage with *E. coli* to increase in the SI of malnourished mice, but facilitated *E. coli*'s increase (Fig.4.3, B-D). We hypothesized that the ability of *Bacteroides* spp. to adhere to³⁷ and forage on⁴⁹ mucus may mediate their ability to colonize SI mucosa. Indeed, wheat germ agglutinin (WGA) staining for N-acetylglucosamine (which is abundant in mucus;^{22,50}) and HCR staining for bacteria showed that bacteria were co-localized with N-acetylglucosamine (Fig.4.9). These results show that *Bacteroides/Parabacteroides* spp. colonization of the intervillus spaces of malnourished mice is possible and may be mediated by adhesion to and foraging on mucus.

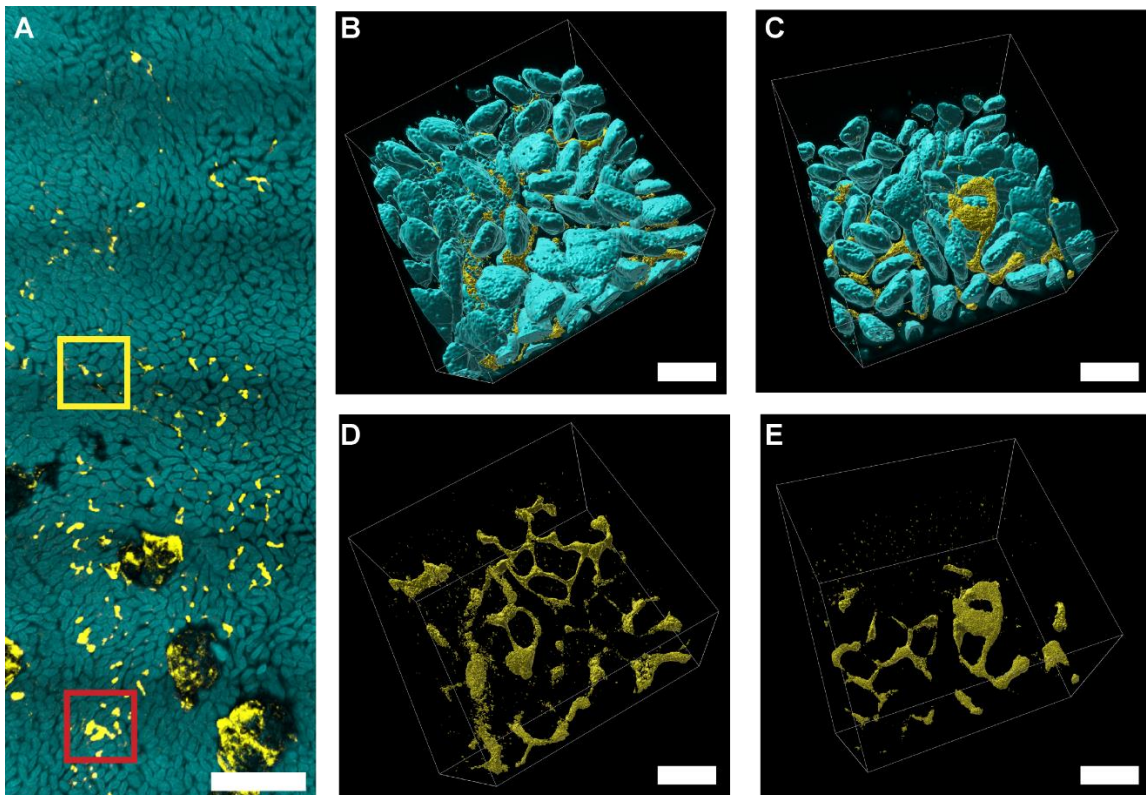
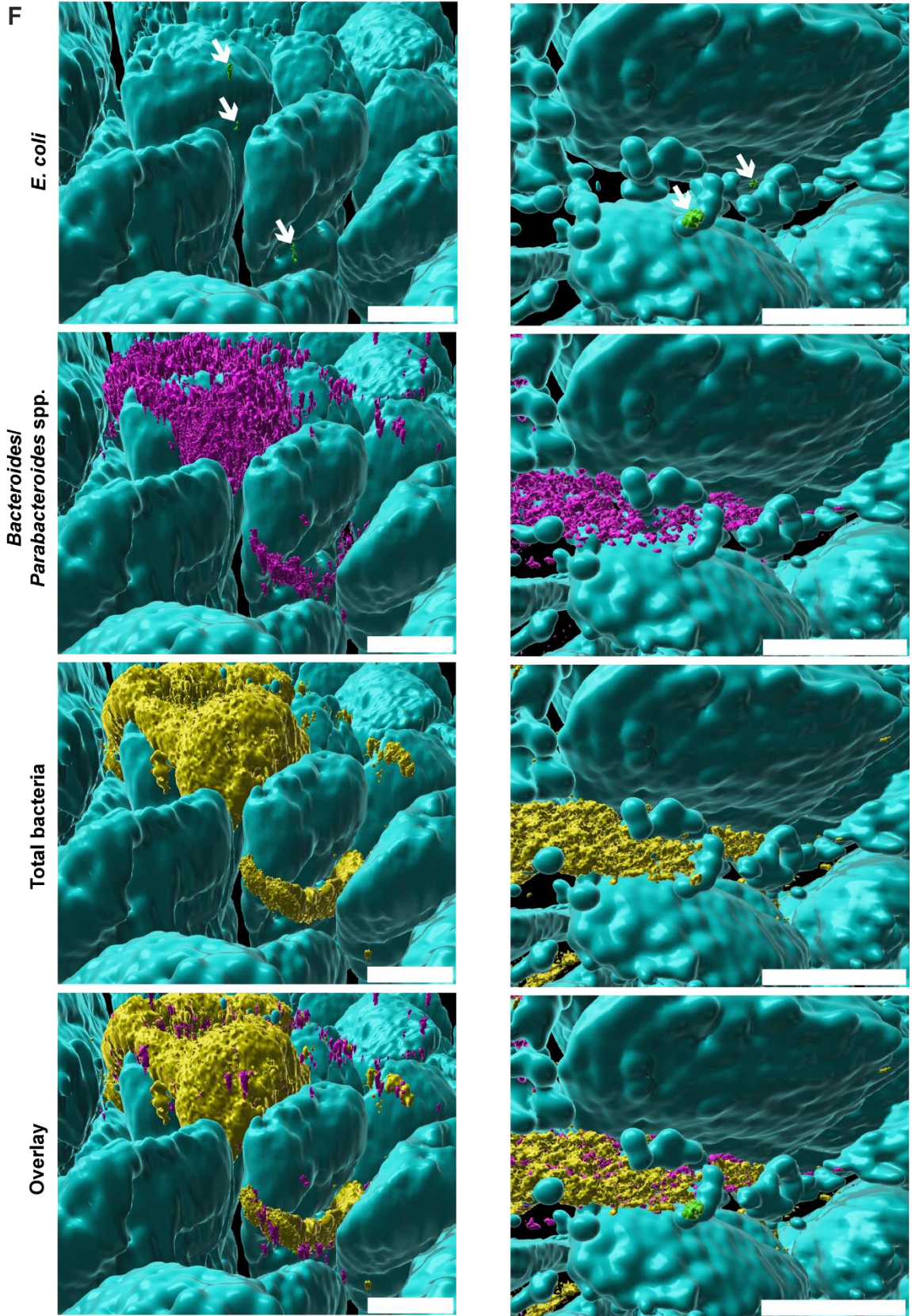


Figure 4. 8. Imaging of mucosal bacteria detected in MAL+EC&BAC day 28 mouse. (A) Low-magnification tile scan showing the two locations where 3D CLARITY images were acquired. Scale bar = 1 mm. (B and C) CLARITY images showing DAPI staining of epithelium/mammalian nuclei (cyan) and HCR v3.0 staining of total bacteria (yellow). Scale bar = 200 μm . (D and E) The same data as shown in B and C but now displaying only total bacterial staining. (F) Mucosal bacterial communities shown in panels B-E at greater magnification to better visualize the abundant *Bacteroides/Parabacteroides* spp. (magenta) and sparse *E. coli* (green, marked with white arrows) cells. Scale bars = 100 μm .



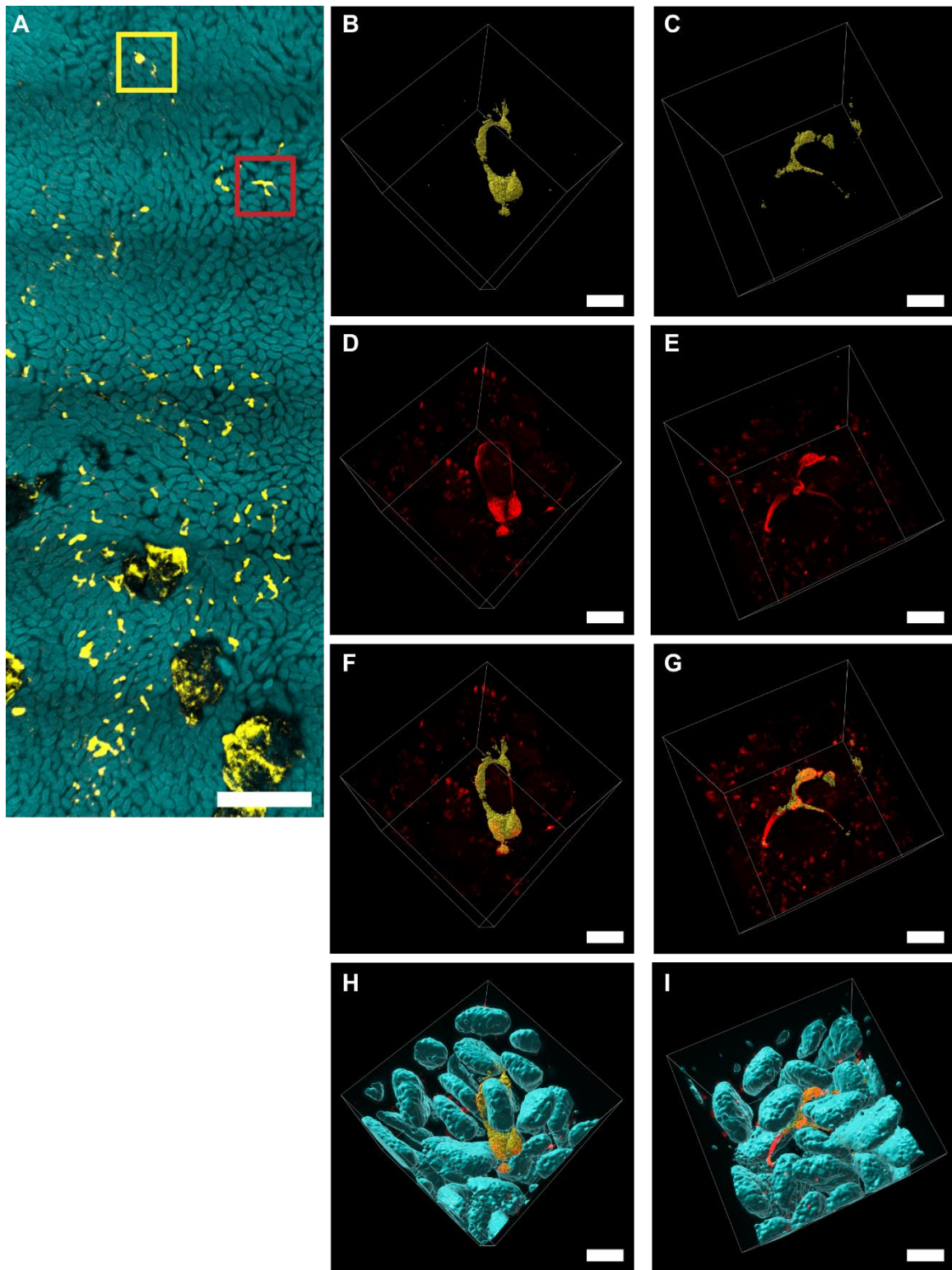


Figure 4.5. Imaging of mucus and mucosal bacteria detected in MAL+EC&BAC day 28 mouse. (A) Low magnification tile scan showing the two locations where the 3D CLARITY images were acquired. Scale bar = 1 mm. (B - I) CLARITY images showing (B and C) total bacteria (yellow), (D and E) WGA staining (red) for

mucus, (F and G) overlay between total bacterial and WGA staining, and (H and I) additional overlay with DAPI staining for epithelium / mammalian nuclei (blue). Scale bars = 100 μ m.

Epithelial cells and mucus are well-represented in large surface aggregates

We hypothesized that the observed large surface aggregates may represent host response to bacterial expansion in the digesta and colonization of the mucosa, so next we characterized the host components of these aggregates. Possibly, the observed aggregation was involved the maintenance of gut homeostasis because MAL+EC&BAC treatment did not substantially alter tissue inflammation (Fig.4.1, D-E) although it led to *E. coli* and *Bacteroides/Parabacteroides* spp. expansion in the jejunum digesta (Fig.4.3, B-D), bacterial retention after a 1 h fast (Fig.4.6, Fig.4.S6, Fig.4.S7), and detectable mucosal colonization (Fig.4.8). Previous studies suggested that secretory immunoglobulin A (sIgA)⁴⁴, mucus⁵¹ and even dietary polymers⁴⁵ play a role in aggregation, however, *in vivo* 3D spatial structure of the hypothesized aggregates remains unknown. The large surface aggregates detected in two MAL+EC&BAC mice, one in the pilot study and one on day 31 of the main experiment, were particularly intriguing because in these aggregates bacteria were surrounded by abundant free host nuclei not part of the epithelium (Fig.4.4B, Fig.4.5A, Fig.4.6B, Fig.4.7D), suggesting that host cells may have also played a role in aggregate formation or that they were subjected to aggregation. To visualize the composition of these aggregates, the MAL+EC&BAC day 31 sample was divided into three smaller pieces for counter-staining with WGA lectin and antibodies to stain for four targets. To visualize host secretion possibly involved in the formation of these aggregates, we stained all pieces with WGA lectin for mucus (Fig.4.10, D-F) and one piece with anti-IgA antibody for sIgA (Fig.4.10B). Furthermore, to identify host cells present in these aggregates, we targeted epithelial cells with anti-EpCAM antibody (Fig.4.10A) and neutrophils and anti-Ly6G antibody (Fig.4.10C); we reasoned that the source of free host cells may be either previously reported villus blunting in response to EC&BAC gavage¹⁹ or intraluminal neutrophil cast formation in response to *Enterobacteriaceae* overgrowth following acute *Toxoplasma gondii* infection¹⁸. WGA staining identified that mucus¹⁸ was abundant in the aggregates (Fig.4.10, D-F) and localized to the center (Fig.4.10 G-I, Fig.4.11), whereas free host nuclei partitioned

to the outer shell (Fig.4.10 G-I, Fig.4.11). Anti-EpCAM staining localized to the villi (which served as an internal positive control) and to free host nuclei (Fig.4.10J), concluding that anti-EpCAM staining was successful and that epithelial cells were abundant in the aggregates. Anti-IgA staining also localized to the aggregates (Fig.4.10K), whereas anti-Ly6G staining was weak (Fig.4.10L), suggesting that secretory IgA but not neutrophils were present in the aggregates. However, anti-IgA and anti-Ly6G staining remains inconclusive because the test samples lacked internal positive controls for these antibodies. Furthermore, non-specific anti-IgA signal was detected on the surface of the hydrogel (Fig.4.10K), further suggesting that anti-IgA signal may have been false positive. Therefore, counterstaining with WGA lectin and antibodies suggested that mucus and epithelial cells were present in our detected large surface aggregates and that they preferentially partitioned to the core and to the shell, respectively.

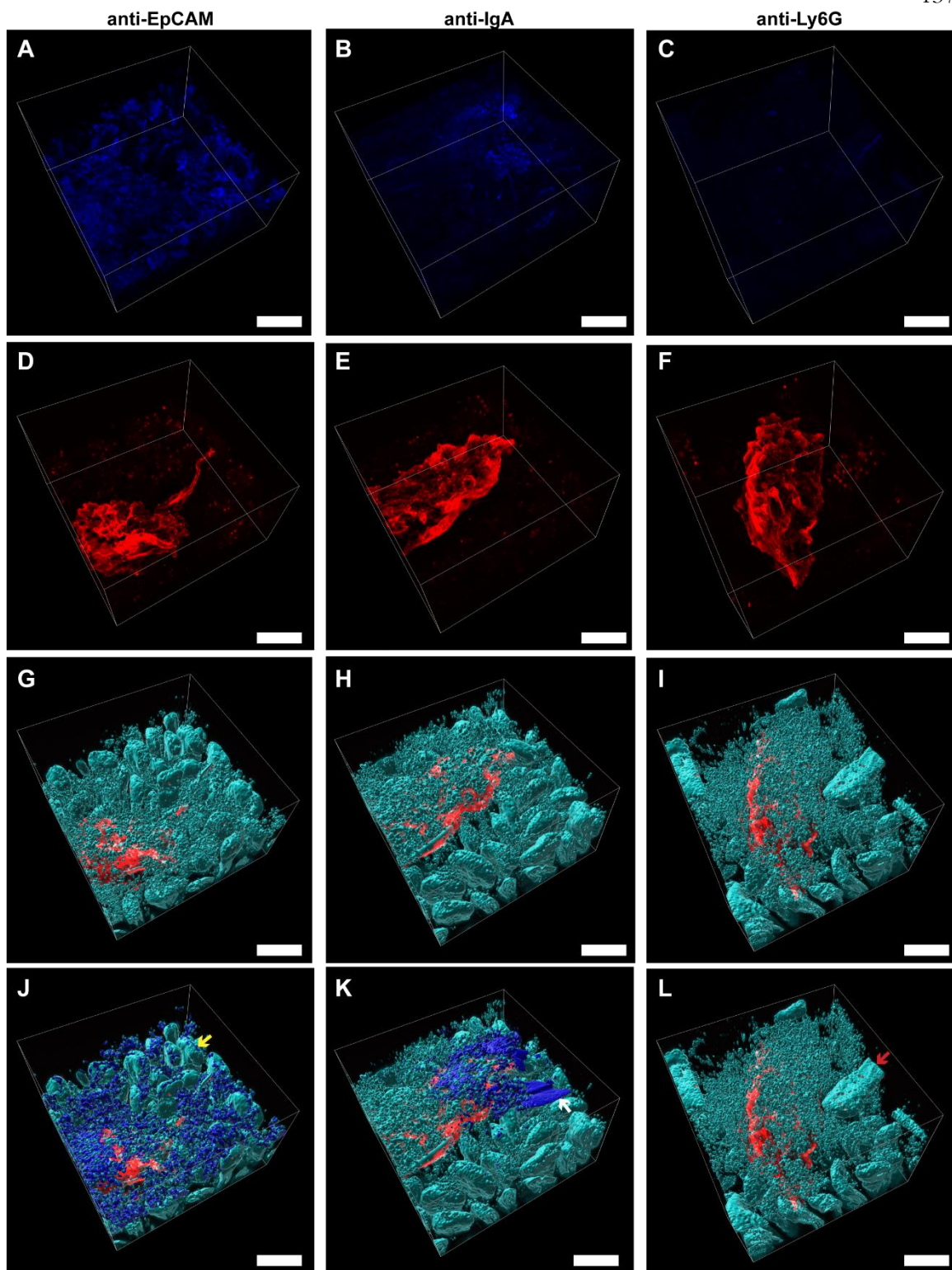


Figure 4. 10. Visualization of host components in large surface aggregates detected in MAL+EC&BAC day 31 mouse. The sample was divided into three smaller pieces and subjected to staining with three different antibodies (blue), WGA for mucus (red), and DAPI for DNA (cyan). (A-C) Antibody staining with various

antibodies: (A) anti-EpCAM for epithelial cells, (B) anti-IgA for secretory IgA, and (C) anti-Ly6G for neutrophils. All samples were stained with 1 $\mu\text{g}/\text{mL}$ antibody for three days, imaged, and displayed under identical settings. (D-F) WGA staining for mucus of the same samples. (G-I) Overlay of DAPI surfaces segmented in Imaris and WGA fluorescence signal. (J-L) Overlay of DAPI and antibody surfaces segmented in Imaris and WGA fluorescence signal. Anti-EpCAM antibody recognized the tip of villi, serving as an internal positive control (yellow arrow). Anti-IgA showed staining of the surface of the hydrogel, suggestive of false positive signal (white arrow). Both free cells and dislodged villi (red arrow) can be seen on the epithelium. Scale bar = 200 μm .

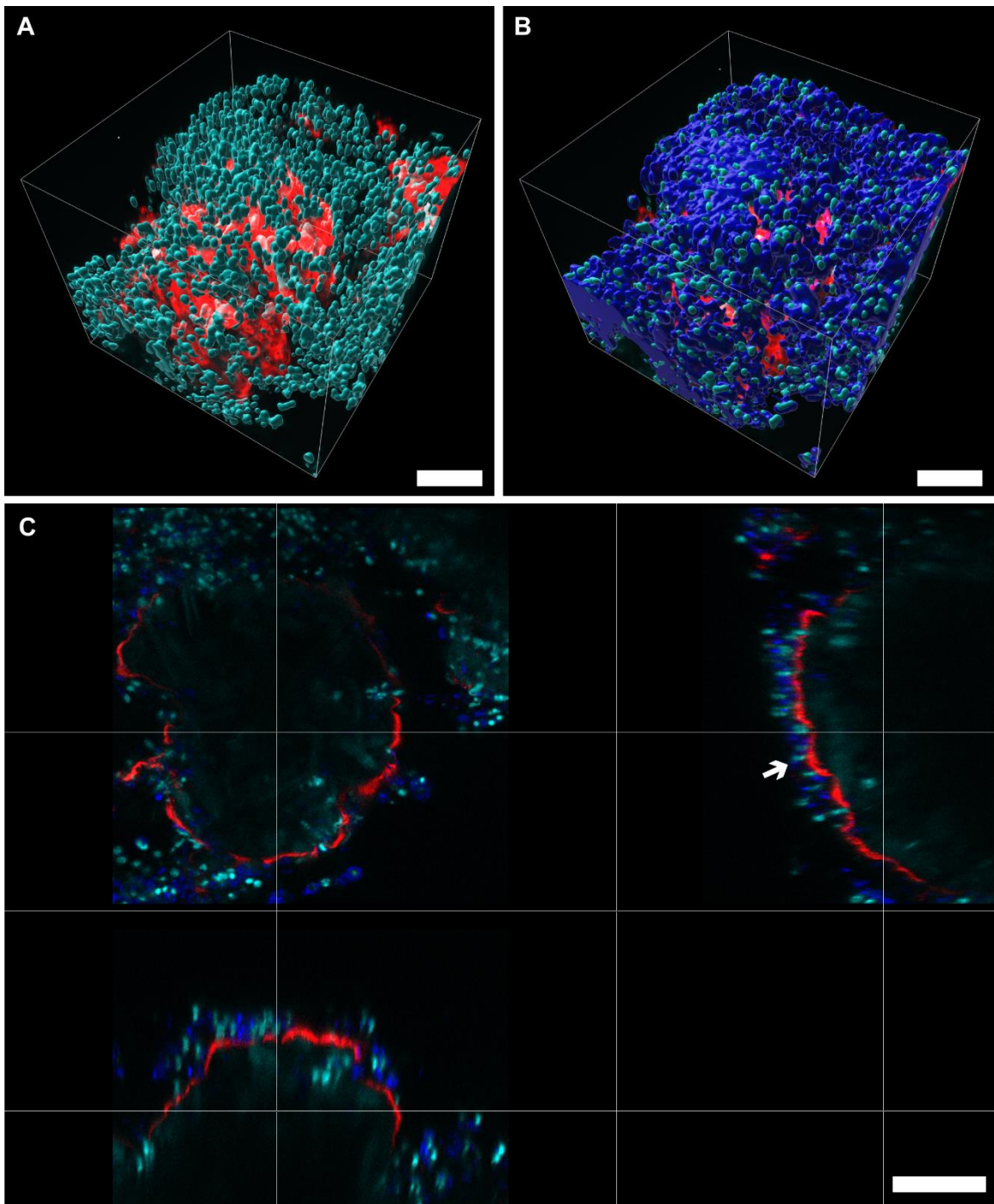


Figure 4. 11. Cross-sectional view of large surface aggregates detected in MAL+EC&BAC day 31 mouse. (A) Overlay of DAPI surfaces (cyan) segmented in Imaris and WGA fluorescence signal (red). (B) Overlay of DAPI and anti-EpCAM surfaces (blue) segmented in Imaris and WGA fluorescence signal. (C) Cross-sectional view of the aggregate across three perpendicular planes. White arrow points to the epithelial cells surrounding the mucus core. The core appears dimmer because large surface aggregates remained opaque during clearing. Scale bar = 100 μm .

Discussion

In this work, we uncovered a chain of dependencies in the surprising *Enterobacteriaceae* and *Bacteroidaceae* association in the SI: *Bacteroides/Parabacteroides* spp. only required malnutrition to increase in the SI, whereas *E. coli* required both malnutrition and co-gavage with *Bacteroides/Parabacteroides* spp. Thus, our results suggested that *Bacteroides/Parabacteroides* spp. expansion in the SI led to *E. coli* expansion. In this particular study, *Bacteroides/Parabacteroides* spp. required the weakening of the host by malnutrition; more broadly, the weakening of the SI by other factors may also promote the growth of *Bacteroidaceae*, which, in turn, may promote the growth of *Enterobacteriaceae*. Various mechanisms maintain host-microbe homeostasis in the SI, such as intestinal motility, oxygen, and secretions of digestive enzymes, bile, mucus, antibodies, and antimicrobials^{20,23,24,31}, and the dysfunction in these mechanisms has been linked to SIBO²⁰; therefore, our findings may be generalizable to SIBO.

Previously, induction of EE phenotype in mice required malnutrition and co-gavage with both *Bacteroides/Parabacteroides* spp. and *E. coli*¹⁹. Although EE phenotype was not reproduced in this study, our findings are complementary and suggest that, in the previous study¹⁹, *Bacteroides/Parabacteroides* spp. expansion in the malnourished SI led to *E. coli* expansion, and that this *E. coli* expansion may have led to EE. Similarly, in humans, colonization of the SI by *Bacteroides/Parabacteroides* spp. may act as a carrier of other disease-promoting species. Several factors may explain poor reproduction of EE phenotype, such as different stress levels experienced by the mice during the gavage, shifts in resident microbiota composition, or even shifts in the phenotype of the gavaged bacteria. Identical human gut bacterial isolates were used in this study as previously reported¹⁹, however, their phenotype may have shifted during rounds of culture in rich medium. In this study, the number of passages was minimized and kept constant across experiments, however, other than rich medium formulations may be required to retain bacterial phenotype. In future studies, more virulent *E. coli* and *Bacteroides/Parabacteroides* spp. isolates could be used to study how bacterial phenotype affects mouse phenotype.

The dependency of *E. coli* on *Bacteroides/Parabacteroides* spp. may rely on modulation of the immune system^{12,36}, metabolic coupling^{10,35}, or adherence to the mucosa^{4,37}. In this work, we evaluated the plausibility of the latter two mechanisms by 3D imaging of empty SI segments, i.e. segments that do not contain digesta. We reasoned that metabolic coupling would be more likely to arise in the empty segments than in the digesta because only complex nutrients inaccessible to *E. coli*, e.g. mucus, may be available in the empty segments. In contrast, both complex and simple nutrients released by host digestion are abundant in the digesta, and previous work suggested that microbial metabolism in the SI digesta is dominated by fast uptake of simple carbohydrates⁵². Therefore, consistent with metabolic modeling of *Enterobacteriaceae* – *Bacteroidaceae* interactions¹⁰, we predicted that *Enterobacteriaceae* would rely on the *Bacteroidaceae*'s ability to forage on mucus⁴⁹ in the empty but not full segments. Furthermore, we reasoned that species with fitness to adhere to the intestinal mucosa would be retained in the empty segments, and that *Enterobacteriaceae* may rely on *Bacteroidaceae*'s ability to bind intestinal mucus³⁷. Our hypotheses were supported: after a 1 h fast, large surface bacterial aggregates were not detected in malnourished mice not exposed to bacteria, but were most prevalent in malnourished mice challenged with the full EC&BAC bacterial cocktail. Both mucosal adhesion and continued growth, with or without metabolic coupling, may have contributed to the observed increase in bacterial biomass on the mucosal surface.

3D imaging of the mucosa with taxonomic resolution did not reject our hypotheses. In one MAL+EC&BAC mouse, for instance, we detected an abundant mucosal bacterial community well-represented by *Bacteroidales*, i.e. the order of *Bacteroides/Parabacteroides* spp., and these mucosal bacteria co-localized with WGA staining for N-acetylglucosamine, which is abundant in mucus^{22,50}. Furthermore, sparse *E. coli* cells associated with abundant *Bacteroidales* in the mucosa. The detection of these events supported the possibility that *Bacteroides/Parabacteroides* spp. colonized the mucosa by adhering to and foraging on mucus, and that *E. coli* benefited. Our observations are in agreement with *E. coli* – *B. fragilis* interactions in the colon, where more mucosa-adherent *E. coli* were detected in the colon of co-colonized than monocolonized mice⁴. Furthermore, in the same study, *B. fragilis* was

shown to decrease mucus thickness *in vitro*. Additionally, the metabolic modeling of *Enterobacteriaceae* – *Bacteroidaceae* interactions predicted that *Bacteroidaceae* depended on oxygen depletion by *Enterobacteriaceae* in a microaerophilic environment¹⁰. Imaging only detected sparse *E. coli* cells in the mucosal bacterial community, questioning whether *E. coli* was responsible for oxygen detoxification. However, resident facultative anaerobes may have been present to protect *Bacteroides/Parabacteroides* spp. from oxygen stress. Therefore, our work suggested that mucus may mediate *Enterobacteriaceae* – *Bacteroidaceae* interactions not only in the colon⁴, but also in the empty SI, and did not exclude the possibility that oxygen consumption by facultative anaerobes is required for colonization of the SI mucosa by *Bacteroides/Parabacteroides* spp.¹⁰.

In this study, our 3D imaging technology of host-microbe interface enabled us to scan large areas of intestinal mucosa, detect rare events, and visualize them in 3D. For the first time, we present 3D images of several SI phenomena that, despite of being known or hypothesized, have not been previously captured in 3D *in vivo* with simultaneous visualization of both the microbe and the host. For example, bacterial aggregation by IgA⁴⁴ or mucus⁵¹ is thought to be an important mechanism of maintaining host-microbe homeostasis, however, the 3D structure of bacterial aggregation remains unknown. Our imaging technology detected aggregates that contained not only abundant mucus but also epithelial cells; furthermore, these aggregates appeared structured, with bacteria and mucus partitioning to the core and epithelial cells – to the outer shell. Thus, our 3D imaging technology motivates future studies into the phenomenon of aggregation in the SI and provides tools for these explorations. Furthermore, while the spatial structure of host-microbe mucosal interface in the large intestine has been extensively studied, this interface in the SI remains poorly understood. For example, 3D imaging has already captured bacteria in cecal crypts [Chapter 2] and proximal colon folds [Chapter 3], whereas 2D imaging has established that bacteria associate closely with epithelium in proximal colon, but are segregated by a dense mucus layer in the distal colon^{14,22,53}. In the SI, mucosal surface is not protected by a dense mucus layer⁵⁴ and is more exposed, however, mucosal immunity, digestive secretion, and intestinal transit effectively protect the host from

bacterial colonization of the mucosa^{20,23,24}. We hypothesized that the likelihood of this rare bacterial colonization of SI mucosa would increase in a host weakened by malnutrition and challenged with the synergistic *E. coli* and *Bacteroides/Parabacteroides* spp. community. For the first time, we present 3D images of a dense bacterial community colonizing the intervillus space of mid SI, penetrating deep in between and wrapping around the villi and associating with loose secreted mucus. Protrusions of villi and microvilli increase the surface area of the SI, therefore, bacterial colonization of the intervillus space also increases the contact area between bacteria and the host. Because this contact area is not protected by a dense continuous mucus layer⁵⁴, which may be further degraded by mucosal colonizers, host uptake of microbial metabolites would be enhanced, and direct contact interactions would be possible. Therefore, our documented dense bacterial colonization of the SI mucosa likely has significant impact on the host.

Materials and Methods

Mice

All animal husbandry and experiments were approved by the Caltech Institutional Animal Care and Use Committee (IACUC protocol #1646). Mouse model was established following the previously published protocol¹⁹ with slight adaptations. On day 1 of the experiment, just-weaned, specific pathogen free (SPF) C57BL/6J males were received from the Jackson Laboratory (JAX) at 21 days of age. Immediately upon arrival, they were randomized across experimental conditions. For the duration of the study, the mice were housed in sterile cages with 4 – 5 mice per cage and had ad libitum access to one of the experimental diets, either complete or malnourishing. The malnourishing diet was deficient in fat and protein, but contained the same amount of calories, vitamins, and minerals on the weight basis¹⁹. Diet formulations were consistent with the previous study¹⁹ except that food dyes were omitted to reduce potential autofluorescence.

Bacterial culture for gavage

Identical clinical isolates were used as in the previous study¹⁹. Bacterial isolates of *Bacteroides dorei*, *Bacteroides ovatus*, *Bacteroides vulgatus*, *Parabacteroides distasonis*, and the two *Escherichia coli* isolates were received from Brett Finley (University of British Columbia), and *Bacteroides fragilis* was received from Emma Allen Vercoe (University of Guelph); the same isolates were used as the isolates used in the original study¹⁹. Isolate identities were confirmed by Sanger sequencing, and our obtained sequences matched complete 16S rRNA sequences of the gavaged bacterial isolates that were provided by E.A. Vercoe. All bacterial isolates were cultured anaerobically at 37 °C; single colonies were cultured on Brucella blood agar plates (A30; Hardy Diagnostics), whereas liquid cultures were grown in brain heart infusion (BHI) medium supplemented with 5 µg/mL hematin, 1 µg/mL vitamin K1 and 250 µg/mL L-cysteine (BHI-SS). To minimize the number of passages, which may result in loss of phenotype, as well as to minimize the risk of cross-contamination, bacteria were plated from frozen one-time-use stocks up to a week prior to the gavage and cultured for 1-2 days. The night before bacterial gavage, the isolates were cultured overnight (for ~14 h) from single colonies in 5 mL of BHI-SS. The next day, stationary overnight cultures were re-inoculated into fresh 5 mL of BHI-SS; the inoculum volume was such that all bacterial isolates reached mid-exponential phase (OD = 0.7–1.0 as measured in transparent 14 mL round-bottom culture tubes) within 2–2.5 h (40-50 µL for *E. coli* and 250-400 µL of *Bacteroides/Parabacteroides* spp. isolates). Exponential phase cultures were pelleted, and the pellets were resuspended in PBS. Bacterial density in PBS suspensions was estimated using our established OD – CFU correlations. Bacterial cocktails were prepared in PBS supplemented with 2.5% sodium bicarbonate at $1/7 \cdot 10^9$ cells/mL density of each clinical isolate, with net bacterial density in *E. coli* + *Bacteroides/Parabacteroides* spp. (EC+BAC) cocktail adding up to 10^9 cells/mL, in *E. coli* only cocktail (EC) – to $2/7 \cdot 10^9$ cells/mL, and in *Bacteroides/Parabacteroides* spp. only – $5/7 \cdot 10^9$ cells/mL. Bacterial cocktails were stored on ice and administered to mice within 1 h of preparation.

Oral gavage

During the third week of the experiment, on days 14, 16, and 18, experimental animals were gavaged with 100 μ L of one of the bacterial cocktails described above or the PBS control. Each time, the mice received the gavage around 1-3 pm. Malnourished mice were gavaged with one of the four possible cocktails (EC&BAC, EC, BAC, or PBS control), whereas well-nourished controls received one of the two cocktails (EC+BAC or PBS control). During the fifth week of the experiment, on days 28, 29, 30, and/or 31 (see sections below), the mice were euthanized.

Terminal sample collection for 16S rRNA gene copy analysis

Six mouse groups were considered in this study: COM+PBS, COM+EC&BAC, MAL+PBS, MAL+BAC, MAL+EC, and MAL+EC&BAC. The mouse groups were staggered across two experiments, with well-nourished controls analyzed one month later (but on the same relative days of the experiment). The mice were euthanized by intraperitoneal (IP) euthasol injection and cardiac puncture during the fifth week of the experiment, on days 28, 29, and 30, with one mouse per group per day. The only exception was the MAL+PBS group: in this group, one mouse was euthanized on day 30 and the other two mice euthanized on day 31. However, because these mice were not exposed to bacteria, we did not anticipate that microbiota composition would change substantially over the course of a few days. Fecal samples were collected from all mice immediately before euthanasia. To collect jejunum digesta, a full SI segment was identified in the upper SI (~2nd quartile of the SI). Samples were stored on ice during sample collection and were moved to -80 °C within 1 h of collection.

General protocol for sample preservation for imaging

See Chapter 3 Methods

Terminal sample collection for imaging from non-fasted mice

During the fifth week of the experiment, on days 28-31, the mice — one mouse in each MAL treatment group (MAL+PBS, MAL+BAC, MAL+EC, and MAL+EC&BAC) — were euthanized by IP euthasol injection and transcardial perfusion and empty jejunum segments identified in mid SI were preserved for imaging following the general protocol for sample preservation for imaging (Chapter 3 methods) with specifications. A4B.08P4 surface-gel-monomer mix was used to polymerize a protective surface gel. After surface gel polymerization, the samples were stored in the fridge, and hydrogel tissue embedding was performed within 3 days. A4B0P4 tissue-gel-monomer mix was used to fortify the tissue; both infusion and polymerization were performed for 3 h.

Terminal sample collection for imaging and host gene expression measurements in fasted mice

Imaging and host gene expression analysis were performed on the same mice. Only the malnourished groups were considered in this study: MAL+PBS, MAL+BAC, MAL+EC, and MAL+EC&BAC. The four mouse groups were staggered across four experiments separated by a week. The mice were euthanized by IP euthasol injection and cardiac puncture during the fifth week of the experiment, on days 28, 29, 30, and 31, with one mouse per group per day. Consistently, food was removed at 10 am and mice were euthanized at 11 am. Tissue preservation for imaging is time consuming; therefore, only a few mice can be analyzed over the course of a single day. Considering that circadian rhythms can affect microbiota⁵⁵, we decided instead to perform processing over the course of 4 days, but consistently euthanize all mice at the same time each day.

Transcardial perfusion after euthasol injection is beneficial to imaging because it removes blood from blood vessels and capillaries and reduces tissue autofluorescence. However,

mRNA transcripts in blood may contribute to the net mRNA levels in the tissues that are normally reported in literature (personal communication, Sarkis Mazmanian). Therefore, mice were euthanized by IP euthasol injection and cardiac puncture. As expected, omitting transcatheter perfusion resulted in strong autofluorescence in blood capillaries within the villi. In image analysis, this autofluorescence was excluded by only considering bacterial staining outside the villi.

After euthanasia, the GIT was dissected and the segments of interest were excised: 2nd, 3rd, and 4th quartile of the SI as well as proximal colon. 3rd quartile of the SI was subjected to tissue preservation for imaging, whereas the rest of the tissues were collected for mRNA analysis. At this point, the tissues for imaging and mRNA analysis were handled in parallel. For mRNA analysis, tissue scrapings were collected in this order: jejunum (2nd quartile of the SI), ileum (4th quartile of the SI), and proximal colon; this order was chosen because, in our experience and as previously reported⁵⁶, mRNA is least stable in jejunum tissue, followed by ileum tissue and proximal colon tissue. Tissue scrapings were transferred immediately to 600 μ L of 1x DNA/RNA Shield (R1100; Zymo) in a Lysing Matrix D tube containing 1.4 mm ceramic spheres (116913050-CF; MP Bio). During the sample-collection procedure, the samples were stored and handled on ice. At the end of the procedure, they were homogenized by bead beating (6.5 m/s for 60 s on FastPrep24 (MP Bio)) before storage at -80 °C.

In parallel, an empty SI segment in the 3rd quartile of the SI was processed for imaging. The general protocol for sample preservation for imaging was followed with specifications (see Chapter 3 methods). A4B.08P1 surface-gel-monomer mix was used to polymerize a protective surface gel. After surface gel polymerization, the tissues proceeded immediately to hydrogel tissue embedding. A1B.01P4 tissue-gel-monomer mix was used to fortify the tissue; the tissues were infused overnight for 18 h and the hydrogel tissue hybrid was polymerized for 5 h.

Bacterial peptidoglycan permeabilization with lysozyme

The day of lysozyme treatment, hydrogel-tissue hybrids were incubated in lysozyme treatment buffer (10 mM Tris HCl, pH=8.0) at RT for 1 h before treatment. Bacterial peptidoglycan layer was then permeabilized with lysozyme (90082; ThermoFisher Scientific) in 10 mM Tris HCl, pH=8.0, at 37 °C for 6 h with shaking; 5 mg/mL of lysozyme was used for A4B.08P4 / A4B0P4 hydrogels, and 1 mg/mL of lysozyme was used for A4B.08P1 / A1B.01P4 hydrogel. After treatment, the hydrogels were rinsed in PBS and then washed three times in excess of PBS over the course of one day.

SDS clearing

A4B.08P4 / A4B0P4 hydrogel-tissue hybrids. Tissues in separate tissue cassettes (22-272416; Thermo Scientific) were cleared together in a large crystalizing dish in 8% SDS (51213; Lonza) in PBS, pH 8.3, at 37 °C and with stirring. Clearing was performed for 3 days without clearing solution changes but with daily pH adjustments. After clearing, the tissues were rinsed in PBS, and then washed in the same setup in PBS at 25 °C and with stirring for 3 days with daily wash solution changes.

A4B.08P1 / A1B.01P4 hydrogel-tissue hybrids. Each piece of tissue was cleared in a separate 50 mL tube filled with 4% SDS in PBS, pH=8.5, at 37 °C and 180 rpm. The tissues were cleared for 3 days, and the clearing solution was exchanged daily. After clearing, the samples were washed for one day at 37 °C in 0.1% TritonX-100 in PBS, and then for an additional day at RT in PBS. Two washes were performed each day, with 50 mL of wash solution per sample per wash.

HCR v2.0 tagging of bacteria (pilot imaging experiment)

The general HCR v2.0 protocol was followed (Chapter 3 Methods) with modifications.

In the first hybridization, the general HCR v2.0 protocol was followed except that each hybridization wash was performed for 1 h rather than 2 h. Hydrogel-tissue hybrids were

hybridized with EUB338-B4 and GAM42a-B5. Hybridization was performed in 5 mL tubes with 5 mL of hybridization solution and with two hydrogel-tissue hybrids grouped in each tube.

In the second hybridization, the general HCR v2.0 protocol was followed except that formamide was excluded from hybridization solution. Hydrogel-tissue hybrids were hybridized with CFB560a-B2 and CFB560b-B2 probes. Hybridization was performed in 5 mL tubes with 5 mL of hybridization solution and with two hydrogel-tissue hybrids grouped in each tube.

Finally, hybridized probes were amplified following the general HCR v2.0 protocol. Specifically, they amplified with B5-AlexaFluor488, B4-AlexaFluor546, and B2-AlexaFluor647 amplifier pairs. Amplification was carried out in hybridization chambers glued to HybriSlip covers; ~1.5 mL was required to fill the chambers depending on the sample size.

Design of HCR v3.0 probes

Two HCR v3.0 probes were designed by Molecular Technologies using complete 16S rRNA sequences of the gavaged bacterial isolates, one probe specific to both *E. coli* isolates but orthogonal to *Bacteroides/Parabacteroides* spp. (Table 3.S1) and one probe specific to all five *Bacteroides/Parabacteroides* spp. but orthogonal to *E. coli* (Table 3.S1). The probes were synthesized by Molecular Technologies and provided as 1 uM stocks. Probe coverage was determined in silico. Specifically, the probes were aligned to 16S rRNA sequences in SILVA 138 NR99 database; only the sequences of the bacterial orders detected in experimental animals by sequencing were considered. Coverage was expressed as percentage of 16S rRNA sequences that aligned with the probe with zero (0MM) or one (1MM) mismatch.

HCR v3.0 tagging of bacteria (imaging of fasted mice)

The general HCR v3.0 protocol was followed [Chapter 3] with modifications (taxon-specific probe concentrations were increased from 10 to 20 nM and the buffers for tissues in whole-mount were substituted with buffers for cells in suspension (Molecular Technologies)). Hydrogel-tissue hybrids were hybridized with the degenerate universal HCR v3.0 probe set (B1 initiator, 4 nM of each degenerate probe), *Bacteroides/Parabacteroides* spp. HCR v3.0 probe (B2 initiator, 20 nM), and *E. coli* HCR v3.0 probe (B3 initiator, 20 nM). Hybridization was carried out in 5 mL tubes with 4 mL of hybridization solution and two hydrogel-tissue hybrids (one tissue from each of two mice from the same mouse group). Hybridized probes were then amplified with B1-AlexaFluor514, B2-AlexaFluor647, and B3-AlexaFluorA594 amplifier pairs. The samples were then stored in 5 µg/mL DAPI and 0.025% sodium in PBS, 5 mL per sample, until imaging.

Antibody and lectin staining

Before antibody staining, hydrogel-tissue hybrids were washed overnight at RT in 100 mM Tris-HCl, pH 8.0, to scavenge any remaining free formaldehyde that may react with antibodies. The hybrids were then blocked overnight at RT in 2% serum (100487-948; Electron Microscopy Sciences) in PBST. Prior to preparing antibody and lectin staining solutions, the stocks were centrifuged at 10,000 g and 4 °C for 10 min to pellet large aggregates. The staining solution for tissues presented in Fig.4.10 consisted of 1 µg/mL antibody conjugated to AlexaFluor546 (either anti-EpCAM (sc-53532 AF546; Santa Cruz Biotechnology), anti-IgA (sc-373823 AF546; Santa Cruz Biotechnology), or anti-Ly6G (sc-53515 AF546; Santa Cruz Biotechnology), 5 µg/mL of WGA-AlexaFluor488 (W11261; ThermoFisher Scientific), 5 µg/mL DAPI (ThermoFisher Scientific) and 2% serum in PBST. The staining solution for tissues presented in Fig. 4.9 and Fig.4.11 consisted of 1 µg/mL of antibody conjugated to AlexaFluor546 (either anti-Ly6G or anti-EpCAM, respectively), 2 µg/mL WGA-AlexaFluor488, 5 µg/mL DAPI and 2% serum in PBST; in the latter experiment, WGA concentration was reduced from 5 µg/mL to 2 µg/mL in recognition that WGA signal was strong and it overwhelmed bacterial signal. The staining was performed for

3 days at RT with gentle shaking. After staining, the samples were rinsed in PBST and then washed 3 times in PBST at RT over the course of one day.

Imaging

All imaging was performed on a Zeiss LSM880 confocal microscope.

Tile scanning with low magnification 5x objective

Entire hydrogel-tissue hybrids were tile-scanned at low magnification with a 5x objective. To mount samples for 5x tile-scanning, they were immobilized on a microscope slide with a silicone isolator (Grace Biolabs) attached to the slide as well. The isolator was filled with PBS and covered with a cover slip. The samples were tile-scanned with 10% overlap for DAPI staining of epithelium and HCR staining of bacteria. In both the pilot and final imaging experiments, 405 nm laser was used to excite DAPI, whereas 546 nm and 514 nm lasers were used to excite HCR tagging of total bacteria in the pilot and final experiments, respectively. The images were then stitched in Zen. All imaging metadata and display metadata are provided in the SI.

20x CLARITY imaging (channel mode)

Stained samples were mounted in refractive index matching solution⁵⁷ (RIMS) (600 mL of 0.02 M phosphate buffer (P5244; MilliporeSigma) + 800 g of Histodenz (CAS #66108-95-0; JINLAN Pharm-Drugs Technology Co.) supplemented with 0.01% sodium azide, pH=7.5, refractive index (RI)=1.47) and incubated overnight. To prevent RIMS dehydration during imaging, RIMS was covered with a layer of Immersion Oil Type FF (16916-04; Electron Microscopy Sciences). In both the pilot and the final experiments, four laser lines were used to image the samples in channel mode. In the pilot experiment, 405, 488, 546, and 633 nm lasers were used, whereas in the final experiment, the 488 nm laser was substituted for a 514 nm laser. Each image was composed of four fields of view imaged with 10% overlap and stitched in Zen at the end. All imaging, display, and segmentation metadata are provided in the SI.

20x CLARITY imaging (spectral mode)

Sample mounting was identical to 20x CLARITY imaging in channel mode. Four lasers were used: 405, 514, 546, and 633 nm. All four lasers were excited at the same time and the signal was collected in 8.9 nm bins. Spectral files for each fluorophore were generated by staining mouse hydrogel-tissue hybrids with a single fluorophore, mounting them in RIMS, imaging them under identical imaging settings, and selecting a region of interest (ROI) in Zen with strong but not saturated signal. All imaging, unmixing, segmentation, and display metadata are provided in the SI.

Image analysis

Images were first segmented in Imaris by creating iso-surfaces for each channel. Identical fluorescence and size thresholds were set for images acquired under identical imaging settings. Post Imaris, the obtained objects were filtered to remove false positives (i.e. objects with weak total bacterial staining), double positives (i.e. objects with strong staining for both taxa), small-size outliers, and objects inside the villi (which represent autofluorescence in blood capillaries based on visual inspection). The remaining objects were then analyzed for their abundance and spatial distribution. For samples stained and images following identical protocols, an identical image analysis procedure was followed. All segmentation metadata and scripts of post-Imaris processing are provided in the SI.

16S rRNA gene copy analysis

DNA from feces and jejunum digesta was extracted using a PowerSoil Pro kit (Qiagen) following manufacturer's instructions with specifications²⁸⁻³⁰. Total bacterial 16S rRNA gene copy load was quantified by droplet digital PCR (ddPCR) on a QX200 droplet generator (#1864002, Bio-Rad Laboratories) following our previously published protocols²⁹. *Enterobacteriaceae* 16S rRNA gene copy load was also quantified by ddPCR using *Enterobacteriaceae*-specific primers⁵⁸ following the same protocol except that annealing temperature was increased from 52 °C to 60 °C. 16S rRNA gene amplicon sequencing,

including library amplification, sequencing, and data processing, was performed following previously published protocols²⁸⁻³⁰. For each sample, fractional abundance obtained by 16S rRNA gene amplicon sequencing was anchored by the total bacterial 16S rRNA gene copy load to obtain absolute abundance.

Host mRNA analysis

After defrosting on ice, homogenized tissue samples preserved in DNA/RNA shield were immediately extracted using a Quick RNA Miniprep Plus kit (Zymo) per manufacturer's instructions. Prior to RNA extractions, a proteinase digestion step was included (60 μ L of Proteinase K digestion buffer and 30 μ L of Proteinase K were added to 600 μ L of the homogenate, and the digestion was carried out for 30 min at 55 °C). During RNA purification, an on-column DNase treatment was performed per manufacturer's instructions. Purified RNA was eluted into 50 μ l of nuclease free water (Ambion). A 1 μ l aliquot of sample was diluted 1:20 for RNA quantification and quality analysis, prior to storing samples at -80 °C. RNA quantification was performed using Qubit HS RNA kit (Q32856; Invitrogen) and RNA quality was assessed using Agilent 2200 TapeStation system with high sensitivity RNA screen tape and sample buffer reagents (Agilent). cDNA was created using a high capacity reverse transcription kit (Applied BioSystems). We added 1.8 μ g total RNA per 20 μ l reaction. Reaction setup was performed on ice per manufacturer's instructions. A Bio-Rad C1000 thermocycler was used to perform cDNA synthesis at 25 °C for 10 min, 37 °C for 120 min, 85 °C for 5 min, and 4 °C degree hold. Glyceraldehyde 3-phosphate dehydrogenase (GAPDH), tumor necrosis factor alpha (TNF- α), and interleukin 6 (IL-6) transcripts were quantified using commercially available Taqman probes (Mm99999915_g1, Mm00443258_m1, and Mm00446190_m1, respectively; Applied Biosystems) and TaqMan Fast Advanced Mastermix (4444556; Applied Biosystems). Targets were detected with the FAM channel using Bio-Rad CFX96 qPCR instrument. Thermocycler conditions: 50 °C for 2 min, 95 °C for 10 min, 40 cycles of 95 °C for 15 sec, 60 °C for 1 min. TNF-alpha and IL-6 transcript levels were normalized to the house keeping gene (GAPDH) by subtracting

housekeeping gene Cq from target gene Cq, with larger difference corresponding to lower expression.

Statistical analyses

Statistical significance was evaluated using the Kruskal-Wallis test.

References:

1. Sheu, C. C., Chang, Y. T., Lin, S. Y., Chen, Y. H. & Hsueh, P. R. Infections caused by carbapenem-resistant Enterobacteriaceae: An update on therapeutic options. *Front. Microbiol.* **10**, (2019).
2. Mukhopadhyay, I., Hansen, R., El-Omar, E. M. & Hold, G. L. IBD-what role do Proteobacteria play? *Nat. Rev. Gastroenterol. Hepatol.* **9**, 219–230 (2012).
3. Bouhnik, Y., Sophie, A. A. & Flourié, B. Bacterial populations contaminating the upper gut in patients with small intestinal bacterial overgrowth syndrome. *Am. J. Gastroenterol.* **94**, 1327–1331 (1999).
4. Dejea, C. M. *et al.* Patients with familial adenomatous polyposis harbor colonic biofilms containing tumorigenic bacteria. *Science.* **359**, 592–597 (2018).
5. Vich Vila, A. *et al.* Gut microbiota composition and functional changes in inflammatory bowel disease and irritable bowel syndrome. *Sci. Transl. Med.* **10**, eaap8914 (2018).
6. Swidsinski, A., Weber, J., Loening-Baucke, V., Hale, L. P. & Lochs, H. Spatial organization and composition of the mucosal flora in patients with inflammatory bowel disease. *J. Clin. Microbiol.* **43**, 3380–3389 (2005).
7. He, G. *et al.* Noninvasive measurement of anatomic structure and intraluminal oxygenation in the gastrointestinal tract of living mice with spatial and spectral EPR imaging. *Proc. Natl. Acad. Sci. U. S. A.* **96**, 4586–4591 (1999).
8. DiBaise, J. K. Nutritional consequences of intestinal bacterial overgrowth. *Pract. Gastroenterol.* 15–28 (2008).
9. Bowler, P. G., Duerden, B. I. & Armstrong, D. G. Wound microbiology and associated approaches to wound management. *Clin. Microbiol. Rev.* **14**, 244–269 (2001).
10. Khazaei, T. *et al.* Metabolic bi-stability and hysteresis in a model microbiome community. *Sci. Adv.* 1–20 (2020).
11. Gabig, T. G., Bearman, S. I. & Babior, B. M. Effects of oxygen tension and pH on the respiratory burst of human neutrophils. *Blood* **53**, 1133–1139 (1979).
12. Rotstein, O. D. *et al.* A soluble Bacteroides by-product impairs phagocytic killing of Escherichia coli by neutrophils. *Infect. Immun.* **57**, 745–753 (1989).
13. Welch, J. L. M., Rossetti, B. J., Rieken, C. W., Dewhirst, F. E. & Borisy, G. G. Biogeography of a human oral microbiome at the micron scale. *Proc. Natl. Acad. Sci. U. S. A.* **113**, E791–E800 (2016).
14. Hansson, G. C. & Johansson, M. E. V. The inner of the two Muc2 mucin-dependent mucus layers in colon is devoid of bacteria. *Gut Microbes* **1**, 51–54 (2010).
15. Johansson, M. E. V. *et al.* Bacteria penetrate the normally impenetrable inner colon mucus layer in both murine colitis models and patients with ulcerative colitis. *Gut* **63**, 281–291 (2014).
16. Datta, S. S., Preska Steinberg, A. & Ismagilov, R. F. Polymers in the gut compress the colonic mucus hydrogel. *Proc. Natl. Acad. Sci. U. S. A.* **113**, 7041–6 (2016).
17. Earle, K. A. *et al.* Quantitative imaging of gut microbiota spatial organization. *Cell Host Microbe* **18**, 478–488 (2015).
18. Molloy, M. J. *et al.* Intraluminal containment of commensal outgrowth in the gut during infection-induced dysbiosis. *Cell Host Microbe* **14**, 318–328 (2013).
19. Brown, E. M. *et al.* Diet and specific microbial exposure trigger features of environmental enteropathy in a novel murine model. *Nat. Commun.* **6**, 7806 (2015).
20. Bohm, M., Siwec, R. M. & Wo, J. M. Diagnosis and management of small intestinal bacterial

- overgrowth. *Nutr. Clin. Pract.* **28**, 289–99 (2013).
21. Helander, H. F. & Fändriks, L. Surface area of the digestive tract-revisited. *Scand. J. Gastroenterol.* **49**, 681–689 (2014).
 22. Johansson, M. E. V., Holmén Larsson, J. M. & Hansson, G. C. The two mucus layers of colon are organized by the MUC2 mucin, whereas the outer layer is a legislator of host-microbial interactions. *Proc. Natl. Acad. Sci. U. S. A.* **108**, 4659–4665 (2011).
 23. Bevins, C. L. & Salzman, N. H. Paneth cells, antimicrobial peptides and maintenance of intestinal homeostasis. *Nat. Rev. Microbiol.* **9**, 356–368 (2011).
 24. Peterson, D. A., McNulty, N. P., Guruge, J. L. & Gordon, J. I. IgA response to symbiotic bacteria as a mediator of gut homeostasis. *Cell Host Microbe* **2**, 328–339 (2007).
 25. Korpe, P. S. & Petri, W. A. Environmental Enteropathy: Critical implications of a poorly understood condition. *Trends Mol. Med.* **18**, 328–336 (2012).
 26. Kelly, P. *et al.* Responses of small intestinal architecture and function over time to environmental factors in a tropical population. *Am. J. Trop. Med. Hyg.* **70**, 412–419 (2004).
 27. Miller, L. S. *et al.* Ileocecal valve dysfunction in small intestinal bacterial overgrowth: A pilot study. *World J. Gastroenterol.* **18**, 6801–6808 (2012).
 28. Bogatyrev, S. R., Rolando, J. C. & Ismagilov, R. F. Self-reinoculation with fecal flora changes microbiota density and composition leading to an altered bile-acid profile in the mouse small intestine. *Microbiome* **8**, 1–22 (2020).
 29. Barlow, J. T., Bogatyrev, S. R. & Ismagilov, R. F. A quantitative sequencing framework for absolute abundance measurements of mucosal and luminal microbial communities. *Nat. Commun.* **11**, (2020).
 30. Bogatyrev, S. R. & Ismagilov, R. F. Quantitative microbiome profiling in luminal and tissue samples with broad coverage and dynamic range via a single-step 16S rRNA gene DNA copy quantification and amplicon barcoding. *bioRxiv* 1–16 (2020). doi:10.1101/2020.01.22.914705
 31. Donaldson, G. P., Lee, S. M. & Mazmanian, S. K. Gut biogeography of the bacterial microbiota. *Nat. Rev. Microbiol.* **14**, 20–32 (2015).
 32. Johnson, J. S. *et al.* Evaluation of 16S rRNA gene sequencing for species and strain-level microbiome analysis. *Nat. Commun.* **10**, 1–11 (2019).
 33. Greene, S. E., Hibbing, M. E., Janetka, J., Chen, S. L. & Hultgren, S. J. Human urine decreases function and expression of type 1 pili in uropathogenic *Escherichia coli*. *MBio* **6**, e00820-15 (2015).
 34. Spaulding, C. N. *et al.* Selective depletion of uropathogenic *E. coli* from the gut by a FimH antagonist. *Nature* **546**, 528–532 (2017).
 35. Samuel, B. S. *et al.* Genomic and metabolic adaptations of *Methanobrevibacter smithii* to the human gut. *Proc. Natl. Acad. Sci. U. S. A.* **104**, 10643–10648 (2007).
 36. Vatanen, T. *et al.* Variation in microbiome LPS immunogenicity contributes to autoimmunity in humans. *Cell* **165**, 842–853 (2016).
 37. Huang, J. Y., Lee, S. M. & Mazmanian, S. K. The human commensal *Bacteroides fragilis* binds intestinal mucin Mucus. *Anaerobe* **17**, 137–141 (2011).
 38. Szarka, L. A. & Camilleri, M. Methods for the assessment of small-bowel and colonic transit. *Semin. Nucl. Med.* **42**, 113–123 (2012).
 39. Read, N. W. *et al.* Transit of a meal through the stomach, small intestine, and colon in normal subjects and its role in the pathogenesis of diarrhea. *Gastroenterology* **79**, 1276–1282 (1980).
 40. Woting, A. & Blaut, M. Small intestinal permeability and gut-transit time determined with low and high molecular weight fluorescein isothiocyanate-dextrans in C3H mice. *Nutrients* **10**, 4–10 (2018).
 41. Donaldson, G. P. *et al.* Gut microbiota utilize immunoglobulin a for mucosal colonization. *Science (80-.)*. **360**, 795–800 (2018).
 42. Schlomann, B. H., Wiles, T. J., Wall, E. S., Guillemin, K. & Parthasarathy, R. Sublethal antibiotics collapse gut bacterial populations by enhancing aggregation and expulsion. *Proc. Natl. Acad. Sci. U. S. A.* **116**, 21392–21400 (2019).
 43. Wiles, T. J. *et al.* Swimming motility of a gut bacterial symbiont promotes resistance to intestinal expulsion and enhances inflammation. *PLoS Biology* **18**, (2020).
 44. Moor, K. *et al.* High-avidity IgA protects the intestine by enchainning growing bacteria. *Nature* **544**, 498–502 (2017).
 45. Preska Steinberg, A. *et al.* High-molecular-weight polymers from dietary fiber drive aggregation of

- particulates in the murine small intestine. *Elife* **8**, 1–33 (2019).
46. Cremer, J. *et al.* Effect of flow and peristaltic mixing on bacterial growth in a gut-like channel. *Proc. Natl. Acad. Sci. U. S. A.* **113**, 11414–11419 (2016).
 47. Welch, J. L. M., Hasegawa, Y., McNulty, N. P., Gordon, J. I. & Borisy, G. G. Spatial organization of a model 15-member human gut microbiota established in gnotobiotic mice. *Proc. Natl. Acad. Sci. U. S. A.* **114**, E9105–E9114 (2017).
 48. Choi, H. M. T. *et al.* Third-generation in situ hybridization chain reaction: Multiplexed, quantitative, sensitive, versatile, robust. *Dev.* **145**, 1–10 (2018).
 49. Bjursell, M. K., Martens, E. C. & Gordon, J. I. Functional genomic and metabolic studies of the adaptations of a prominent adult human gut symbiont, *Bacteroides thetaiotaomicron*, to the suckling period. *J. Biol. Chem.* **281**, 36269–36279 (2006).
 50. Holmén Larsson, J. M., Thomsson, K. A., Rodríguez-Piñeiro, A. M., Karlsson, H. & Hansson, G. C. Studies of mucus in mouse stomach, small intestine, and colon. III. Gastrointestinal Muc5ac and Muc2 mucin O-glycan patterns reveal a regiospecific distribution. *Am. J. Physiol. Gastrointest. Liver Physiol.* **305**, G357–63 (2013).
 51. MacKenzie, D. A. *et al.* Strain-specific diversity of mucus-binding proteins in the adhesion and aggregation properties of *Lactobacillus reuteri*. *Microbiology* **156**, 3368–3378 (2010).
 52. Zoetendal, E. G. *et al.* The human small intestinal microbiota is driven by rapid uptake and conversion of simple carbohydrates. *ISME J.* **6**, 1415–1426 (2012).
 53. Kamphuis, J. B. J., Mercier-Bonin, M., Eutamène, H. & Theodorou, V. Mucus organisation is shaped by colonic content; A new view. *Sci. Rep.* **7**, 1–13 (2017).
 54. Atuma, C., Strugala, V., Allen, A. & Holm, L. The adherent gastrointestinal mucus gel layer: Thickness and physical state in vivo. *Am. J. Physiol. Liver Physiol.* **280**, G922–G929 (2001).
 55. Leone, V. *et al.* Effects of diurnal variation of gut microbes and high-fat feeding on host circadian clock function and metabolism. *Cell Host Microbe* **17**, 681–689 (2015).
 56. Fleige, S. & Pfaffl, M. W. RNA integrity and the effect on the real-time qRT-PCR performance. *Mol. Aspects Med.* **27**, 126–139 (2006).
 57. Yang, B. *et al.* Single-cell phenotyping within transparent intact tissue through whole-body clearing. *Cell* **158**, 945–958 (2014).
 58. Castillo, M. *et al.* Quantification of total bacteria, enterobacteria and lactobacilli populations in pig digesta by real-time PCR. *Vet. Microbiol.* **114**, 165–170 (2006).

Supplementary Information

Contributions

- Roberta Pocevičiute (R.P.) designed the study, performed all experiments (except as specified below), collected data (except as specified below), analyzed the data, made plots and wrote the manuscript.
- Said Bogatyrev (S.B.) and R.P. planned the tail-cup study; S.B. designed the tail-cups and monitored animals during tail-cup intervention. S.B. assisted R.P. in sample collection for bulk analyses (not imaging).
- Anna Romano (A.R.) and R.P. optimized host gene expression quantification and extracted RNA from mouse tissue scrapings. A.R. quantified mRNA in the extracts. A.R. also contributed to DNA extraction from and 16S rRNA quantification in fecal and digesta samples.
- Jacob Barlow (J.B.) and A.R. prepared 16S rRNA sequencing libraries.
- Amanda Hazel Dilmore (A.H.D.) extracted DNA from fecal and digesta samples and quantified 16S rRNA targets in the DNA extracts. A.H.D. optimized protein extraction from fecal samples and ran preliminary lipocalin-2 measurements in feces by ELISA.
- Octavio Mondragon-Palomino (O.M.P.) and R.P. performed preliminary imaging and sequencing experiments.

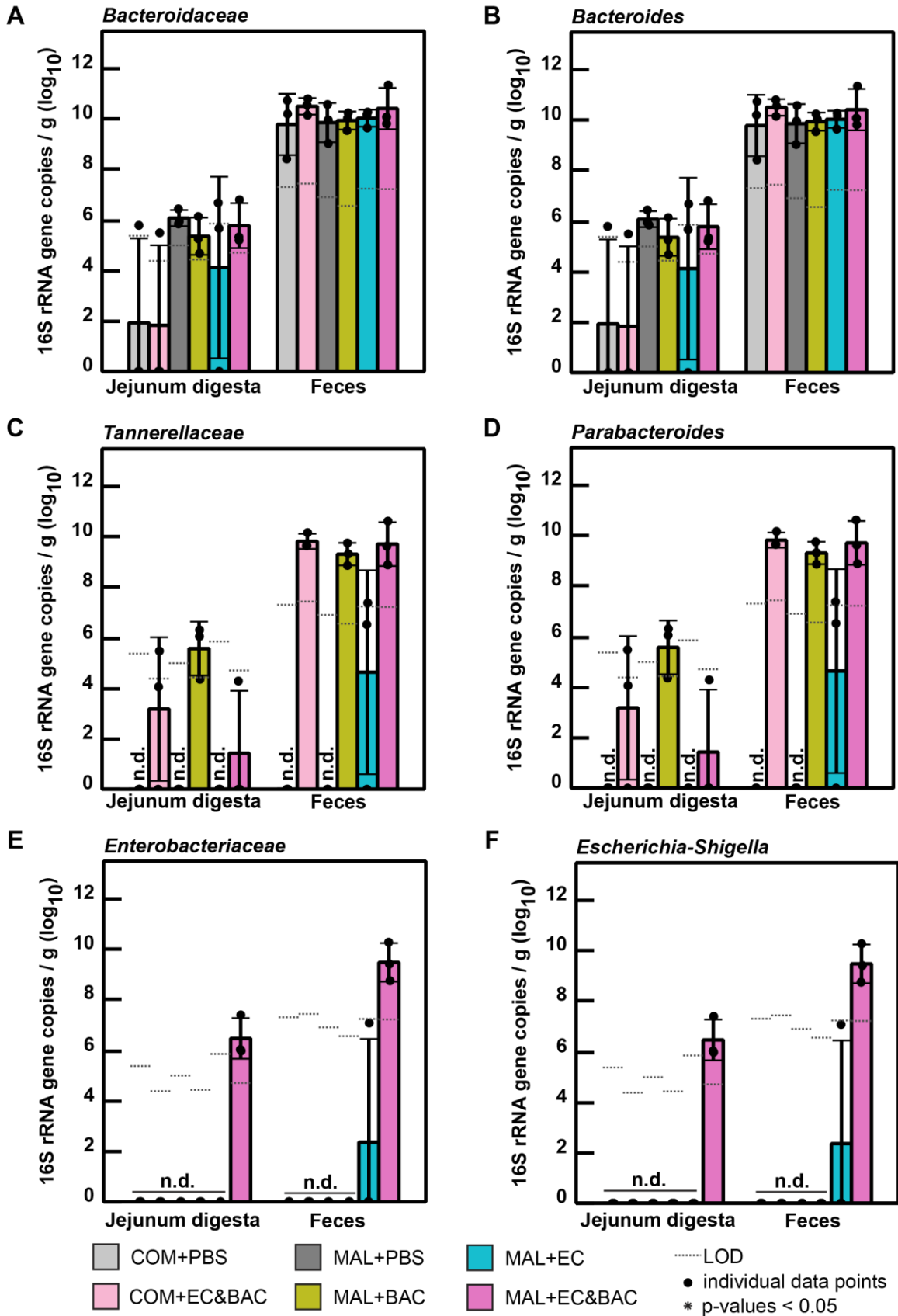


Figure 4. S1. Absolute quantification of 16S rRNA gene copies of three key families that are solely represented by a single genus. (A) *Bacteroidaceae* family, (B) *Bacteroides* genus, (C) *Tannerellaceae* family, (D) *Parabacteroides* genus, (E) *Enterobacteriaceae* family, and (F) *Escherichia-Shigella* genus. Each animal group contained 3 mice euthanized over the course of 3 consecutive days (28, 29, and 30), one mouse per group per day. COM: complete, well-nourishing diet. MAL: malnourishing diet low in protein and fat, but containing the same amount of calories, vitamins, and minerals on the mass basis. PBS: no bacteria gavage control. BAC: gavage with five *Bacteroides/Parabacteroides* spp. isolates. EC: gavage with two *E. coli* isolates. EC&BAC: gavage with all seven bacterial isolates. LOD: limit of detection expressed as group average. Statistical significance was evaluated using Kruskal-Wallis test.

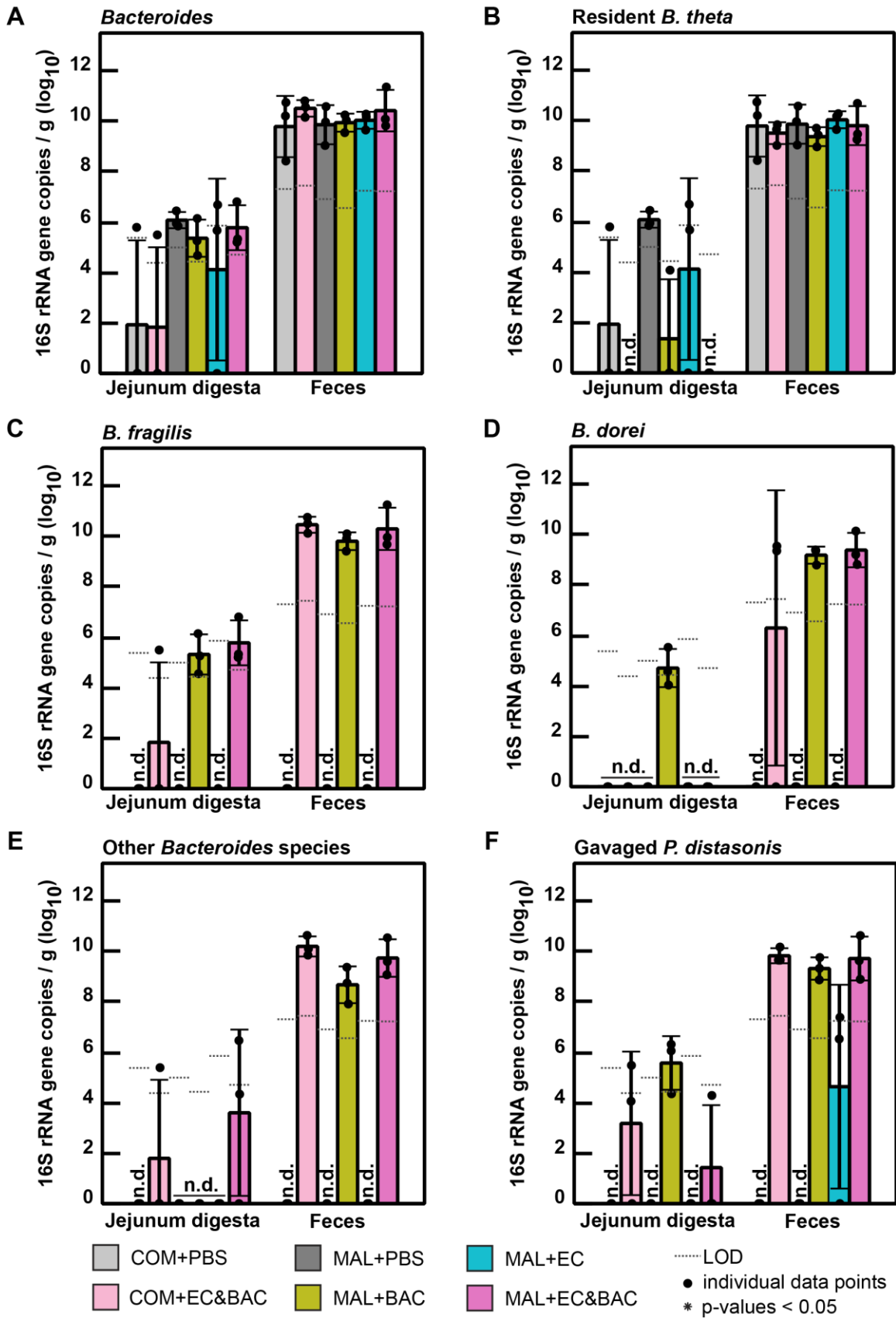


Figure 4. S2. Absolute quantification of 16S rRNA gene copies of *Bacteroides* and *Parabacteroides* genera in jejunum digesta and feces. (A) *Bacteroides* genus, (B) resident *B. theta* species, (C) gavaged *B. fragilis*, (D) gavaged *B. dorei*, (E) other gavaged *Bacteroides* (*B. ovatus* and *B. vulgatus*) that are grouped into the same feature in sequencing analysis, (F) gavaged *P. distasonis*. Each animal group contained 3 mice euthanized over the course of 3 consecutive days (28, 29, and 30), one mouse per group per day. COM: complete, well-nourishing diet. MAL: malnourishing diet low in protein and fat, but containing the same amount of calories, vitamins, and minerals on the mass basis. PBS: no bacteria gavage control. BAC: gavage with five *Bacteroides/Parabacteroides* spp. isolates. EC: gavage with two *E. coli* isolates. EC&BAC: gavage with all seven bacterial isolates. LOD: limit of detection expressed as group average. Statistical significance was evaluated using Kruskal-Wallis test.

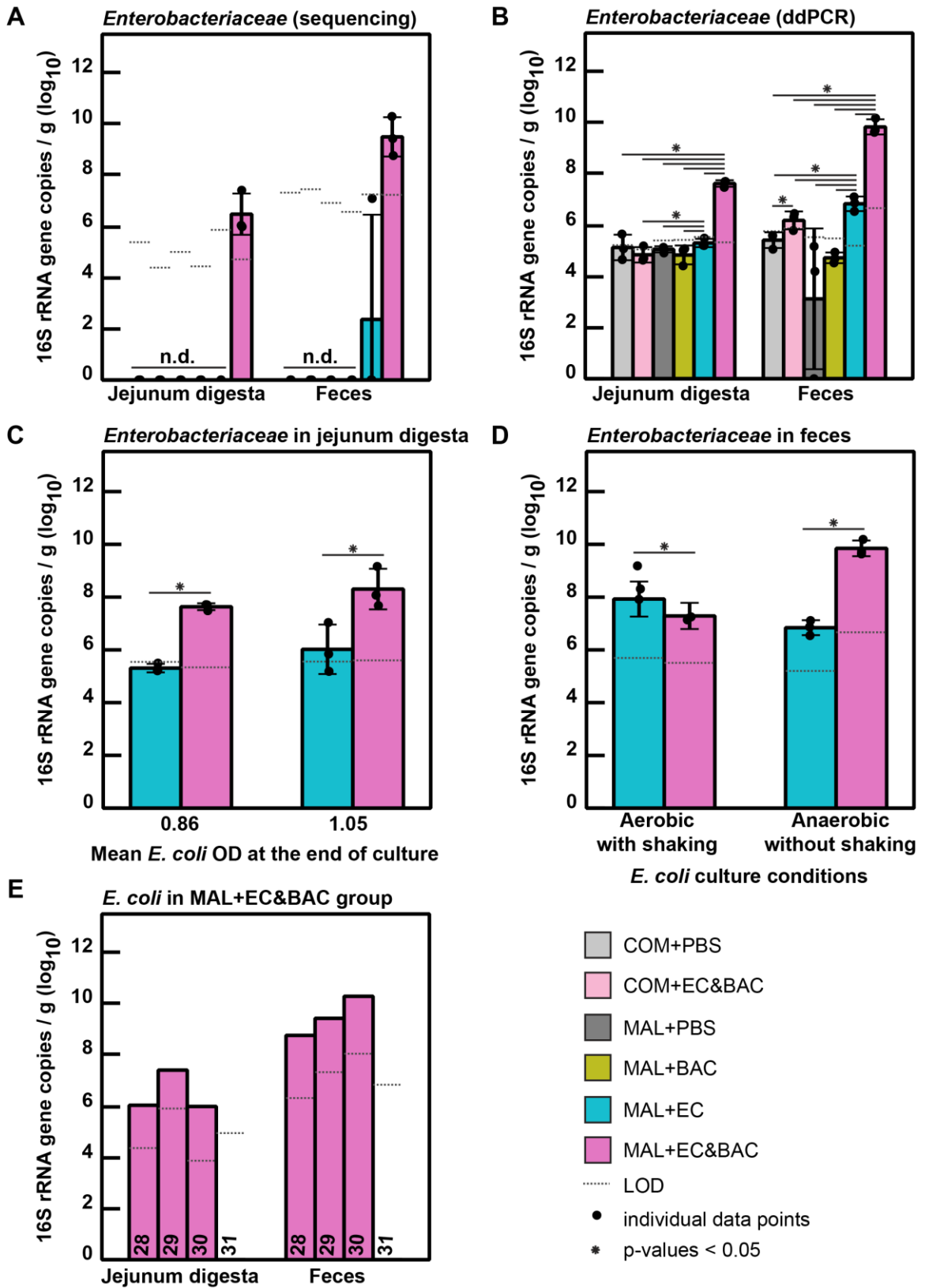


Figure 4. S3. Absolute quantification of *Enterobacteriaceae* in mouse GIT by different methods and across experiments as well as mice. (A) *Enterobacteriaceae* 16S rRNA quantification in jejunum digesta and feces by sequencing and anchoring to the total 16S rRNA gene copy load in the same experiment as shown in Fig.4.2 and Fig.4.3. (B) *Enterobacteriaceae* 16S rRNA gene copy quantification in jejunum digesta and feces by ddPCR in the same experiment as shown in panel (A) and Fig.4.2 and Fig.4.3. In panels (A) and (B), each animal group contained 3 mice euthanized over the course of 3 consecutive days (28, 29, and 30), one mouse per group per day. (C) *Enterobacteriaceae* 16S rRNA gene copy quantification by ddPCR in jejunum digesta in the experiment presented in panels (A-B) (left) and in an independent experiment performed more than a year apart (right) showing that the effect is reproduced despite variability of *E. coli* optical density (OD) at the end of culture. In both experiments, *E. coli* were cultured anaerobically without shaking. (D) *Enterobacteriaceae* 16S rRNA quantification by ddPCR in feces in the experiment shown in panels (A-B) (right) and in an experiment where *E. coli* were cultured aerobically with shaking (left), suggesting that aerobic culture with shaking does not reproduce the observed effect. (E) The same data as shown in panel (A) but now showing *Enterobacteriaceae* 16S rRNA gene copy quantification across individual mice in the MAL+EC&BAC group only, with one mouse euthanized per day. *Enterobacteriaceae* loads were stable on days 28-30 but undetectable by sequencing on Day 31. COM: complete, well-nourishing diet. MAL: malnourishing diet low in protein and fat, but containing the same amount of calories, vitamins, and minerals on the mass basis. PBS: no bacteria gavage control. BAC: gavage with five *Bacteroides/Parabacteroides* spp. isolates. EC: gavage with two *E. coli* isolates. EC&BAC: gavage with all seven bacterial isolates. LOD: limit of detection expressed as group average. Statistical significance was evaluated using Kruskal-Wallis test.

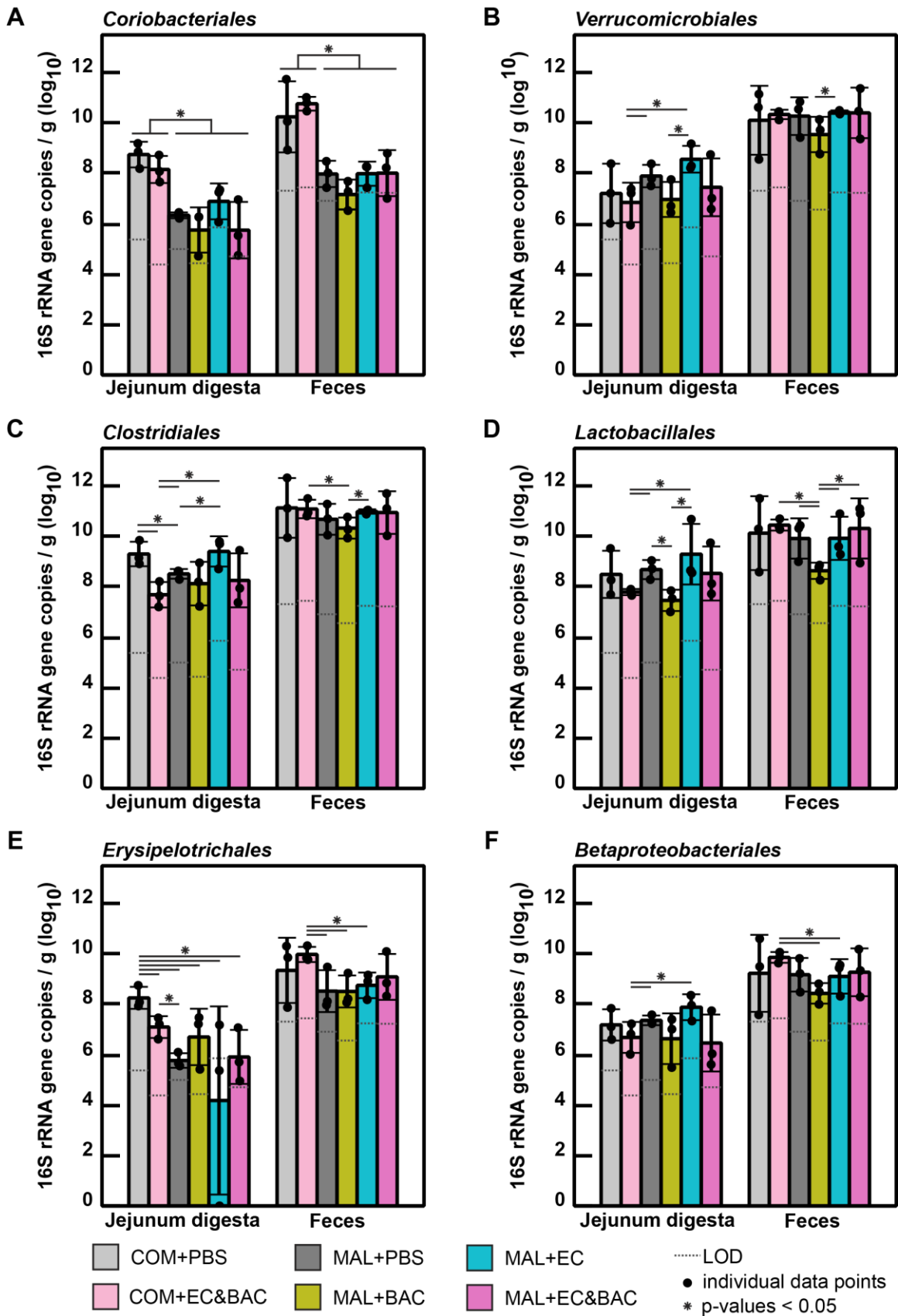


Figure 4. S4. Absolute quantification of 16S rRNA gene copy abundance of the resident bacterial orders in jejunum digesta and feces across six mouse groups. (A) *Coriobacteriales*, (B) *Verrucomicrobiales*, (C) *Clostridiales*, (D) *Lactobacillales*, (E) *Erysipelotrichales*, and (F) *Betaproteobacteriales*. Each animal group contained 3 mice euthanized over the course of 3 consecutive days (28, 29, and 30), one mouse per group per day. COM: complete, well-nourishing diet. MAL: malnourishing diet low in protein and fat, but containing the same amount of calories, vitamins, and minerals on the mass basis. PBS: no bacteria gavage control. BAC: gavage with five *Bacteroides/Parabacteroides* spp. isolates. EC: gavage with two *E. coli* isolates. EC&BAC: gavage with all seven bacterial isolates. LOD: limit of detection expressed as group average. Statistical significance was evaluated using Kruskal-Wallis test.

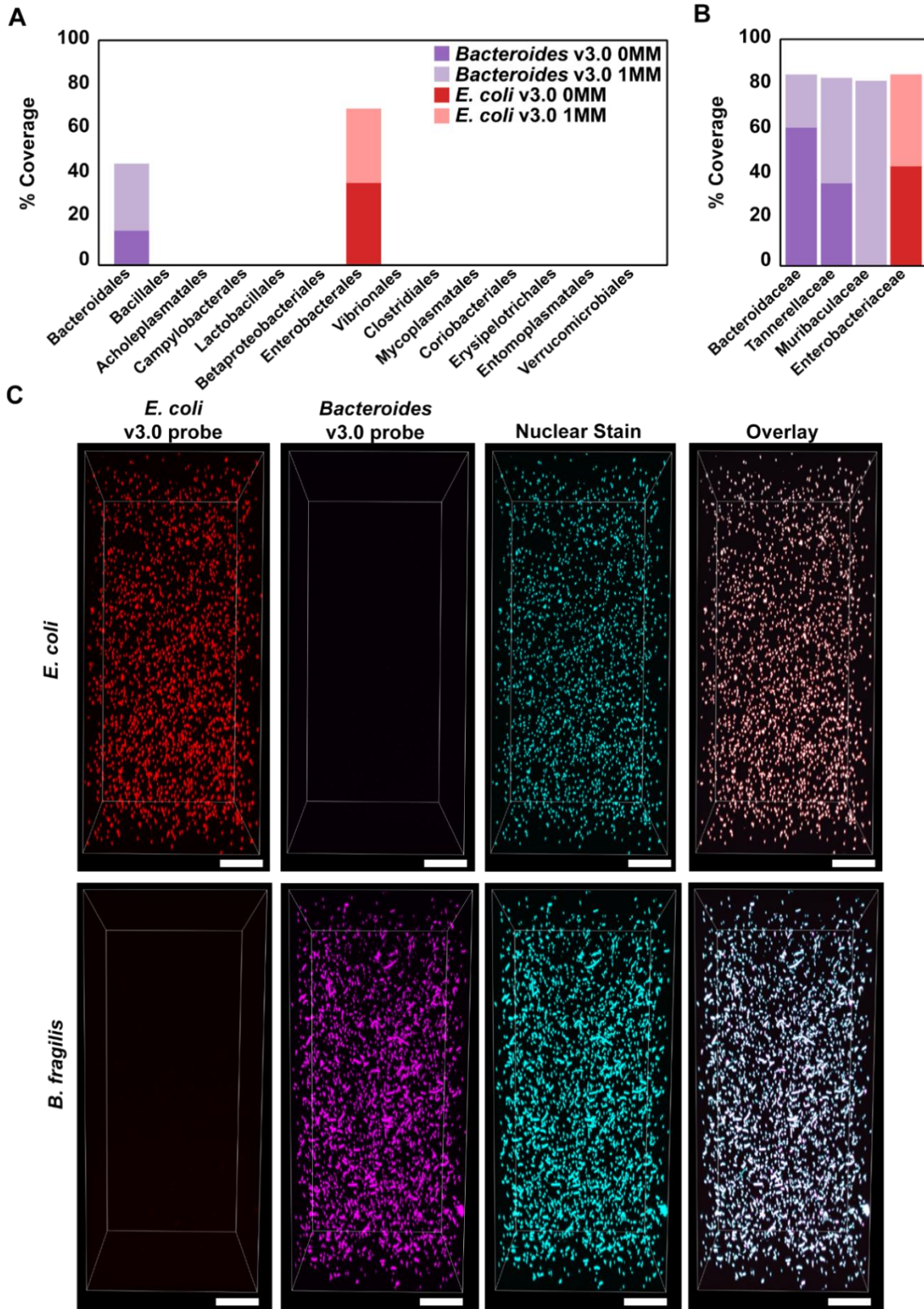


Figure 4. S5. HCR v3.0 probes designed using full 16S rRNA sequences of the gavaged bacterial isolates. One probe was designed for the two *E. coli* isolates and one for the five *Bacteroides/Parabacteroides* spp. isolates (referred to in the figure as *Bacteroides* probe) without a mismatch. (A) Coverage of bacterial orders detected (by sequencing) in the experimental mice with no mismatches (0MM) or 1 mismatch (1MM). (B) Coverage of relevant families in *Bacteroidales* and *Enterobacterales* orders. In panels (A) and (B) coverage is expressed as % of sequences in SILVA database that align with the probes if the specified number of mismatches is allowed. (C) Probe validation *in vitro* showing that the probes recognize their target, but do not cross-react with a model off-target even deep in the hydrogel. The validation was performed using single-isolate *in vitro* hydrogels, either *E. coli* or *B. fragilis*. Both hydrogels were stained with the two taxon-specific HCR v3.0 probes and counterstained with a nuclear stain. Scale bar = 100 μ m.

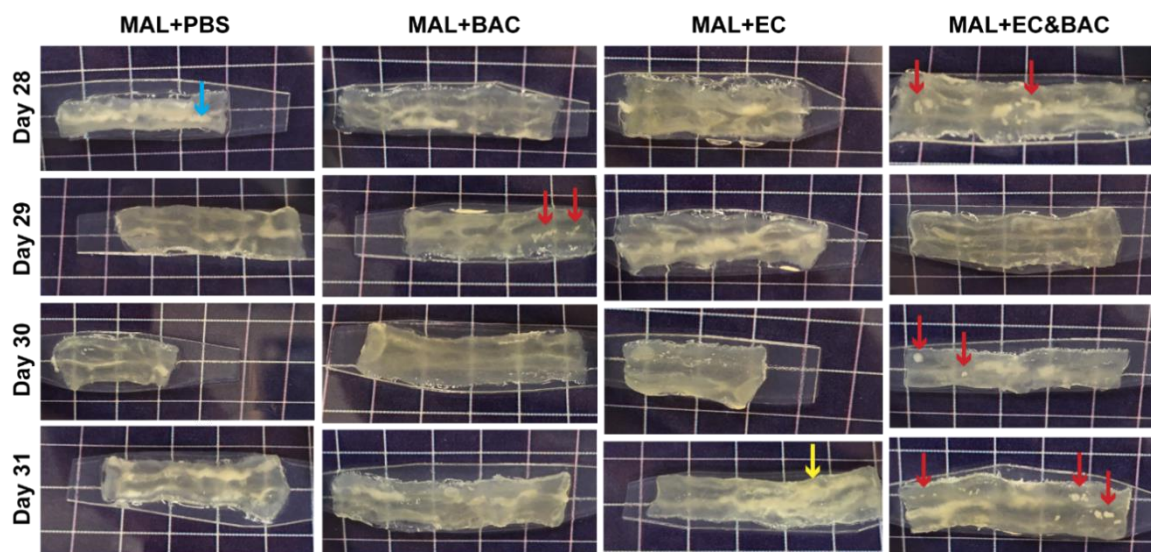
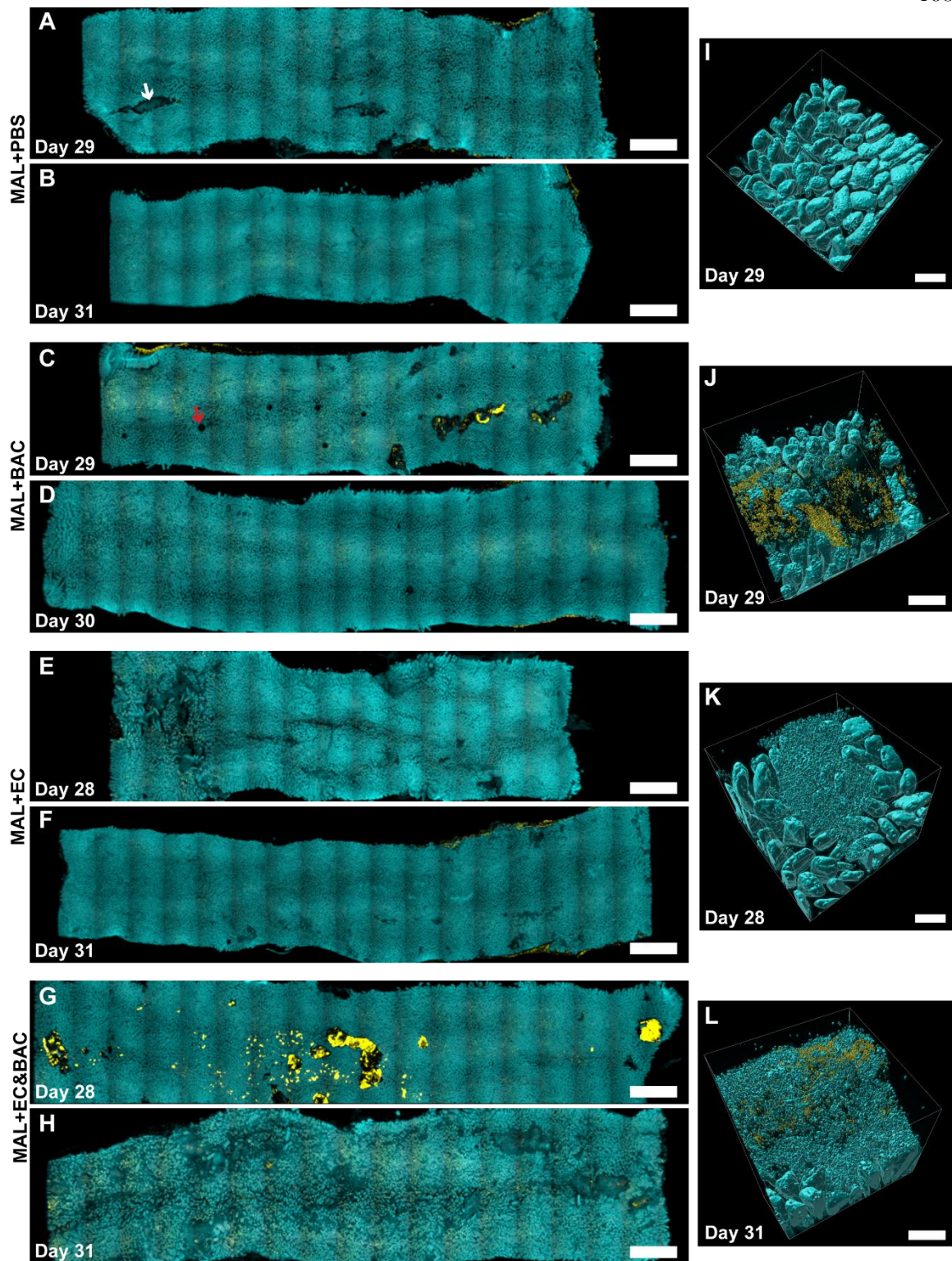


Figure 3. S6. Photos of empty jejunum segments after clearing. The mice were euthanized over the course of 4 consecutive experimental days (Day 28 (1st row), Day 29 (2nd row), Day 30 (3rd row) and Day 31 (4th row) of the experiment), with one mouse per group per day. Consistently, the mice were fasted for 1 h from 10 to 11 am and euthanized at 11 am, and the empty segment was identified in the 3rd quartile of the SI. On the mucosal side (facing out of the paper plane), large opaque tissue aggregates (red arrows) were visible in one mouse in MAL+BAC group (Day 29), and three mice in MAL+EC&BAC group (Day 28, 30 and 31). On the muscle side (facing into the paper plane), mesenteric margin (blue arrow) or tissue glue (yellow arrow) used to bond tissues to a solid support could give to opacity. However, opacity on the muscle side of the sample did not interfere with 3D imaging of the mucosa. Grid size = 6 mm.



imaged. Uneven illumination of a 5x objective used in the acquisition result in ripples. The streaks in the first MAL+PBS tissue occurred during tissue dissection (white arrow). The dark circles in the first MAL+BAC tissue are air bubbles trapped under the cover slip during tile scan acquisition (red arrow). Scale bar = 2 mm. (I-L) Example 3D CLARITY images for each group. Scale bar = 200 μm .